INTERNATIONAL DOCTORAL PROGRAM
IN SCIENCE
Double doctoral degree

Developments in holographic complexity and quantum information

Nicoló Zenoni

Dissertation presented in partial
fulfillment of the requirements
for the degree of
Doctor of Science (PhD): Physics -
Dottore di ricerca in Science
Ciclo XXXIV
S.S.D.: FIS/02

Supervisors:
Prof. Roberto Auzzi
Prof. Giuseppe Nardelli
Prof. Nikolay Bobev

December 2022

Developments in holographic complexity and quantum information

Nicoló ZENONI

N. Matricola (UCSC): 4816137
U-number (KU Leuven): 0132386

Coordinator:
Prof. Luca Gavioli
(Università Cattolica del Sacro Cuore)

Examination committee:
Prof. Mauro Spera, chair
(Università Cattolica del Sacro Cuore)
Prof. Roberto Auzzi, supervisor
(Università Cattolica del Sacro Cuore)
Prof. Giuseppe Nardelli, supervisor
(Università Cattolica del Sacro Cuore)
Prof. Nikolay Bobev, supervisor
(KU Leuven)
Prof. Fausto Borgonovi
(Università Cattolica del Sacro Cuore)
Prof. Thomas Van Riet
(KU Leuven)
Prof. Alice Bernamonti
(Università degli studi di Firenze)

Dissertation presented in partial fulfillment of the requirements for the degree of
Doctor of Science (PhD): Physics - Dottore di ricerca in Science
Ciclo XXXIV
S.S.D.: FIS/02

December 2022

"Never dance with tears in your eyes"
Ziggy

Acknowledgments

There are several people who have actively or indirectly contributed to this thesis, and deserve my sincere gratitude.

Foremost, I would like to thank my supervisors. Finding it needless to dwell on their fundamental scientific contributions, I express my gratitude to Prof. Roberto Auzzi and Prof. Giuseppe Nardelli for advises and precious assistance on matters that go beyond the research activity, and to Prof. Nikolay Bobev for his great hospitality and prompt availability. I can't thank all of you enough for allowing me to work in a relaxed and friendly atmosphere.

I thank the members of the Doctoral Committee for useful comments on my thesis. Thanks to Prof. Fausto Borgonovi for giving me the opportunity to hold Quantum Mechanics exercises lectures at Università Cattolica del Sacro Cuore. It has been an inspiring and amusing experience.

I'm grateful to Prof. Mauro Spera for notifying us about the role that Riemannian submersions could play in the relation between unitary and state complexity.

I'm also very thankful to all the people I collaborated with in these four years. In particular, I express my thanks to Prof. Gianni Tallarita and Dr. Fidel Ivan Schaposnik Massolo for their crucial contribution in the numerical approach to subregion volume complexity in Vaidya spacetime.

A special thank goes to Stefano, Andrea, and Bruno for the fruitful (and funny!) online discussions. How to forget the long meeting at night (ok, I forgive you, it happened only once).

I'm really grateful to the KU Leuven doctoral student Vincent Van Hemelryck for taking care of the Dutch translation of my abstract.

I would also like to thank the Ermenegildo Zegna's Group for awarding me the Ermenegildo Zegna Founder's Scholarship, which financially supported my PhD

research project.

I thank the Theoretical Physics Group at KU Leuven for having welcomed me with warmth and kindness.

Thanks to all the guys of the 2019 Solvay Doctoral School too. I learned a lot and had a great time with you in Paris and Geneva.

Importantly, I wish to thank Selene, Silvia, Chahan, and the (ex and current) PhD students in Brescia with whom I shared this experience: Andrea (spero che riusciremo a vederci più spesso in futuro e ad incastrare qualche partita di tennis), Vale, Cassio, Vincenzo, Luca, Iuliia, Ali, Alessandra, Chiara.

Thanks a lot to Paolo and Sonia for their useful tips on the bureaucratic stuff.

Thanks to my office mates Giulia, Nicola, and especially Sana for the really good time we spent at the "second floor office".

Grazie a Laura, con cui ho condiviso un fantastico anno in Belgio. Ebbene sì, fantastico nonostante l'improvvisa pandemia, i mesi di lockdown, Ziggy e la casa di Eric con annessi e connessi. Nei mesi difficili del 2020 non so come avrei fatto senza qualcuno su cui fare affidamento. Grazie.

Grazie a Teo, a partire dagli indimenticabili sei mesi passati in Belgio come coinquilini. Uno dei periodi più belli, durante il quale ho trovato un amico su cui contare al di fuori del dottorato. Grazie per avere alleggerito l'ultima fase di questa esperienza.

Doveroso tornare a Stefanone, con cui ho per brevi periodi condiviso uno dei tanti uffici tra cui ho peregrinato. Al di là delle collaborazioni scientifiche, grazie per i chiarimenti, i consigli, le lunghe chiacchierate.

Grazie infine a tutte le persone esterne all'università che mi sono state vicine in questi anni.

Un grazie di cuore a Marty, tu e Teo mi avete sempre fatto sentire a casa.

Grazie a Paolo e Ale per esserci sempre.

Grazie a mamma, papà, Matteo, e alla nonna. Qualunque frase fatta risulterebbe banale. Semplicemente, grazie di tutto.

Abstract

In the holographic framework, complexity is supposed to capture the interior of black holes, overcoming the limitations of entanglement entropy. This thesis debates the interplay between the two quantities, covering complexity aspects in the quantum information and holographic realms.

Complexity quantifies the hardness of implementing an operator or preparing a quantum state through elementary operations. Huge arbitrariness stems from the identification of operations with high computational cost. For an n-qubit system, we detect a choice compatible with exponential lower bounds and chaotic behavior of operator complexity, as required to mimic black hole interiors. Then, we analyze the relation between operator and state complexity using the formalism of Riemannian submersions.

Several candidates have been proposed for the dual of state complexity: the volume, the gravitational action, and the spacetime volume of proper bulk regions. Specializing to subsystems, we explore the conjectures in various static settings, finding that subsystem complexity and entanglement entropy contain different information. The same conclusion holds for a holographic global quench, during which subsystem volume complexity evolves non-monotonically in time, contrary to entanglement entropy.

Finally, we study an example of local quench in which entanglement entropy suffices to discern between diverse holographic realizations.

Sommario

Nel contesto olografico, si ritiene che la complessità catturi l'interno di buchi neri, superando i limiti dell'entropia di entanglement. Questa tesi discute l'interrelazione tra le due quantità, trattando aspetti della complessità negli ambiti dell'informazione quantistica e dell'olografia.

La complessità quantifica la difficoltà nell'implementare un operatore o preparare uno stato tramite operazioni elementari. Considerevole arbitrarietà emerge dall'identificazione di operazioni con elevato costo computazionale. Per un sistema di n qubit, rileviamo una scelta compatibile con un comportamento caotico della complessità di operatori, richiesto per mimare l'interno di buchi neri. Analizziamo poi la relazione tra complessità di operatori e stati mediante il formalismo delle sommersioni Riemanniane.

Diversi candidati sono stati proposti come duale della complessità di stati: il volume, l'azione gravitazionale, e il volume di spaziotempo di opportune regioni. Specializzandoci su sottosistemi, esploriamo le congetture in varie configurazioni statiche, deducendo che la complessità per sottosistemi e l'entropia di entanglement contengono differente informazione. La medesima conclusione si applica ad un modello olografico di quench globale, per il quale la complessità di volume per sottosistemi evolve in maniera non monotòna, contrariamente all'entropia di entanglement.

Infine, studiamo un esempio di quench locale per cui l'entropia di entanglement risulta sufficiente a discernere tra diverse realizzazioni olografiche.

Beknopte samenvatting

Complexiteit wordt verondersteld de binnenkant van zwarte gaten op een holografische manier te beschrijven en zo de beperkingen van verstrengelingsentropie te overstijgen. Dit proefschrift behandelt aspecten van complexiteit in de kwantuminformatie en holografie, en stelt de rol van de verstrengelingsentropie in vraag.

Complexiteit kwantificeert de hardheid van een operator implementeren of een kwantumtoestand voorbereiden door middel van elementaire operaties. Enorme willekeur komt voort uit de identificatie van operaties met hoge rekenkosten. Voor een systeem van n qubits detecteren we een bestraffing die compatibel is met chaotisch gedrag en voldoet aan exponentiële ondergrenzen van operatorcomplexiteit, zoals vereist om het interieur van zwarte gaten na te bootsen. Vervolgens analyseren we de relatie tussen operator- en toestandscomplexiteit met behulp van het formalisme van Riemanniaanse submersies.

Er zijn verschillende kandidaten voorgesteld voor de duale van de toestandscomplexiteit: het volume, de zwaartekracht actie en het ruimtetijdvolume van de passende bulkgebieden. Gespecialiseerd in subsystemen, we onderzoeken de vermoedens in diverse statische configuraties, vinden dat de subsysteem complexiteit draagt andere informatie dan verstrengelingsentropie. Dezelfde conclusie geldt voor een holografische globale quench, waarbij de subsysteem-volumecomplexiteit niet monotoon te evolueren, in tegenstelling tot verstrengelingsentropie.

Ten slotte bestuderen we een voorbeeld van lokale quench waarin verstrengelingsentropie voldoende is om onderscheid te maken tussen diverse holografische realisaties.

Contents

List of Figures

List of Tables

Chapter 1

Introduction

The quantum gravity puzzle. Several aspects of our Universe have been unraveled thanks to two cornerstones of modern physics: *general relativity*, a classical theory of gravity formulated by Einstein in 1915, and *quantum mechanics*, progressively developed at the beginning of the twentieth century thanks to the contributions of disparate physicists. Working side by side, but each in its own regime of validity, the two theories cover the whole range of physical scales, from the macroscopic domain governed by general relativity, to the subatomic world ruled by quantum mechanics. The success of the two descriptions relies on the fact that they are generally independent of each other: at the macroscopic level quantum effects are negligible, whereas at the microscopic level gravity is weak compared to the other fundamental (electromagnetic, weak, and strong) forces.
However, this strict distinction fades when a system exerts an extremely high gravitational field on small scales, as it happens at the singularity from which our Universe originated, or in the interior of *black holes* (BHs). In both cases, general relativity and quantum mechanics are required to cooperate. The naive quantization of general relativity, although, leads to a non-predictive (technically, a *non-renormalizable*) theory, which has left an important missing piece in the fundamental physics for many years.

Ironically, the breakthrough came thanks to a theory developed for a completely different purpose. Physicists realized that *string theory*, originally aimed to the description of strong interactions between particles, perfectly fits in the *quantum gravity* puzzle. As all the major scientific revolutions, string theory is accompanied by a drastic paradigm shift: instead of ideal point-like particles, the basic constituents of Nature are supposed to be oscillating one-dimensional

strings. In this picture, each observed physical particle is characterized by specific oscillation modes of the constituent strings. Notably, the *graviton*, responsible for the mediation of the gravitational force, is among such particles. So, string theory can be regarded as a putative unifying theory for all the fundamental interactions, including the gravitational one.

The Plato's cave. It was in this fruitful scenario that in 1997 Maldacena [1] came out with one of the most exciting discoveries of the last decades. What goes under the acronym of AdS/CFT is something incredibly deep, which builds a fundamental bridge between specific theories of gravity and quantum field theories enjoying conformal invariance, known as *conformal field theories* (CFTs). The bottom line is that classical general relativity and quantum mechanics are not totally unrelated, but rather two sides of the same coin, two complementary representations of the same reality.

The highly effective analogy with the Plato's cave, borrowed from Polyakov [2], conveys the message pretty well. In the Plato's myth, prisoners are forced to watch the projected shadows of real objects on a wall. Having never experienced the outside world, the men are not aware that what they stare at on the wall is just the fictitious remnant of a higher-dimensional external reality. The AdS/CFT correspondence parallels our struggle in studying strongly coupled CFTs to the condition of the prisoners into the cave. The $(3+1)$-dimensional Minkowski spacetime, where a CFT can be located, lies at the boundary of a $(4+1)$-dimensional world, named *anti-de Sitter* (AdS) *spacetime*, which is governed by a gravitational theory. The crucial and profound difference with the Plato's allegory is that the two descriptions are *equivalent*: the reality on the $(3+1)$-dimensional boundary contains exactly the *same* information as the reality into the $(4+1)$-dimensional world. Similarly to a *hologram*, in passing from higher to lower dimensions information is not lost, but simply written in a harder language, that of CFTs. Moreover, when the gravitational theory is classical, the lower-dimensional CFT is strongly coupled. So, once the dictionary translating one language into the other has been understood, the classical gravitational theory can be employed to address challenging problems in the strongly coupled quantum realm.

Holography is rooted well before AdS/CFT, in the wake of the formulation of the *laws of BH mechanics*. By analogy with the laws of thermodynamics, the picture of a BH as a thermodynamic system has emerged. As such, a BH radiates with a temperature proportional to its *surface gravity* [3] and is characterized by a thermal entropy, which was discovered by Bekenstein and Hawking to be proportional to the area of the BH event horizon [3, 4]. The scaling of the entropy with the area, rather than the volume, suggests that a BH may admit a lower-dimensional description in terms of boundary degrees of freedom roughly quantified by the thermal entropy, thus paving the way towards

holography. In 1994, based on this important result and on a preliminary idea by t'Hooft [5], Susskind introduced in string theory the *holographic principle*, basically the thought that gravitational systems may be fully described by lower-dimensional systems [6]. Shortly after, AdS/CFT provided a concrete realization of this principle.

Far from being limited to an equivalence between a four-dimensional and a five-dimensional theory, AdS/CFT can be generalized to arbitrary d boundary dimensions and $d+1$ bulk dimensions. Moreover, the correspondence holds true for spacetimes resembling AdS nearby the boundary, referred to as *asymptotically* AdS spacetimes. Imagine for instance to introduce a BH deep inside AdS. This obviously modifies the bulk spacetime, but far away from the BH the geometry is essentially indistinguishable from vacuum AdS. This does not mean that the CFT placed at the boundary of AdS is insensible to the existence of the BH. As any object into the Plato's cave casts a distinctive shadow on the wall, any modification of AdS spacetime leaves a perceivable mark in the boundary CFT. The sign left by BHs is *temperature*. Technically, a gravitational theory in $(d+1)$-dimensional AdS containing a BH is equivalent to a d-dimensional CFT at finite temperature, living at the AdS boundary. Bearing in mind the depiction of a BH as a thermodynamic system with a given temperature, this should not be surprising.

Quantum information and gravity. The great opportunity to access strongly interacting quantum systems modeled by CFTs at finite temperature with the common methods of classical gravitation has generated a wave of excitement in the whole physics community. As a result, unexpected connections between high energy physics and other disparate subject areas have been unveiled. Among the applications of AdS/CFT, we mention the study in the field of *nuclear physics* of the properties of the quark-gluon plasma [7], which is supposed to reproduce the state of the early Universe soon after the Big Bang, and the investigation in the field of *condensed-matter physics* of so-called holographic superconductors [8]. In this thesis we will mostly focus on another interrelation, elapsing between gravity and *quantum information*, the science studying the amount of information encoded in quantum states.

The first hint of a bridge between these two seemingly distinct branches may be probably traced back to the dawn of holography, namely to the Bekenstein-Hawking formula. Indeed, this finding links an information theory quantity, as the entropy, to a gravitational system, as a BH. But this is just the top of the iceberg. The fundamental unit of quantum information is the *qubit*, the quantum version of the classical *bit*. A system of qubits can be in an *entangled* state. This happens when a measurement performed on a single qubit also reveals the state of the others, no matter how far apart they are. An estimation of the degree of entanglement for a given bipartition of a system is provided by the *von*

Neumann entropy, aka *entanglement entropy*, which can be thought of as the entropy detected by an observer who cannot directly access the whole system. In a way, the effect can be likened to the presence of an event horizon hiding the inaccessible region. Emboldened by this interpretation, one may ask whether the Bekenstein-Hawking outcome applies to the entanglement entropy too. The key answer came in 2006 by Ryu and Takayanagi, who proposed the entanglement entropy of a CFT state to be related to the area of extremal surfaces into the higher-dimensional AdS spacetime [9, 10]. This remarkable prescription has acted as a source of inspiration for the search of further mappings between quantum information notions and geometrical quantities. The same source that partly inspires the present thesis work.

A probe of black hole interiors. Let us go back to the model of a BH in AdS. Every BH, being it eternal or formed by the gravitational collapse of matter, is not a static object. Rather, its interior keeps growing, and it does for extremely long times. In the Plato's allegory, when some modifications are performed on an object into the cave, something should happen to its shadow too. Similarly, the evolution of the BH interior should be somehow detectable in the quantum thermal system accommodated at the AdS boundary. A guess would be to look at entanglement entropy, which can act as a probe of quantum thermalization processes. However, it ceases to evolve once the system reaches the thermal equilibrium, which happens well before the BH interior stops growing. So, there should be some features of quantum states to which entanglement entropy is not sensitive. In 2014 Susskind proposed that the solution should be sought in the quantum information repository, among the quantities not taken into account until then by the high energy physics community. It was time for *computational complexity* to enter the game [11].

Complexity was introduced in the field of computer science to assess the difficulty of a computational task. In the context of quantum systems, the task can be visualized as the construction of a quantum state from a reference one by the implementation of elementary operations, called *gates*. A sequence of gates constitutes a *circuit*. Clearly, a given task can be accomplished by several circuits. Complexity of the target state looks at the optimal one, and is thus defined as the minimum number of gates doing the job. In chaotic random circuits, complexity has been shown to increase at a constant rate for a time exponential in the number of qubits involved by the circuit, prior to saturation to an exponential value [12]. The major appealing feature which caught Susskind's attention is the growth of complexity long after thermalization, just like the interior of a BH. Hence the proposal that the gravitational counterpart of complexity should explore the physics beyond the BH event horizon. But the road to establishing a new entry in the AdS/CFT dictionary is long and steep.

The challenge is two-fold. First, the gravitational quantity corresponding to

complexity needs to be specified. A good candidate should measure the BH interior, and should evolve in time in the same way as complexity for chaotic systems. At the state of the art, we recognize three main proposals: the volume of the wormhole traversing the BH (CV conjecture) [11, 13, 14], the gravitational action of a properly defined causal region stretching far beyond the event horizon (CA conjecture) [15], and the spacetime volume of the same region (CV 2.0 conjecture) [16]. All the three quantities evolve and respond to perturbations likewise complexity in random circuits. Recently, it has been argued that such features are shared by an infinite class of observables ("does complexity equal anything?") [17, 18]. This uncertainty in the selection of the gravitational dual may reflect the ambiguities affecting complexity, such as the choice of reference state and simple gates. More comments on the holographic proposals can be found in Ch. 2, where useful details for the comprehension of the rest of the thesis are addressed too.
Second, AdS/CFT does not involve a general quantum mechanical system, but a far more complicated quantum field theory, which calls for a continuous definition of complexity more suitable than the discrete counting of gates. One of the promising approaches to attack the issue is based on the generalization of a geometric method originally proposed by Nielsen in the context of qubits systems [19]. Actually, the Nielsen's approach, dating back to around 2005, aimed at finding lower bounds to quantum complexity, thus treating the geometric formulation as a convenient *approximation*. Lately, *complexity geometry* has been reevaluated as a proper *definition* of quantum complexity.

Geometry of quantum complexity. It is good to pause here and sketch the Nielsen's approach. Complexity is roughly a measure of how "far" the initial configuration is from the target one. The farther the two configurations, the more complex the target state. To fix ideas, let us take as states the whole Earth times a single spin up and the whole Earth times a single spin down. Though the two states are orthogonal, it is pretty easy to build one from the other: it just requires the flipping of a single spin. In the complexity sense, the two states are near. The story would be completely different if the two Earths had also different meteorological conditions, in which case the two states would be far in complexity [20]. Now, let us imagine any state of a quantum system to be represented by a point on a manifold. In this picture, the distance between states acquires a clear geometric interpretation: it is the *length* of the *shortest* path leading from the initial to the target point. Traveling a path means to apply a *unitary* transformation, as the time evolution operator. Clearly, by just changing the phase of a state no progress is made in reaching the target. So, it is not restrictive to employ *special unitary* transformations, which disregard the overall phase. To be brief, in the following we will refer to them simply as unitary transformations. As a path is composed by single steps in specific directions, a unitary transformation consists of a sequence of fundamental gates,

gradually transforming the initial state into the target one. However, gates are not equally hard to be implemented. For instance, it is reasonable to suppose that entangling two spins requires much more computational effort than flipping a single spin. The hardness of a fundamental operation can be reproduced by stretching the manifold in the corresponding direction. As a result, the motion in hard directions costs more in terms of distance, and is thus discouraged in the selection of the optimal path. The "stretching scheme", specified by a set of coefficients named *penalty factors*, which dictate the directions to be stretched and the amount of deformation, crucially affects the complexity properties.

One of the points we address in this thesis is to understand which kind of penalization schedules cause complexity geometry to reproduce the behavior of BH interiors, which in turn is mimicked by complexity in chaotic random circuits. To gain some insights, in Ch. 3 we focus on a system of a large number n of qubits, and we study two penalization schemes: the *draconian* model, in which all gates acting on more than two qubits are equally penalized, and the *progressive* model, in which penalties scale exponentially with the number of qubits involved by the corresponding gate. We start by analyzing the complexity of implementing a unitary operator acting on an n-qubits state, e.g. the time evolution operator. To this purpose, we work on the manifold of special unitary transformations $\mathrm{SU}(2^n)$. A fundamental property we ask for is that maximal complexity geometry, namely the maximum distance between any pair of points on the unitary manifold, is exponential in n. While in the draconian case an exponential lower bound was already been found by Nielsen and collaborators [21], we provide a first evidence of such a bound in the progressive model. Another feature we look at is *ergodicity* of geodesics, required for complexity geometry to be compatible with quantum chaos. Ergodicity is intimately related to negativity of sectional curvatures [22], that is attained for large penalty factors. We argue that in the draconian model negative curvatures are divergent, whereas in the progressive model they remain finite. A smooth behavior of sectional curvatures is necessary for complexity geometry to respond to perturbations as quantum circuit complexity [23], making the progressive schedule more suitable than the draconian one. One may feel puzzled about the huge arbitrariness in the choice of penalty factors, which must be fixed at hand, especially in view of their influence on the properties of complexity. A preliminary answer to this objection has been put forward in [24], where it has been conjectured that long-distance complexity geometry is essentially the same for a wide family of penalization schemes.

The outcomes we have discussed so far refers to the so-called *unitary complexity*. We can take advantage of this notion to determine complexity of a quantum state. Indeed, a quantum state can be built in many ways through the application of a proper unitary operator to a reference state. *State complexity* is defined as

the minimal complexity of all operators completing the task. In the geometric approach, this translates into the length of shortest paths on the *complex projective space* $\mathbb{CP}^{2^n-1}$, being the manifold of n-qubits states where directions differing by an overall phase are identified. While the unitary manifold $\mathrm{SU}(2^n)$ is homogeneous, the state manifold $\mathbb{CP}^{2^n-1}$ is not, which makes the analysis much harder. For instance, the non-homogeneity of the state manifold causes sectional curvatures to be position-dependent. To bypass the obstacle, we propose to work in the formalism of *Riemannian submersions* [25], of which the relation between unitary and state complexity is a particular realization. In this frame, sectional curvatures on the state manifold can be inherited by sectional curvatures on the unitary manifold [25], and do not necessarily demand for a direct inspection. The same holds for geodesics on the space of states [26], whose length is interpreted as state complexity. Anyway, we also provide a closed-form expression for the metric on the state manifold with unspecified penalization schedule, which potentially gives us access to the main geometric properties of interest.

Extending the Nielsen's method to quantum field theories, complexity has been studied for a particular class of states, referred to as *Gaussian states*, in non-interacting quantum field theories containing bosons [27, 28] or fermions [29, 30]. Even though the quantum theories in which we expect a match with the gravitational results are strongly interacting CFTs, complexity geometry in the non-interacting regime already reproduces the general ultra-violet divergences structure of the holographic proposals. Partial extensions of complexity geometry to two-dimensional [31, 32] and higher-dimensional [33] CFTs has been later put forward.

Complexity for mixed states. All the machinery we have been discussing applies to *pure states*. The quantum information concept for which the holographic dual is known, namely entanglement entropy, is not only a property of states, but also depends on the bipartition of a system into smaller subsystems. In general, a subsystem can be in a *mixed state*, expressing the impossibility for an observer to access the whole system. In these cases, similarly to the entropy, complexity calls for a generalization. The new quantity playing this role, which we refer to as *subregion complexity*, should obviously reduce to the more familiar complexity notion when the subsystem is extended to the whole system. To date, there are several candidates [34], most of which rely on the *purification* procedure. Instead of seeing the subsystem state from the limiting observer's point of view, a purification describes it as the remnant of the state of a larger system after tracing out the external degrees of freedom. The state being traced out is known as *purification*, and its complexity is well-posed. Actually, a purification is not unique. The now familiar way out is to simply pick the optimal purification, that is to say the less complex one. This leads

to a possible definition of subregion complexity, named *purification complexity*, as the minimum complexity of all existing purifications. With this technique, subregion complexity has been studied for the thermal and vacuum state of a free quantum field theory [35], and for the vacuum state of two-dimensional CFTs [36]. An alternative definition is based on splitting the construction of the target state into two steps: preparation of the spectrum and preparation of the basis of eigenstates. Once the spectrum is prepared through the purification procedure, the target state can be built by a change of basis. The complexity in performing this last task is referred to as *basis complexity*. See for instance [37] for an application of this method to Gaussian states in a lattice of harmonic oscillators.

With a new entry in the quantum information catalog, the tantalizing next step is to search for a gravitational counterpart, with the main guiding principles being the three holographic conjectures for complexity. Going back to the takeaway message of AdS/CFT, a CFT is equivalent to a gravitational theory in higher-dimensional AdS. Then, if an observer can only access a CFT subregion, we reasonably expect this limitation to also affect the gravitational theory. The AdS region encoding all information on the boundary CFT state of a subsystem is referred to as *entanglement wedge*, and is identified with the causal bulk region anchored at the Ryu-Takayanagi surface and the boundary subsystem itself [38]. In turn, the gravitational partner of subregion complexity is conjectured to be nothing else but the gravitational partner of complexity (volume, action or spacetime volume) restricted to the entanglement wedge. We talk about subregion-CV [39], subregion-CA, and subregion-CV 2.0 conjecture [40], respectively. Each holographic proposal may correspond to a different definition of subregion complexity in the boundary CFT, or some conjectures may be discarded. The latter possibility may additionally be used as an argument to rule out some of the original proposals for holographic complexity. With that in mind, in Ch. 4-6 we explore the three conjectures for subregion complexity in various settings.

In Ch. 4, we explicitly compute subregion-CA and subregion-CV 2.0 for a boundary line segment in both AdS_3 and the Banados-Teitelboim-Zanelli (BTZ) spacetime [41, 42], which represents an eternal BH in AdS_3. In order to regularize the computation, we cutoff the spacetime nearby the boundary, where divergences arise. The actual result is obtained in the limit of vanishing cutoff. Subregion-CA and subregion-CV turn out to be the sum of a linearly divergent term in the cutoff, a finite constant, and a term proportional to the entanglement entropy of the mixed state localized on the boundary segment. For a two-segments subregion additional terms appear, suggesting that the interconnection between subregion complexity and entanglement entropy, if it exists, is not so straightforward. We also comment on the dependence of subregion-CA on

an arbitrary scale $\tilde{L}$, arising from the null boundary counterterm ensuring reparametrization invariance of the full gravitational action. The parameter $\tilde{L}$ strongly affects properties such as additivity and temperature behavior, posing doubts on the physical interpretation of subregion-CA. A possibility is to associate this ambiguity to the degree of arbitrariness characterizing subregion complexity, such as the choice of reference state.

In Ch. 5 we work with a deformation of AdS_3, known as *warped* AdS (WAdS) spacetime [43, 44]. Along the way towards a putative duality involving asymptotically non-AdS spacetimes, such as de Sitter or Minkowski, WAdS represents a midway point for which we have more control on the field theory dual. A duality is in fact conjectured [45, 46] between a gravitational theory in asymptotically WAdS and a boundary *warped conformal field theory* (WCFT), being a $(1+1)$-dimensional non-relativistic field theory whose global symmetries are a subgroup of those of a CFT [47–49]. This WAdS/WCFT correspondence is an interesting laboratory in which to look for generalizations of holographic results. Remarkably, entanglement entropy in WCFTs has been shown to match the gravitational computations in WAdS [50–54]. This motivates us to test the holographic proposals for subregion complexity in asymptotically WAdS.
In detail, we explore all the three conjectures for a two-sided (non-)rotating BH in WAdS, taking as a subregion the whole left (right) boundary time slice. Compared to the BTZ case, additivity and temperature dependence of subregion-CA are not influenced by the arbitrary length scale $\tilde{L}$ arising from the action counterterm. Instead, we detect a correlation between the sign of specific heat at constant angular momentum and the temperature behavior of holographic subregion complexity.

Even though subregion complexity in quantum field theory is still in its infancy, in the conclusions of this thesis we outline a preliminary comparison of our holographic results with purification and basis complexity expectations.

Quantum information and quenches. Other settings in which quantum information can be employed to uncover interesting physics are out-of-equilibrium systems. Simple prototypes of thermalization processes are represented by *quantum quenches*, which describe the unitary evolution of quantum states after a sudden modification of physical parameters [55, 56]. In this context, entanglement entropy has proved to be a powerful diagnostic tool [57–60]. Thanks to the AdS/CFT correspondence, the challenging investigation of far from equilibrium processes taking place in a strongly coupled d-dimensional CFT can be traced back to dynamical problems in the $(d+1)$-dimensional bulk gravitational theory [61–65]. Complexity has also been employed as a probe of quantum quenches, both by field theories [66, 67] and holographic methods [68–72]. It would be valuable to check whether subregion complexity can be used for the same purpose.

In Ch. 6 we move in this direction, calculating subregion-CV for a boundary line segment in $(2+1)$-dimensional Vaidya spacetime. This background represents the formation of an AdS BH caused by the gravitational collapse of a shell of null matter falling from the spacetime boundary. The corresponding process in the dual CFT is a *global quench*, triggered by an homogeneous injection of energy into the whole system [73]. Similarly to entanglement entropy, we find that holographic subregion complexity reaches a constant value after thermalization. However, while entanglement entropy monotonically increases [74, 75], subregion complexity manifests a maximum prior to saturation. Again, the two quantum information concepts seem to provide different information.

Global quenches are not the only family of non-equilibrium phenomena. For example, we can imagine to locally perturb a system and to study how the perturbation spreads. This process is modeled by a *local quench*, which is holographically realized by the free fall of a massive object in AdS [76]. In Ch. 7, drawing a parallel between a falling BH and a falling monopole, we address the question of how the details of the object impact the quench physics. Compared to the BH quench, the monopole quench is additionally accompanied by the expansion of a scalar condensate. Surprisingly, whether energy conservation of the quenches hold, the holographic energy-momentum tensor does not significantly distinguish between the two bulk configurations. Instead, holographic entanglement entropy accomplishes the job. The BH quench is indeed compatible with the propagation of free Einstein-Podolski-Rosen pairs of entangled quasiparticles generated by the perturbation [57], while the monopole quench is interested by a concomitant expansion of the scalar condensate. Being sensitive to the spread of entanglement, entanglement entropy turns out to be an efficient probe to discern the two holographic realizations. Quantum information expresses its tight interconnection with gravity.

We conclude our journey in Ch. 8, with a summary of the main original results and some tips for further developments.

Chapter 2

Holography and complexity

In this chapter, mainly following the reviews [77–83], we introduce the fundamental notions necessary to understand the rest of the thesis. In Sec. 2.1 we explain the core ideas of the AdS/CFT correspondence. In Sec. 2.2, after briefly introducing the notion of entanglement entropy, we discuss its holographic interpretation in the context of CFTs as the area of minimal surfaces in higher-dimensional AdS. This prescription, due to Ryu and Takayanagi, represents a milestone in the discovery of a deep interconnection between gravity and quantum information, and will be employed several times throughout the thesis. Despite its central role for the understanding of how the bulk spacetime emerges from the boundary CFT, in Sec. 2.3 we argue that entanglement entropy is not enough to probe the interior of BHs. This job is supposed to be fulfilled by computational complexity, a quantum information quantity measuring the hardness of building quantum states. In Sec. 2.4 we describe the time evolution of complexity in quantum circuits and the way it reacts to perturbations. Both features of complexity are mimicked by the model of a particle moving on a two-dimensional hyperbolic space, which is outlined in Sec. 2.5. The toy model, in which complexity is identified with the distance of the particle from the origin of the hyperbolic space, hints at a possible continuous definition of complexity. As such, it represents an interesting playground to anticipate the importance of negative curvature in relation to complexity, that we discuss in the next chapter. Finally, in Sec. 2.6 we turn to the holographic interpretation of complexity as a quantity exploring BH interiors. To this regard, we discuss the conjectured gravitational counterparts and comment on their pros and cons.

2.1 The AdS/CFT correspondence

Dualities have proven to be important tools to deepen our comprehension of several physical phenomena, by unveiling intimate connections between them. Basically, a *duality* establishes a mathematical equivalence between two physically different theories. Concretely, the dual theories lead to the same result for physical observables. One of the most stimulating breakthroughs of the last decades is the proposal of a duality between gravitational theories and specific gauge theories without gravity. In particular, this *gauge/gravity duality*, better known as *AdS/CFT correspondence*, involves a theory of gravity in anti-de Sitter (AdS) spacetime and a lower-dimensional conformal field theory (CFT) living on the AdS boundary. This discovery paved the way for both a new interpretation of gravity and an alternative approach to investigate strongly coupled field theories. Prior to getting into the details of the correspondence, we briefly introduce the two protagonists of our story.

2.1.1 AdS spacetime

Anti-de Sitter spacetime in $d+1$ dimensions (AdS_{d+1}) is a solution to the Einstein's field equations in vacuum

$$R_{\mu\nu} - \frac{1}{2} R\, g_{\mu\nu} = -\Lambda\, g_{\mu\nu} \tag{2.1.1}$$

with negative scalar curvature R and negative cosmological constant Λ:

$$R = -\frac{d(d+1)}{L^2}\,, \qquad \Lambda = -\frac{d(d-1)}{2L^2}\,. \tag{2.1.2}$$

The parameter L is called AdS *curvature radius* and denotes the typical length scale of the geometry. AdS_{d+1} can be naturally described by an embedding into the higher-dimensional flat space $\mathbb{R}^{2,d}$ with signature $(-,+,\ldots,+,-)$. Namely, it is the set of points $\left(X^0, X^1, \ldots, X^{d+1}\right)$ constrained by

$$-\left(X^0\right)^2 + \sum_{i=1}^{d} \left(X^i\right)^2 - \left(X^{d+1}\right)^2 = -L^2\,. \tag{2.1.3}$$

The analogy with the hypersphere definition makes it clear that AdS_{d+1} has isometry group $\mathrm{SO}(2,d)$. We point out that this group contains $(d+2)(d+3)/2$ generators, which is the maximum number of isometry generators allowed in $d+1$ dimensions. Therefore, AdS spacetime is said to be *maximally symmetric*.

Among the possible coordinate systems satisfying eq. (2.1.3), we just focus on the two choices employed in this thesis work.

The first set (τ, ω^i, r), referred to as *static coordinates*, is given by

$$\begin{aligned} X^0 &= L\sqrt{1+r^2}\,\cos\tau\,, \qquad X^{d+1} = L\sqrt{1+r^2}\,\sin\tau\,, \\ X^i &= Lr\omega^i\,, \qquad \sum_{i=1}^{d}\left(\omega^i\right)^2 = 1\,. \end{aligned} \tag{2.1.4}$$

In the above expressions, $\tau \in [0, 2\pi[$ is a compact timelike coordinate, ω^i with $i = 1, \ldots, d$ are coordinates parametrizing a $(d-1)$-dimensional sphere, and $r \in [0, +\infty[$ is a radial coordinate. In order to avoid closed timelike curves, we consider the universal cover obtained by a decompactification of the timelike coordinate, which is thus assumed to range in $-\infty < \tau < +\infty$.
Introducing the area element $d\Omega_{d-1}^2 = \sum_{i=1}^{d}\left(d\omega^i\right)^2$, the AdS_{d+1} metric in static coordinates reads

$$ds^2 = L^2\left[-\left(1+r^2\right)d\tau^2 + \frac{dr^2}{1+r^2} + r^2 d\Omega_{d-1}^2\right], \tag{2.1.5}$$

The second set (t, x^i, z), referred to as *Poincaré coordinates*, is described by

$$\begin{aligned} X^0 &= \frac{z}{2}\left[1 + \frac{|\vec{x}|^2 - t^2 + L^2}{z^2}\right], \qquad X^i = \frac{Lx^i}{z}\,, \\ X^d &= \frac{z}{2}\left[1 + \frac{|\vec{x}|^2 - t^2 - L^2}{z^2}\right], \qquad X^{d+1} = \frac{Lt}{z}\,. \end{aligned} \tag{2.1.6}$$

Here $t \in]-\infty, +\infty[$ is the time coordinate, $\vec{x} = \left(x^1, \ldots, x^{d-1}\right)$ are Cartesian coordinates, and $z \in [0, +\infty[$ is the radial coordinate.
The AdS_{d+1} metric with this choice is

$$ds^2 = \frac{L^2}{z^2}\left[-dt^2 + dz^2 + \sum_{i=1}^{d-1}\left(dx^i\right)^2\right]. \tag{2.1.7}$$

Contrary to static coordinates, Poincaré coordinates does not cover the whole AdS spacetime, but only a portion named *Poincaré patch*. Note that the resulting spacetime is obtained as a foliation by d-dimensional Minkowski slices at constant z. In Fig. 2.1 we display a schematic representation for $d = 2$.
The Minkowski plane at $z = 0$ is the *AdS boundary*, the metric on which is apparently divergent. Actually, the boundary metric can be extracted from eq. (2.1.7) by

$$ds_b^2 = \lim_{z\to 0} f(t, x^i)\frac{z^2}{L^2}\,ds^2 = f(t, x^i)\left[-dt^2 + \sum_{i=1}^{d-1}\left(dx^i\right)^2\right], \tag{2.1.8}$$

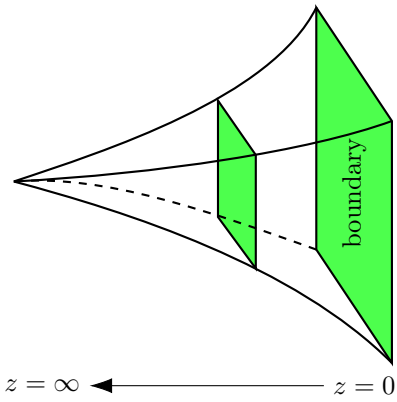

Figure 2.1: AdS_3 spacetime in Poincaré coordinates. Each z-constant slice is a two-dimensional Minkowski spacetime.

with $f(t, x^i)$ a smooth positive function. We thus have a family of boundary metrics differing by a multiplicative coordinate-dependent function. As we will promptly see, such a function can be modified by a conformal transformation, bringing from one member of the family to another. For this reason AdS spacetime is said to have a *conformal boundary*. While Poincaré AdS (2.1.7) has a conformally flat boundary $\mathbb{R}^{1,d-1}$ at $z = 0$, global AdS (2.1.5) has a spherical boundary $S^{d-1} \times \mathbb{R}$ at $r \to +\infty$ with metric $ds_b^2 = f(\tau, \omega^i) \left[-d\tau^2 + d\Omega_{d-1}^2\right]$.

2.1.2 CFT

The second player in the gauge/gravity duality is a conformally invariant quantum field theory (QFT) accommodated at the AdS boundary. Before discussing the nice properties of such QFTs, we specify what we mean by conformal invariance.

The conformal group. A *conformal transformation* is a map $x^\mu \to x'^\mu$ which leaves the spacetime metric tensor $g_{\mu\nu}$ invariant up to a positive coordinate-dependent scale factor:

$$g_{\mu\nu}(x) \to \Upsilon(x)\, g_{\mu\nu}(x)\,. \tag{2.1.9}$$

In other words, conformal transformations preserve angles and the causal structure of spacetime, mapping a timelike (spacelike or null) interval into a timelike (spacelike or null) interval.
In spacetime dimensions $d = 2$ the group of conformal transformations is infinite dimensional. Indeed, describing the two-dimensional spacetime as the complex plane parametrized by $z \in \mathbb{C}$, each holomorphic map $z \to z' = w(z)$ of the

plane into itself represents a conformal transformation. The generators of such transformations $l_n = -z^{n+1}\partial_z$ and their complex conjugates $\bar{l}_n = -\bar{z}^{n+1}\partial_{\bar{z}}$ satisfy the *Witt algebra*

$$\begin{gathered}[l_m\,,l_n] = (m-n)\,l_{m+n}\,, \qquad \big[\bar{l}_m\,,\bar{l}_n\big] = (m-n)\,\bar{l}_{m+n}\,, \\ \big[l_m\,,\bar{l}_n\big] = 0\,,\end{gathered} \tag{2.1.10}$$

with $m, n \in \mathbb{Z}$. Remarkably, the algebra is closed by the subgroups $\{l_{-1}, l_0, l_1\}$ and $\big\{\bar{l}_{-1}, \bar{l}_0, \bar{l}_1\big\}$, which form the finite dimensional subalgebra $\mathfrak{sl}(2,\mathbb{R}) \oplus \mathfrak{sl}(2,\mathbb{R})$. At the quantum level, as a consequence of normal ordering, the corresponding operators L_m span the so-called *Virasoro algebra*, which is obtained as a *central extension* of the Witt algebra:

$$[L_m\,,L_n] = (m-n)\,L_{m+n} + \frac{c}{12}(n^3-n)\delta_{m+n,0}\,. \tag{2.1.11}$$

The parameter c denotes the *central charge* of the quantum theory.
In spacetime dimensions $d > 2$ the conformal group is drastically reduced. In particular, we recognize four elementary conformal transformations:

- Translation $x^\mu \to x^\mu + a^\mu$, generated by $P_\mu = -i\partial_\mu$.
- Lorentz transformation $x^\mu \to M^\mu_\nu x^\nu$, generated by $L_{\mu\nu} = -i\,(x_\mu\partial_\nu - x_\nu\partial_\mu)$.
- Dilatation $x^\mu \to \lambda x^\mu$, generated by $D = -ix^\mu\partial_\mu$.
- Special conformal transformation $x^\mu \to \frac{x^\mu - b^\mu x^2}{1-2b\cdot x+b^2x^2}$, generated by $K_\mu = i\left(2x_\mu x^\nu\partial_\nu - x^2\partial_\mu\right)$.

Translations and Lorentz transformations form the *Poincaré group*, which is thus contained into the conformal group. In Minkowski spacetime $g_{\mu\nu} = \eta_{\mu\nu} = \mathrm{diag}(-1,1,\ldots,1)$ the generators obey the conformal algebra:

$$\begin{aligned}
&[D, P_\mu] = iP_\mu\,, \qquad [D, K_\mu] = -iK_\mu\,, \\
&[P_\mu, K_\nu] = 2i(\eta_{\mu\nu}\,D - L_{\mu\nu})\,, \qquad [L_{\mu\nu}, K_\rho] = i(\eta_{\mu\rho}\,K_\nu - \eta_{\nu\rho}\,K_\mu)\,, \\
&[L_{\mu\nu}, P_\rho] = i(\eta_{\mu\rho}\,P_\nu - \eta_{\nu\rho}\,P_\mu)\,, \\
&[L_{\mu\nu}, L_{\rho\sigma}] = i(\eta_{\mu\rho}\,L_{\nu\sigma} + \eta_{\nu\sigma}\,L_{\mu\rho} - \eta_{\mu\sigma}\,L_{\nu\rho} - \eta_{\nu\rho}\,L_{\mu\sigma})\,.
\end{aligned} \tag{2.1.12}$$

After adjusting the generators into the form

$$J_{ab} = \begin{pmatrix} L_{\mu\nu} & -\frac{P_\mu - K_\mu}{2} & -\frac{P_\mu + K_\mu}{2} \\ \frac{P_\mu - K_\mu}{2} & 0 & D \\ \frac{P_\mu + K_\mu}{2} & -D & 0 \end{pmatrix}\,, \qquad a,b = 0,1,\ldots,d+1\,, \tag{2.1.13}$$

it is straightforward to check that

$$[J_{ab}, J_{cd}] = i\left(\tilde{\eta}_{ac}\, J_{bd} + \tilde{\eta}_{bd}\, J_{ac} - \tilde{\eta}_{ad}\, J_{bc} - \tilde{\eta}_{bc}\, J_{ad}\right) , \tag{2.1.14}$$

where $\tilde{\eta}_{ab} = \mathrm{diag}(-1, 1, \ldots, 1, -1)$. The new relation is just the algebra of rotations in a $(d+2)$-dimensional spacetime with signature $(-, +, \ldots, +, -)$. That is to say, the conformal group in d dimensions is $\mathrm{SO}(2, d)$, the same as the isometry group of $(d+1)$-dimensional AdS.

Conformal field theories. Field theories enjoying conformal invariance are referred to as conformal field theories (CFTs). Classically, conformal invariance is realized when the action of the theory is left unchanged under transformations belonging to the conformal group. Let us assume that a field theory on flat d-dimensional spacetime has translational and Lorentz invariance, so that its energy-momentum tensor $T_{\mu\nu}$ is conserved ($\partial^\mu T_{\mu\nu} = 0$) and symmetric ($T_{\mu\nu} = T_{\nu\mu}$). Then, following an infinitesimal conformal transformation $x^\mu \to x^\mu + \varepsilon^\mu$, the classical action varies as

$$\delta S \sim \int d^d x\, T^\mu_\mu\, \partial_\nu \varepsilon^\nu \, . \tag{2.1.15}$$

Clearly, if the energy-momentum tensor is traceless, the classical action is automatically invariant. In some cases, for this condition to be realized, Poincaré and scale invariance are enough. To get a grasp on this, let us recall the crucial result of *Noether's theorem*: for every continuous symmetry a conserved current exists. For a theory to be scale invariant, the energy-momentum tensor must be expressible as the divergence of a current [84]

$$T^\mu_\mu = \partial_\mu J^\mu \, . \tag{2.1.16}$$

Hence, the conserved dilation current reads

$$J^\mu_D = x^\nu T^\mu_\nu - J^\mu \, . \tag{2.1.17}$$

For unitary theories in $d = 2$, under some technical assumptions, it has been shown that the energy-momentum tensor can be improved to be traceless without requiring full conformal invariance [85]. Generalization to higher dimensions is guessed, but a proof is lacking.

This nice story is inevitably wrecked by the quantization. Indeed, a field theory quantization is usually accompanied by the introduction of a renormalization scale, which obviously spoils the scale invariance. As a result, the coupling constants g of the theory vary with the energy scale μ as dictated by the beta function $\beta_g = \mu \frac{dg}{d\mu}$. Conformal invariance is recovered at the quantum level whether the beta function vanishes. This can be accomplished for particular values of the coupling constants g_*, named *fixed points*, or for any value of g. In

the latter case the CFT is finite, and there is a whole manifold of fixed points. The most celebrated example is the $\mathcal{N} = 4$ supersymmetric[1] Yang-Mills (SYM) theory in $d = 4$ spacetime dimensions, which contains a gauge field, four Weyl fermions, and six real scalars, all in the adjoint representation of a non-abelian gauge group.

Conformal symmetry imposes pretty strong constraints, one of which is about the form of correlation functions involving up to three operators. We here focus on particular spinless operators, referred to as *quasi-primary fields*, which under a conformal map $x^\mu \to x'^\mu$ transform as

$$\Phi(x) \to \Phi'(x') = \left|\frac{\partial x'}{\partial x}\right|^{-\Delta/d} \Phi(x)\,. \tag{2.1.18}$$

The multiplicative factor $|\dots|$ is the Jacobian of the coordinate change, and Δ is known as the *conformal dimension* of the field. Unitarity of the CFT imposes limitations on the possible values of Δ, depending on the way the field transforms under Lorentz operations. For a scalar field in d dimensions, on which we will come back later, the *unitarity bound* is

$$\Delta \geq \frac{d-2}{2}\,. \tag{2.1.19}$$

Another restriction dictated by conformal invariance concerns the form of correlation functions. In particular, the correlation function of two spinless quasi-primary fields is non-vanishing only if their conformal dimensions are equal $\Delta_1 = \Delta_2$, in which case we have

$$\langle \Phi_1(x_1)\Phi_2(x_2)\rangle = C_{12}\,|x_1 - x_2|^{-2\Delta_1}\,. \tag{2.1.20}$$

Defining $\Delta = \Delta_1 + \Delta_2 + \Delta_3$, the three-point function is instead

$$\langle \Phi_1(x_1)\Phi_2(x_2)\Phi_3(x_3)\rangle = C_{123}\prod_{i<j}^{3} |x_i - x_j|^{\Delta - 2\Delta_i - 2\Delta_j}\,. \tag{2.1.21}$$

With four or more points we can build conformally invariant functions depending on the distance between points. Therefore, conformal symmetry is not enough to constraint the form of n-point functions with $n \geq 4$.

2.1.3 AdS/CFT

We now come to the central point of the present discussion. As we have seen, the isometry group of $(d+1)$-dimensional AdS is the same as the symmetry

[1] Supersymmetric theories contain the same number of bosonic and fermionic degrees of freedom. The value of $\mathcal{N}$ is related to the number of generators of supersymmetric transformations, which turn bosons into fermions and viceversa.

group of a d-dimensional CFT, namely $\mathrm{SO}(2,d)$. For the special case $d=2$, the group factorizes as $\mathrm{SO}(2,2)=\mathrm{SL}(2,\mathbb{R})\times\mathrm{SL}(2,\mathbb{R})$. This strong clue of a deep connection between a gravitational theory in AdS_{d+1} and a CFT_d is apparently limited by the different dimensionality of the two candidates. Anyway, this is not the only case in which a gravitational system admits a lower-dimensional description. A celebrated forerunner is represented by the *Bekenstein-Hawking formula* [3, 4]

$$S_{\mathrm{BH}}=\frac{\mathcal{A}}{4G}\,, \tag{2.1.22}$$

which relates the *entropy* of a black hole (BH) to the area of its event horizon.[2] By elaborating eq. (2.1.22) and a t'Hooft's idea [5], Susskind guessed that the degrees of freedom of a gravitational system are encoded at its boundary [6]. In other words, similarly to a hologram, the whole information on gravity may be stored into a lower-dimensional spacetime. The AdS/CFT correspondence, figured out by Maldacena [1], realizes such a *holographic principle* in an extremely innovative way.

The environment from which the original formulation of AdS/CFT came out is type IIB superstring theory[3] in ten-dimensional flat spacetime. Open and closed strings, with distinct and coincident endpoints, respectively, are not the only fundamental constituents of superstring theory. Indeed, objects with p spatial dimensions named *Dirichlet branes* (Dp-branes) can also be introduced. Such defects are dynamical, so they move in time describing a (p+1)-dimensional worldvolume. According to the strength of the interaction between strings, Dp-branes can be seen either as anchoring objects for open strings (weak interaction) or sources of gravitational fields curving the background (strong interaction). Taking a bunch of N coincident D3-branes in ten-dimensional flat spacetime, Maldacena found out that in the low energy limit type IIB superstring theory decouples as:

- **Weak coupling perspective.** $\mathcal{N}=4$ SYM with gauge group $SU(N)$ on the $(3+1)$-dimensional worldvolume described by the N D3-branes $\bigoplus$ type IIB supergravity in ten-dimensional flat spacetime

[2] In its original form, the Bekenstein-Hawking formula reads

$$S_{BH}=\frac{k_B c^3\mathcal{A}}{4G\hbar}\,.$$

This expression comprises all the fundamental physical constants, thus bridging the fundamental theories of physics describing both the macroscopic and the microscopic phenomena: thermodynamics (Boltzmann constant k_B), general relativity (speed of light in vacuum c and Newton's gravitational constant G), and quantum mechanics (reduced Planck's constant $\hbar$). Unless otherwise specified, in this thesis we will work in natural units $k_B=c=\hbar=1$.

[3] Type IIB is one of the consistent closed superstring theories in ten-dimensional spacetime. Contrary to type IIA superstring theory, it violates parity.

- **Strong coupling perspective.** Type IIB supergravity on $\mathrm{AdS}_5 \times S^5$ $\bigoplus$ type IIB supergravity in ten-dimensional flat spacetime

Since the physics in the two perspectives should be equivalent, the non-common factors should correspond to each other as well. This led to the original formulation of the AdS/CFT correspondence: *$\mathcal{N} = 4$ SYM with gauge group $SU(N)$ on $\mathbb{R}^{1,3}$ is dual to type IIB superstring theory on $AdS_5 \times S^5$.*

Noticeably, $\mathcal{N} = 4$ SYM is not only a finite CFT, but also a supersymmetric theory. Therefore, its symmetry group is larger than the conformal group $\mathrm{SO}(2,4)$. Namely, there is an additional $\mathrm{SU}(4)_R$ group reflecting the so-called *R-symmetry*, which rotates the supersymmetry generators. On the other side of the correspondence, the additional factor $\mathrm{SU}(4) = \mathrm{SO}(6)$ is traced back to the five-sphere S^5, whose radius is identified with the AdS_5 curvature radius L. Therefore, the two theories involved in AdS/CFT still share the same symmetry group.

We stress that S^5 is compact, so by dimensional reduction we can neglect it and consider an effective theory in AdS_5. The CFT_4 can be put on the AdS_5 (conformal) boundary, coinciding with $\mathbb{R}^{1,3}$. We thus obtain a remarkable realization of the holographic principle: the gravitational theory into the bulk spacetime can be fully described in terms of the CFT located on the lower-dimensional boundary.

A weak/strong duality. So far we have been a bit sloppy regarding the regimes of validity of the Maldacena's conjecture. To get insights into this point, let us specify the parameters involved in the two theories. A string theory is characterized by the fundamental string length ℓ_s and by the string coupling g_s, controlling the interaction strength between strings. We also add to the list the length scale L specifying the radius of both AdS_5 and S^5. On the other hand, $\mathcal{N} = 4$ SYM is characterized by the number of colors N and the Yang-Mills coupling g_{YM}. It is customary to replace g_{YM} by the so-called *t'Hooft coupling*

$$\lambda = g_{YM}^2 N \,. \tag{2.1.23}$$

The parameters of the two theories are related by the simple relations

$$\frac{\lambda}{N} = 2\pi g_s \,, \qquad \lambda = \frac{1}{2}\frac{L^4}{\ell_s^4} \,. \tag{2.1.24}$$

To fully exploit the power of AdS/CFT correspondence, we would like to extract information on one theory by performing tractable computations into the other. The simplest choice is to work with classical supergravity, which can be obtained by string theory in the limit $g_s \to 0$ (no quantum corrections) and $\ell_s << L$ (strings become particles). From eq. (2.1.24), the latter requirement imposes

$\lambda >> 1$, meaning that the dual CFT is strongly coupled. At this point, we can suitably tune $N \to \infty$ so that the former condition is also met. In this regime, AdS/CFT relates a *weakly coupled* theory of gravity to a *strongly coupled* CFT. To put it differently, we can replace the challenging analysis of strongly coupled quantum field theory, where non-perturbative effects are not under control, by manageable weakly coupled classical gravity. This is what makes AdS/CFT a high-powered theoretical tool.
In the classical approximation $g_s \to 0$, the requirement $\ell_s << L$ can be relaxed by considering the *t'Hooft limit* $N \to \infty$ and λ arbitrarily fixed. This regime is referred to as the *strong version* of AdS/CFT, in which case the gravitational side is a classical string theory.
In its strongest form AdS/CFT is valid for *any* value of the parameters N and λ, but computations must be carried out with the full quantum string theory.

Up to now we have specialized to $\text{AdS}_5/\text{CFT}_4$, involving a field theory in four-dimensional flat spacetime. In this picture, with a vein of poetry, we could say that our world (without gravity!) sits at the boundary of a negatively curved spacetime comprising a fifth dimension we are not aware of. Leaving behind us this appealing imagery, in the following we will consider generalizations of the Maldacena's conjecture to arbitrary boundary dimensions d and to bulk spacetimes with the same asymptotic structure as AdS_{d+1}, referred to as *asymptotically* AdS spacetimes.

The AdS/CFT dictionary. The gauge/gravity duality relates theories which are expressed in extremely different languages. So, we need a proper vocabulary to understand how they speak to each other. Eq. (2.1.24) is one of the entries of this so-called *holographic dictionary*, translating gravitational quantities into CFT ones. Besides the mapping between parameters, one would also like to learn the mapping between observables. To grasp this point, let us work with Poincaré coordinates $(t, \vec{x}, z) = (x, z)$. A central assertion for the *field/operator map*, due to Gubser, Klebanov, Polyakov [86], and Witten [87], is that a bulk field $\Phi(x, z)$ in AdS_{d+1} corresponds to a particular operator $\mathcal{O}(x)$ in the dual CFT_d, and the way they are linked is driven by the boundary behavior $z \to 0$ of the bulk field. More specifically, the field $\Phi_0(x)$, defined as the coefficient of the leading-order expansion $\Phi(x, z) \sim f(z)\Phi_0(x)$ around $z = 0$, acts as a source for the dual operator $\mathcal{O}(x)$. In Euclidean signature $(+, \dots, +)$, the generating functional of CFT correlators thus reads

$$e^{W[\Phi_0]} = \left\langle e^{\int d^d x\, \Phi_0(x)\, \mathcal{O}(x)} \right\rangle_{CFT} . \tag{2.1.25}$$

The bulk field $\Phi(x, z)$ is taken as a solution of the equation of motions derived from the supergravity effective action I_{sugra}, with boundary condition specified

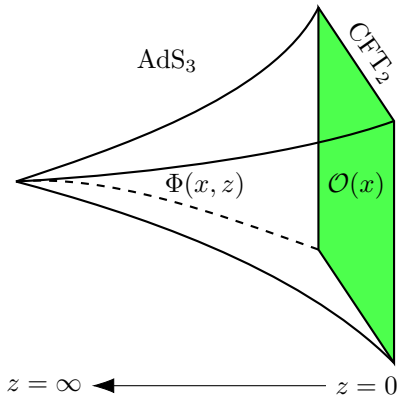

Figure 2.2: According to the field/operator map, each field $\Phi(x,z)$ in AdS$_{d+1}$ corresponds to a proper operator $\mathcal{O}(x)$ in the boundary CFT$_d$. The figure specializes to $d=2$.

by $\Phi_0(x)$. From here, we get the fundamental formula:

$$W\left[\Phi_0\right] = I_{sugra}\left[\Phi\right]\big|_{\Phi(x,z)\sim f(z)\,\Phi_0(x)}\ . \tag{2.1.26}$$

Basically, the CFT generating functional depending on the *off-shell* boundary configuration $\Phi_0(x)$ is identified with the *on-shell* gravitational action computed on the solution $\Phi(x,z)$. Clearly, the effective action I_{sugra} is valid when the gravitational theory is weakly coupled and classical, which in turn happens if the dual CFT is strongly coupled. So, in the realm where any known perturbative approach breaks down, a complicated quantum object as the correlator

$$\langle \mathcal{O}(x_1)\dots\mathcal{O}(x_n)\rangle_{CFT} = \left.\frac{\delta^n W}{\delta\Phi_0(x_1)\dots\delta\Phi_0(x_n)}\right|_{\Phi_0=0} \tag{2.1.27}$$

can be computed by taking ordinary derivatives of a classical on-shell action. Eq. (2.1.26) is believed to also hold for the strongest version of AdS/CFT. In this case, we get the prominent *GKPW formula*

$$Z_{CFT} = Z_{\text{string}}\,, \tag{2.1.28}$$

stating the equivalence between the partition functions $Z = e^W$ of a CFT$_d$ and of a full string theory in AdS$_{d+1}$.

Below we list some possible choices for the source $\Phi_0(x)$ and the corresponding CFT_d operator $\mathcal{O}(x)$:

$$\begin{aligned} \text{Scalar field } \phi(x) &\longleftrightarrow \text{Scalar operator } O(x) \\ \text{Gauge field } A_\mu(x) &\longleftrightarrow \text{Current } J_\mu(x) \\ \text{Spin-two field } h_{\mu\nu}(x) &\longleftrightarrow \text{Energy-momentum tensor } T_{\mu\nu}(x) \end{aligned} \tag{2.1.29}$$

The mass m of each bulk field is related to the conformal dimension Δ of the dual operator as follows:

- Scalar field and massive spin-two field: $m^2L^2 = \Delta(\Delta - d)$.
- Gauge field: $m^2L^2 = (\Delta - 1)(\Delta + 1 - d)$.
- Massless spin-two field: $m^2 = 0$, $\Delta = d$.

Scalar field example. Let us enter the details of the field/operator map focusing on a scalar field with mass m_ϕ^2 into AdS_{d+1}. Solving the Klein-Gordon equation obtained from the scalar action in curved spacetime

$$S \sim \int d^dx\, dz\, \sqrt{-g}\left(g^{mn}\partial_m\phi\,\partial_n\phi + m_\phi^2\phi^2\right) , \tag{2.1.30}$$

we find two independent asymptotic modes:

$$\phi(x,z) \sim \phi_0(x)\, z^{d-\Delta} + \phi_1(x)\, z^{\Delta} , \tag{2.1.31}$$

with Δ the larger root of the mass constraint $m_\phi^2L^2 = \Delta(\Delta - d)$:

$$\Delta = \frac{d}{2} + \sqrt{\frac{d^2}{4} + m_\phi^2L^2} . \tag{2.1.32}$$

The mode $z^{d-\Delta}$ gives a divergent action at the boundary $z = 0$, so it is called *non-normalizable*. On the other hand, the mode z^Δ provides a finite action, and is thus defined *normalizable*. By dimensional arguments, we must interpret $\phi_0(x)$ as the *source* for the dual scalar operator $O(x)$. After fixing $\phi_0(x)$, the other solution $\phi_1(x)$ can be expressed as a function of $\phi_0(x)$ itself. Namely, $\phi_1(x)$ is interpreted as the *vacuum expectation value* (VEV) $\langle O(x)\rangle$ of the dual operator, whose conformal dimension is the corresponding exponent Δ.
However, this is not the end of the story. Contrary to the Minkowski case, scalar fields in AdS can have a negative mass m_ϕ^2 and still remain stable. By the way, stability breaks down for masses below a threshold value. The stability condition for a scalar field in AdS_{d+1}, known as the *Breitenlohner-Freedman*

(BF) *bound*, reads $m_\phi^2 L^2 \geq -d^2/4$ [88]. Now, the lower the mass, the higher the value of $d - \Delta$. Clearly, in the mass range $-d^2/4 \leq m_\phi^2 L^2 < -d^2/4 + 1$ both Δ and $d - \Delta$ are above the unitarity bound (2.1.19), so they can both be taken as honest conformal dimensions for the dual scalar operator $O(x)$. This degree of arbitrariness corresponds to the choice of either $\phi_0(x)$ or $\phi_1(x)$ as the source of $O(x)$ [89].

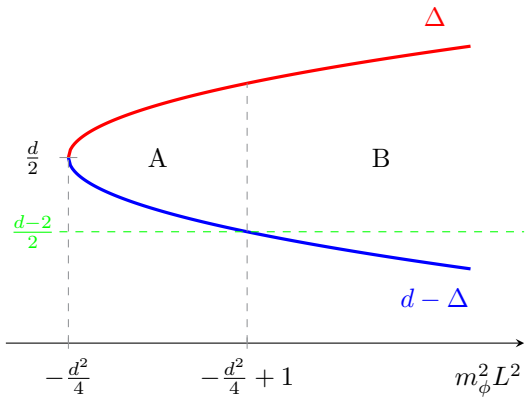

Figure 2.3: Possible values of the conformal dimension of the CFT_d operator $O(x)$ as a function of the mass of the scalar field $\phi(x)$ in AdS_{d+1}. The unitarity lower bound is shown in green. In the mass range A we can have dual operators with conformal dimension Δ or $d - \Delta$. Instead, in the mass range B we can only have a dual operator with conformal dimension Δ.

Summarizing:

- For $m_\phi^2 L^2 \geq -d^2/4 + 1$, $\phi_0(x)$ is interpreted as a source and $\phi_1(x)$ as a VEV of the dual scalar operator $O(x)$, whose conformal dimension is Δ.
- For $-d^2/4 \leq m_\phi^2 L^2 < -d^2/4 + 1$, either $\phi_0(x)$ or $\phi_1(x)$ can be interpreted as a source for the dual scalar operator $O(x)$, whose conformal dimension is Δ or $d - \Delta$, respectively.

As we will see in Ch. 7, in the second case we have a rich catalog of quantization conditions.

2.2 Entanglement entropy and Ryu-Takayanagi proposal

One of the basic ideas of the AdS/CFT correspondence is that the bulk spacetime emerges from the degrees of freedom of the boundary CFT. A milestone along the path towards this interpretation is the Bekenstein-Hawking formula (2.1.22), which tells us that the number of degrees of freedom of a BH scales as the area and not as the volume. Inspired by this remarkable result and AdS/CFT, Ryu and Takayanagi proposed a similar formula for the computation of the *entanglement entropy* of subsystems in strongly coupled CFTs.

Prior to describing the Ryu and Takayanagi's key result, it is worth introducing the notion of entanglement entropy. To this purpose, let us consider a quantum system with Hilbert space $\mathcal{H}$. Dividing the total system into two subsystems A and B, the total Hilbert space can be expressed as the direct product of the Hilbert spaces of the two subsystems, namely $\mathcal{H} = \mathcal{H}_A \otimes \mathcal{H}_B$. Given a pure state $|\psi\rangle \in \mathcal{H}$, the corresponding density matrix is $\rho = |\psi\rangle\langle\psi|$. An observer in A, who has not access to B, would describe the state of the system by the *reduced density matrix*

$$\rho_A = \mathrm{Tr}_B \, |\psi\rangle\langle\psi| \ , \tag{2.2.1}$$

obtained by tracing the density matrix ρ over the Hilbert space $\mathcal{H}_B$. Quantum mechanics teaches us that, in principle, a measurement on the state ρ_A by an observer in A can also shed some light on the state of the subsystem B. When this happens, the two subsystem are said to be *entangled*. The degree of entanglement of the pure state $|\psi\rangle$ for the chosen bipartition can be measured by the entanglement entropy of the subsystem A, defined as the *von Neumann entropy* of the reduced density matrix ρ_A:

$$S(A) = -\mathrm{Tr}_A \left(\rho_A \ln \rho_A\right) \ , \tag{2.2.2}$$

where the trace is taken over the Hilbert space $\mathcal{H}_A$. In case the state $|\psi\rangle$ of the whole system is pure we can interchange the role of the two subsystems A and B, so that $S(A) = S(B)$.
The entanglement entropy $S(A)$ has some useful properties:

- *Subadditivity*: for any pair of subsystems A and B we get

$$S(A) + S(B) \geq S(A \cup B) \, . \tag{2.2.3}$$

- *Strong subadditivity*: for any two subsystems A and B we have

$$S(A) + S(B) \geq S(A \cup B) + S(A \cap B) \, . \tag{2.2.4}$$

Note that for disjoint subsystems ($A \cap B = \emptyset$) the inequality reduces to subadditivity.

In continuous d-dimensional QFTs, the splitting of the total system into subsystems A and B is intended as a spatial bipartition on a Cauchy slice Σ,[4] representing a spacelike $(d-1)$-dimensional surface on which the state of the total system lives. Due to the continuity of the system, the entanglement entropy S_A is obviously UV divergent, so it calls for a regularization. The regularization procedure can be accomplished by putting the theory on a lattice and sending the spacing between neighboring sites to zero, or by working in a region of width $\varepsilon \to 0$ around the interface between A and B, thus regulating the short range entanglement between the interior and exterior of A itself. The computation of entanglement entropy in QFTs can be performed by the replica trick [90], which we do not describe in this thesis. While for CFTs in $d = 2$ dimensions the conformal symmetry allows to calculate the entanglement entropy in several situations [91–93], for general QFTs in dimensions $d > 2$ the issue appears to be tractable just for free field theories [81, 94].

Here comes the breakthrough of Ryu and Takayanagi. They conjectured that the entanglement entropy of a spatial region A in a strongly coupled CFT_d is given by the area of a codimension-two[5] *minimal* surface γ_A anchored at ∂A and extending into AdS_{d+1}, on which boundary the CFT is located [9, 10]:

$$S(A) = \frac{\mathcal{A}(\gamma_A)}{4G} \,. \tag{2.2.5}$$

For the sake of clarity, in Fig. 2.4 we illustrate the proposal.
The *Ryu-Takayanagi* (RT) *formula* (2.2.5) generalizes the Bekenstein-Hawking formula (2.1.22) to AdS spacetime. Indeed, $S(A)$ can be thought of as the entropy measured by an observer who can only access subsystem A, thus interpreting the inaccessible subsystem B as the interior of a (fictitious) BH. In this sense, the minimal surface γ_A, named *RT surface*, can be regarded as a holographic screen for an observer in A. Actually, when the bulk spacetime contains a BH and subsystem A is extended to the whole Cauchy slice Σ, the RT surface wraps the BH event horizon and $S(A) = S_{BH}$ [9, 10].

As we have stressed in Subsec. 2.1.1, the AdS metric is divergent at the boundary, causing the holographic entanglement entropy (2.2.5) to diverge as well. A regularization can be performed by computing the area of γ_A up

[4] A Cauchy slice defines a moment of simultaneity in the QFT. Strictly speaking, Σ is a Cauchy slice on a Lorentzian manifold $\mathcal{M}$ if every inextendible differentiable timelike curve on $\mathcal{M}$ intersects Σ at precisely one point.

[5] The codimension of a hypersurface is defined as the difference between the dimension of the ambient spacetime and the dimension of the hypersurface itself. For instance, a codimension-two hypersurface in AdS_{d+1} has dimensions $d-1$.

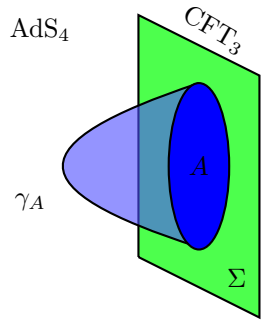

Figure 2.4: Pictorial representation of the RT formula. The spatial region A on the Cauchy slice Σ in the boundary CFT is shown in blue. The RT surface γ_A is anchored at the edges of the region A and extends into the bulk spacetime. The figure does not show the time direction.

to a cutoff surface introduced nearby the AdS boundary. This regularizing procedure corresponds to putting a UV cutoff in the boundary CFT [95], as we have discussed above. The regularized holographic entanglement entropy (2.2.5) evaluated in three-dimensional AdS has been found to reproduce the entanglement entropy of a two-dimensional CFT [9]. Then, the RT formula provides a further evidence of validity of the AdS/CFT correspondence. Besides this, it inspires a fascinating idea: quantum information notions of CFT states tell us how the bulk spacetime emerges from the boundary theory.

We conclude this section by stressing that the original RT proposal was formulated for static states in the dual CFT. Later, a covariant prescription valid for time-dependent states has been introduced by Hubeny, Rangamani, and Takayanagi (HRT) [96]. Similarly to the RT formula, the HRT prescription relates the entanglement entropy of a CFT spatial region A to the area of an *extremal* codimension-two surface Γ_A extending into the bulk, anchored at ∂A, and smoothly deformable to A itself:

$$S(A) = \frac{\mathcal{A}(\Gamma_A)}{4G} \,. \tag{2.2.6}$$

The HRT surface Γ_A represents a covariant generalization of the RT surface to dynamical backgrounds, and in the static case it reduces to the RT surface itself.

2.3 Entanglement entropy is not enough

2.3.1 The thermofield double state

One of the outcomes of the AdS/CFT correspondence is that a field in AdS spacetime is dual to an operator in the boundary CFT. An analog map exists between asymptotically AdS *bulk geometries* and CFT *states*. The simplest example is vacuum AdS_{d+1}, which corresponds to the vacuum state in the boundary CFT_d. In the same spirit, a Schwarzschild AdS_{d+1} BH is dual to the thermal state in the boundary CFT_d. For the purposes of this thesis, an honorable mention is deserved by eternal[6] Schwarzschild AdS BHs, whose maximally extended Penrose diagram, shown in Fig. 2.5, has two boundaries, one on the left and one on the right.

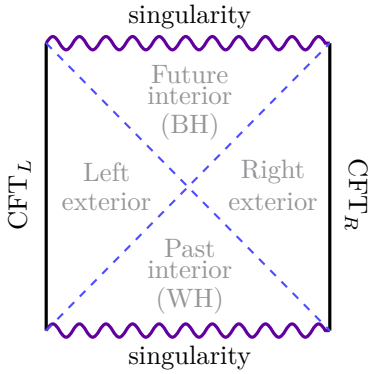

Figure 2.5: Penrose diagram describing the causal structure of an eternal AdS_{d+1} BH. We recognize four regions: the future interior, which is the proper BH, the past interior, referred to as white hole (WH), and the left and right exteriors. The horizontal lines represent the past and future singularities inside the WH and BH, the vertical lines denote the spacetime boundaries on which the dual CFTs live, and the diagonal lines are the event horizons of the WH and BH. Each point of the diagram hides a $(d-1)$-dimensional sphere, which shrinks nearby the singularities.

Maldacena argued that this geometry is equivalent to two identical non-interacting CFTs, each of which located at the left (CFT_L) and right (CFT_R)

[6]Eternal BH solutions contemplate a peculiar region named white hole (WH), which does not exist for BHs formed by gravitational collapse. The WH is in a sense the time reversal of a BH. While objects can just enter a BH but never escape, objects can just escape from a WH but never enter it.

boundaries of the two-sided spacetime. The two field theories are entangled and the state on the total Hilbert space $\mathcal{H} = \mathcal{H}_L \otimes \mathcal{H}_R$ is the so-called *thermofield double* (TFD) state [97]

$$|TFD\rangle = \frac{1}{\sqrt{Z(\beta)}} \sum_n e^{-\frac{\beta E_n}{2}} |E_n\rangle_L \otimes |E_n\rangle_R \ . \tag{2.3.1}$$

In the above expression, β is the inverse temperature, $Z(\beta)$ is the partition function of one copy of the CFT, and the sum runs over all the eigenstates of the total system. The motivation for this assertion lies in the fact that an observer in each of the asymptotic regions into the bulk spacetime witnesses a Schwarzschild AdS BH, which we have argued to be dual to the CFT thermal state. In fact, the trace of the TFD state over the full left (or right) system returns the thermal density matrix of the remaining CFT:

$$\begin{aligned} \mathrm{Tr}_L \left(|TFD\rangle\langle TFD| \right) &= \frac{1}{Z(\beta)} \sum_n e^{-\beta E_n} |E_n\rangle_R \langle E_n|_R \\ &= \frac{e^{-\beta H_R}}{Z(\beta)} \\ &= \rho_R^{\mathrm{th}} \ , \end{aligned} \tag{2.3.2}$$

hence the name thermofield double. Moreover, the presence of the event horizon prevents observers in the left and right asymptotic regions of the bulk spacetime from communicating with each other. More precisely, the only way for an observer to send a message to the other is through the *wormhole*, or *Einstein-Rosen* (ER) *bridge*, connecting the two sides of the BH. This is reflected in the lack of interaction between the two boundary CFTs, which are, although, entangled. As a remarkable conclusion, the spatial connectivity of the bulk spacetime arises from entanglement [98]. This seminal observation gave inspiration to the idea that the two apparent (but not effective!)[7] violations of locality represented by entanglement and ER bridges are intimately related. The resulting conjecture, which goes under the name of ER=EPR (where the second entry stands for Einstein-Podolsky-Rosen, who pointed out the celebrated paradox involving quantum entanglement [99]), states that the connection of two systems by an ER bridge is a sufficient and necessary condition for them to be entangled [100].

[7] On the one hand, no local operation performed on one member of an entangled pair can influence the other faster than a classical signal. On the other hand, no causal signal can be sent from one side of an eternal BH to the other, see for instance Fig. 2.5.

2.3.2 Time evolution of entanglement entropy

In light of ER=EPR, one may be tempted to conclude that entanglement fully describes the BH interior. Actually, the ER bridge is a dynamical object, even for eternal AdS BHs. So, to get a comprehensive view, we must discuss how entanglement entropy evolves in time.

Let us go back to the field theory state dual to the eternal AdS BH. The TFD state (2.3.1) can be viewed as the initial configuration at times $t_L = t_R = 0$, where each time refers to one of the two independent field theories CFT_L and CFT_R. The time-evolved TFD state reads

$$\begin{aligned} |TFD(t_L, t_R)\rangle &= e^{-iH_L t_L} e^{-iH_R t_R} |TFD\rangle \\ &= \frac{1}{\sqrt{Z(\beta)}} \sum_n e^{-\frac{\beta E_n}{2}} e^{-iE_n(t_L+t_R)} |E_n\rangle_L \otimes |E_n\rangle_R \,, \end{aligned} \tag{2.3.3}$$

where $H_{L,R}$ denote the Hamiltonians of the left and right theories. There are two possibilities of choosing the boundary times [101]: either t_L and t_R grows in opposite directions ($t_L = -t_R$), or t_L and t_R increase in the same direction ($t_L = t_R$). The first choice is equivalent to evolving the TFD state with the Hamiltonian $H_L - H_R$, leading to

$$t_L \to t_L + \Delta t \,, \qquad t_R \to t_R - \Delta t \,, \tag{2.3.4}$$

which clearly leaves the state invariant. Indeed, this transformation is generated by the time Killing vector of the bulk spacetime. The second choice, instead, entails a natural time evolution driven by the Hamiltonian $H_L + H_R$. Thus, in order to investigate the dynamics of the system, we employ the latter option, assuming both times to grow upward and defining $t_L = t_R = t_b/2$.

We now turn to the entanglement entropy, exploiting the power of the RT (or, accordingly, the HRT) proposal. Namely, the entanglement entropy of a CFT subsystem can be simply estimated by the area of extremal surfaces anchored at the boundary subregion itself. In static backgrounds, extremal surfaces never penetrates BH event horizons [102]. However, in dynamical situations the HRT surface can act as a probe of the BH interior. This is the case of eternal AdS BHs with the choice $t_L = t_R$, which enforces time dependence and causes the entanglement entropy of a boundary subregion to potentially evolve in time. If the boundary subsystem is the union of half of the space on each of the two boundaries, the HRT surface traverses the BH at any time. Then, classically, entanglement entropy linearly grows forever [101]. But this is not the most general situation. Let us consider a boundary subsystem given by the union of finite regions in both the left and right theories. At early times the HRT

surface still connects the asymptotic subregions and explores the BH interior. After a time of order $t_b \approx \beta$, the extremal surface stretches along the spacelike direction in the BH interior, leading to a linear growth of the entanglement entropy, as in the previous case. However, at a time of the same order as the subregion size, known as *thermalization time*, the extremal surface is pushed out of the BH and becomes disconnected. From this time on, the entanglement entropy saturates at the constant thermal value [101]. Nevertheless, as it is clear from the Penrose diagram in Fig. 2.5, the ER bridge continues to grow for times much longer than the thermalization scale of the system. It is thus clear that the entanglement entropy is not enough to capture the late time dynamics of the BH interior [14].

2.4 Gate complexity

Contrary to the ER bridge traversing an eternal BH from side to side, the entanglement entropy in the dual field theory stops growing when the system thermalizes. The same story repeats for all the established CFT entries in the holographic dictionary. By the way, if we believe in AdS/CFT, a quantity should exist in the dual field theory which keeps evolving for long times after the thermalization, mimicking the dynamics of the ER bridge. Susskind guessed this quantity to be *quantum computational complexity* of the dual state [14]. Prior to justifying the reasoning behind this proposal, we introduce complexity from the quantum information perspective.

2.4.1 Computational complexity: the origin

Computational complexity was originally introduced in the context of computer science to quantify the difficulty of performing a task. The basic ingredients involved in the complexity definition are a system, a set of states, and a collection of *simple operations*. Let us pick up a state of our set, which we refer to as *reference state*, and consider the problem of transforming such a state into a *target state*, again chosen from the same set. Suppose we are only allowed to consecutively apply to the reference state the simple operations at our disposal. Complexity is defined as the *minimum number* of operations required to accomplish the task.

A classical example. For the sake of clarity, let us borrow an instructive example from [14]. We consider a classical system of n bits of information, each of which can be in two states, say 0 and 1. A state of the system is given by a sequence of n binary digits. For consistency, we identify the states obtained by

flipping the values of all the n digits, e.g. $(0110\dots) = (1001\dots)$. We are now left with the choices of the reference state and of the notion of simple operation. The simplest state that immediately comes in mind is a sequence of identical digits, either 0 or 1: $(000\dots) = (111\dots)$. On the other hand, the simplest operation is the switching of a single digit: $0 \leftrightarrow 1$. Note that every state can be built from the reference one by applying a finite number of such consecutive operations. Complexity of the target state is simply defined as the minimum number of digit-flipping doing the job. Clearly, no state requires more than $n/2$ simple operations to be constructed this way.[8] So, the maximum complexity is just $\mathcal{C}_{\max} = n/2$. We point out that at the classical level complexity is not that different from entropy, at least quantitatively. Indeed, in the present model the maximum entropy, measuring the disorder of the system, is also linear in the number of bits: $S_{\max} = n \log 2$.

A quantum example. We now introduce quantum mechanics into the problem, considering the equivalent system constituted by n *quantum bits* (qubits). The crucial difference with the classical case is that a state of the quantum system, up to a normalization constraint and an overall phase, is specified by 2^n complex parameters:

$$|\psi\rangle = \sum_{i=1}^{2^n} \alpha_i \, |i\rangle \ , \tag{2.4.1}$$

where $|i\rangle$ are elements of the basis of the Hilbert space $\mathbb{CP}^{2^n-1}$. Specifically, each $|i\rangle$ is a product state of n one-qubit states, which can be either $|0\rangle$ or $|1\rangle$. The exponential scaling in n of the number of parameters needed for characterizing a state, against the linear scaling of the previous case, is at the origin of the huge discrepancy between classical and quantum complexity.
Reasonably, the simplest state of the quantum system is marked by two conditions: all the n qubits are in the same one-qubit state and there is no entanglement between qubits. As before, if we identify the states obtained from each other by flipping all the one-qubit states, which can be done by a global SU(2) rotation, it is not restrictive to identify as the reference state

$$|\psi_R\rangle = |000\dots\rangle \ . \tag{2.4.2}$$

Quantum states should transform following the laws of quantum mechanics. Therefore, we just allow *unitary operations*. Furthermore, we neglect transformations which only change the phase of the state, making no progress in the construction of the target state. As a result, we end up with transformations belonging to $\mathrm{SU}(2^n)$, the group of special unitary operators acting on n-qubits systems. Among the $U \in \mathrm{SU}(2^n)$, the simple operations will involve a small number of qubits. Since operators acting on one qubit are not able to create

[8] The most complex states are specified by an equal number of 0 and 1 entries.

entanglement, we are forced to also admit in our set two-qubits transformations. We refer to one-qubit and two-qubits operations as *quantum gates*.
Now, a generic state of the form (2.4.1) can be constructed by acting on the reference state with a special unitary transformation as

$$|\psi_T\rangle = U\,|\psi_R\rangle\ . \tag{2.4.3}$$

Bearing in mind the general complexity definition, we are interested in special unitary transformations U coming from the composition of quantum gates:

$$U = g_k g_{k-1} \dots g_1\,. \tag{2.4.4}$$

This assembling of quantum gates gives rise to a *quantum circuit*. We here distinguish between two notions:

- *Unitary complexity*, quantifying the hardness of building a given unitary operator. This can be identified with the number of gates in the optimal circuit.
- *State complexity*, quantifying the hardness of building a given state. This can be defined as the lowest complexity of any operator building the state from the reference one:

$$\mathcal{C}(|\psi_T\rangle) = \min_U \mathcal{C}(U)\,, \tag{2.4.5}$$

  provided that eq. (2.4.3) holds.

Whereas maximum entropy is still $S_{\max} = n \log 2$, maximum quantum complexity is $\mathcal{C}_{\max} \approx e^n$, due to the large number of parameters necessary to specify the quantum state.

We stress that the above discussion can be readily adapted to quantum systems of n qudits, each of which can be regarded as a K-levels system. In this case, the Hilbert space is $\mathbb{CP}^{K^n-1}$, and the unitary group acting on states is $\mathrm{SU}(K^n)$. Generalizations trivially follows.

2.4.2 Time evolution of complexity

We now turn to the original question of finding a quantum information notion which continues to grow after the system has come to thermal equilibrium. Mainly following [22], we investigate the time evolution of quantum complexity, showing that it fulfills this requirement.

Strictly speaking, throughout this chapter we specialize on quantum circuits containing only two-qubits gates. Moreover, we require the circuit to be *random*, meaning that in every step *each* qubit is randomly paired with another and a randomly chosen quantum gate acts on the pair. We just impose the set of gates to be *universal*, so that any unitary operation can be expressed as a sequence of a finite number of gates. Under this assumption, in every step exactly $n/2$ gates act, involving all qubits. Clearly, unitary complexity is still defined as the minimum number of gates composing the circuit. If we think of the steps as units of discretized time τ, such a parallel computing mimics the Hamiltonian evolution better than the gate composition of eq. (2.4.4). In Fig. 2.6 we sketch a random circuit:

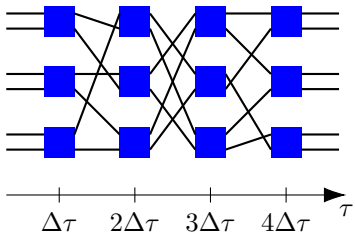

Figure 2.6: Random circuit involving $n = 6$ qubits and four steps. Each black line represents a qubit, and each blue square denotes a gate. In every step three pairs of qubits are randomly formed, and a gate acts on each pair.

Let us consider a unitary operator $U(\tau)$, and explore how its complexity evolves in time. To answer this question, we must count the number of gates in the optimal circuit preparing $U(\tau)$ at a given time. Since $n/2$ gates are implemented at every time step, surely $U(\tau)$ can be prepared by a circuit composed of a number of gates equal to

$$N_{\text{gates}}(\tau) = \frac{n\tau}{2}\,. \tag{2.4.6}$$

However, the optimal circuit is in general shorter, implying that

$$\mathcal{C}\left(U(\tau)\right) \leq N_{\text{gates}}(\tau)\,. \tag{2.4.7}$$

To fix ideas, we can focus on the evolution operator $U(\tau) = e^{-iH\tau}$, generated by an Hamiltonian containing only one and two-qubits gates. At initial times, the operator is "close" to the identity, so that the corresponding circuit is short. Therefore, it is reasonable to suppose that the defining circuit is also the more efficient for some time interval. In this regime $\mathcal{C}\left(U(\tau)\right) = N_{\text{gates}}(\tau)$, and complexity linearly grows. By the way, in Subsec. 2.4.1 we have argued that $\mathcal{C}_{\text{max}} \approx e^n$, so complexity eventually stops increasing. Even though the linear

growth cannot last forever, it is guessed to last as long as possible [103]:

$$\mathcal{C}\left(U(\tau)\right) = \frac{n\tau}{2}\,, \qquad \tau \lesssim e^n\,. \tag{2.4.8}$$

Recently, both the initial linear growth and the exponential maximal value of complexity have been proven [12] in random quantum circuits. When complexity is near to its maximum value, the growth rate appreciably slows down. At this point, complexity fluctuates in proximity of $\mathcal{C}_{\max}$ for a long time, as it can be understood from the fact that the majority of unitary operators has maximum complexity. The leaping around highly complex operators continues until the system runs into a *quantum recurrence*, causing complexity to rapidly fall down to near the sub-exponential initial value. This extremely rare event takes place after a doubly exponential time $\tau \approx e^{e^n}$, and is related to *Poincaré recurrence theorem*, basically stating that dynamical quantum systems exploring a phase space eventually returns to their initial state. After the quasi-periodic quantum recurrence, complexity resumes increasing and the entire cycle keeps repeating itself. In Fig. 2.7 we outline the conjectured time evolution of unitary complexity in random circuits:

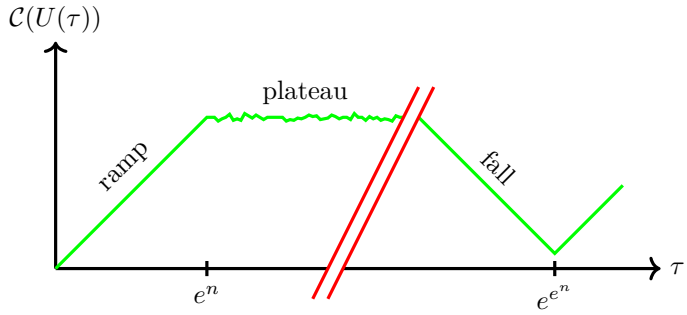

Figure 2.7: Putative time evolution of unitary complexity of the operator $e^{-iH\tau}$, reproducing a picture in [104]. The "ramp" regime has been proved in [12].

2.4.3 Quantum chaos and switchback effect

As we will promptly see, the circuit whose complexity evolution is displayed in Fig. 2.7 is *chaotic*. A hallmark of quantum chaos is the strong influence of initial conditions on the time evolution. Namely, a small change of the initial configuration causes drastic modifications of the state at later times, a phenomenon which has poetically been described by Lorenz (at the suggestion

of colleagues) as the flap of a butterfly's wings in Brazil setting off a tornado in Texas.

In the random circuit introduced in the previous subsection, chaos can be captured by *precursors* [22, 82, 105], peculiar operators which are sensible to the spread of a perturbation into the system. To construct a precursor, let us start from an operator W modeling a small perturbation on the system. Concretely, we take an operator W acting on a small number of qubits, say one for simplicity. To investigate the effect of this perturbation on the operator itself at a given time τ, we turn back time with the inverse of the evolution operator $U(-\tau) = e^{iH\tau}$, we then apply W, and we finally come back to the present by applying $U(\tau) = e^{-iH\tau}$. The resulting precursor

$$W(\tau) = U(\tau)\, W\, U(-\tau) \tag{2.4.9}$$

measures how the operator in the present would have been had we inserted a perturbation in the past. Indeed, if no perturbation is inserted ($W = \mathbb{1}$) the precursor does not change with time: $W(\tau) = \mathbb{1}$. On the other hand, if the system is chaotic we expect $W(\tau)$ to become more and more complex as time passes, due to the dramatic effects of the initial perturbation W.

Let us study how the complexity of $W(\tau)$ varies with time. Naively, one may consider the circuit formed by concatenating the three operators $U(-\tau)$, W, and $U(\tau)$. After τ time steps, $U(\tau)$ has been implemented by acting with $m = n\tau/2$ gates. So, the precursor is surely reproduced by the circuit

$$W(\tau) = g_1^\dagger \dots g_m^\dagger\, W\, g_m \dots g_1\,. \tag{2.4.10}$$

In general, this is not the optimal way of building $W(\tau)$. In fact, a shorter circuit may exist which does the same job, implying that

$$\mathcal{C}(W(\tau)) \leq \mathcal{C}(U(\tau)) + \mathcal{C}(W) + \mathcal{C}(U(-\tau))\,. \tag{2.4.11}$$

To understand this point, let us borrow the "epidemic model" introduced in [105]. We regard the qubit on which W acts as an infected qubit. At initial time $\tau = 0$, W clearly commutes with $U(\tau)$, and $\mathcal{C}(W(\tau)) = \mathcal{C}(W) = 1$. After one time step, the infected qubit is randomly paired with a healthy qubit and a gate acts on the pair. We say that the healthy qubit is infected, meaning that W commutes with all the gates composing $U(\tau)$ except for the one acting on the infected pair. So, a huge cancellation between the gates in $U(\tau)$ and $U(-\tau)$ occurs. At the next time step, supposing that the infected qubits are not paired again, which happens with a small probability of $\mathcal{O}(n^{-1})$, four qubits become infected and so on. The infection spreads exponentially, until all qubits are infected. We schematically illustrate the infection process in Fig. 2.8.

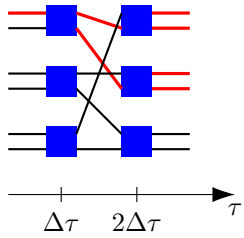

Figure 2.8: Spreading of the epidemic in a random circuit involving $n = 6$ qubits and two steps. Infected qubits are represented by red lines. At each step, any infected qubit contaminates the healthy qubit it is randomly paired with.

Let us define the *size* of the precursor $s(\tau)$ as the number of infected qubits at time τ. In the following step $\tau + \Delta\tau$ such a number increases of the amount

$$\Delta s = \frac{n-s}{n-1}\, s\,, \tag{2.4.12}$$

being $(n-s)/(n-1)$ the probability that an infected qubit pairs with a healthy one. Hence, the epidemic follows the differential equation

$$\frac{ds}{d\tau} = \frac{n-s}{n-1}\, s\,, \tag{2.4.13}$$

which at large n is solved by

$$s(\tau) = \frac{n\, e^{\tau}}{n + e^{\tau}}\,. \tag{2.4.14}$$

So, in agreement with our expectations, at early times $s(\tau) \sim e^{\tau}$, whereas at large times the epidemic has spread all over the system and $s(\tau) \sim n$. It is convenient to introduce the parameter $\tau_* = \log n$, called *scrambling time*, that allows us to write eq. (2.4.14) as

$$s(\tau) = \frac{n\, e^{\tau-\tau_*}}{1 + e^{\tau-\tau_*}}\,. \tag{2.4.15}$$

Since for $\tau - \tau_* >> 1$ the number of infected qubits saturates, the scrambling time τ_* can be interpreted as the time it takes for the perturbation to spread over the entire system.

We emphasize that the only gates contributing to the complexity of the precursor are the ones that actively participate in the infection process, the others getting canceled as explained around eq. (2.4.11). At each time step, $s(\tau')/2$ of such gates appear in $U(-\tau')$ and the same number is contained into $U(\tau')$. Therefore,

the complexity of the precursor $W(\tau)$ is obtained by summing up the values of $s(\tau')$ up to time τ:

$$\begin{aligned} \mathcal{C}(W(\tau)) &= \int_0^\tau s(\tau')\, d\tau' = n \log\left(1 + e^{\tau - \tau_*}\right) \\ &\sim \begin{cases} e^\tau & \text{if } \tau_* - \tau >> 1\,, \\ n(\tau - \tau_*) & \text{if } \tau - \tau_* >> 1\,. \end{cases} \end{aligned} \tag{2.4.16}$$

While at early times complexity grows exponentially, long after the scrambling time it manifests a linear growth. This delay in the linear regime, causing complexity to be decreased by $n\tau_*$ with respect to the case linear growth immediately appears, is known as *switchback effect*, and is a hallmark of complexity for chaotic systems. At the light of this, the random circuits we have been considering are called *fast scramblers*, since there is no way for a perturbation to spread over a system faster than $\tau_* = \log n$ [106].

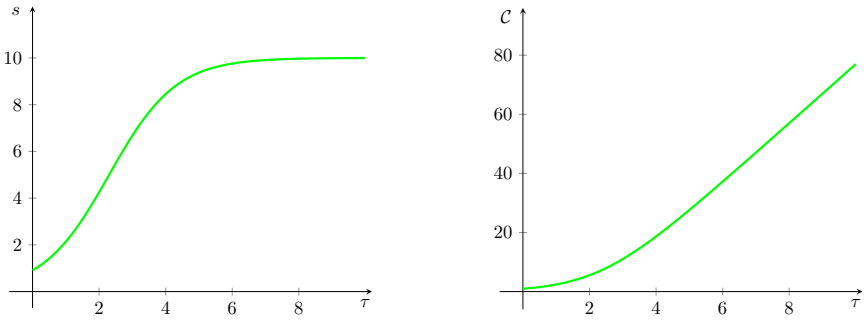

Figure 2.9: Size and complexity of the precursor as functions of time for $n = 10$.

2.5 A geometric model for complexity

In the previous section, we have described fundamental properties of computational complexity in chaotic quantum circuits. Surprisingly, the complexity time evolution and the switchback effect that we have detected in these systems are mirrored by a peculiar geometric model introduced in [22], which we now present. As we will discuss in Ch. 3, this interesting playground gives us necessary conditions for more formal geometric definitions of complexity to reproduce the switchback effect.

2.5.1 The setup

Let us consider a two-dimensional hyperbolic space with curvature radius $L = n/2$, whose metric is

$$ds^2 = \frac{n^2}{4}\left(d\rho^2 + \sinh^2\rho\, d\theta^2\right) . \tag{2.5.1}$$

This space, called *Poincaré disk*, is nothing but a constant-time slice of AdS_3 spacetime in static coordinates (2.1.5), where we have defined $r = \sinh\rho$. As the name suggests, the manifold has the topology of a disk, with center at $\rho = 0$ and a boundary at $\rho \to +\infty$. A crucial property of our model is that the *Gaussian curvature*[9] of the hyperbolic plane is equal to $-4/n^2$.
We now compactify our space by introducing an equilateral hyperbolic polygon centered at $\rho = 0$ with $4g$ sides, where g denotes the genus of the manifold. In order to avoid conical singularities, we identify the sides of the polygon two by two:

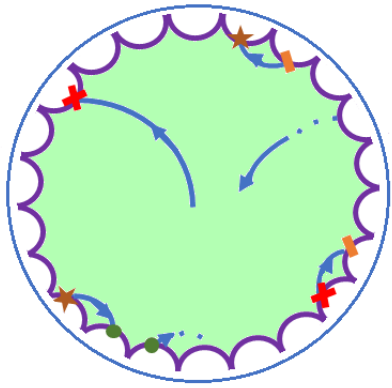

Figure 2.10: Poincaré disk compactified by the introduction of an hyperbolic polygon (in purple). Identified sides are marked with the same symbol. The blue curve represents an example of particle trajectory, starting from the disk center.

The claim is that the motion of a non-relativistic particle on such a negatively

[9] To define this notion, let us imagine to intersect a surface Ξ with normal planes at a given point p. Each intersection with a normal plane determines a curve ξ with a certain curvature. The Gaussian curvature of Ξ at the point p is the product of the maximal and minimal values of the curvature of any possible ξ. Remarkably, for a two-dimensional space the Gaussian curvature is half the scalar curvature.

curved space with Gaussian curvature $-4/n^2$ reproduces the time evolution of complexity for an n-qubits random circuit. In the geometric setup, complexity is identified with the distance of the particle from the center of the disk, measured along the shortest geodesic. In particular, maximum complexity is given by the length ℓ of the longest minimal geodesic starting from the center of the disk. To match the quantum circuit result $\ell \approx e^n$, we can properly tune the number of polygon sides $4g$. Indeed, by the *Gauss-Bonnet theorem*[10] we know that the volume of the compactified disk is roughly the same as the genus: $V \sim g$. On the other hand, under the assumption $\ell >> n$, the volume of the Poincaré disk with maximum distance ℓ from the center reads

$$V = \frac{n^2\pi}{2} \int_0^{\ell/L} d\rho \, \sinh \rho \sim n^2 e^{2\ell/n} \, . \tag{2.5.3}$$

Putting all together, we conclude that taking $g \approx e^{e^n}$ the maximum distance from the center scales exponentially with n.

2.5.2 Time evolution of the distance from the disk center

A further test of matching between complexity in a random circuit and our geometric model has to be searched in the dynamics of the non-relativistic particle moving on the compactified Poincaré disk. Let us suppose that the particle starts from the center $\rho = 0$. With the passing of time, due to the background geometry the particle freely propagates towards the boundary of the disk with constant velocity. In this regime, the distance from the origin (read complexity) linearly grows. Eventually, at the maximum distance ℓ from the center, the particle hits one of the polygon sides. Then, it re-enters the space from the identified side, see Fig. 2.10. Recalling that geodesics on the Poincaré disk are circumferences centered at the boundary, it is clear that the particle approaches the origin, turns away, hits again one of the polygon sides and so on. In general, the approaching to the disk center lasts for a very short time, causing the distance to fluctuate around its maximum value. This continuous exiting and re-entering the manifold goes on for a long time. Indeed, the only way for this process to stop is that the particle re-enters the compactified disk with a small deviation with respect to the radial direction, so that moving on the

[10] For a two-dimensional manifold $\mathcal{M}$ with boundary $\partial\mathcal{M}$, the Gauss-Bonnet theorem reads

$$\int_{\mathcal{M}} K \, d\mathcal{A} + \int_{\partial\mathcal{M}} \kappa_g \, ds = 2\pi\chi(\mathcal{M}) \, . \tag{2.5.2}$$

In the above expression, K is the Gaussian curvature of $\mathcal{M}$, κ_g measures how $\partial\mathcal{M}$ deviates from a geodesic (so, it vanishes for geodesics), and $\chi(\mathcal{M})$ is the *Euler characteristic* of $\mathcal{M}$. Denoting by g the genus of the manifold and by b the number of boundaries, we have $\chi(\mathcal{M}) = 2 - 2g - b$.

corresponding geodesic it approaches the disk center. However, the probability for the particle of reaching a distance $\Delta\mathcal{C}$ less than the maximum value ℓ from the center is pretty small. Explicitly, since the motion on the Poincaré disk is *ergodic*, meaning that the particle trajectories uniformly cover the whole space, such a probability can be estimated as the inverse volume within a distance $\ell - \Delta\mathcal{C}$ from the disk center:

$$P\left(\ell - \Delta\mathcal{C}\right) \sim \frac{1}{V\left(\ell - \Delta\mathcal{C}\right)} \sim e^{-2\Delta\mathcal{C}/n}\,. \tag{2.5.4}$$

In order to obtain sub-exponential distances, we must take $\Delta\mathcal{C} \sim \ell \approx e^n$, leading to a recurrence time of $O(e^{e^n})$. We thus conclude that the simple geometric model at hand agrees with the complexity evolution sketched in Fig. 2.7.

2.5.3 Switchback effect

Last but not least, we show that the toy model at hand mimics the switchback effect which characterizes complexity of chaotic quantum systems. As we have seen, this phenomenon can be detected by the complexity of the precursor $W(\tau) = e^{-iH\tau}We^{iH\tau}$. In the geometric model we are describing, the implementation of any unitary operator can be represented by a geodesic on the compact two-dimensional negatively curved manifold, where the center $\rho = 0$ can be identified with the identity operator $\mathbb{1}$. So, the precursor is described by three consecutive curves:

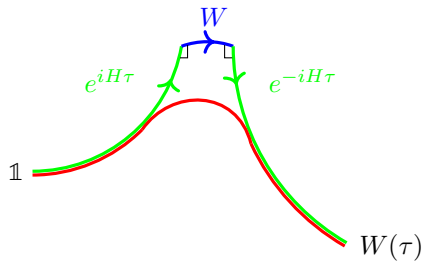

Figure 2.11: Precursor $W(\tau)$ in the geometric model. The green curves denote the forward and backward time evolution operator and the blue curve the perturbation operator W. The red curve represents the shortest geodesic reproducing $W(\tau)$.

Complexity of an operator is interpreted as the length of the corresponding geodesic. Similarly to the discussion in Subsec. 2.4.3, the length of the path obtained by concatenating the three curves $e^{iH\tau}$, W, and $e^{-iH\tau}$ provides an

overestimate of the complexity of the precursor. Indeed, shortcuts generally exists which lead to a shortest path, as in Fig. 2.11. Then, complexity of the precursor can be computed as the distance from the disk center measured along the optimal curve. If we travel on a geodesic for a distance s_1, turn of 90 degrees, move for a distance $2s_2$, rotate of 90 degrees and move again for a distance s_1, the geodesic distance s_3 between the starting and the final points satisfies [22]

$$\cosh\left(\frac{s_3}{L}\right) = \cosh^2\left(\frac{s_2}{L}\right) + \sinh^2\left(\frac{s_2}{L}\right)\cosh\left(\frac{2s_1}{L}\right) , \tag{2.5.5}$$

with L the curvature radius of the manifold. By applying this formula to the precursor path of Fig. 2.11, we get

$$\begin{aligned}\cosh\left(\frac{2\,\mathcal{C}(W(\tau))}{n}\right) &= \cosh^2\left(\frac{\mathcal{C}(W)}{n}\right) + \sinh^2\left(\frac{\mathcal{C}(W)}{n}\right)\cosh\left(\frac{4\,\mathcal{C}\left(e^{-iH\tau}\right)}{n}\right) \\ &= \cosh^2\left(\frac{1}{n}\right) + \sinh^2\left(\frac{1}{n}\right)\cosh\left(2\,\tau\right) ,\end{aligned} \tag{2.5.6}$$

where use has been made of the fact that $L = n/2$, $2s_2 = \mathcal{C}(W) = 1$, and $s_1 = \mathcal{C}\left(e^{-iH\tau}\right) = n\tau/2$. At early and late times we can expand the result, getting

$$\mathcal{C}(W(\tau)) = \begin{cases} e^{\tau}/2 & \text{if } \tau_* - \tau >> 1\,, \\ n(\tau - \tau_*) & \text{if } \tau - \tau_* >> 1\,, \end{cases} \tag{2.5.7}$$

with $\tau_* = \log n$ the scrambling time. So, the length of the precursor shortest geodesic matches the asymptotic behaviors of the precursor complexity in the random circuit model, see eq. (2.4.16). Noticeably, the geometrical model reproduces the switchback effect. In this case, the delay in the linear growth of complexity can be ascribed to the presence of shortcuts reducing the length of the naive geodesic.

2.5.4 Remarks about length and action

In the above argument, we have identified complexity of a unitary operator with the length of the corresponding geodesic passing from the center of the disk. However, we could have defined complexity as the on-shell action along the same curve [22, 23]. The two definitions lead to the same conclusions, up to a different normalization of the manifold metric that we here discuss.

Starting from the metric

$$ds^2 = L^2\left(d\rho^2 + \sinh^2\rho\, d\theta^2\right) , \tag{2.5.8}$$

the geodesic length reads

$$l = L \int \sqrt{\dot{\rho}^2 + \dot{\theta}^2 \sinh^2 \rho}\, d\tau \,, \tag{2.5.9}$$

while the action can be expressed as

$$S = \frac{L^2}{2} \int \left(\dot{\rho}^2 + \dot{\theta}^2 \sinh^2 \rho\right) d\tau \,. \tag{2.5.10}$$

In the above expressions the dot represents a derivative with respect to time τ. During the motion along a geodesic, both the particle velocity and energy are conserved:

$$v = L\sqrt{\dot{\rho}^2 + \dot{\theta}^2 \sinh^2 \rho}\,, \qquad E = \frac{v^2}{2} = \frac{L^2}{2}\left(\dot{\rho}^2 + \dot{\theta}^2 \sinh^2 \rho\right) . \tag{2.5.11}$$

As we have discussed, complexity should linearly grow as $\mathcal{C} = n\tau/2$.
In the length picture, this condition is equivalent to $v = n/2$, which in turn requires $L = n/2$. Then, the Gaussian curvature scales as $-1/n^2$.
In the action picture, we should rather impose $E = n/2$, which is accomplished for $L^2 = n$. This gives a manifold whose Gaussian curvature scales as $-1/n$.
In both cases we conclude that the geometric toy model reflects the main features of complexity evolution for a quantum system of n qubits provided that the background geometry has a negative Gaussian curvature polynomial in n^{-1}.

2.6 Complexity and black holes

In this section we discuss the connection between quantum complexity and BHs in the AdS/CFT framework. As an important step towards the holographic interpretation of complexity, we first argue that BHs can be interpreted as quantum circuits. This similarity completes an ideal triangle of analogies involving random circuits, the toy model introduced in Sec. 2.5, and BHs.

2.6.1 Black holes as quantum circuits

The first description of BHs as processors of quantum information is due to Hayden and Preskill [107], who guessed that the BH internal dynamics is well described by a random circuit composed by two-qubits gates, as the one we have introduced at the beginning of Subsec. 2.4.2. The number of qubits n required to properly model the BH can be reasonably assumed to be proportional to

the BH entropy (2.1.22): $n \approx S_{BH}$. Based on this pattern, in [106] the BH scrambling time, defined as the time it takes for a qubit perturbation to spread over the whole event horizon, has been found to be

$$t_* = \frac{\beta}{2\pi} \log S_{BH} \,, \tag{2.6.1}$$

where β is the inverse BH temperature and the time is measured by an asymptotic clock. To make contact with the quantum circuits we have studied so far, we introduce the dimensionless time

$$\tau = \frac{2\pi t}{\beta} \,. \tag{2.6.2}$$

With this definition we have $\tau_* = \log S_{BH} \approx \log n$, which is in fact the scrambling time for a random circuit, see Subsec. 2.4.3. In other words, *no physical systems scramble information faster than BHs.*

As a consequence to the BH-circuit analogy, the unitary complexity evolution outlined in Subsec. 2.4.2 can be rephrased as shown in Fig. 2.12:

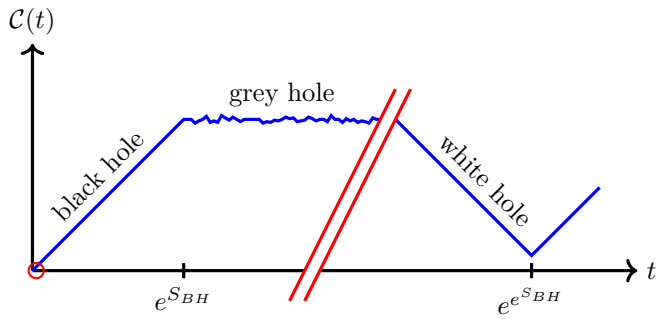

Figure 2.12: Putative time evolution of unitary complexity for a BH, which can be thought of as a chaotic system with finite temperature. The thermalization process occupies the tiny region enclosed in the red circle. The image reproduces a picture in [103].

In the initial stage, complexity keeps growing for a time exponential in the thermal entropy, until it approaches its maximum value. This regime has been identified with the evolution of the actual BH. After complexity has reached the near-maximum value, the system enters a complexity equilibrium phase, which lasts for a doubly exponential time. Then, quantum recurrence causes

complexity to decrease to sub-exponential values. Such an unstable regime has been proposed to correspond to the complexity evolution of a white hole [103].[11]

During the BH era, from the quantum circuit analysis we expect complexity to grow as in eq. (2.4.8):

$$\frac{d\mathcal{C}}{d\tau} \approx n \approx S_{BH} \,. \tag{2.6.3}$$

By exploiting eq. (2.6.2), the rate of complexification measured by an asymptotic observer reads

$$\frac{d\mathcal{C}}{dt} \approx T\, S_{BH} \,, \tag{2.6.4}$$

with $T = \beta^{-1}$ the BH temperature. We emphasize that this regime lasts for an exponential time $t \sim e^n$, which is much bigger than the thermalization scale, estimated as $t_{\text{therm}} < n^p$ for some positive integer p [14]. Therefore, complexity overcomes the limitations of entanglement entropy, which saturates at the thermalization time.

The complexification rate (2.6.4) is extremely high. Actually, it is believed to be the highest possible: *no systems can implement quantum gates faster than BHs*. This conclusion is based on the *Lloyd's bound*, which conjectures that the maximum allowed computational speed of a system is proportional to its energy E [108]. The bound can be reformulated in terms of complexity as [15]

$$\frac{d\mathcal{C}}{dt} \leq \frac{2E}{\pi\hbar} \,. \tag{2.6.5}$$

For a BH, the Lloyd's bound reads

$$\frac{d\mathcal{C}}{dt} \leq \frac{2M}{\pi\hbar} \,, \tag{2.6.6}$$

with M the BH mass. For neutral BHs we have $M \sim TS_{BH}$, so the upper bound on the complexification rate is assumed to be saturated.
If the BH has a conserved charge, as the angular momentum J or the electric charge Q, a tighter bound is given by

$$\frac{d\mathcal{C}}{dt} \leq \frac{2}{\pi\hbar} \left[(M - \Omega J - \Phi Q) - (M - \Omega J - \Phi Q)_{\text{GS}} \right] \,, \tag{2.6.7}$$

in which Ω and Φ are the angular velocity and the electrostatic potential, respectively. The second term in the right hand side is computed for the ground state (GS), which is determined for fixed values of Ω and Φ. The modified

[11] Referring to the Penrose diagram shown in Fig. 2.5, the white hole is clearly related to the BH by a time-reversal symmetry. Under this transformation, a complexity growth is mapped to a complexity decreasing.

Lloyd's bound (2.6.7) is in general violated by charged AdS BHs. A refined version avoiding this issue has been suggested in [109]:

$$\frac{d\mathcal{C}}{dt} \leq \frac{1}{\pi\hbar}\left[(M-\Omega J-\Phi Q)_{+}-(M-\Omega J-\Phi Q)_{-}\right] . \tag{2.6.8}$$

The first and second contributions in the right hand side are meant to be evaluated at the outer and inner BH horizon, respectively. Henceforth, when referring to the Lloyd's bound we will have in mind eq. (2.6.8). We stress that the original Lloyd's bound is based on the assumption that gates transform a state into an orthogonal one. In general, this is not the case for simple gates employed in the complexity definition. Therefore, we will consider the Lloyd's bound as an appreciated feature rather than a strict condition to be verified by complexity.

2.6.2 Holographic complexity

In the previous subsection we have pinpointed striking similarities between the dynamics of BH interiors and random quantum circuits. We now go back to the two-sided eternal AdS BH introduced in Sec. 2.3, turning to the central question of finding a dual CFT quantity capable of fully describing the evolution of BH interiors. The result in eq. (2.6.4) hints that complexity of the TFD state keeps growing far after the system thermalization, just like the ERB traversing the two-sided AdS BH. In light of this, complexity seems to answer our question. However, we are left with a further basic inquiry: which bulk quantity measuring the size of the ERB is dual to complexity of the boundary TFD state? Below we discuss the main proposals.

CV conjecture. Naively, one may look at the volume of the ERB as the candidate geometric quantity exploring the BH interior. Similarly to the Ryu-Takayanagi prescription, one may consider an elongation of the ERB up to the boundary time-slice on which the dual TFD state lives. Roughly speaking, complexity of the TFD state at the given boundary times $|TFD(t_L,t_R)\rangle$ may be conjectured to correspond to the space volume of the resulting hypersurface. To formalize this idea, Susskind and collaborators have proposed [13, 14] to slice the bulk geometry with codimension-one surfaces anchored at both the left and right spacetime boundaries. The major requirements are that the slices do not intersect each other and that they stay away from the BH singularity. This is accomplished by *maximal volume slices*, examples of which are shown in Fig. 2.13.

As we have previously discussed, for the TFD state to manifest a non-trivial dynamics we must take $t_L = t_R = t_b/2$, which defines a boundary condition for

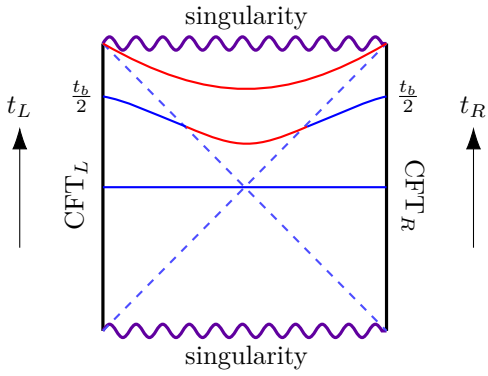

Figure 2.13: Penrose diagram for a two-sided eternal AdS BH, illustrating some maximal slices involved in the CV conjecture. In the d-dimensional case, every point of the Penrose diagram hides a $(d-2)$-dimensional sphere. So, every curve into the diagram is a $(d-1)$-dimensional surface, the red part of which represents the ERB traversing the BH.

the bulk slice. At initial time $t_b = 0$, the maximal slice lies at constant time and crosses the bifurcation surface in the center of the Penrose diagram in Fig. 2.13. As the boundary time t_b grows, the ERB size increases too, as it is clear from the figure. In the limit $t_b \to \infty$ the maximal slice, corresponding to the red curve in Fig. 2.13, is entirely into the BH. By symmetry arguments, its volume has been found to satisfy [13, 14]

$$\lim_{t_b \to \infty} \frac{dV}{dt_b} = \frac{8\pi G L}{d-1} T S_{BH} \,, \tag{2.6.9}$$

where d is the dimension of the bulk spacetime with curvature radius L, T is the BH temperature and S_{BH} is the Bekenstein-Hawking entropy. A comparison between this outcome and eq. (2.6.4) has led to the *complexity = volume* (CV) *conjecture*, stating that complexity of the CFT state living on the boundary time-slice Σ is proportional to the volume of the maximal codimension-one bulk surface $\mathcal{B}$ anchored at Σ [11, 13, 14]:

$$\mathcal{C}_V(\Sigma) = \max_{\partial \mathcal{B} = \Sigma} \frac{V(\mathcal{B})}{GL} \,. \tag{2.6.10}$$

A further evidence in support of the interpretation of $\mathcal{C}_V$ as the complexity of the CFT state comes from the switchback effect. In the holographic scenario, perturbing the TFD state with a precursor $U(t_0)\, W_{L(R)}\, U(-t_0)$ acting on the left (right) system is equivalent to introduce on the left (right) spacetime boundary a particle at the past time $t_{L(R)} = -t_0$. With the passing of time, the

particle falls towards the BH event horizon, describing a null shock wave which perturbs the geometry [110]. As a result, the volume of the maximal slice gets modified. It has been shown [13, 82] that at time $\tau_b = 2\pi t_b/\beta = 0$ the volume complexity (2.6.10) reproduces the expected result $\mathcal{C}_V = S_{BH} \log\left(1 + e^{|\tau_0| - \tau_*}\right)$ of eq. (2.4.16). The conjecture also passes the same test in presence of localized non-symmetric shock waves [111] and multiple shock waves [13, 112].

The CV proposal (2.6.10) can be generalized to any asymptotically AdS spacetime by substituting the AdS curvature radius L with a suitable scale R depending on the background geometry. Obviously, in the absence of BH there is no ERB, so $\mathcal{C}_V$ is time-independent. In Fig. 2.14, we sketch an example of maximal codimension-one bulk surface in global AdS_3:

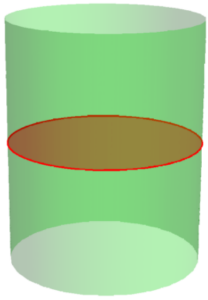

Figure 2.14: Illustration of the CV conjecture in global AdS_3. The red curve represents the boundary time slice Σ. The maximal codimension-one surface $\mathcal{B}$ is shown in faded red.

Explicit calculations in different asymptotically AdS spacetimes such as neutral, charged [113], and rotating BHs [114] have revealed that the volume complexity growth rate is a positive monotonic function of the boundary time t_b. Moreover, at late time the complexification rate saturates the Lloyd's bound from below, meaning that the bound is never violated. In [115], a holographic proof of the Lloyd's bound has been supplied for asymptotically AdS spacetimes of $3+1$ or higher dimension, provided that the weak energy condition is satisfied. Strictly speaking, contrary to eq. (2.6.8), in certain regimes the bound is non-linear in the energy. A saturation of the Lloyd's bound has also been obtained in asymptotically non-AdS spacetimes like warped AdS, where the late time rate depends on the details of the background geometry [116]. This non-universality of volume complexity, already clear from the appearance of the scale R which should be fixed by hand, is one of the major drawbacks of the CV conjecture. Another disadvantage is the lack of a deep reasoning behind the choice of the maximal slice among all the ones attached to the same Σ.

CA conjecture. To solve the unfulfilling features of the CV conjecture, in [15] a new proposal has been put forward. In particular, the maximal codimension-one surface anchored at the boundary time-slice Σ is replaced by the union of all the spacelike codimension-one surfaces attached to the same Σ. The resulting spacetime region, named *Wheeler-DeWitt* (WDW) *patch*, coincides with the *domain of dependence*[12] of each of the involved slices, and is thus bounded by past and future null rays sent from Σ into the bulk.

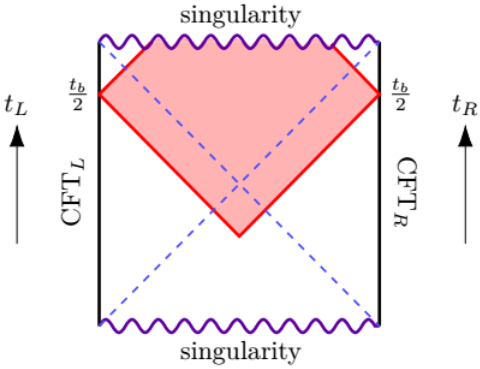

Figure 2.15: Penrose diagram for a two-sided eternal AdS BH, illustrating the WDW patch involved in the CV conjecture. The WDW patch, shown in red, can be easily determined by drawing ingoing and outgoing null lines from the boundaries at times $t_L = t_R = t_b/2$.

As it is obvious from Fig. 2.15, the WDW patch penetrates into the BH, and is thus a good substitute for the ERB as a geometric construction related to complexity of the boundary state. Starting from the CV conjecture we have

$$\mathcal{C} = \frac{V}{GL} = \frac{VL}{GL^2} \sim -\frac{V_{WDW}\,\Lambda}{G}\,, \tag{2.6.11}$$

where $V_{WDW} \sim VL$ is the spacetime volume of the WDW patch and $\Lambda \sim -1/L^2$ is the cosmological constant of asymptotically AdS spacetime. The observation that $V_{WDW}\,\Lambda/G$ is proportional to the Einstein-Hilbert action

$$I_{EH} = \frac{1}{16\pi G}\int_{WDW} d^dx\sqrt{-g}\,(R - 2\Lambda)\,, \tag{2.6.12}$$

where g and R are the metric determinant and the scalar curvature of the bulk spacetime, has inspired the *complexity = action* (CA) *conjecture*, stating

[12] The domain of dependence of a slice $\mathcal{B}$ is the set of points which are fully determined by conditions specified at $\mathcal{B}$ itself.

that complexity of the CFT state defined on the boundary time-slice Σ is proportional to the gravitational action of the associated WDW patch:

$$\mathcal{C}_A(\Sigma) = \frac{I_{WDW(\Sigma)}}{\pi\hbar}\,. \tag{2.6.13}$$

To clarify the proposal, in Fig. 2.16 we show the WDW patch in global AdS_3:

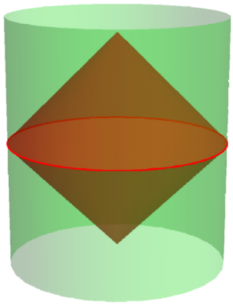

Figure 2.16: Illustration of the CA conjecture in global AdS_3. The red curve denotes the boundary time slice Σ. The WDW patch associated to Σ is shown in faded red.

We stress that the CA conjecture involves the *complete* gravitational action including the boundary terms, and not only the Einstein-Hilbert action (2.6.12). We will thoroughly illustrate all the contributions to I_{WDW} in Sec. 4.1.
Not only the CA conjecture (2.6.13) gets through the same shock wave trials as the CV conjecture [117], but it also gets rid of the undefined scale affecting the volume complexity. However, as we will see, the action complexity is in turn affected by an arbitrary length scale arising from counterterms for the null boundaries of the WDW patch. Moreover, the $\mathcal{C}_A$ growth rate for neutral, charged [113], and rotating AdS BHs [114, 118] has been found to asymptotically approach the Loyd bound from above, violating the conjectured threshold for the computational rate. The universality of the CA conjecture is so solid that the same outcome is featured by exotic solutions such as BHs in warped AdS [119].

CV 2.0 conjecture. One of the biggest disadvantages of the CA conjecture is the violation of the Lloyd's bound. To circumvent the issue, in [16] a further holographic dual of complexity has been proposed. The basic idea is to look at the *thermodynamic volume* $V_{\rm th}$ appearing into the *extended* first law of BH thermodynamics [120]:

$$dM = TdS + \Omega dJ + \Phi dQ + V_{\rm th}dP\,. \tag{2.6.14}$$

In this formalism, the cosmological constant is interpreted as a pressure $P = -\Lambda/(8\pi G)$, whose conjugate quantity is the volume $V_{\rm th}$ of a proper space region. For a neutral two-sided AdS BH, such a region covers the BH interior. Therefore, starting from the Einstein-Hilbert action of the WDW patch we get[13]

$$\lim_{t_b\to\infty}\frac{dI_{EH}}{dt_b}\sim\frac{\Lambda}{G}\lim_{t_b\to\infty}\frac{dV_{WDW}}{dt_b}\sim -PV_{\rm th}\,. \tag{2.6.15}$$

On the other hand, recalling that $\Lambda\sim -1/L^2$, we note that

$$I_{EH}\sim\frac{\Lambda}{G}V_{WDW}\sim -\frac{V_{WDW}}{GL^2}\,. \tag{2.6.16}$$

Putting all together, we deduce that the growth rate of the normalized spacetime volume of the WDW patch $V_{WDW}/(GL^2)$ is given by the product $PV_{\rm th}$. Noticeably, at least for large AdS BHs the thermodynamic quantities M, TS, and $PV_{\rm th}$ are quantitatively the same up to an $O(1)$ constant [16]. So, the normalized spacetime volume of the WDW patch saturates the Lloyd's bound at late times. This observation has led to the *complexity = spacetime volume* (CV 2.0) *conjecture*, relating complexity of the CFT state localized on the boundary time-slice Σ to the spacetime volume of the corresponding WDW patch:

$$\mathcal{C}_{V2.0}(\Sigma)=\frac{V_{WDW(\Sigma)}}{GL^2}\,. \tag{2.6.17}$$

Contrary to the CA conjecture, the Lloyd's bound has been shown to be respected for neutral, electrically charged, and rotating AdS BHs [16]. Additionally, the CV 2.0 conjecture manifests the switchback effect when the AdS BH is perturbed by a light shockwave [113].

In the following table we summarize the main features of the three holographic conjectures:

	Linear growth	**Lloyd's bound**	**Switchback effect**	**Drawbacks**
$\mathcal{C}_V$	✓	✓	✓	Choice of the maximal slice, ambiguous scale R
$\mathcal{C}_A$	✓	×	✓	Ambiguity in the null boundaries counterterms
$\mathcal{C}_{V2.0}$	✓	✓	✓	Ambiguous scale

Table 2.1: Pros and cons of the holographic conjectures CV, CA, and CV 2.0.

[13] The relation between V_{WDW} and $V_{\rm th}$ has been explicitly computed in [16].

Beyond the holographic conjectures. A common peculiarity of the three proposals we have introduced is that holographic complexity grows linearly at late times, and the increasing lasts forever. Such a behavior is in sharp contrast with the expected time evolution shown in Fig. 2.12, where complexity saturates at a time exponential in the BH entropy. The discrepancy can be understood from the fact that classical gravity, which is employed in the holographic computation, does not provide an exhaustive picture of the system. Progress in this direction has been made in [121], where semi-classical corrections to the CV conjecture have been computed for BHs in two bulk dimensions. As an outcome, $\mathcal{C}_V$ enters the plateau regime at both a value and a time exponential in the BH entropy, in agreement with the predictions from quantum circuits.

As a final remark, we stress that what makes the three holographic conjectures putative candidates for the gravitational dual of complexity are basically two properties: the late time linear growth and the switchback effect in response to shockwaves. It has been argued that in asymptotically AdS spacetime there is an infinite class of quantities defined on codimension-one surfaces [17] and on codimension-zero regions [18] which share both features (complexity = anything?). Such a result lends itself to a double interpretation: either there are some arguments to pick the volume of the maximal slice and the gravitational action (spacetime volume) of the WDW patch, as dictated by the CV and CA (CV 2.0) conjectures, or the freedom of selecting the gravitational dual is related to the intrinsic ambiguity in the complexity definition.

Chapter 3

Geometry of quantum complexity

This chapter is an adaptation of the published article [122]. *At the beginning of Sec. 3.1, a thorough introduction to complexity geometry has been added.*

As we have discussed in the previous chapter, computational complexity is supposed to capture the interior evolution of BHs in a holographic fashion. As a starting point to understand complexity of CFT states dual to AdS BH geometries, it is worth gaining a complete comprehension of complexity in the much simpler case of quantum mechanics. In Sec. 2.4 we have presented the traditional notion of unitary complexity for a quantum system of n qubits, based on the counting of the minimal number of gates required to build up a quantum circuit implementing the target unitary transformation U_{T}. This so-called gate complexity is affected by several drawbacks [20]:

- The set of elementary gates needs to be specified.
- The infinite-dimensional set of unitary operators cannot be constructed exactly by implementing a discrete number of gates. So, we must introduce a tolerance ε with which we want to approximate the target unitary U_{T}. Namely, we consider our circuit U_{C} to fulfill the job whether

$$1 - 2^{-n} \operatorname{Tr}\left(U_{\mathrm{C}}^{\dagger} U_{\mathrm{T}}\right) < \varepsilon \,. \tag{3.0.1}$$

- Two unitary operators (or states) which are "near" according to their inner-product, or equivalently whose inner-product is large, can be "far"

in complexity, and viceversa.[1] Consequently, moving around the unitary manifold (or the Hilbert space), gate complexity is *discontinuous*.

Even though the first two ambiguities can be fixed by taking as elementary gates all the one and two-qubits operators, under which choice any unitary transformation can be constructed exactly, the third issue is an intrinsic feature of gate complexity. In this chapter, we explore the geometric approach proposed by Nielsen [19, 21, 123, 124], which represents a way out of the problem. Actually, *complexity geometry* was introduced to find lower bounds of gate complexity. We will instead take the geometric definition of complexity as being the fundamental one.

Mainly following [124], in Sec. 3.1 we review some geometric notions that are useful to investigate unitary complexity, and we derive an explicit formula for sectional curvatures on the unitary manifold. In Sec. 3.2 we consider the explicit examples of one and two-qubits systems, which are interesting nutshells to uncover generic behaviors of unitary complexity. We then move in Sec. 3.3 to the general case of n qubits, focusing on the extent to which some choices of penalties affect the properties of unitary complexity. In Sec. 3.4 we explore state complexity and comment on its connection to unitary complexity, framing the discussion with the formalism of Riemannian submersions. We also derive a closed-form expression for the metric on the space of states and apply it to the instructive case of a one-qutrit system. In Sec. 3.5 we finally present a geometric argument which strongly indicates that, for a suitable choice of penalties, the maximum complexity scales exponentially with the number of qubits n. Details of some calculations are deferred to Appendix A.

3.1 Unitary complexity

The general idea by Nielsen is to replace the discrete counting of gates with the continuous flowing between points on the unitary manifold $\mathrm{SU}(2^n)$. Namely, if we choose the elementary gates to be $g_l = e^{-iT_l\delta t}$, where T_l are the generators of the $\mathfrak{su}(2^n)$ algebra, in the limit $\delta t \to 0$ the circuit made by small steps becomes a continuous path on $\mathrm{SU}(2^n)$. More precisely, we can define

$$U_{\mathrm{T}}(t) = \overleftarrow{\mathcal{P}}\, e^{-i\int_0^t H(\tau)d\tau}\,, \tag{3.1.1}$$

in which the path-ordering symbol $\overleftarrow{\mathcal{P}}$ reflects the fact that the rightmost gate acts first. The traceless Hermitian operator $H(\tau)$ can be expressed as a linear

[1] For instance, the state of a big system times a single spin up and the state of an identical system times a single spin down are orthogonal (far in inner-product), but can be easily built from each others by flipping the spin (near in complexity).

combination of the $\mathfrak{su}(2^n)$ generators:

$$H(\tau) = \sum_I Y^I(\tau)\, T_I\,, \tag{3.1.2}$$

where the *control functions* $Y^I(\tau)$ specify which gates act at time τ. In this geometric setup, unitary complexity is defined as the length of the *shortest geodesic* connecting the target unitary $U_{\rm T}(t)$ to the identity:

$$\mathcal{C}(U_{\rm T}(t)) = \min_Y \int_0^t F(Y(\tau))\, d\tau\,. \tag{3.1.3}$$

The minimization over the control functions parallels the construction of the optimal circuit in the gate complexity perspective. The function F is referred to as *cost function*, and dictates the way we measure distances on the unitary manifold. The most common choice is

$$F_k\left(Y\right) = \left(\sum_I \left|Y^I\right|^k\right)^{1/k}\,, \tag{3.1.4}$$

with k an integer number. In the following we will specialize to $k=2$, in which case the cost function coincides with the distance induced by the Riemannian metric on the unitary manifold:[2]

$$F_2\left(Y(\tau)\right) = \sqrt{\langle H(\tau), H(\tau)\rangle_0}\,, \qquad \langle H, K\rangle_0 = \frac{{\rm Tr}\left(H\,K\right)}{2^n}\,. \tag{3.1.5}$$

At this stage, the unitary manifold is endowed with the usual *inner-product metric*

$$ds_U^2 = \sum_{I,J} {\rm Tr}\left(idU\,U^\dagger T_I\right)\delta_{IJ}{\rm Tr}\left(idU\,U^\dagger T_J\right)\,, \tag{3.1.6}$$

which is *bi-invariant*, meaning that it does not change under both left $U \to U_{\rm L}U$ and right $U \to UU_{\rm R}$ translations.[3] Clearly, all tangent directions T_I are treated the same. However, in order to define complexity in this context we need to translate the notions of elementary and hard gates in the geometric language. Hard transformations are obtained by stretching the corresponding directions on the unitary manifold, assigning to the respective generators T_I a penalty factor $q_I > 1$. Consequently, the cost function is modified as

$$F_{2,q}\left(Y(\tau)\right) = \sqrt{\sum_I q_I \left|Y^I\right|^2} = \sqrt{\langle H(\tau), H(\tau)\rangle}\,, \qquad \langle H, K\rangle = \frac{{\rm Tr}\left(H\,\mathcal{G}(K)\right)}{2^n}\,. \tag{3.1.7}$$

[2] Throughout this thesis we assume the normalization convention ${\rm Tr}\left(T_I T_J\right) = 2^n\delta_{IJ}$.

[3] To explicitly see this, we note that the metric can be expressed as $ds_U^2 = {\rm Tr}\left(dU^\dagger dU\right)$.

Here $\mathcal{G}$ is an Hermitian linear operator associating to every component T_I of the operator it acts on the proper penalty factor q_I:

$$\mathcal{G}(H) = \sum_I q_I \, Y^I \, T_I \, . \tag{3.1.8}$$

In our application, we suppose the inner-product $\langle \dots \rangle$ to be independent of the group point U. So, the inner-product can be defined at the origin of the unitary manifold and then mapped to every point of the manifold by right-translations. The resulting metric

$$ds^2_U = \sum_{I,J} \mathrm{Tr}\left(idU\, U^\dagger T_I\right) \langle T_I, T_J \rangle \mathrm{Tr}\left(idU\, U^\dagger T_J\right) \, , \tag{3.1.9}$$

named *complexity metric*, is automatically left unchanged by any right-translation, and is thus a *right-invariant metric* [125, 126]. The underlying reason for this choice can be understood from the fact that gates act on the right. Indeed, let us consider a target operator U_{T} which is constructed by implementing m gates starting from the operator W [23]:

$$U_{\mathrm{T}} = g_m \dots g_1 W \, . \tag{3.1.10}$$

The minimum number of gates necessary to move from W to U_{T} does not change if we right-translate both operators by an arbitrary unitary U_{R}:

$$U_{\mathrm{T}} U_{\mathrm{R}} = g_m \dots g_1 W U_{\mathrm{R}} \, . \tag{3.1.11}$$

In other words, the complexity of building U_{T} out of W equals the complexity of building $U_{\mathrm{T}} U_{\mathrm{R}}$ out of $W U_{\mathrm{R}}$, for any U_{R}. The same is not true for left-translations, in which case

$$U_{\mathrm{L}} U_{\mathrm{T}} = U_{\mathrm{L}} g_m \dots g_1 W = \left(U_{\mathrm{L}} g_m \dots g_1 U_{\mathrm{L}}^\dagger\right) U_{\mathrm{L}} W \, . \tag{3.1.12}$$

Clearly, m gates are in general not enough to implement the operator $U_{\mathrm{L}} g_m \dots g_1 U_{\mathrm{L}}^\dagger$. Therefore, complexity distance is right-invariant but not left-invariant. By the way, since any point on the manifold can be mapped to another by right-translations, the space of unitary operators is *homogeneous*.

3.1.1 Connection and geodesic equation

Several geometric properties of the unitary manifold can be inferred by the Levi-Civita connection ∇. A Levi-Civita connection compatible with the metric (3.1.7) is given by the *Koszul's formula* [127], which, thanks to the fact that the

inner-product can be computed at the identity (and therefore is constant in a suitable basis), simplifies to

$$-2i\langle\nabla_X Y, Z\rangle = \langle[X,Y],Z\rangle + \langle[Z,X],Y\rangle - \langle[Y,Z],X\rangle\,, \tag{3.1.13}$$

where X, Y, Z are right-invariant fields interpreted as Hermitian matrices at the origin. Eq. (3.1.13) allows us to define

$$\nabla_X Y = \frac{i}{2}\left([X,Y] + \mathcal{G}^{-1}([X,\mathcal{G}(Y)] + [Y,\mathcal{G}(X)])\right)\,. \tag{3.1.14}$$

Setting $Y = X$ in eq. (3.1.14), we obtain the geodesic equation, which is nothing but the Euler-Arnold[4] equation [126]

$$\dot{X} + i\mathcal{G}^{-1}\left([X,\mathcal{G}(X)]\right) = 0\,. \tag{3.1.15}$$

In general, we expect geodesics to have an intricate behavior. Eq. (3.1.15) admits a simple class of solutions, given by the exponential of an eigenvector of the penalty operator $\mathcal{G}$. We refer to such solutions as *exponential geodesics*, and we study their conjugate points in Sec. 3.5.

3.1.2 Comments on the choice of basis

Homogeneity of the unitary manifold allows us to work in a neighborhood of the origin, a tangent vector to which is an element of the Lie algebra $\mathfrak{su}(2^n)$. From now on, we pick up as a basis T_I of this algebra the set of generalized Pauli matrices σ, which are nothing but tensor products of n matrices, each of which can be either an SU(2) Pauli matrix σ_i $(i = x\,, y\,, z)$ or the identity $\mathbb{1}_2$. A generalized Pauli matrix is characterized by a *weight* w_σ, defined as the number of SU(2) Pauli matrices appearing in the tensor product σ, i.e. the number of qubits involved by the corresponding operator. In this basis, we will consider only diagonal metrics $\mathcal{G}(\sigma) = q_\sigma\sigma$, so that the inner-product (3.1.7) reads

$$\langle\rho,\sigma\rangle = q_\sigma\delta_{\rho\sigma}\,, \tag{3.1.16}$$

where q_σ represents the penalty factor for the generator σ normalized as $\mathrm{Tr}\left(\sigma^2\right) = 2^n$. The case $q_\sigma = 1$ for all σ, which we refer to as *non-penalized choice*, corresponds to the usual inner-product metric on SU(2^n).

As a consequence of the algebra of SU(2) Pauli matrices, the basis of generalized Pauli matrices has some properties that will play a fundamental role in the computations that follow:

[4] Recent applications of the Euler-Arnold equations to complexity were discussed in [31, 32].

- Two elements of the basis ρ and σ either commute or anti-commute:

$$\rho\,\sigma = (-1)^d\,\sigma\,\rho\,. \tag{3.1.17}$$

  Here d is the number of qubits on which both ρ and σ act, but with a *different* SU(2) Pauli matrix. For a given ρ with weight $w \neq 0$, the number of generalized Pauli matrices σ anti-commuting with it is[5]

$$4^{n-w} \sum_{d\,odd=1}^{w} \binom{w}{d} 2^w = \frac{4^n}{2^w} \sum_{k=0}^{\left[\frac{w-1}{2}\right]} \binom{w}{2k+1} = \frac{4^n}{2}\,, \tag{3.1.18}$$

  where $[\dots]$ denotes the integer part. Remarkably, this number does not depend on the weight w.

- The commutator of two elements of the basis ρ and σ (if not vanishing) is proportional to another element of the basis. Therefore, the penalty $q_{[\rho,\sigma]}$ is well-defined. In case $[\rho,\sigma] = 0$, we set by definition $q_{[\rho,\sigma]} = 1$.

3.1.3 Riemann tensor

We now go back to the investigation of the unitary manifold geometry considering the basis of generalized Pauli matrices, which can be viewed as right-invariant frame fields. In this basis, the curvature tensor is [124]

$$R_{\rho\sigma\tau\mu} = \langle \nabla_\rho \tau\,, \nabla_\sigma \mu\rangle - \langle \nabla_\sigma \tau\,, \nabla_\rho \mu\rangle - \langle \nabla_{i[\rho\,,\sigma]}\tau\,, \mu\rangle\ . \tag{3.1.19}$$

Using eq. (3.1.14), we find:

$$\nabla_\rho \tau = i\,c_{\rho\,,\tau}\,[\rho\,,\tau]\ , \qquad c_{\rho\,,\tau} \equiv \frac{1}{2}\left(1 + \frac{q_\tau - q_\rho}{q_{[\rho\,,\tau]}}\right)\ . \tag{3.1.20}$$

Thus, the Riemann tensor reads

$$\begin{aligned} R_{\rho\sigma\tau\mu} = {} & c_{\rho\,,\tau}\,c_{\sigma\,,\mu}\,\langle i\,[\rho\,,\tau]\ , i\,[\sigma\,,\mu]\rangle - c_{\sigma\,,\tau}\,c_{\rho\,,\mu}\,\langle i\,[\sigma\,,\tau]\ , i\,[\rho\,,\mu]\rangle \\ & - c_{[\rho\,,\sigma]\,,\tau}\ \langle i\,[i\,[\rho\,,\sigma]\ ,\tau]\ ,\mu\rangle\ . \end{aligned} \tag{3.1.21}$$

It is important to note that the component $R_{\rho\sigma\tau\mu}$ vanishes unless the product of the corresponding generalized Pauli matrices $\rho\sigma\tau\mu$ is proportional to the

[5] We necessarily have d odd and $1 \leq d \leq w$. To construct a generator σ with a given d, we assign to d out of the w qubits involved by ρ an SU(2) Pauli matrix different than the one assigned by ρ, and to the other $w - d$ qubits either the same SU(2) Pauli matrix assigned by ρ or the identity. Then, we fill out each of the remaining $n - w$ entries in the σ tensor product with either an arbitrary SU(2) Pauli matrix or the identity.

identity. Another interesting observation is that, since eq. (3.1.21) depends just on commutators, the Riemann curvature of a subgroup of unitary operators does not depend on the metric data outside the subgroup itself. For instance, complexity on a one-qubit subgroup depends just on penalties of generators acting on that particular subgroup.

3.1.4 Sectional curvatures

The *sectional curvature* $K(v,w)$ at a point U_0 of a manifold is defined as the Gaussian curvature of the 2-dimensional submanifold spanned by geodesics whose tangent vector at U_0 lies in the plane determined by (v,w). The general expression for the sectional curvature is [128]

$$K(v,w) = \frac{R_{\alpha\beta\gamma\delta} v^\alpha w^\beta w^\gamma v^\delta}{(v_\alpha v^\alpha)(w_\beta w^\beta) - (v_\alpha w^\alpha)^2} \,. \tag{3.1.22}$$

Note that the quantity $K(v,w)$ does not depend on the particular choice of vectors v and w on the plane (v,w).

By homogeneity of the unitary manifold, it is not restrictive to focus on the sectional curvatures at the origin. Since the generalized Pauli matrices are orthogonal but not normalized, see eq. (3.1.16), the sectional curvature in the plane defined by two of them is

$$K\left(\rho\,,\sigma\right) = \frac{R_{\rho\sigma\sigma\rho}}{q_\rho\, q_\sigma} \,. \tag{3.1.23}$$

From eq. (3.1.21) we find

$$R_{\rho\sigma\sigma\rho} = c_{\rho\,,\sigma}\, c_{\sigma\,,\rho} \left\langle i\left[\rho\,,\sigma\right]\,, i\left[\sigma\,,\rho\right]\right\rangle - c_{[\rho\,,\sigma]\,,\sigma} \left\langle i\left[i\left[\rho\,,\sigma\right]\,,\sigma\right]\,,\rho\right\rangle \,. \tag{3.1.24}$$

If ρ and σ commute, $K(\rho,\sigma)$ clearly vanishes.
If ρ and σ do not commute, from eq. (3.1.17) we get $[\rho,\sigma] = 2\rho\sigma$.
A direct calculation gives:

$$\left\langle i\left[\rho\,,\sigma\right]\,, i\left[\rho\,,\sigma\right]\right\rangle = 4\, q_{[\rho\,,\sigma]}\,, \qquad \left\langle i\left[i\left[\rho\,,\sigma\right]\,,\sigma\right]\,,\rho\right\rangle = -4\, q_\rho\,. \tag{3.1.25}$$

Also noting that $q_{[[\rho\,,\sigma]\,,\sigma]} = q_\rho$, we get the sectional curvature for $[\rho\,,\sigma] \neq 0$:

$$K\left(\rho\,,\sigma\right) = \frac{1}{q_\rho\, q_\sigma} \left[-3\, q_{[\rho\,,\sigma]} + 2\left(q_\rho + q_\sigma\right) + \frac{\left(q_\rho - q_\sigma\right)^2}{q_{[\rho\,,\sigma]}}\right] \,. \tag{3.1.26}$$

Eq. (3.1.26) reveals that $K\left(\rho\,,\sigma\right)$ is positive unless $q_{[\rho\,,\sigma]}$ is big enough compared to q_ρ and q_σ. In other words, negative sectional curvatures are necessarily

associated to commutators of the form

$$[\text{easy}\,,\text{easy}] = \text{hard}\,, \tag{3.1.27}$$

where easy and hard refer to small and large penalty factors, respectively. This result is consistent with the analysis in [20].

The sign of sectional curvatures plays a key role in relation to ergodicity. Roughly speaking, a geodesic flow is called ergodic if its typical geodesic will eventually explore all the allowed portions of the unitary manifold. From a general theorem [129], we know that geodesic flow on a manifold whose sectional curvatures are all negative is ergodic. Unfortunately, this result is not directly applicable to unitary complexity. Indeed, the sectional curvatures of the one-qubit subspace depend just on the one-qubit penalty factors, and at least two out of three independent sectional curvatures in the one-qubit directions are always positive (see Sec. 3.2.1). By the way, some examples in which ergodicity is preserved in the presence of some positive sectional curvatures exist, e.g. [130].

Ergodicity and negativity of sectional curvatures are necessary ingredients for a quantum chaotic behavior of complexity geometry [23]. To get a feeling of this, let us consider two geodesics starting at the origin of the unitary manifold and evolving under infinitesimally close local Hamiltonians. If the sectional curvature in the direction of such tangent vectors is negative, geodesics diverge. This positive geodesic deviation expresses a strong dependence on initial conditions, that is an essential feature of chaos.

3.1.5 Ricci tensor and curvature

The Ricci tensor is obtained from the Riemann tensor as $R_{\sigma\tau} = g^{\rho\mu} R_{\rho\sigma\tau\mu}$. Given that in our basis the metric is diagonal and $R_{\rho\sigma\tau\mu}$ is non-vanishing only for $\rho\sigma\tau\mu \propto \mathbb{1}$, we deduce that $R_{\sigma\tau}$ is diagonal too. Geometrically, the Ricci tensor can be interpreted as a sum of suitable sectional curvatures. In particular, given an orthonormal basis $\{e_k\}$ with $k = 1, \ldots, N$ and such that $e_1 = v$, the Ricci tensor is completely determined by [128]

$$R_{\alpha\beta} v^\alpha v^\beta = \sum_{k=2}^{N} K(v, e_k)\,. \tag{3.1.28}$$

In the same way, the scalar curvature can be expressed as

$$R = \sum_{k=1}^{N} R_{\alpha\beta} e_k^\alpha e_k^\beta = \sum_{\sigma,\,\rho} K\left(\rho\,,\sigma\right)\,. \tag{3.1.29}$$

Thus, in order to get a negatively curved unitary manifold it is enough that negative sectional curvatures dominate over positive ones. Even though we do not know about any mathematical theorem relating the sign of R to ergodic geodesic flows, we expect this property to be a detector of ergodicity.

3.2 Few qubits

As an explicit application of the technology introduced in the previous section, we start by considering the simplest cases of one-qubit and two-qubits systems. More specifically, we investigate the behavior of sectional and scalar curvatures in relation to various penalization of the algebra generators. As we will see, some outcomes generalize to systems of large number of qubits.

3.2.1 One qubit

The generators of the $\mathfrak{su}(2)$ algebra are simply the Pauli matrices $\{\sigma_x, \sigma_y, \sigma_z\}$. Without loss of generality, we choose as penalty factors $q_{\sigma_x} = 1$, $q_{\sigma_y} = Q$, and $q_{\sigma_z} = P$. From eq. (3.1.26), the sectional curvatures $K_{ij} \equiv K(\sigma_i, \sigma_j)$ are

$$\begin{aligned} K_{xy} &= \frac{-3P^2 + 2P + 2PQ + Q^2 + 1 - 2Q}{PQ}\,, \\ K_{xz} &= \frac{-3Q^2 + 2Q + 2PQ + P^2 + 1 - 2P}{PQ}\,, \\ K_{yz} &= \frac{-3 + 2P + 2Q + P^2 + Q^2 - 2PQ}{PQ}\,, \end{aligned} \tag{3.2.1}$$

and the scalar curvature is

$$R = -2\frac{(Q-P)^2 - 2(P+Q) + 1}{PQ}\,. \tag{3.2.2}$$

The signs of sectional and scalar curvatures are shown in Fig. 3.1, from which we deduce that two out of the three sectional curvatures in eq. (3.2.1) are positive in the whole parameter space. An important remark is that these quantities are not enough to compute the sectional curvature in an arbitrary plane, which can be extracted from the Riemann tensor. We checked that the values in eq. (3.2.1) correspond for all P, Q to the maxima and minima of the sectional curvature.

In Sec. 2.4 we have seen that the maximal complexity in chaotic systems is large, in general exponential in the number of degrees of freedom. Even though

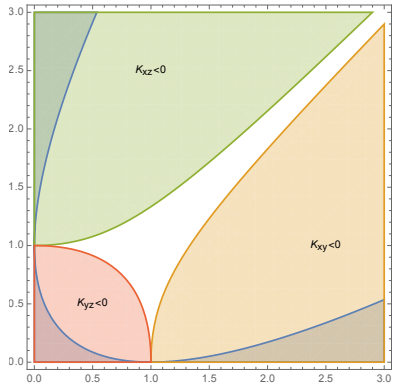

Figure 3.1: Regions of negativity of sectional curvatures in the (P, Q) plane. In the white region all the sectional curvatures are positive. The blue shaded regions correspond to a negative scalar curvature.

it might seem unreasonable to require this to happen in systems of few qubits, a toy model with large maximal complexity can be obtained in the limit of penalties P, Q approaching infinity.
A possibility is to set

$$P = 1\,, \qquad Q \to \infty\,, \tag{3.2.3}$$

in which case the sectional and scalar curvatures diverge:

$$R = 8 - 2Q\,, \qquad K_{xz} = 4 - 3Q\,, \qquad K_{xy} = K_{yz} = Q\,. \tag{3.2.4}$$

Another option is

$$P = Q \to \infty\,, \tag{3.2.5}$$

leading to small and positive curvatures:

$$R = \frac{8}{P} - \frac{2}{P^2}\,, \qquad K_{xy} = K_{xz} = \frac{1}{P^2}\,, \qquad K_{yz} = \frac{4}{P} - \frac{3}{P^2}\,. \tag{3.2.6}$$

Finally, we can take

$$P = \beta Q \to \infty\,, \tag{3.2.7}$$

with $\beta > 0$ a constant. In this limit, we find that the sectional curvatures approach to finite constants. For $\beta \neq 1$, the scalar curvature is negative and equal to $R = -2(\beta - 1)^2/\beta$.
Although all these limits share an infinite volume of the unitary manifold (measured with the complexity metric), they are very different from the point

of view of complexity. In the case (3.2.3) one generator is forbidden, but the two non-penalized generators are enough to build whatever unitary we want: maximal complexity is finite. On the other hand, in the cases (3.2.5) and (3.2.7) two generators are forbidden, and the only allowed generator can produce just a special class of unitary, i.e. rotations along the x axis: maximal complexity goes to infinity.

3.2.2 Two qubits

The two-qubits case is the simplest environment in which we can investigate what happens if operators are penalized according to the number of qubits they act on. To address this question, we take $q_\sigma = A$ for generators with weight $w_\sigma = 1$ and $q_\sigma = B$ for generators with weight $w_\sigma = 2$. The non-vanishing sectional curvatures $K(\rho, \sigma)$ in eq. (3.1.26) can take three values:

$$a = \frac{1}{A}\,, \qquad b = \frac{A}{B^2}\,, \qquad c = \frac{4B - 3A}{B^2}\,. \tag{3.2.8}$$

The value a arises when $w_\rho = w_\sigma = 1$, the value c when $w_\rho = w_\sigma = 2$, and the value b when $w_\rho \neq w_\sigma$. The multiplicity of each value is[6]

$$N_a = 12\,, \qquad N_b = 72\,, \qquad N_c = 36\,. \tag{3.2.9}$$

Summing up the non-vanishing sectional curvatures with their multiplicity, we get the scalar curvature

$$R = -12\,\frac{3\,A^2 - 12\,AB - B^2}{AB^2}\,. \tag{3.2.10}$$

Let us specialize to $A = 1$ and $B = q > 1$, thus penalizing the weight-two generators, denoted as *hard* (h), compared to the weight-one generators, denoted as *easy* (e). The scalar curvature reads

$$R = 12\,\frac{-3 + 12\,q + q^2}{q^2}\,, \tag{3.2.11}$$

and is always positive. Remarkably, no singularity appears in the curvature if we send $q \to \infty$. In this penalization scheme, the structure of the algebra of generators is

$$[\mathrm{e}\,,\mathrm{e}] = \mathrm{e}\,, \qquad [\mathrm{e}\,,\mathrm{h}] = \mathrm{h}\,, \qquad [\mathrm{h}\,,\mathrm{h}] = \mathrm{e}\,, \tag{3.2.12}$$

which gives rise to positive sectional curvatures, as discussed in Subsec. 3.1.4. Consequently, the most intuitive choice of penalties is not appropriate to mimic complexity of chaotic systems (see also [20] for the same conclusion).

[6] We will present a general formula for the counting of non-vanishing sectional curvatures in Appendix A.1.

If we instead make the more unrealistic choice of penalizing the weight-one generators, setting $A = p > 1$ and $B = 1$, the scalar curvature becomes

$$R = -12\,\frac{3\,p^2 - 12\,p - 1}{p}\,. \tag{3.2.13}$$

In this case, the structure of the algebra of generators is reversed

$$[\mathrm{h}\,,\mathrm{h}] = \mathrm{h}\,, \qquad [\mathrm{e}\,,\mathrm{h}] = \mathrm{e}\,, \qquad [\mathrm{e}\,,\mathrm{e}] = \mathrm{h}\,, \tag{3.2.14}$$

and gives rise to negative sectional curvatures at large enough p. This result provides a quantitative explanation to some intuitions discussed in [20].

We point out that the algebra structures (3.2.12) and (3.2.14) always arise when we split the set of generators into two classes, one of which is a maximal subalgebra.

3.3 Many qubits

Having gained some intuition on complexity of unitary operators for one-qubit and two-qubits systems, we now consider quantum systems composed by an arbitrary number n of qubits. We are mostly interested in the large-n limit, which, even though still far from thoroughly modeling quantum field theories involved in holography, under particular conditions manifest chaotic effects that parallel the dynamics of black holes [20, 82]. In this perspective, in Sec. 2.6 we have outlined striking similarities between the switchback effect in quantum circuits and the way black holes react to shock wave perturbations [13, 82, 112]. In Sec. 2.5, we have argued that the switchback effect takes place in a toy model based on the motion of a particle on a negatively curved two-dimensional space, provided that the Gaussian curvature of the manifold scale as $1/n$ or $1/n^2$ in the large-n limit (depending on the identification of complexity with geodesic distance or action along the geodesic) [22, 23]. Recalling that the sectional curvature defined in eq. (3.1.22) is the Gaussian curvature of a two-dimensional submanifold, we can regard the toy geometry as a two-dimensional section of the unitary manifold [23]. Thus, in order to get a satisfying description of the switchback effect in the context of complexity geometry, the typical sectional curvatures of the unitary manifold should be negative and should scale as $1/n$ or $1/n^2$ for large-n. Regardless of the convention we consider (distance of action), the takeaway message is that divergence of sectional curvatures for $n \to \infty$ gives rise to a singular behavior that should be avoided. For few qubits systems, in which case this requirement is meaningless, negative curvature is still a necessary ingredient to reproduce the switchback effect [131].

3.3.1 Preliminaries

With the purpose of exploring which penalization schemes suitably reproduce the aforementioned properties of curvatures, in this section we analyze different choices, all characterized by the penalties being just functions of the weight of the corresponding generator: $q_\sigma = q_\sigma(w_\sigma)$. To ease the notation, we denote the penalty associated to a generator of weight $w_\sigma = w$ by q_w. The number of such generators is

$$\mathcal{N}_w = 3^w \binom{n}{w} . \tag{3.3.1}$$

As described in Sec. 3.1.4, if two generalized Pauli matrices ρ and σ commute, the sectional curvature $K(\rho, \sigma) = 0$.[7] If instead ρ and σ do not commute, the value of the sectional curvature $K(\rho, \sigma)$ depends just on the penalties of ρ, σ, and their commutator. With our assumptions, this translates into a dependence on the weights of the involved generators. Setting $w_\rho = M$ and $w_\sigma = N$, the weight of $[\rho, \sigma]$ can take the values (see Appendix A.1)

$$w_r = |M - N| + 1 + 2r \,, \tag{3.3.2}$$

where the integer r has the following range

$$\begin{aligned} &0 \leq r \leq \min\left(N-1, \left[\frac{n-(M-N)-1}{2}\right]\right) \qquad \text{for} \quad M \geq N \,, \\ &0 \leq r \leq \min\left(M-1, \left[\frac{n-(N-M)-1}{2}\right]\right) \qquad \text{for} \quad M < N \,, \end{aligned} \tag{3.3.3}$$

with $[\dots]$ the integer part. In light of this, it is convenient to define the curvature of the section spanned by generators with weight $w_\rho = M$ and $w_\sigma = N$ by $K(\rho, \sigma) \equiv K(M, N, r)$. From eq. (3.1.26), we have

$$K(M,N,r) = \frac{1}{q_M q_N}\left(-3\, q_{w_r} + 2\,(q_M + q_N) + \frac{(q_M - q_N)^2}{q_{w_r}}\right) . \tag{3.3.4}$$

Denoting the multiplicity of such sectional curvatures by $\mathcal{N}(M, N, r)$, an explicit expression of which is derived in Appendix A.1, the scalar curvature can be computed as

$$R = \sum_{M,N} \sum_{r} \mathcal{N}(M,N,r)\, K(M,N,r) \,. \tag{3.3.5}$$

In this section, we employ such a formalism to investigate the geometric properties of the unitary manifold for various penalization schedules.

[7] Given a generalized Pauli matrix, $4^n/2$ basis generators commute with it, see eq. (3.1.18). So, about one half of the total sectional curvatures vanish by construction, independently of the penalty factors.

3.3.2 Draconian penalties

Any operator in $\mathrm{SU}(2^n)$ can be built as a combination of one-qubit and two-qubits operators [132]. This result suggests the somewhat minimal choice of penalty factors

$$q_w = \begin{cases} 1 & \text{for } w \leq 2\,, \\ q & \text{for } w > 2\,, \end{cases} \tag{3.3.6}$$

studied in detail in [124]. This penalization scheme does not distinguish between different values of the weight $w > 2$, and was thus called *draconian* in [20]. The possible values of sectional curvatures, given by eq. (3.3.4), are summarized in Table 3.1:

	$[\rho\,,\sigma] \in e$	$[\rho\,,\sigma] \in h$
$\rho, \sigma \in e$	$K = 1$	$K = 4 - 3q$
$\rho, \sigma \in h$	$K = \frac{4\,q-3}{q^2}$	$K = \frac{1}{q}$
$\rho \in e,\, \sigma \in h$	$K = q$	$K = \frac{1}{q^2}$

Table 3.1: Values of non-vanishing sectional curvatures for all choices of ρ, σ in the draconian model. We denote by e and h the set of easy ($w \leq 2$) and hard ($w > 2$) generators, respectively.

For $q = 1$ we recover the non-penalized choice, which corresponds to a bi-invariant metric on $\mathrm{SU}(2^n)$. In this case all the non-vanishing sectional curvatures are equal and positive. The interesting region with negative curvature is instead at large q, in which limit it makes sense to consider only the sectional curvatures at leading orders. In particular, we keep just the $\mathcal{O}(q)$ and the $\mathcal{O}(1)$ terms. In this approximation, the only non-vanishing sectional curvatures are

$$\begin{aligned} &K(1,1,0) = K(2,1,0) = K(2,2,0) = 1\,, \\ &K(3,2,0) = q\,, \qquad K(2,2,1) = 4 - 3q\,, \end{aligned} \tag{3.3.7}$$

with multiplicities

$$\begin{aligned} &\mathcal{N}(1,1,0) = 6n\,, \qquad \mathcal{N}(2,1,0) = \mathcal{N}(2,2,0) = 18n(n-1)\,, \\ &\mathcal{N}(3,2,0) = \mathcal{N}(2,2,1) = 54n(n-1)(n-2)\,. \end{aligned} \tag{3.3.8}$$

Then, the scalar curvature is

$$R = -54n(n-1)(n-2)q + 6n(36n^2 - 99n + 64) + \mathcal{O}(1/q)\,, \tag{3.3.9}$$

in agreement with the exact result computed in [124]. From there we find that, in order to get a negative scalar curvature, q has to grow exponentially with n. Namely, we need $q \propto 4^n$ or larger. In this regime the scalar curvature is dominated by a small number (polynomial in n) of sectional curvatures whose magnitude grows like $|K| \approx q \approx 4^n$. Such a singular behavior, as discussed in [23], prevents this model from describing some fundamental processes of complexity evolution, such as the switchback effect.

3.3.3 Towards a more sustainable taxation policy

In order to avoid the singular geometry arising from the draconian schedule, in [23] a *moderate* choice was advocated:

$$q_w = \begin{cases} 1 & \text{for } \ w \leq 2\,, \\ c\, 4^{w-2} & \text{for } \ w > 2\,, \end{cases} \tag{3.3.10}$$

where c is an $\mathcal{O}(1)$ positive constant. The exponential scaling $q_w \propto 4^w$ is suggested by the draconian model, in which case the condition $q \propto 4^n$ ensures a negative curvature. By contrast, in the moderate model (3.3.10) typical[8] sectional curvatures are negative and vanishes polynomially in the large-n limit, enabling the switchback effect.

Despite the moderate schedule goes in the direction of a more progressive taxation than the draconian one, there is still a minor source of inequality: the very low income guys at $w = 1$ are taxed just the same as the working class at $w = 2$. In order to promote social justice, we are motivated to introduce the following choice of penalties (see also [104])

$$q_w = \alpha^{w-1}\,, \tag{3.3.11}$$

which we refer to as *progressive*. The constant $\alpha > 1$ generalizes the scaling at large w to $q_w \propto \alpha^w$, and can be used as an expansion parameter for the analytic understanding of the model. In particular, from eq. (3.3.4) we see that sectional curvatures scale at most as α^0 at large α. We point out that, with the progressive schedule (3.3.11), the maximal complexity is infinite by construction at fixed n for $\alpha \to \infty$, since one-qubit operators are not enough to produce the most general operator in the unitary space (for instance, they cannot produce operators which entangle two previously unentangled qubits). Physically, we are thus interested in the limit of large but finite α.

[8] A typical section is defined as a two-dimensional surface on the unitary manifold whose tangent plane is spanned by linear combinations of two Hamiltonians containing only generators of weight $w = 2$.

In principle, the progressive model can be generalized as

$$q_w = \begin{cases} 1 & \text{for } w \leq w_0 \,, \\ \alpha^{w-w_0} & \text{for } w > w_0 \,, \end{cases} \tag{3.3.12}$$

with $w_0 \geq 2$. With this choice of penalties, we expect that the maximal complexity at fixed n does not diverge for $\alpha \to \infty$, because the combination of one-qubit and two-qubits operators allows us to build an arbitrary operator in the unitary space. From eq. (3.3.4), we see that at large α sectional curvatures scale at most as α^{w_0-1}. As the curvature diverges, the large α limit of (3.3.12) provides a singular geometry.

3.3.4 Progressive penalties

In this subsection, we consider the basic progressive model (3.3.11) and explore the geometry of the resulting unitary manifold, deferring the cumbersome calculations to Appendix A.2.
At the leading order in α, the only non-vanishing sectional curvatures take the values $K = 1$ and $K = -3$ with multiplicities

$$\mathcal{N}_+ = 6n\left(2 \times 7^{n-1} - 4^n + 3\right) \,, \qquad \mathcal{N}_- = \frac{\mathcal{N}_+}{2} - 3n \,, \tag{3.3.13}$$

respectively. The scalar curvature is thus

$$R = -\frac{\mathcal{N}_+}{2} + 9n = 3n\left(4^n - 2 \times 7^{n-1}\right) \,, \tag{3.3.14}$$

which is negative for $n \geq 3$. The correction of the curvature at the next-to-leading order is

$$\delta R^{(1)} = \frac{9}{2} n(n-1) \frac{4^n}{\alpha} \,. \tag{3.3.15}$$

In order to get a feeling on the average sectional curvature, we divide R by the total number of sectional curvatures between couples of elements in the basis, which we denote by

$$\eta = (4^n - 1)^2 - (4^n - 1) \,. \tag{3.3.16}$$

The average sectional curvature becomes tiny at large n and α, i.e.

$$\bar{K} = \frac{R}{\eta} \approx -\frac{6}{7} n \left(\frac{7}{16}\right)^n + \frac{9}{4^n} \frac{n(n-1)}{2} \frac{1}{\alpha} \,. \tag{3.3.17}$$

At higher order in α, we do not have an analytic expression for the generic n qubits case. However, if n is fixed to be some not too large value, we can explicitly compute the exact $\bar{K}$ at all orders, since the computation involves

sums containing a finite number of terms. The exact average sectional curvature is plotted in Fig. 3.2 as a function of α for a few values of n. Note that nothing special happens for the value $\alpha = 4$, which instead plays an important role in the draconian model. Interestingly, there is a minimum at finite α. An explicit analysis reveals that the series for $\bar{K}$ in the expansion parameter α^{-1} is, at large n, an alternate sign series with slow rate of convergence. For example, in order to get the $\bar{K}$ minimum in the plot for $n = 10$, we have to expand up to the order α^{-5}.

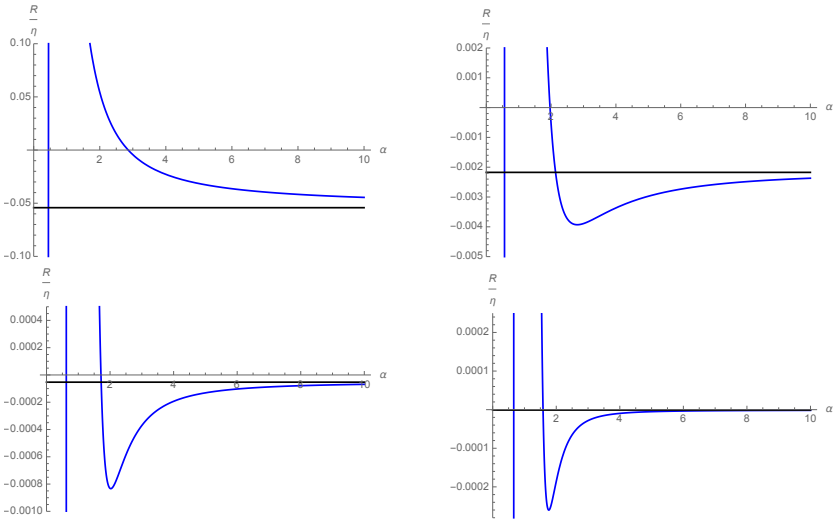

Figure 3.2: Exact value of R/η (blue curve) plotted as a function of α in the case of progressive penalties, for $n = 5, 10, 15, 20$. The asymptotic value at $\alpha \to \infty$ of eq. (3.3.17) is shown in black. The minimum in the picture appears for $n \geq 8$. Increasing n, the minimum moves at a lower value of α and its shape tends to become more and more steep. Note that when $n = 20$, for $\alpha \sim 4$ the $\mathcal{O}(\alpha^0)$ average sectional curvature is already very close to the exact result.

In conclusion to this investigation, we remark that the progressive penalization scheme for $\alpha \to \infty$ has many similarities with the one-qubit case for $P = \beta Q \to \infty$ and $\beta \neq 1$, see eq. (3.2.7). In both models we expect maximal complexity to diverge, while sectional curvatures remain finite, so that R approaches a negative finite value.

3.4 State complexity

Up to now, we have specialized to the complexity of *unitaries*. In this section, we shift the focus on the geometry of the space of *states*. Geometrically, this space is obtained as a quotient of the space of unitary operators, where all the transformations that build the same state (up to a phase) starting from a reference one are identified. Complexity of the target state is then defined as the minimum complexity of all the identified unitaries. Interpreting the state complexity as the length of minimal curves on the space of states defines a map between two Riemannian manifolds, which turns out to be a *Riemannian submersion*. After recalling its general definition in Subsec. 3.4.1, in Subsec. 3.4.2 we apply the formalism of Riemannian submersions to complexity geometry for a system of n qubits, obtaining an expression for the metric on the space of states with arbitrary penalty factors. Besides this achievement, in Subsec. 3.4.3 we introduce the O'Neill's formula, which provides a lower bound on the curvature of the space of states. As explicit applications of the collected results, in Subsecs. 3.4.4 and 3.4.5 we consider the simple but instructive cases of one-qubit and one-qutrit systems, respectively. Finally, in Subsec. 3.4.6 we explore the underlying relation between geodesics on the unitary and state manifolds.

3.4.1 Submersions

In this subsection, we briefly review the concept of Riemannian sumbersion, referring to the textbooks [127, 133] for more details. Let us consider two Riemannian manifolds $(M, g_{\alpha\beta})$ with dimension m and $(B, h_{\alpha\beta})$ with dimension $b < m$, and a smooth map $\pi : M \to B$ with surjective differential $d\pi$. For any $y \in M$, the differential $d\pi : TM \to TB$ induces a linear map between the vector spaces T_yM and T_xB, where $x = \pi(y)$. Since $d\pi$ is surjective, it has maximal rank, and thus a kernel of dimension $f = m - b$. We call $\mathcal{V}_y = \ker(d\pi_y)$ the *vertical space* at y. Its orthogonal complement in T_yM, induced by the metric g, is called the *horizontal space* at y and denoted by $\mathcal{H}_y$. For the submersion to be Riemannian, $\mathcal{H}_y$ has to be identified with T_xB in an isometric way. In other words

$$g(X, Y) = h(d\pi(X), d\pi(Y)), \qquad \forall\, X, Y \in \mathcal{H}_y\ . \tag{3.4.1}$$

For the sake of clarity, a pictorial depiction is shown in Fig. 3.3.

Among the known examples of Riemannian submersions, we are here interested in quotients of Riemannian manifolds by an isometric group action (see for example the textbooks [127, 133]). In particular, let G be a closed subgroup of the isometry group of $(M, g_{\alpha\beta})$, and take $B = M/G$. Then, a metric on B

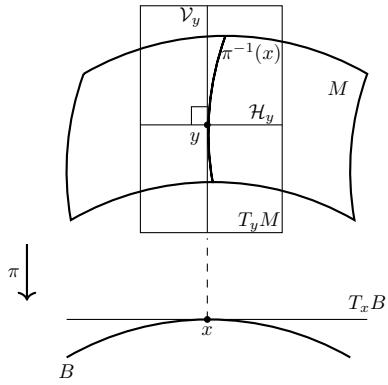

Figure 3.3: Schematic representation of a submersion, based on [133].

exists such that the projection $\pi : M \to B = M/G$ is a Riemannian submersion [127, 133]. As we will see in the following sections, this construction helps us in understanding properties of the space of states starting from the space of unitaries.

3.4.2 Submersions and complexity geometry

We now apply the notion of Riemannian submersion to complexity geometry. To this purpose, we take $M = \mathrm{SU}(2^n)$ provided with a right-invariant metric (the unitary space), and G as the subgroup of the isometries of M which leaves the reference state invariant up to a phase, namely $G = \mathrm{SU}(2^n - 1) \times \mathrm{U}(1)$. Explicitly, an element V of G, which we refer to as *unbroken* subgroup, acts on the reference state $|\psi_0\rangle$ as

$$V\,|\psi_0\rangle = e^{i\phi}\,|\psi_0\rangle\ . \tag{3.4.2}$$

Consequently, a unitary U which prepares the state $|\psi\rangle$ starting from the reference one

$$U|\psi_0\rangle = |\psi\rangle \tag{3.4.3}$$

is physically equivalent to an operator of the form $U' = UV$, which build the same state up to a phase:

$$U'|\psi_0\rangle = e^{i\phi}|\psi\rangle\,, \qquad \Longrightarrow \qquad U' \sim U\,. \tag{3.4.4}$$

The group B of such equivalence classes represents the space of states. So, as we have previously commented, the projection π from the unitary space to the

space of states

$$\pi : \mathrm{SU}(2^n) \to B = \frac{\mathrm{SU}(2^n)}{\mathrm{SU}(2^n-1)\times \mathrm{U}(1)} = \mathbb{CP}^{2^n-1} \tag{3.4.5}$$

is an isometric submersion. We are now going to prove this remarkable result by fixing a specific coordinate system.
To make contact with Sec. 3.1, we consider a diagonal penalty matrix in the basis of the generalized Pauli matrices, with the property (see eq. (3.1.16))

$$\langle \rho, \sigma \rangle = q_\sigma \, \delta_{\rho\sigma} = \frac{q_\sigma}{2^n} \mathrm{Tr}(\rho\, \sigma) \, . \tag{3.4.6}$$

In order to determine the metric on the space of states it is convenient to perform a change of basis. In particular, we pick up a basis that distinguishes between broken generators ρ_j and unbroken ones τ_a:

$$\omega_l = (\rho_j, \tau_a) \, , \qquad 1 \le j \le 2(2^n-1) \, , \qquad 1 \le a \le (2^n-1)^2 \, , \tag{3.4.7}$$

with normalization

$$\mathrm{Tr}\,(\omega_l\, \omega_m) = \delta_{lm} \, . \tag{3.4.8}$$

The generators of the two bases are related by

$$\sigma = \sum_l \omega_l \, \mathrm{Tr}\,(\omega_l\, \sigma) \, , \qquad \omega_l = \frac{1}{2^n} \sum_\sigma \sigma \, \mathrm{Tr}\,(\omega_l\, \sigma) \, . \tag{3.4.9}$$

We can thus express the penalty scalar product in the basis ω_l as

$$M_{lm} = \langle \omega_l, \omega_m \rangle = \frac{1}{2^{2n}} \sum_\sigma q_\sigma \, \mathrm{Tr}\,(\omega_l\, \sigma)\, \mathrm{Tr}\,(\omega_m\, \sigma) \, . \tag{3.4.10}$$

Introducing the following notation for the exponential of broken and unbroken generators

$$U_\Theta = e^{i\theta_j \rho_j} \, , \qquad V_\Lambda = e^{i\lambda_a \tau_a} \, , \tag{3.4.11}$$

where θ_j denote the coordinates in the space of states and λ_a the additional coordinates in the unitary space, a generic element of $\mathrm{SU}(2^n)$ can be written as $U = U_\Theta V_\Lambda$. We can then compute

$$dU U^\dagger = (dU_\Theta V_\Lambda + U_\Theta dV_\Lambda) V_\Lambda^\dagger U_\Theta^\dagger = dU_\Theta U_\Theta^\dagger + U_\Theta dV_\Lambda V_\Lambda^\dagger U_\Theta^\dagger \, , \tag{3.4.12}$$

with

$$dU_\Theta = \frac{\partial U_\Theta}{\partial \theta_j} \, d\theta_j \, , \qquad dV_\Lambda = \frac{\partial V_\Lambda}{\partial \lambda_a} \, d\lambda_a \, . \tag{3.4.13}$$

In this way, the right-invariant forms defined on $\mathrm{SU}(2^n)$ are given by

$$X_r = -i \, \mathrm{Tr}(dU U^\dagger \omega_r) = -i (\mathrm{Ad}_{U_\Theta^\dagger})_{rs} \, \mathrm{Tr}\left[\left(U_\Theta^\dagger dU_\Theta + dV_\Lambda V_\Lambda^\dagger \right) \omega_s \right] \, , \tag{3.4.14}$$

in which we have used the adjoint action

$$U_\Theta^\dagger \, \omega_r \, U_\Theta = (\mathrm{Ad}_{U_\Theta^\dagger})_{rs} \omega_s \, . \tag{3.4.15}$$

We can now write the metric in the unitary space as

$$ds^2 = M_{rs} X_r X_s = \tilde{M}_{lm} (u_l + v_l)(u_m + v_m) \, , \tag{3.4.16}$$

where

$$\begin{aligned} &\tilde{M}_{lm} = M_{rs} (\mathrm{Ad}_{U_\Theta^\dagger})_{rl} (\mathrm{Ad}_{U_\Theta^\dagger})_{sm} \, , \\ &u_l = -i \, \mathrm{Tr} \left(U_\Theta^\dagger dU_\Theta \, \omega_l \right) \, , \qquad v_l = -i \, \mathrm{Tr} \left(dV_\Lambda V_\Lambda^\dagger \, \omega_l \right) \, , \end{aligned} \tag{3.4.17}$$

in such a way that $\tilde{M}_{lm}$ depends just on θ_j, u_l contains just $(\theta_j, d\theta_j)$, and v_l includes just $(\lambda_a, d\lambda_a)$. Note that this decomposition also holds if M_{lm} is a generic symmetric matrix. By distinguishing between broken and unbroken generators $\omega_l = (\rho_j, \tau_a)$ as in eq. (3.4.7), we trivially have that $v_j = 0$. Then, the unitary metric (3.4.16) reads

$$\begin{aligned} ds^2 &= \begin{pmatrix} u_i & u_a + v_a \end{pmatrix} \begin{pmatrix} \tilde{M}_{ij} & \tilde{M}_{ib} \\ \tilde{M}_{aj} & \tilde{M}_{ab} \end{pmatrix} \begin{pmatrix} u_j \\ u_b + v_b \end{pmatrix} \\ &= (\tilde{M}_{ij} - \tilde{M}_{ic} \tilde{M}_{ca}^{-1} \tilde{M}_{aj}) u_i u_j + \tilde{M}_{ab} f_a f_b \, , \end{aligned} \tag{3.4.18}$$

where we have defined

$$f_a = v_a + u_a + \tilde{M}_{ad}^{-1} \tilde{M}_{dj} u_j \, . \tag{3.4.19}$$

Since the term $\tilde{M}_{ab} f_a f_b$ in eq. (3.4.18) is positive-definite, the problem of finding the minimal infinitesimal operator which synthesizes the state with coordinates $\theta_j + d\theta_j$ from the state with coordinates θ_j is solved by the equation $f_a = 0$. Consequently, the metric on the space of states $\mathbb{CP}^{2^n - 1}$ can be identified as

$$ds_S^2 = (\tilde{M}_{ij} - \tilde{M}_{ic} \tilde{M}_{ca}^{-1} \tilde{M}_{aj}) u_i u_j \, . \tag{3.4.20}$$

This construction generalizes the result in [20] to an arbitrary number of qubits. We explicitly checked that the metric on $\mathbb{CP}^1$ (single qubit case) coincides with the result found in [20]. In Subsec. 3.4.5 we will apply our result to qutrits. From eq. (3.4.18), it follows that the projection map

$$\pi : (\theta_j, \lambda_a) \mapsto (\theta_j) \tag{3.4.21}$$

is a Riemannian submersion, where $\pi^{-1}(\theta_j)$, for fixed θ_j, is parametrized by λ_a. The explicit expression for the horizontal space at arbitrary θ_j is given by $f_a(X) = 0$ for any generic vector X in the tangent space.

3.4.3 Submersions and curvature

As we have previously discussed, sectional curvatures play a central role in determining the properties of complexity geometry. Contrary to the space of unitaries, non-homogeneity of the space of states makes the computation of the corresponding sectional curvatures K_S more challenging. The close connection between the unitary and state manifolds, expressed in the language of Riemannian submersions, helps us in circumventing this obstacle. Namely, *O'Neill's formula* [25] relates the sectional curvatures K_S on the state manifold to the sectional curvatures K on the unitary manifold, which are much easier to deal with. In details, O'Neill's formula reads

$$K_S(\tilde{h}_1, \tilde{h}_2) = K(h_1, h_2) + \frac{3}{4} \frac{|\mathcal{V}([h_1, h_2])|^2}{|h_1|^2 |h_2|^2 - \langle h_1, h_2 \rangle^2} , \tag{3.4.22}$$

where h_k are horizontal fields in the unitary space, $[h_1, h_2]$ is their commutator, $\tilde{h}_k = d\pi(h_k)$ are vector fields in the state space, $\langle \dots \rangle$ is the scalar product from the metric on the unitary manifold, $| \dots |$ is the norm induced by such a scalar product, and $\mathcal{V}$ is the projector on the vertical space.

O'Neill's formula shows that the sectional curvature of a plane tangent to the space of states can always be expressed as the sectional curvature of an appropriate plane tangent to the unitary space plus a positive-definite contribution coming from the commutator of horizontal vectors. Therefore, this expression can be used to compute the curvatures on the state manifold without even knowing its metric.

For illustrative purposes, in the next sections we explicitly apply the toolkit of Riemannian submersions to the simplest cases of one-qubit and one-qutrit systems.

3.4.4 Submersion for one qubit

The geometry of a one-qubit system has been extensively studied in [20]. In this section we review such an analysis in the light of the results of Riemannian submersions.

The space of states $\mathbb{CP}^1$ has the topology of a sphere, named *Bloch sphere*. Starting from the reference state $|\psi_0\rangle$, corresponding to the north pole, we can build the state $|\psi\rangle$ specified by the (θ, ϕ) angles by implementing the following unitary

$$U_\Theta = \exp\left[\frac{i\,\theta}{2} \left(\sigma_x \cos\phi + \sigma_y \sin\phi\right)\right] , \tag{3.4.23}$$

with $0 \leq \theta \leq \pi$ and $0 \leq \phi < 2\pi$. On the other hand, the reference state is left invariant up to a phase by the action of the transformation

$$V_\Lambda = \exp\left(i \frac{\sigma_z}{2} \lambda \right) . \tag{3.4.24}$$

Consequently, the SU(2) transformation preparing the generic state $|\psi\rangle$ is

$$U = U_\Theta V_\Lambda = \begin{pmatrix} e^{\frac{i\lambda}{2}} \cos\left(\frac{\theta}{2}\right) & i \sin\left(\frac{\theta}{2}\right) e^{-\frac{1}{2} i(\lambda+2\phi)} \\ i \sin\left(\frac{\theta}{2}\right) e^{\frac{1}{2} i(\lambda+2\phi)} & e^{-\frac{i\lambda}{2}} \cos\left(\frac{\theta}{2}\right) \end{pmatrix} . \tag{3.4.25}$$

The submersion from the unitary to the state manifold is realized by the projection

$$\pi : (\lambda, \theta, \phi) \mapsto (\theta, \phi) , \tag{3.4.26}$$

and the vertical space is spanned by ∂_λ.

The metric on the unitary space with penalties $q_{\sigma_x} = 1$, $q_{\sigma_y} = Q$, and $q_{\sigma_z} = P$ is

$$ds^2 = \frac{1}{4} \left\{ (\mathrm{Tr}[i dU U^\dagger \sigma_x])^2 + Q \, (\mathrm{Tr}[i dU U^\dagger \sigma_y])^2 + P \, (\mathrm{Tr}[i dU U^\dagger \sigma_z])^2 \right\} , \tag{3.4.27}$$

where

$$dU = \frac{\partial U}{\partial \theta} d\theta + \frac{\partial U}{\partial \phi} d\phi + \frac{\partial U}{\partial \lambda} d\lambda . \tag{3.4.28}$$

Using the unitary metric, we can find the horizontal vector fields, which are defined to be orthogonal to the vertical direction ∂_λ:

$$\begin{aligned} h_1 &= \partial_\theta - \frac{(Q-1)\sin(\theta)\sin(2\phi)}{2\left(P\cos^2(\theta) + \sin^2(\theta)\left(Q\cos^2(\phi) + \sin^2(\phi)\right)\right)} \partial_\lambda , \\ h_2 &= \partial_\phi + \frac{-2P\cos^2(\theta) + 2P\cos(\theta) - \sin^2(\theta)((Q-1)\cos(2\phi) + Q + 1)}{2\left(P\cos^2(\theta) + \sin^2(\theta)\left(Q\cos^2(\phi) + \sin^2(\phi)\right)\right)} \partial_\lambda . \end{aligned} \tag{3.4.29}$$

Note that $d\pi(h_1) = \partial_\theta$, $d\pi(h_2) = \partial_\phi$.
We can now use eq. (3.4.22) to find the curvature of the state manifold:

$$R = 2K_S(\tilde{h}_1, \tilde{h}_2) = 2K(h_1, h_2) + \frac{3}{2} \frac{|\mathcal{V}([h_1, h_2])|^2}{|h_1|^2 |h_2|^2 - \langle h_1, h_2 \rangle^2} . \tag{3.4.30}$$

An explicit calculation gives

$$R = \frac{\alpha}{\beta} , \tag{3.4.31}$$

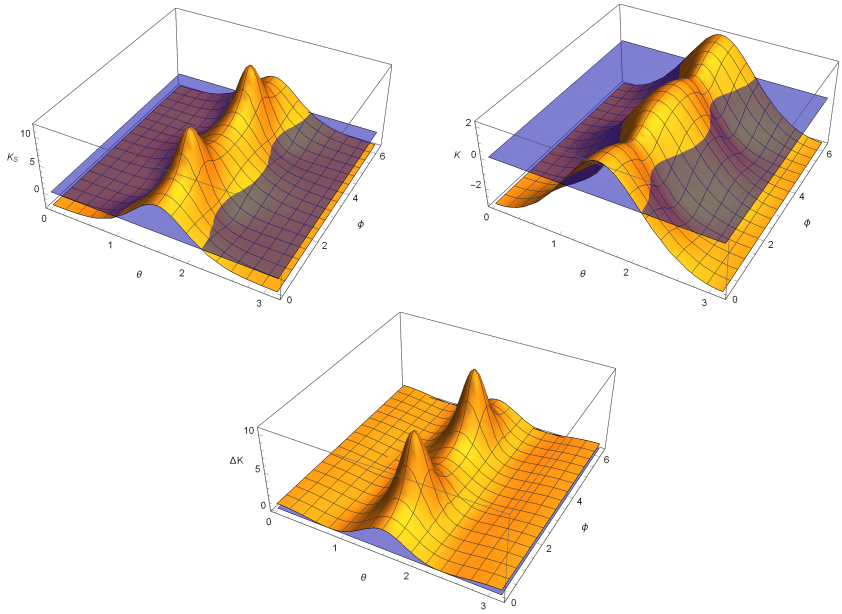

Figure 3.4: Comparison of $K_S(\tilde{h}_1, \tilde{h}_2)$, $K(h_1, h_2)$, and ΔK as functions of (θ, ϕ) for the numerical values $P = 6$, $Q = 3$.

where

$$\alpha = 8\left\{-2(Q-1)\left[Q^2 - P^2 + P + (P-1)(P-Q)^2\cos^2\theta\right]\sin^2\theta\cos^2\phi\right.$$
$$+(P-1)\left[-2\left(P^2 - Q^2 + Q\right) - (P-1)(Q-1)(P-Q)\cos^2\theta\right]\cos^2\theta + P^2$$
$$\left.+(P-1)(P-Q)(Q-1)^2\sin^4\theta\cos^4\phi + (P+Q)(Q-1)\right\} ,$$

$$\beta = PQ\left[(P-1)\cos^2\theta + (Q-1)\sin^2\theta\cos^2\phi + 1\right]^2 ,$$

which matches the expression directly obtained from the states metric in [20]. A plot of $K_S(\tilde{h}_1, \tilde{h}_2)$, $K(h_1, h_2)$, and their difference ΔK is shown in Fig. 3.4 for particular values of the penalties.

3.4.5 Submersion for one qutrit

Up to now we have specialized our discussion to systems of qubits, which are the most relevant in the quantum information context. In general, one may be

interested in *qudits*, representing m-level systems. In this section we consider the simplest generalization, namely the system of one qutrit ($m = 3$), and we show how the formalism of Riemannian submersions can be readily applied.
In the case at hand, the unitary manifold is $M = \mathrm{SU}(3)$, containing as a maximal subgroup $G = \mathrm{SU}(2) \times \mathrm{U}(1)$. The corresponding state manifold is $M/G = \mathbb{CP}^2$, which is parametrized by four real coordinates (θ_i, ϕ_i) with $0 \leq \theta_i \leq \pi$, $0 \leq \phi_i \leq 2\pi$ and $i = 1, 2$. Conventionally, in the one-qutrit basis $\{|0\rangle, |1\rangle, |2\rangle\}$, we take as a reference and target states

$$|\psi_0\rangle = \begin{pmatrix} 1 \\ 0 \\ 0 \end{pmatrix}, \qquad |\psi\rangle = \begin{pmatrix} \cos\theta_1 \\ e^{i\phi_1} \sin\theta_1 \cos\theta_2 \\ e^{i\phi_2} \sin\theta_1 \sin\theta_2 \end{pmatrix}. \tag{3.4.32}$$

The unitary transformation preparing $|\psi\rangle$ from the reference state is[9]

$$\begin{aligned} U_\Theta^{(3)} &= \frac{1}{\sqrt{1 + z_i \overline{z}^i}} \begin{pmatrix} 1 & -\overline{z}_j \\ z_i & \sqrt{1 + z_i \overline{z}^i}\,\delta_{ij} - \frac{z_i \overline{z}_j}{1 + \sqrt{1 + z_i \overline{z}^i}} \end{pmatrix}, \\ z_1 &= \frac{e^{i\phi_1} \sin\theta_1 \cos\theta_2}{\cos\theta_1}, \qquad z_2 = \frac{e^{i\phi_2} \sin\theta_1 \sin\theta_2}{\cos\theta_1}. \end{aligned} \tag{3.4.33}$$

The group of transformations leaving the reference state invariant up to a phase is $G = \mathrm{SU}(2) \times \mathrm{U}(1)$. In order to construct the proper element of such a group we follow an iterative procedure. First, the SU(2) factor can be inherited from the single qubit result of eq. (3.4.25)

$$U^{(2)} = \begin{pmatrix} e^{i\lambda_2} \cos\lambda_1 & -e^{-i(\lambda_2+\lambda_3)} \sin\lambda_1 \\ e^{i(\lambda_2+\lambda_3)} \sin\lambda_1 & e^{-i\lambda_2} \cos\lambda_1 \end{pmatrix}. \tag{3.4.34}$$

Then, embedding the matrix in SU(3) and adding an overall global phase

$$p = \begin{pmatrix} e^{i2\lambda_4} & 0 & 0 \\ 0 & e^{-i\lambda_4} & 0 \\ 0 & 0 & e^{-i\lambda_4} \end{pmatrix}, \tag{3.4.35}$$

corresponding to the U(1) factor, we get

$$V_\Lambda^{(3)} = \begin{pmatrix} e^{2i\lambda_4} & 0 & 0 \\ 0 & e^{i(\lambda_2-\lambda_4)} \cos\lambda_1 & -e^{-i(\lambda_2+\lambda_3+\lambda_4)} \sin\lambda_1 \\ 0 & e^{i(\lambda_2+\lambda_3-\lambda_4)} \sin\lambda_1 & e^{-i(\lambda_2+\lambda_4)} \cos\lambda_1 \end{pmatrix}, \tag{3.4.36}$$

which depends on four real coordinates λ_i.

[9] In this section, the superscript (K) refers to the group $\mathrm{SU}(K)$ to which the element belongs.

Prior to determining the metric on the space of states from eq. (3.4.20), we need to specify the penalty matrix M_{rs}. As we have pointed out at the end of Subsec. 3.2.2, commutators of the form $[\mathrm{e}\,,\mathrm{e}] = \mathrm{h}$, which are expected to give rise to negative curvature, always occur when we penalize the generators of a maximal subalgebra. This corresponds to choose as a penalty matrix

$$M_{rs} = \mathrm{diag}(P, P, P, P, 1, 1, 1, 1) \tag{3.4.37}$$

with $P > 1$, where the first four components refer to the generators τ_a of $\mathrm{SU}(2) \times \mathrm{U}(1)$, and the last four components to the broken generators ρ_i. Note that by taking $0 < P < 1$ we instead penalize the broken generators ρ_i, and an algebra of the form $[\mathrm{e}\,,\mathrm{e}] = \mathrm{e}$ is realized. In this case we expect the space manifold to not manifest regions with a negative scalar curvature.

To check these expectations, we analytically compute the metric on the state manifold given by eq. (3.4.20) starting from the left-invariant form u_i defined in eq. (3.4.17). The result is

$$\begin{aligned} ds_S^2 = {} & d\theta_1^2 + \frac{2P\sin^2\theta_1}{A(\theta_1)} d\theta_2^2 + \frac{2P\sin^2\theta_1\cos^2\theta_2}{A(\theta_1)} d\phi_1^2 + \frac{C(\theta_1,\theta_2)}{A(\theta_1)B(\theta_1)} d\phi_2^2 \\ & + \frac{2P\sin^4\theta_1\cos^2\theta_2}{A(\theta_1)B(\theta_1)} D(\theta_1) \left(\cos^2\theta_2 (d\phi_1 - d\phi_2)^2 + 2 d\phi_1 d\phi_2\right) , \end{aligned} \tag{3.4.38}$$

where

$$\begin{aligned} & A(\theta_1) \equiv (P-1)\cos(2\theta_1) + P + 1\,, \qquad B(\theta_1) \equiv (P-1)\cos(4\theta_1) + P + 1\,, \\ & C(\theta_1,\theta_2) \equiv P\sin^2\theta_1 \left[B(\theta_1) - \cos(2\theta_2)\left(2P\cos(2\theta_1) + (P-1)\sin^2(2\theta_1)\right)\right] , \\ & D(\theta_1) \equiv 3(P-1)\cos(2\theta_1) + P - 3\,. \end{aligned}$$

The resulting scalar curvature is

$$\begin{aligned} R = {} & \frac{15}{2}\left(\frac{1}{P} - 1\right) + \frac{56P}{A^2(\theta_1)} + \frac{96P}{B^2(\theta_1)} + \frac{4 - 4P(3P+14)}{(P+3)\,A(\theta_1)} \\ & + \frac{-8(P-1)(9P+19)\cos^2\theta_1 + 3P(P-18) + 3}{(P+3)\,B(\theta_1)}\,. \end{aligned} \tag{3.4.39}$$

We observe that the metric depends only on the angular coordinates θ_i, while the Ricci scalar just on θ_1. This is due to the amount of symmetries in the penalty matrix of eq. (3.4.37). In the left Fig. 3.5 we plot the Ricci scalar as a function of θ_1 for different values of the penalty P.
As expected, when $0 < P < 1$ the scalar curvature is everywhere positive, and it reaches a constant value $R = 24$ when $P = 1$, corresponding to the

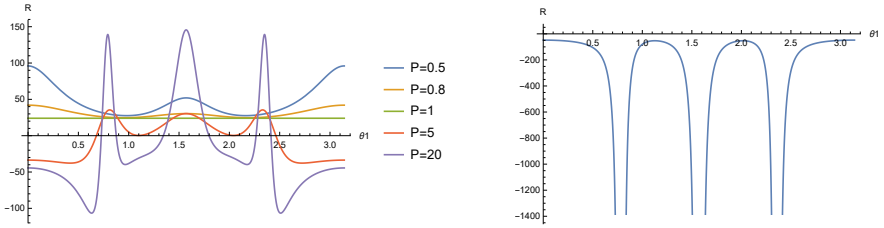

Figure 3.5: On the left: Scalar curvature in eq. (3.4.39) for the state space $\mathbb{CP}^2$ with penalty factors P applied to all the generators of the maximal subgroup. On the right: Scalar curvature for $P \to \infty$ in eq. (3.4.40).

non-penalized choice. On the other hand, when $P > 1$ there is always a region with negative curvature which increases its size accordingly to the increasing of the penalty. In the limiting case $P \to \infty$, meaning that the motion along the maximal subgroup directions is forbidden, the Ricci scalar reads

$$\lim_{P\to\infty} R = -\frac{3}{2}\left\{[11\,\sec(2\theta_1)+12]\sec(2\theta_1)+4\,\sec^2\theta_1+5\right\}\,. \tag{3.4.40}$$

As it can be seen in the right Fig. 3.5, in this case the Ricci scalar is negative and contains singularities. In the opposite limit $P \to 0$, we instead obtain an everywhere positive and divergent Ricci scalar, due to the singular term scaling as P^{-1}. The behavior of the curvature in this limit is similar to the one-qubit case with $Q = 1$ and arbitrary P, which was studied in detail in [20].

3.4.6 Submersions and geodesics

The computation of state complexity can be reformulated as the search of the shortest geodesic connecting a state to the reference one. Riemannian submersions helps us out again, relating geodesics in the state manifold B to geodesics in the unitary manifold M. An important result is that if a geodesic in M is *horizontal*[10] at some point, then it remains horizontal. The projection of a horizontal geodesic in M by the submersion $\pi : M \to B$ is still a geodesic in the space of states B. Moreover, being our unitary space M complete, every geodesic of B can be built as the projection of a horizontal geodesic in M [26]. It is important to stress that the projection of a non-horizontal geodesic in general does not provide a geodesic on B.

According to eq. (3.1.15), a simple class of geodesics on the unitary manifold is given by the exponential of an eigenvector of the penalty operator $\mathcal{G}$. Combining

[10] A geodesic is called horizontal if the vector field on the curve is horizontal.

with the previous result, the exponential of an eigenvector of $\mathcal{G}$ which is also orthogonal to the unbroken subgroup at the origin is projected to a geodesic in the state space B. In the one-qubit case, which we will thoroughly examine in Subsec. 3.5.3, such horizontal eigenvectors are trivially identified with the σ_x and σ_y generators of $\mathfrak{su}(2)$. In the remainder of this section, we discuss how to determine broken generators that are also eigenvectors of $\mathcal{G}$ in the $n > 1$ case, supposing as before that penalties depend just on the weight.

To get a feeling on the problem, we start from a two-qubits system. Taking as reference state $|00\rangle$, the unbroken subgroup is generated by

$$\begin{gathered}
\mathbb{1} \otimes \sigma_z \,, \qquad \sigma_z \otimes \mathbb{1} \,, \qquad \sigma_z \otimes \sigma_z \,, \\
\sigma_x \otimes (\mathbb{1} - \sigma_z) \,, \qquad \sigma_y \otimes (\mathbb{1} - \sigma_z) \,, \qquad (\mathbb{1} - \sigma_z) \otimes \sigma_x \,, \qquad (\mathbb{1} - \sigma_z) \otimes \sigma_y \,, \\
\sigma_x \otimes \sigma_y - \sigma_y \otimes \sigma_x \,, \qquad \sigma_x \otimes \sigma_x + \sigma_y \otimes \sigma_y \,.
\end{gathered} \tag{3.4.41}$$

Namely, the generators in the first line change the phase of the reference state, whereas the remaining generators leave the reference state completely invariant. The orthogonal complement to the unbroken subgroup is generated by

$$\begin{gathered}
\sigma_x \otimes (\mathbb{1} + \alpha\, \sigma_z) \,, \quad \sigma_y \otimes (\mathbb{1} + \alpha\, \sigma_z) \,, \quad (\mathbb{1} + \alpha\, \sigma_z) \otimes \sigma_x \,, \quad (\mathbb{1} + \alpha\, \sigma_z) \otimes \sigma_y \,, \\
S_2^- = \sigma_x \otimes \sigma_y + \sigma_y \otimes \sigma_x \,, \qquad S_2^+ = \sigma_x \otimes \sigma_x - \sigma_y \otimes \sigma_y \,,
\end{gathered} \tag{3.4.42}$$

where the coefficient α, depending on the penalty factors, is chosen to ensure orthogonality with the unbroken generators in eq. (3.4.41). Note that just $S_2^\pm$ in eq. (3.4.42) have a definite weight $w = 2$, so these are the only generators of horizontal exponential geodesics.

We now generalize this argument to the n-qubits case. Taking as a reference state $|00\ldots0\rangle$, an infinitesimal transformation with weight $w = n$ containing just the $\sigma_{x,y}$ SU(2) Pauli matrices acts on it as

$$|00\ldots0\rangle \to |00\ldots0\rangle + \epsilon\, |11\ldots1\rangle \,, \tag{3.4.43}$$

with ϵ an infinitesimal complex number. Since ϵ has two real degrees of freedom, this class of 2^n operators comprises $2^n - 2$ unbroken generators (with $\epsilon = 0$) and 2 broken ones. The latter can be built by introducing

$$A_s^n = \frac{1}{\binom{n}{s}} \sum_{(k_1,\ldots,k_n)} \sigma_{k_1} \otimes \ldots \otimes \sigma_{k_n} \,, \tag{3.4.44}$$

where the sum runs over all the permutations $(k_1, \ldots, k_n)$ which include s generators σ_y and $n-s$ generators σ_x. Then, the two operators

$$S_n^+ = \sum_{0\le k\le n}^{k \text{ even}} i^k A_k^n \,, \qquad S_n^- = \sum_{1\le k\le n}^{k \text{ odd}} i^{k+1} A_k^n \,, \tag{3.4.45}$$

are both broken by the reference state and orthogonal to all the unbroken $w = n$ generators containing just σ_x and σ_y. This construction generalizes the operators in the last line of eq. (3.4.42).

We now look for other generators orthogonal to the vertical space. Inspired by the two-qubits case, we consider the $2n$ operators of the form

$$S_{n-1}^{\pm} \otimes (\mathbb{1} + \alpha_1 \sigma_z) \,, \tag{3.4.46}$$

with the coefficient α_1 chosen to guarantee the orthogonality with the unbroken generators $S_{n-1}^{\pm} \otimes (\mathbb{1} - \sigma_z)$. Note that the operators (3.4.46) are linear combinations of $w = n, n-1$ generators.
Iterating the construction, we take $1 \le s < n$ and we focus on the $2\binom{n}{s}$ operators

$$S_{n-s}^{\pm} \otimes (\mathbb{1} + \alpha_s \sigma_z)^s \,, \tag{3.4.47}$$

with α_s determined by the condition of orthogonality to the unbroken operators $S_{n-s}^{\pm} \otimes (\mathbb{1} - \sigma_z) \bigotimes_{i=1}^{b} \mathbb{1} \bigotimes_{j=1}^{c} \sigma_z$, where b, c are some integer numbers. For each integer s, the operators in eq. (3.4.47) are linear combinations of generators with weight

$$n - s \le w \le n \,. \tag{3.4.48}$$

This procedure leads to all the $2(2^n - 1)$ horizontal vectors in the unitary space, which project to the $\mathbb{CP}^{2^n-1}$ directions in the state space. From eq. (3.4.48), we argue that in case penalties q_w depend on the weight w of generators, as in the progressive model, the $s = 0$ broken unitaries $S_n^{\pm}$ are the only horizontal eigenvectors of $\mathcal{G}$. Consequently, the only horizontal exponential geodesics are generated by linear combinations of S_n^+ and S_n^-.
If instead some penalties for different weights are degenerate, we can find more eigenvectors of $\mathcal{G}$ which are orthogonal to the unbroken subgroup. For instance, in the draconian model all the generators with weight $3 \le w \le n$ are equally penalized, implying that all the broken unitaries with $0 \le s \le n-3$ generate horizontal exponential geodesics. In Subsecs. 3.5.4 and 3.5.5, we will exploit these outcomes to gain information on state complexity for the draconian and progressive model, respectively.

3.5 Towards an exponential complexity

The definitions of unitary and state complexity require to determine the shortest path connecting the identity to a given unitary transformation, or the reference state to the target state, respectively. As we have previously seen, an important result concerning Riemannian submersions is that geodesics in the space of states can be obtained as projections of horizontal geodesics in the unitary space. A convenient way to address the problem of finding globally minimizing geodesics is thus to start from the unitary manifold. The naive answer would be to move along a single geodesic flowing from the identity to the operator of interest. Even though at short distances this is the right solution, it eventually breaks down. Indeed, for a given geodesic there exists a point, named *cut point*, after which the geodesic ceases to globally minimize the distance from its starting point [134]. The set of all the cut points of geodesics starting from U_0 is called *cut locus* of U_0, and it encodes useful information on the manifold topology.
Due to the homogeneity of the unitary manifold, it would be enough to study the cut locus of the identity. However, this is not an easy task (see [20, 134] for results in the context of a one-qubit system). We will instead tackle the problem of finding minimal paths by looking at *conjugate points*, which are defined as pairs of points on a manifold that can be joined by a continuous one-parameter family of geodesics. From a general result, a given geodesic starting from U_0 fails to be globally minimizing after its first conjugate point. Contrary to cut points, the converse is not true: there could be a globally shorter path *well before* a conjugate point is reached. This obstruction can be circumvented in case the position of the conjugate point, according to the bi-invariant non-penalized metric on the unitary manifold, is near to the identity. When this happens, the cut point is unlikely to appear before the conjugate point.

In this section, we exploit the techniques developed in the previous discussion to find explicit classes of geodesics and their conjugate points, which play an important role in the determination of the optimal path. Our main purpose is to probe how different choices of penalty factors influence an important order-zero property that complexity must satisfy in order to fit the expectations in [103]: in the limit of large number of qubits n, the maximal complexity should scale exponentially with n.

3.5.1 Conjugate points and Raychaudhuri's equation

A useful tool to investigate conjugate points is the *Raychaudhuri's equation*, that we briefly recall (see e.g. [135] for a comprehensive review). Let us consider a

congruence of geodesics[11] orthogonal to a family of hypersurfaces in an arbitrary Riemannian manifold. We denote by u^α the tangent vector field to the geodesics, satisfying $u^\alpha u_\alpha = 1$. Supposing the geodesics to be in affine parametrization, we have $u^\beta \nabla_\beta u^\alpha = 0$, where ∇_β is the covariant derivative. In order to examine the evolution of geodesics, we introduce *deviation vectors* ξ^α between neighboring geodesics, such that $\xi^\alpha u_\alpha = 0$. All information on how geodesics fail to remain parallel is contained in the tensor

$$B_{\alpha\beta} = \nabla_\beta u_\alpha \,, \tag{3.5.1}$$

which dictates the behavior of the deviation vectors through $u^\beta \nabla_\beta \xi^\alpha = B^\alpha_\beta \xi^\beta$. In case the congruence of geodesics is orthogonal to a family of hypersurfaces, $B_{\alpha\beta}$ can be shown to be symmetric. Moreover, defining the transverse part of the manifold metric $g_{\alpha\beta}$ as

$$h_{\alpha\beta} = g_{\alpha\beta} - u_\alpha u_\beta \,, \tag{3.5.2}$$

$B_{\alpha\beta}$ can be decomposed into a trace and traceless part

$$B_{\alpha\beta} = \frac{1}{d-1} \Theta \, h_{\alpha\beta} + \sigma_{\alpha\beta} \,, \tag{3.5.3}$$

where d is the manifold dimension, $\Theta = B^\alpha_\alpha$ is the *expansion scalar* and $\sigma_{\alpha\beta}$ the (traceless and symmetric) *shear tensor*. The expansion scalar Θ measures the rate of change of an infinitesimal volume ΔV transverse to the congruence, i.e.

$$\Theta = \frac{1}{\Delta V} \frac{d\,\Delta V}{d\lambda} \,, \tag{3.5.4}$$

where λ is the affine parameter running along a reference geodesic of the family. If the scalar Θ approaches $-\infty$ at some point λ_0 along a geodesic, it detects the presence of a conjugate point for the geodesics congruence. In other words, the geodesic we are moving on ceases to be globally minimizing for points with $\lambda > \lambda_0$. The evolution of Θ along the geodesic flow is governed by the Raychaudhuri's equation [136]

$$\frac{d\Theta}{d\lambda} = -\frac{1}{d-1}\Theta^2 - \sigma^{\alpha\beta}\sigma_{\alpha\beta} - R_{\alpha\beta}u^\alpha u^\beta \,, \tag{3.5.5}$$

where $R_{\alpha\beta}$ is the Ricci tensor. In the next subsection, we will find explicit solutions $\Theta(\lambda)$ to the Raychaudhuri's equation (3.5.5) for a special class of geodesics.

[11] A congruence of geodesics in a region $\mathcal{R}$ is a family of non-intersecting curves such that each point of $\mathcal{R}$ belongs to one and only one curve.

3.5.2 An application to a simple class of geodesics

As we have seen in Subsec. 3.1.1, the geodesic equation on the unitary manifold admits a class of solutions given by the exponential of an eigenvector of the penalty operator $\mathcal{G}$. For such exponential geodesics, the tangent vector u^α is an element of an orthonormal basis in the algebra, such that $g_{\alpha\beta}u^\alpha(\sigma)u^\beta(\sigma) = 1$. Considering the metric in eq. (3.1.16), the contracted Ricci tensor

$$R_\sigma = R_{\alpha\beta}u^\alpha(\sigma)u^\beta(\sigma) = \frac{R_{\sigma\sigma}}{q_\sigma} \tag{3.5.6}$$

is constant along such curves, making the Raychaudhuri's equation more manageable. Analytic solutions to eq. (3.5.5) can be found in case the shear tensor $\sigma_{\alpha\beta}$ vanishes along the geodesics congruence.
Let us suppose this condition to hold, and let us consider a family of geodesics starting at the same point, implying $\Theta \to \infty$. In this case, we can neglect the term $R_{\alpha\beta}u^\alpha u^\beta$ in eq. (3.5.5), corresponding to taking the flat space limit. This approximation leads to

$$\frac{d\Theta}{d\lambda} + \frac{1}{d-1}\,\Theta^2 = 0 \qquad \Rightarrow \qquad \Theta = \frac{d-1}{\lambda - k}\,, \tag{3.5.7}$$

with k an integration constant. For the family of geodesics to start at the same point $\lambda = 0$, we set $k = 0$. Let us now look at

$$\frac{d\Theta}{d\lambda} + \frac{1}{d-1}\,\Theta^2 + R_\sigma = 0\,. \tag{3.5.8}$$

Requiring that at small λ the solution reproduces the flat space one, we find

$$\Theta = \sqrt{(d-1)R_\sigma}\,\cot\left(\sqrt{\frac{R_\sigma}{d-1}}\,\lambda\right)\,. \tag{3.5.9}$$

The conjugate point shows up only for $R_\sigma > 0$, namely at

$$\lambda_0 = \frac{\pi\sqrt{d-1}}{\sqrt{R_\sigma}}\,. \tag{3.5.10}$$

However, the shear tensor is in general non-vanishing. So the value λ_0, obtained by neglecting the positive-definite term $\sigma^{\alpha\beta}\sigma_{\alpha\beta}$ in eq. (3.5.5), gives us an upper bound to the position λ_c of the conjugate point along the geodesic:

$$\lambda_c \leq \lambda_0 = \frac{\pi\sqrt{d-1}}{\sqrt{R_\sigma}}\,. \tag{3.5.11}$$

Note that, keeping the Ricci curvature fixed, λ_0 scales exponentially with the number of qubits due to the factor $\sqrt{d-1} \approx 2^n$. This is a first evidence of the exponential nature of the maximal complexity.

We remark that particular situations exist in which $\sigma_{\alpha\beta} = 0$ and the bound (3.5.11) is saturated. To explore when this condition is verified, we consider the equation for the evolution of $\sigma_{\alpha\beta}$ [137], which in Euclidean signature reads[12]

$$\begin{aligned}\frac{D\sigma_{\alpha\beta}}{d\lambda} = &-\frac{2\,\Theta}{d-1}\sigma_{\alpha\beta} - \sigma^{\gamma}_{\alpha}\sigma_{\beta\gamma} + \frac{1}{d-1}h_{\alpha\beta}\sigma^{\gamma\delta}\sigma_{\gamma\delta} \\ &- C_{\alpha\gamma\beta\delta}\,u^{\gamma}u^{\delta} - \frac{1}{d-2}\bar{R}_{\alpha\beta}\,.\end{aligned} \tag{3.5.12}$$

In the above equation,

$$\bar{R}_{\alpha\beta} = h^{\gamma}_{\alpha}h^{\delta}_{\beta}R_{\gamma\delta} - \frac{1}{d-1}R_{\gamma\delta}h^{\gamma\delta}h_{\alpha\beta} \tag{3.5.13}$$

is the projected trace-free part of $R_{\alpha\beta}$ and

$$\begin{aligned}C_{\alpha\gamma\beta\delta} = &\frac{R_{\alpha\delta}g_{\gamma\beta} - R_{\alpha\beta}g_{\gamma\delta} + R_{\gamma\beta}g_{\alpha\delta} - R_{\gamma\delta}g_{\alpha\beta}}{d-2} \\ &- R_{\alpha\gamma\beta\delta} + \frac{g_{\alpha\beta}g_{\gamma\delta} - g_{\alpha\delta}g_{\gamma\beta}}{(d-1)\,(d-2)}\,R\end{aligned} \tag{3.5.14}$$

is the Weyl tensor. From eq. (3.5.12) we get that $\sigma_{\alpha\beta} = 0$ provided that

$$C_{\alpha\gamma\beta\delta}\,u^{\gamma}u^{\delta} + \frac{1}{d-2}\bar{R}_{\alpha\beta} = 0\,. \tag{3.5.15}$$

We now separately compute both terms involved in the above expression. Considering the metric in eq. (3.1.16), we get

$$C_{\alpha\gamma\beta\delta}\,u^{\gamma}(\sigma)u^{\delta}(\sigma) = \frac{C_{\alpha\sigma\beta\sigma}}{q_{\sigma}}\,. \tag{3.5.16}$$

Recalling that in our basis $R_{\alpha\sigma\beta\sigma} = -R_{\alpha\sigma\sigma\beta} \neq 0$ only if $\alpha = \beta \neq \sigma$ and that both the metric and the Ricci tensor are diagonal (see Sec. 3.1), we conclude that $C_{\alpha\sigma\beta\sigma} \neq 0$ only if $\alpha = \beta \neq \sigma$. Thus the only non-vanishing components of the Weyl tensor contracted with the normalized velocity are

$$C_{\rho\alpha\rho\beta}\,u^{\alpha}(\sigma)u^{\beta}(\sigma) = q_{\rho}\left[K\,(\rho\,,\sigma) - \frac{R_{\rho}+R_{\sigma}}{d-2} + \frac{R}{(d-1)\,(d-2)}\right]\,, \tag{3.5.17}$$

[12] We denote the directional covariant derivative as $\frac{D\sigma_{\alpha\beta}}{d\lambda} = u^{\gamma}\nabla_{\gamma}\sigma_{\alpha\beta}$.

with $\rho \neq \sigma$. Regarding the tensor $\bar{R}_{\alpha\beta}$, a direct calculation reveals that the only non-vanishing components of the transverse part of the metric are $h_{\rho\rho} = q_\rho$ with $\rho \neq \sigma$. Consequently, $\bar{R}_{\alpha\beta}$ vanishes unless $\alpha = \beta \neq \sigma$, in which case

$$\bar{R}_{\rho\rho} = q_\rho \left[R_\rho - \frac{1}{d-1} \left(R - R_\sigma \right) \right] . \tag{3.5.18}$$

Putting eqs. (3.5.17) and (3.5.18) together, we deduce that $\sigma_{\alpha\beta}$ vanishes along the congruence if

$$q_\rho \left[K\left(\rho\,,\sigma\right) - \frac{1}{d-1} R_\sigma \right] = 0 \tag{3.5.19}$$

for every $\rho \neq \sigma$.
In other words, a geodesic given by the exponential of σ develops a conjugate point exactly at $\lambda_c = \lambda_0$ whether $(d-1)K\left(\rho\,,\sigma\right) = R_\sigma$ for every $\rho \neq \sigma$. If the algebra contains elements ρ commuting with σ, this condition is equivalent to $R_\sigma = 0$. Therefore, the only non-trivial case in which the condition is verified is a one-qubit system, which we will study in detail in the next subsection.

3.5.3 Conjugate points for one qubit

In the following, we employ the results introduced in the previous discussion to some concrete examples, the simplest of which is a one-qubit system. As in Subsec. 3.2.1, we introduce the penalties $q_{\sigma_x} = 1$, $q_{\sigma_y} = Q$, and $q_{\sigma_z} = P$. The resulting unitary manifold is a generalized Berger sphere, which can be parametrized by the Euler angles $(\theta_x, \theta_y, \theta_z)$. Expressing a group element as

$$U = e^{i\theta_z \sigma_z} e^{i\theta_y \sigma_y} e^{i\theta_x \sigma_x} , \tag{3.5.20}$$

the metric tensor extracted from eq. (3.4.27) reads (see also [20])

$$g_{ij} = \frac{1}{2} \begin{pmatrix} \Xi & \Psi & 2P \sin 2\theta_y \\ \Psi & \Sigma & 0 \\ 2P \sin 2\theta_y & 0 & 2P \end{pmatrix} , \tag{3.5.21}$$

where

$$\Xi = 2 \left[P \sin^2 2\theta_y + \cos^2 2\theta_y \left(Q \sin^2 2\theta_z + \cos^2 2\theta_z \right) \right] ,$$
$$\Psi = (1-Q) \cos 2\theta_y \sin 4\theta_z \,, \qquad \Sigma = (Q-1) \cos 4\theta_z + Q + 1 \,.$$

As it can be directly checked starting from the metric in eq. (3.5.21), the exponential of generators $\sigma_x, \sigma_y, \sigma_z$ are geodesics. Such operators are given by

$$\begin{aligned} G_x: &\quad \theta_x = \lambda\,, \qquad \theta_y = \theta_z = 0\,, \\ G_y: &\quad \theta_y = \frac{\lambda}{\sqrt{Q}}\,, \qquad \theta_x = \theta_z = 0\,, \\ G_z: &\quad \theta_z = \frac{\lambda}{\sqrt{P}}\,, \qquad \theta_x = \theta_y = 0\,. \end{aligned} \tag{3.5.22}$$

We have seen that the presence of conjugate points for this class of geodesics can be detected by the Ricci tensor

$$\begin{aligned} R_x &= \frac{2(1-(P-Q)^2)}{PQ}\,, \\ R_y &= \frac{2(Q+P-1)(Q-P+1)}{PQ}\,, \\ R_z &= \frac{2(P+Q-1)(P-Q+1)}{PQ}\,, \end{aligned} \tag{3.5.23}$$

where we denote $R_{x,y,z} \equiv R_{\sigma_x,\sigma_y,\sigma_z}$. As we have shown in Subsec. 3.5.2, each geodesic G_k with $k = x, y, z$ develops a conjugate point at

$$\lambda_c \leq \lambda_0\,, \qquad \lambda_0 = \frac{\pi\sqrt{2}}{\sqrt{R_k}}\,, \tag{3.5.24}$$

provided that $R_k > 0$. In Fig. 3.6 we depict the regions of the parameter space (P, Q) in which this happens. Following the discussion at the end of Subsec. 3.5.2, the bound on the position of the conjugate point of G_k is saturated if $R_k = 2K_{ki} = 2K_{kj}$, with $i \neq j \neq k$. We have then a few exact results:

- for $P = Q$, G_x has a conjugate point at $\lambda_c = \pi P$ (see Fig. 3.6)[13];
- for $P = 1$, G_y has a conjugate point at $\lambda_c = \frac{\pi}{\sqrt{Q}}$;
- for $Q = 1$, G_z has a conjugate point at $\lambda_c = \frac{\pi}{\sqrt{P}}$.

[13] In the picture, the three-dimensional Berger sphere is projected to the three-dimensional Euclidean space by the mapping $y_i = \frac{2a_i}{1+b}$, with

$$a_1 = \sin\theta_x \cos\theta_y \cos\theta_z + \cos\theta_x \sin\theta_y \sin\theta_z\,, \quad a_2 = \cos\theta_x \sin\theta_y \cos\theta_z - \sin\theta_x \cos\theta_y \sin\theta_z\,,$$

$$a_3 = \cos\theta_x \cos\theta_y \sin\theta_z + \sin\theta_x \sin\theta_y \cos\theta_z\,, \quad b = \cos\theta_x \cos\theta_y \cos\theta_z - \sin\theta_x \sin\theta_y \sin\theta_z\,.$$

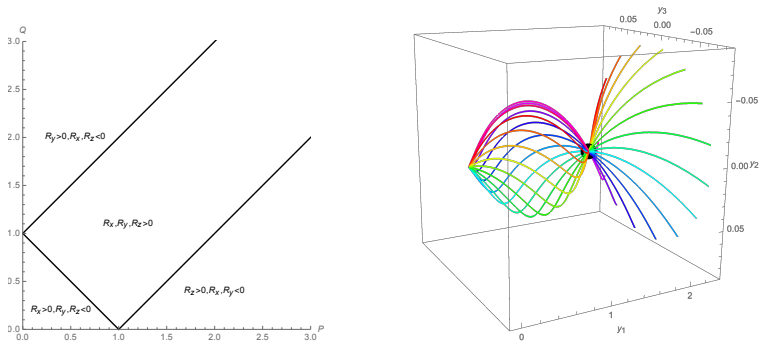

Figure 3.6: Left: Regions where each $R_{x,y,z}$ is positive. Right: Exact conjugate point (the black spot) of G_x for $P = Q = 0.4$ in stereographic projection.

It is interesting to consider the limit in eq. (3.2.3), with $P = 1$ and $Q \to \infty$. In this case G_y is the only exponential geodesic with a conjugate point, which moves at $\lambda = \pi/\sqrt{Q}$ and $\theta_y = \pi/Q$. Then, the geodesic G_y stops being minimizing very close to the origin. For this reason, sending the penalty Q to infinity does not correspond to getting a large complexity in the σ_y direction: a shortcut with length scaling as $1/\sqrt{Q}$ is certainly available just after the conjugate point. This behavior, that is related to a singular limit in the curvature (3.2.4), is an indication of low maximal complexity. The same conclusion applies to the specular case $Q = 1$ and $P \to \infty$, and is a distinctive hallmark of penalizing a single generator. Indeed, it is a known fact that the maximal distance of a point on the Berger sphere from the identity is never larger than a $\mathcal{O}(1)$ number, independently of the value of the penalty [20, 138].
Another limit worth mentioning is $P = Q \to \infty$, as in eq. (3.2.5). Here, the Ricci curvatures are all positive:

$$R_x = \frac{2}{P^2}\,, \qquad R_y = R_z = \frac{4}{P} - \frac{2}{P^2}\,. \tag{3.5.25}$$

Consequently, G_x has an exact conjugate point at $\theta_x = \lambda = \pi P$, whereas $G_{y,z}$ have conjugate points at $\lambda \lesssim \pi\sqrt{P/2}$, corresponding to θ_y, θ_z of $\mathcal{O}(1)$. As expected from the curvatures in eq. (3.2.6), there is no singularity in geodesics. Note that, while the distance of conjugate points of $G_{y,z}$ diverges, their position in the coordinate $\theta_{y,z}$ approaches a finite value for $P \to \infty$. The limit of large penalty may indeed correspond to a large maximal complexity, because no obvious shortcuts are available. Such an empirical conclusion is supported by numerical computations: the points with large complexity lay nearby the conjugate point, so maximal complexity scales as $\sqrt{P}$. This agrees with the diameter of the Berger sphere with two equal penalty factors [138].

We now explore geodesics on the state manifold $\mathbb{CP}^1$, providing us with information on state complexity. As explained in Subsec. 3.4.6, geodesics in $\mathbb{CP}^1$ can be obtained as projections of horizontal geodesics in the unitary manifold through a Riemannian submersion π. Taking as a reference state $|0\rangle$, the unbroken subgroup is generated by σ_z. Therefore, the exponential geodesics $G_{x,y}$ shot in the orthogonal directions are horizontal. For any P, Q, the projection of these curves by the submersion π gives us geodesics on the space of states. To numerically check this result, we solved the geodesic equations derived from the states metric, which in Bloch sphere coordinates (θ, ϕ) reads

$$g_{ij} = \frac{1}{\Upsilon} \begin{pmatrix} \Omega_{11} & \Omega_{12} \\ \Omega_{21} & \Omega_{22} \end{pmatrix} , \tag{3.5.26}$$

with

$$\Omega_{11} = P\cos^2\theta\cos^2\phi + PQ\cos^2\theta\sin^2\phi + Q\sin^2\theta\,,$$

$$\Omega_{12} = \Omega_{21} = P(Q-1)\sin\theta\cos\theta\sin\phi\cos\phi\,,$$

$$\Omega_{22} = P\sin^2\theta\left(Q\cos^2\phi + \sin^2\phi\right)\,,$$

$$\Upsilon = 4\left[\sin^2\theta\sin^2\phi + P\cos^2\theta + Q\sin^2\theta\cos^2\phi\right]\,.$$

In Fig. 3.7 we show the geodesics on the Bloch sphere for the case $P = Q = 10$. The figure reveals that the region of maximal complexity is located just before the conjugate point in the σ_y direction. Such a point lies inside the *drop* delimited by the self intersection of the black curve. As it is clear from the figure, no geodesics of length less than λ can penetrate inside the drop.

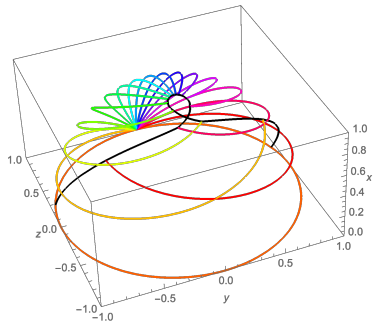

Figure 3.7: Geodesics with length $\lambda = 2.5$ for $P = Q = 10$, starting from the reference state $(\theta, \phi) = (0, 0)$. The geodesics are plotted in different colors, and their endpoints are joined by the black curve.

3.5.4 Conjugate points for the draconian model

In order to study conjugate points in the draconian model we make use of the results from [124] for R_σ, where σ is a generalized Pauli matrix with weight w:

$$\begin{aligned}
w = 1\,, &\qquad R_\sigma = 2\,(3n-2) + \frac{1}{q^2}\left(\frac{4^n}{2} - 2\,(3n-2)\right)\,,\\
w = 2\,, &\qquad R_\sigma = -24\,q\,(n-2) + 8\,(6n-11) + \frac{1}{q^2}\left(\frac{4^n}{2} - 8\,(3n-5)\right)\,,\\
w = 3\,, &\qquad R_\sigma = 12\,q + \frac{1}{q}\left(\frac{4^n}{2} + 36\,(n-3)\right) - \frac{1}{q^2}12\,(3n-8)\,,\\
w \geq 4\,, &\qquad R_\sigma = \frac{1}{q}\left(\frac{4^n}{2} + 4w\,(3n-2w)\right) - \frac{1}{q^2}4w\,(3n-2w)\,.
\end{aligned} \tag{3.5.27}$$

These expressions are valid for arbitrary number of qubits n and penalty q. In particular, for $q = 1$ we recover the non-penalized choice $q_w = 1$, where all the R_σ are the same, namely $R_\sigma = 4^n/2$. The requirement to have a negative scalar curvature is that q scales at least as $q \propto 4^n$.

In studying conjugate points along the exponential geodesics, it is important to keep track not only of the distance λ from the identity, but also of the position in a coordinate θ, which runs along the geodesic and does not scale with the penalty. Such a θ can be defined as the geodesic length measured by the non-penalized bi-invariant metric. In our normalization conventions, an exponential geodesic can be expressed as

$$U_\sigma(\theta) = e^{i\theta\sigma}\,, \tag{3.5.28}$$

where σ is the generalized Pauli matrix tangent to the geodesic. Note that this curve comes back to the identity after a period

$$\theta_p = 2\pi\,. \tag{3.5.29}$$

In the large n limit of the non-penalized case $q_w = 1$, the upper bound on the location of the conjugate point in eq. (3.5.11) gives

$$\lambda_0 = \theta_0 \approx \pi\sqrt{2} \tag{3.5.30}$$

for all the weights w. Therefore, the cut point is met for $\lambda \leq \lambda_0$ in every direction. This implies that the maximal complexity is less than $\pi\sqrt{2}$, which is independent of n.

Let us now consider the regime with negative scalar curvature $q \approx 4^n$. By means of eq. (3.5.11) with $d = 4^n - 1$, we get an estimate of the distance of conjugate points from the identity:

$$\begin{aligned} w = 1\,, \qquad & \lambda_0 \approx \frac{\pi\, 2^n}{\sqrt{6n}}\,, \qquad \theta_0 = \lambda_0\,, \\ w = 3\,, \qquad & \lambda_0 \approx \frac{\pi\, 2^n}{\sqrt{12q}} \approx \frac{\pi}{\sqrt{12}}\,, \qquad \theta_0 = \frac{\lambda_0}{\sqrt{q}} \approx \frac{1}{2^n}\frac{\pi}{\sqrt{12}}\,, \\ w \geq 4\,, \qquad & \lambda_0 \approx \pi\sqrt{2q} \approx \sqrt{2}\pi\, 2^n\,, \qquad \theta_0 = \frac{\lambda_0}{\sqrt{q}} \approx \sqrt{2}\pi\,, \end{aligned} \tag{3.5.31}$$

where θ_0 is the geodesics length according to the bi-invariant metric.
The geodesics with $w = 1$ have a conjugate point after a length exponential in n. However, from eq. (3.5.29) we have $\theta_p \ll \theta_0$ at large n, meaning that the geodesics pass through the identity many times before reaching θ_0. So, this cannot correspond to a cut point.
The geodesics with $w \geq 4$ instead have a conjugate point at θ_0 of $\mathcal{O}(1)$, with a length scaling exponentially in n. Unfortunately, we do not have a strong indication that the cut point coincides with the conjugate point, so we cannot conclude that maximal complexity is exponential in n. Still, being θ_0 of $\mathcal{O}(1)$, the possibility that the cut and conjugate points coincide is not as unrealistic as in the $w = 1$ case. Note that, with very good approximation, the distance of the conjugate point from the identity is independent of w for $w \geq 4$.
Finally, the geodesic with $w = 3$ have $\theta_0 \approx 0$. Therefore, the conjugate point is very close (according to the bi-invariant metric) to the identity and it is reasonably a cut point. However, the distance λ_0 from the identity is of $\mathcal{O}(1)$, so this does not teach us anything about the possible exponential growth of complexity at large n. Also, the exponential dependence $\theta_0 \propto 2^{-n}$ shows that draconian penalties are by construction singular.

Regarding the complexity of states, at the end of Subsec. 3.4.6 we have argued that all the tangent directions orthogonal to the vertical space with $0 \leq s \leq n-3$, see eq. (3.4.48), generate exponential geodesics projectable by a Riemannian submersion π. The above considerations can thus be extended to the state manifold, with a caveat on the position of conjugate points.
Let us consider a horizontal geodesic in the unitary manifold M

$$\gamma(t) : [a, b] \to M \tag{3.5.32}$$

and let $\gamma(t_0)$ be the first conjugate point along the geodesic starting from $\gamma(a)$. Then, the projected geodesic $\beta(t) = \pi(\gamma(t))$ has a conjugate point for $t_0' \leq t_0$ [26]. In other words, the conjugate point of the projected geodesics might occur before.

3.5.5 Conjugate points for the progressive model

We come back to the more promising penalization model $q_w = \alpha^{w-1}$ and investigate the location of conjugate points of exponential geodesics. In Appendix A, we compute the Ricci contraction with the unit vector pointing in the direction of a generalized Pauli matrix σ of weight w at the leading order in α. The result is

$$R_w = 2w\left(2^{w-1} - 2^{2(n-w)+1}\right) \tag{3.5.33}$$

for $w > 1$ and $R_1 = 2$. Thus, R_w is positive for $w = 1$ and

$$w > \frac{2}{3}(n+1)\,. \tag{3.5.34}$$

The conjugate point for $w = 1$ is estimated at

$$\lambda_0 = \theta_0 = \frac{\pi\, 2^n}{\sqrt{2}}\,. \tag{3.5.35}$$

Again, eq. (3.5.29) tells us that $\theta_p \ll \theta_0$ at large n, so this conjugate point cannot correspond to a cut point.
On the contrary, the conjugate points for the generators at large w satisfying eq. (3.5.34) gives us interesting information. In this class, the largest positive component of the Ricci tensor is

$$R_n = n(2^n - 4)\,, \tag{3.5.36}$$

so the exponential geodesics generated by a σ of weight $w = n$ have a conjugate point at

$$\lambda_0 \approx \frac{\pi\, 2^{n/2}}{\sqrt{n}}\,, \qquad \theta_0 = \frac{\lambda_0}{\alpha^{n/2}} \approx \frac{\pi\, 2^{n/2}}{\sqrt{n}\,\alpha^{n/2}}\,. \tag{3.5.37}$$

The smallest positive value of R_w is instead realized for slightly different values of the integer w, depending on the value of n modulo 3. In particular, we have to distinguish among the following cases:

$$\begin{aligned}
&n = 3a\,, \qquad w = \frac{2n+3}{3}\,, \qquad R_w = 2^{2n/3}\left(1 + \frac{2n}{3}\right) \approx n\, 2^{2n/3} 0.67\,,\\
&n = 3a+1\,, \qquad w = \frac{2n+4}{3}\,, \qquad R_w = 2^{2n/3}\,(n+2)\,2^{1/3} \approx n\, 2^{2n/3} 1.26\,,\\
&n = 3a+2\,, \qquad w = \frac{2n+5}{3}\,, \qquad R_w = 2^{2n/3}\frac{7(2n+5)}{6\cdot 2^{1/3}} \approx n\, 2^{2n/3} 1.85\,,
\end{aligned} \tag{3.5.38}$$

where a is an non-negative integer. In all cases $R_w \approx n\, 2^{2n/3}$ up to order one factors. This gives a conjugate point at

$$\lambda_0 \approx \frac{\pi\, 2^{2n/3}}{\sqrt{n}}\,, \qquad \theta_0 = \frac{\lambda_0}{\alpha^{n/3}} \approx \frac{\pi\, 2^{2n/3}}{\sqrt{n}\,\alpha^{n/3}}\,. \tag{3.5.39}$$

Intermediate values of the weight give conjugate points distances scaling in between the ones in eqs. (3.5.37) and (3.5.39). In order to have small θ_0 in the large n limit in such results, we must necessarily take $\alpha > 4$. In addition, the value of α should be large enough to trust the leading order result in eq. (3.5.33). Indeed, from Fig. 3.2 the Ricci curvature seems to converge to the asymptotic value at large α quite fast.
Since $\theta_0 \to 0$ for large n, we expect the exponential geodesics with $2n/3 < w < n$ to be globally minimizing up to θ_0. This strongly indicates that the cut point distance of such geodesics is in the window

$$\frac{\pi\, 2^{n/2}}{\sqrt{n}} \leq \lambda_0 \leq \frac{\pi\, 2^{2n/3}}{\sqrt{n}}\,. \tag{3.5.40}$$

Consequently, the maximal complexity is bigger than

$$\lambda_{\max} = \frac{\pi\, 2^{2n/3}}{\sqrt{n}}\,, \tag{3.5.41}$$

and scales exponentially in n.

One may wonder if this is just an artifact of the large α limit: in fact in this regime we expect the maximal complexity to diverge by construction. In order to clarify this subtle point, let us consider higher order corrections to R_w and to λ_0. In Appendix A we show that the $\mathcal{O}(\alpha^{-1})$ term vanishes for all the Ricci components apart from $w = 2$, which does not contribute to conjugate points. So we need to go to $\mathcal{O}(\alpha^{-2})$.

To make the computation simpler we focus on $w = n$, that provides the larger value of R_w at the leading order. In this case, the non-vanishing α^{-2} terms in the sectional curvatures in eqs. (A.2.1) and (A.2.2) contributing to R_n are

$$\begin{aligned}
&\delta K^{(2)}(n,2,0) = -\frac{3}{\alpha^2}\,, \qquad \delta K^{(2)}(n,3,0) = \frac{2}{\alpha^2}\,,\\
&\delta K^{(2)}(n,n-2,0) = -\frac{2}{\alpha^2}\,, \qquad \delta K^{(2)}(n,n-1,0) = \frac{1}{\alpha^2}\,,\\
&\delta K^{(2)}(n,N,1) = \frac{1}{\alpha^2}\,, \qquad \text{for } \; 4 \leq N \leq n-1\,.
\end{aligned} \tag{3.5.42}$$

A direct calculation gives

$$R_n = n(2^n - 4) + \frac{(n-1)n\left((2^n - 16)\, n - 2\,(2^n - 4)\right)}{6\alpha^2} \approx n\, 2^n + \frac{n^3 2^n}{6\alpha^2}\,. \quad (3.5.43)$$

Then, at the next-to-leading order in α, the length of the geodesic built from the exponential of a $w = n$ generator before the conjugate point is

$$\lambda_0 \approx \frac{\pi\, 2^{n/2}}{\sqrt{n}} \left(1 - \frac{1}{12\alpha^2} n^2\right)\,. \quad (3.5.44)$$

In order to trust the approximation, α should just grow slightly faster than n for large n, for example quadratically. From this polynomial increase of α with n, we get an exponential increase of complexity. We believe this to be a strong indication that maximal complexity is exponentially large in n with a progressive choice of penalties.

We remark that our argument does not provide a rigorous proof to this property. For example, we have neglected the shear term in the Raychaudhuri's equation, which may cause the conjugate point to appear before. It would be interesting to improve the analysis studying the impact of these terms. We leave this as a problem for future investigation.

We conclude our discussion with a brief comment about state complexity. In Subsec. 3.4.6, we have inferred that in the progressive model there is a two-dimensional space of vectors which are both orthogonal to the vertical space and eigenstates of the penalty operator. Such vectors are given by arbitrary linear combinations of $S_n^{\pm}$ in eq. (3.4.45), which contain only generators of weight $w = n$. Therefore, the previous calculation in unitary space for $w = n$ also applies to state complexity, with the caveat that the conjugate point in the space of states might occur before [26].

3.6 Discussion

In this chapter we have studied several aspects of complexity geometry for systems of n qubits, referring to the definition introduced by Nielsen and collaborators [124]. We have focused on the two different but strongly related notions of unitary and state complexity, quantifying the difficulty of building a unitary operator [19, 21, 123, 124, 139] and a state [11, 13, 14, 82], respectively.

Regarding unitary complexity, defined on the homogeneous manifold $\mathrm{SU}(2^n)$, two basic properties are required for complexity to manifest a chaotic behavior: the geometry must be negatively curved and maximal complexity must be

exponentially large in the number of qubits n.
Consistently with the analysis in [20], in Sec. 3.1 we have shown that negative sectional curvatures $K(\rho, \sigma)$ are always associated to easy generators ρ, σ whose commutator provides a hard generator, where easy and hard refers to small and large penalty factors, respectively.
On the other hand, in Sec. 3.5 we have proposed an argument to unveil the exponential scaling of complexity, based on the search of parametric regimes in which the angular position of conjugate points approaches the identity, while their complexity distance from the identity is exponential in n.

In Sec. 3.2 we have investigated the one-qubit system, which is as simple as useful to unravel some basic properties of complexity geometry for generic n. On the one hand, at least two out of three sectional curvatures in the Pauli matrices basis are positive. But eq. (3.1.26) teaches us that sectional curvatures $K(\rho, \sigma)$ depend just on the penalties of the generators ρ, σ and their commutator. So, since all generators acting just on a specific qubit form a closed subalgebra of $\mathfrak{su}(2^n)$, we deduce that for generic n some sectional curvatures are necessarily positive as well. On the other hand, some large penalties regimes in the one-qubit case generalize to large n. There are two prototypical situations:

1) $P = 1$ and $Q \to \infty$, see eq. (3.2.3). Easy generators are enough to construct any unitary operator, so maximal complexity is finite. Some sectional curvatures diverge, thus the geometry is singular.

2) $P = \beta Q \to \infty$ with $\beta \neq 1$, see eq. (3.2.7). Easy generators are not enough to construct any unitary operator, so maximal complexity goes to infinity. Sectional curvatures do not diverge and negative values can be realized.

For large n we have a huge arbitrariness in the choice of penalty factors. In Sec. 3.3, we have analyzed two prototypes:

1) draconian penalties, defined by eq. (3.3.6). In the large penalty limit, for fixed n, complexity does not diverge, and the scalar curvature in eq. (3.3.9) becomes negative and singular. There are no regimes in which conjugate points give us information on the exponential nature of complexity.

2) progressive penalties, defined by eq. (3.3.11). In the large penalty limit, for fixed n, complexity diverges, and the scalar curvature in eq. (3.3.14) is negative and finite. We have a robust indication of exponential scaling of complexity.

We point out that our conjugate points-based argument does not provide a strict proof to the scaling of maximal complexity. Though our method is

inconclusive for draconian penalties, in which case an exponential lower bound to maximal complexity was already been found by Nielsen et al. [21] by exploiting gate complexity, it provides a first evidence for progressive penalties. Recently, in [140] an exponential scaling of maximal unitary complexity for both the draconian and the progressive model has been proved by means of the *Bishop-Gromov theorem* [141], which upper bounds the volume of geodesic balls in homogeneous manifold. The same conclusion has been drawn in [142] by approximating complexity geometry with gate complexity, and lower bounding the length of a path on the unitary manifold by the number of gates required to reproduce the corresponding unitary operator.

In Sec. 3.4, we have observed that unitary and state complexity [14], which is more relevant for holographic applications, are directly related by Riemannian submersions [25, 26, 133]. By employing this formalism, we have provided a closed-form expression for the metric in the space of states, see eq. (3.4.20). In principle, one may extract from such a metric sectional curvatures and geodesics. However, Riemannian submersions allow us to avoid these cumbersome computations.
In particular, sectional curvatures of the states manifold are related to sectional curvatures of the unitary manifold by O'Neill's formula [25]. Moreover, geodesics in the space of states can be found as projections of horizontal geodesics from the unitary space, whose conjugate points are realized for a complexity equal or less than the unitary one.

Chapter 4

Subregion complexity in AdS_3 and in the BTZ black hole

This chapter is an adaptation of the published article [143]. Below, we add a brief introduction to complexity of mixed states and its holographic interpretation. Sec. 4.1 has been inserted to illustrate the various contributions to the gravitational action. The comments on the choice of the gravitational action counterterm for null boundaries at the end of Sec. 4.1 are adapted from Sec. 3.5 of the published article [144].

In the previous chapter we have introduced a formalism to investigate complexity of *pure states* in n qubits systems. In analogy to entanglement entropy, it is interesting to extend the notion of complexity to *mixed states*. Three main proposals for a quantum information notion quantifying the difficulty of building mixed states have been put forward in [34].
The first proposal, named *purification complexity*, is based on the idea of substituting the target mixed state ρ with a *purification* of the state itself. Namely, if ρ is a density matrix on a Hilbert space H_A, a Hilbert space H_B and a pure state $|\psi\rangle$ on $H_A \otimes H_B$ can always be introduced such that $\rho = \mathrm{Tr}_{H_B}(|\psi\rangle\langle\psi|)$. The state $|\psi\rangle$ represents a purification of ρ.
The other possibilities, named *spectrum complexity* and *basis complexity*, split the process of building the target state ρ into two steps: creation of the spectrum and creation of the basis of eigenstates.
Basically, the three notions of mixed state complexity can be defined as follows:

- Purification complexity $\mathcal{C}_P$ is identified with the lowest complexity of all purifications of the target mixed state ρ.

- Spectrum complexity $\mathcal{C}_S$ is defined as the lowest purification complexity of all states ρ_{spec} with the same spectrum as ρ.
- *B*asis complexity $\mathcal{C}_B$ corresponds to the complexity of building ρ from the less complex ρ_{spec}.

For the sake of clarity, we provide a schematic illustration of such definitions:

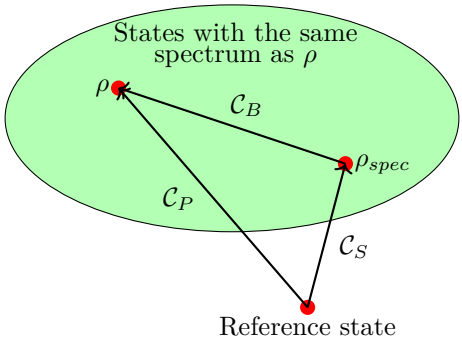

Figure 4.1: The three main definitions of mixed state complexity. The picture is a reproduction of a figure contained in [34].

In principle, a good definition of mixed state complexity is expected to reduce to state complexity in case the target state is pure. For this reason spectrum complexity, which gives $\mathcal{C}_S = 0$ for pure states, can be discarded [34]. Investigation of purification complexity in QFTs have been conducted in [35, 36, 66], while a study of basis complexity for harmonic lattices has been carried out in [37]. Another possibility is to relate mixed state complexity to *quantum fidelity susceptibility* [39], which asses how close two states are. Fidelity susceptibility defines a *Fisher information metric*, that directly measures the distance between mixed states with no need to perform the purification procedure. See [37, 145] for works in this direction.

In the AdS/CFT framework, the question raises of which bulk quantity is dual to some notion of mixed state complexity in the boundary CFT. As a known result in holography, the reduced density matrix living in a CFT subregion corresponds to a causal codimension-zero bulk region named *entanglement wedge*, which is attached to the RT surface and the boundary subregion [38]. It is thus natural to conjecture that mixed state complexity is dual to the same quantities involved in the holographic complexity proposals (see Subsec. 2.6.2), restricted to their intersection with the entanglement wedge. The resulting conjectures are:

- *Subregion-CV* [39], relating complexity of a state defined in a boundary region $\mathcal{A}$ to the volume of the extremal codimension-one bulk surface $\mathcal{R}_{\mathcal{A}}$ bounded by $\mathcal{A}$ and its HRT surface $\Gamma_{\mathcal{A}}$ [96]:

$$\mathcal{SC}_V(\mathcal{A}) = \max_{\partial \mathcal{R}_{\mathcal{A}} = \mathcal{A} \cup \Gamma_{\mathcal{A}}} \left[\frac{V(\mathcal{R}_{\mathcal{A}})}{GL} \right] . \tag{4.0.1}$$

- *Subregion-CA* [40] (or *subregion-CV 2.0*), relating complexity of the boundary mixed state to the gravitational action I (or the spacetime volume V_{bulk}) of the intersection $\mathcal{W}_{\mathcal{A}}$ between the WDW patch and the entanglement wedge of the boundary subregion $\mathcal{A}$:

$$\mathcal{SC}_A(\mathcal{A}) = \frac{I(\mathcal{W}_{\mathcal{A}})}{\pi \hbar} , \qquad \mathcal{SC}_{V2.0}(\mathcal{A}) = \frac{V_{bulk}(\mathcal{W}_{\mathcal{A}})}{GL^2} . \tag{4.0.2}$$

In Fig. 4.2 we show a sketch of the three holographic proposals:

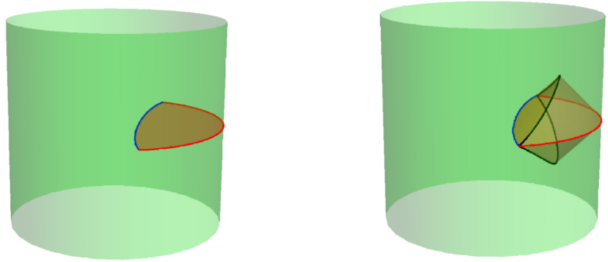

Figure 4.2: Illustration of the proposed gravitational counterparts of mixed state complexity in global AdS$_3$. The red and blue curves represents the boundary subregion A and its RT surface $\gamma_{\mathcal{A}}$, respectively. On the left: Subregion-CV conjecture. The extremal codimension-one surface $\mathcal{R}_{\mathcal{A}}$ whose volume is interpreted as subregion complexity is shown in red. On the right: Subregion-CA and subregion-CV 2.0 conjectures. The boundaries of the entanglement wedge and of the WDW patch are shown in orange and pink, respectively.

In order to identify the correct quantum field theory dual, the holographic conjectures have been tested in several scenarios, e.g. [144, 146–156]. In this chapter we focus on the case of planar AdS$_3$ and the Banados-Teitelboim-Zanelli (BTZ) black hole [41, 42], taking as a boundary subregion a line segment.

4.1 Recipe for the gravitational action computation

According to the (subregion-)CA conjecture, (subregion) complexity is dual to the gravitational action of a bulk spacetime region $\mathcal{W}$ bounded by null codimension-one surfaces. Boundary terms providing a well-defined variational principle in such cases have been discussed in [157, 158]. The resulting action reads

$$I = I_{\mathcal{W}} + I_{\mathcal{B}} + I_{\mathcal{J}} + I_{ct}\,, \tag{4.1.1}$$

where $I_{\mathcal{W}}$ is the Einstein-Hilbert action of the codimension-zero spacetime region, $I_{\mathcal{B}}$ is the contribution from the codimension-one bounding surfaces, $I_{\mathcal{J}}$ is the term coming from the codimension-two joints at the intersection of the bounding surfaces, and I_{ct} is a counterterm which guarantees the reparametrization invariance of the action. We now describe each term in detail.

Both AdS$_3$ and BTZ spacetime are solutions to the Einstein's field equations obtained by the *Einstein-Hilbert action*

$$I_{EH} = \frac{1}{16\pi G}\int d^3x\sqrt{-g}\,(R - 2\Lambda)\,, \tag{4.1.2}$$

where g denotes the determinant of the spacetime metric. The scalar curvature and cosmological constant are

$$R = -\frac{6}{L^2}\,, \qquad \Lambda = -\frac{1}{L^2}\,, \tag{4.1.3}$$

with L the AdS curvature radius. The action contribution $I_{\mathcal{W}}$ is given by eq. (4.1.2), by restricting the integral to the region $\mathcal{W}$ of interest.

The codimension-one boundary contributions can be divided into two main terms:

$$I_{\mathcal{B}} = I_{\text{GHY}} + I_{\mathcal{N}}\,. \tag{4.1.4}$$

The first contribution, coming from timelike and spacelike boundaries, is the *Gibbons-Hawking-York* (GHY) *action* [159, 160]

$$I_{\text{GHY}} = \frac{1}{8\pi G}\int_{\mathcal{B}} d^2x\sqrt{|h|}\,K\,. \tag{4.1.5}$$

In this expression, $h_{\mu\nu}$ is the induced metric on $\mathcal{B}$ and $K = h^{\mu\nu}K_{\mu\nu}$ is the trace of the *extrinsic curvature* $K_{\mu\nu} = h^{\rho}_{\mu}h^{\sigma}_{\nu}\nabla_{\rho}n_{\sigma}$, where n_σ is the outward-directed normal to the surface $\mathcal{B}$. The second term, coming from null boundaries, is [157, 158]

$$I_{\mathcal{N}} = \int_{\mathcal{B}} dS\, d\lambda\, \sqrt{\gamma}\, k\,, \tag{4.1.6}$$

where λ runs along the null geodesics generating the surface $\mathcal{B}$, S is the transverse spatial directions to such generators, and γ is the determinant of the induced metric on S. The constant κ is defined by the geodesic equation

$$k^\mu \nabla_\mu k^\alpha = \kappa\, k^\alpha \,, \tag{4.1.7}$$

with k^μ the null generator. In other words, κ measures the failure of λ to be an affine parameter. Consequently, we can set $\kappa = 0$ by a wise parametrization choice, getting rid of the term $I_{\mathcal{N}}$.

At the intersection of bounding codimension-one surfaces, where the boundary is non-smooth, the joint term $I_{\mathcal{J}}$ comes into play. The joint contributions involving just timelike and spacelike intersecting surfaces have been investigated in [161]. In our computations, we will meet only joints involving at least one null boundary. In this case, the proper action contribution is [157]

$$I_{\mathcal{J}} = \frac{1}{8\pi G} \int_{\mathcal{J}} dx\, \sqrt{\sigma}\, \mathfrak{a} \,, \tag{4.1.8}$$

where σ is the determinant of the induced metric on the codimension-two joint surface and $\mathfrak{a}$ depends on the kind of joint. Let us denote by $\mathbf{k}, \tilde{\mathbf{k}}$ the one-forms normal to null boundaries, by $\mathbf{t}$ the one-form normal to a spacelike boundary, and by $\mathbf{s}$ the one-form normal to a timelike boundary. We take such one-forms to be outward-directed from the spacetime region of interest. Following the conventions of [40, 162], we have

$$\mathfrak{a} = \begin{cases} \zeta \log \left| \frac{\mathbf{k}\cdot\tilde{\mathbf{k}}}{2} \right| & \text{null-null joints, with } \zeta = -\operatorname{sign}(\mathbf{k}\cdot\tilde{\mathbf{k}}) \operatorname{sign}(\hat{\mathbf{k}}\cdot\tilde{\mathbf{k}}) \,, \\ \zeta \log |\mathbf{k}\cdot\mathbf{t}| & \text{spacelike-null joints, with } \zeta = -\operatorname{sign}(\mathbf{k}\cdot\mathbf{t}) \operatorname{sign}(\hat{\mathbf{s}}\cdot\mathbf{k}) \,, \\ \zeta \log |\mathbf{k}\cdot\mathbf{s}| & \text{timelike-null joints, with } \zeta = -\operatorname{sign}(\mathbf{k}\cdot\mathbf{s}) \operatorname{sign}(\hat{\mathbf{t}}\cdot\mathbf{k}) \,, \end{cases} \tag{4.1.9}$$

in which $\hat{\mathbf{t}}$, $\hat{\mathbf{s}}$ and $\hat{\mathbf{k}}$ are vectors in the tangent space of the appropriate surface $\mathcal{B}$, orthogonal to $\mathcal{J}$ and outward-directed from the bulk region $\mathcal{W}$. For the sake of clarity, we show a schematic representation of these three kinds of joint in Fig. 4.3.

The joint contributions in eq. (4.1.8) are affected by the arbitrariness of choosing the normalization of null normals $\mathbf{k}, \tilde{\mathbf{k}}$. Such an ambiguity can be partially removed by requiring that $\mathbf{k}\cdot\partial_t = \pm\alpha$ at the spacetime boundary [40, 113, 162], with ∂_t the timelike Killing vector in the boundary theory and α a positive constant. Still, the constant α can be arbitrarily chosen. For the gravitational action to be invariant under reparametrization, the counterterm

$$I_{ct} = \frac{1}{8\pi G} \int_{\mathcal{B}} dS\, d\lambda\, \sqrt{\gamma}\, \Theta\, \log \left| \tilde{L}\, \Theta \right| \tag{4.1.10}$$

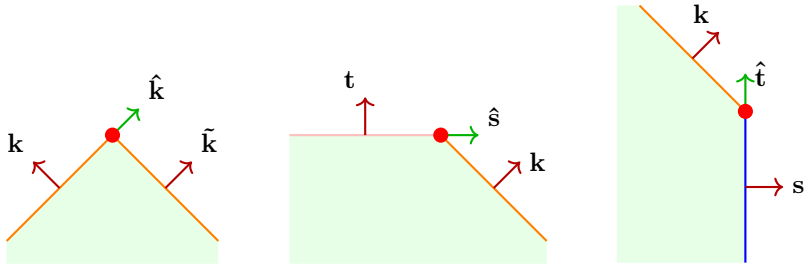

Figure 4.3: The three kinds of joints involving null boundaries, with explicit orientation of the normal one-forms and tangent vectors. Null surfaces are shown in orange, spacelike surfaces in pink, and timelike surfaces in blue.

must be added for each null boundary [157]. In the above expression, $\tilde{L}$ is an arbitrary length scale and $\Theta = \partial_\lambda \log \sqrt{\gamma}$ is the expansion scalar of the congruence of *null* geodesics on $\mathcal{B}$, defined similarly to eq. (3.5.4). Even though the surface term (4.1.10) has been found to not modify the complexity of formation and the late time complexity growth rate for eternal black holes, in such cases it does affect the intermediate time behavior [113]. In dynamical scenarios it is crucial to reproduce important features of complexity, such as the conjectured late time bound on the growth rate and the switchback effect [69, 70]. Therefore, we will always include the counterterm I_{ct} in our computations.

We point out that the counterterm ensuring reparametrization invariance of the action is not necessarily unique. To discuss this, we borrow some notation from [157]. Let us consider a null hypersurface $\mathcal{B}$ defined by the function $\Phi(x^\mu) = 0$. The hypersurface can be described by parametric equations $x^\mu(\lambda, \theta^A)$, where λ is an affine parameter of null geodesics and θ^A is constant on each null generator on the hypersurface. Both the vectors

$$k^\mu = \frac{\partial x^\mu}{\partial \lambda}\,, \qquad e^\mu_A = \frac{\partial x^\mu}{\partial \theta^A}\,, \tag{4.1.11}$$

are tangent to $\mathcal{B}$, while k_μ is the null normal to the hypersurface. We denote by

$$\gamma_{AB} = g_{\mu\nu} e^\mu_A e^\nu_B \tag{4.1.12}$$

the induced metric on the transverse directions θ_A and by

$$B_{AB} = e^\mu_A e^\nu_B \nabla_\mu k_\nu\,, \tag{4.1.13}$$

the tensor describing the behavior of the congruence of null generators, similarly to eq. (3.5.1). In principle, in presence of null boundaries we can add to the

integrand in eq. (4.1.10) any functional of combinations of the Riemann tensor $\hat{R}_{ABCD}$ computed from the transverse induced metric γ_{AB}, without spoiling the variational principle [157]. Moreover, terms containing the tensor B_{AB} are also allowed. Therefore, a priori we could have a counterterm of the type

$$\mathcal{L}_{\rm ct}(\hat{R}, \hat{R}_{AB}, \hat{R}_{ABCD}, B_{AB}, \Theta)\,, \tag{4.1.14}$$

chosen so that the gravitational action is invariant under diffeomorphisms. When computing the gravitational action in this thesis, we will always work in $(2+1)$-dimensional spacetimes. Consequently, the null hypersurface $\mathcal{B}$ is two-dimensional and the induced metric γ_{AB} is one-dimensional, which implies

$$\hat{R}_{ABCD} = 0\,, \qquad \hat{R}_{AB} = 0\,, \qquad \hat{R} = 0\,, \qquad B_{AB} = \frac{1}{2}\Theta\,\gamma_{AB}\,. \tag{4.1.15}$$

This leads to dramatic restrictions in the choice of the counterterm, leaving no space for curvature terms other than the geodesic expansion parameter Θ which we have already included in eq. (4.1.10).

4.2 Subregion complexity for a segment in AdS$_3$

As a warm-up, we review the AdS$_3$ calculation of subregion-CA for a boundary segment [35, 40, 163]. AdS$_3$ spacetime can be built as a solution of a gravity theory with negative cosmological constant, whose bulk action is given in eq. (4.1.2). As we have seen in Subsec. 2.1.1, the metric in Poincaré coordinates reads

$$ds^2 = \frac{L^2}{z^2}\left(-dt^2 + dz^2 + dx^2\right)\,, \tag{4.2.1}$$

with L the AdS length. In the holographic picture, this geometry is dual to a CFT$_2$ with central charge

$$c = \frac{3L}{2G}\,. \tag{4.2.2}$$

We take as a boundary subregion a strip of length l at the constant time-slice $t = 0$. Exploiting the translation invariance in the x-direction, it is not restrictive to consider a symmetric strip $x \in \left[-\frac{l}{2}, \frac{l}{2}\right]$. The relevant spacetime region in our computation is the intersection between the entanglement wedge [38] of the subregion and the WDW patch [15, 117] anchored at the boundary time-slice. The gravitational action diverges, so a regularization is required. This can be accomplished in two common ways [40], which are illustrated in Fig. 4.4:

- Regularization A: the WDW patch is anchored at the spacetime boundary $z = 0$ and a cutoff is then introduced at $z = \varepsilon$.

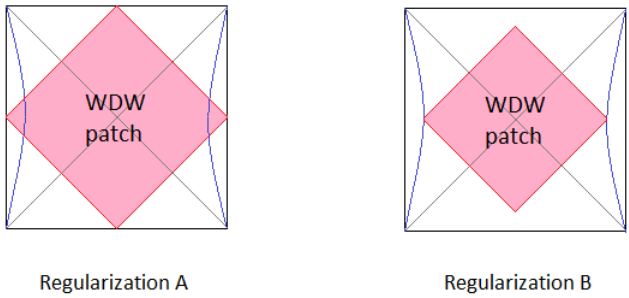

Figure 4.4: The two regularization choices commonly used in the (subregion-)CA conjecture. The Penrose diagram of an eternal two-sided AdS BH has been chosen for illustrative purposes.

- Regularization B: the WDW patch is anchored at the cutoff surface $z = \varepsilon$.

Throughout this thesis work, we will mostly use regularization B; a comparison with regularization A is discussed in Appendix B.1. Note that in regularization B the intersection points between the WDW patch, the entanglement wedge, and the cutoff $z = \varepsilon$ represent codimension-three joints (see Fig. 4.5), which we have not taken account of in eq. (4.1.1) but a priori can contribute to the gravitational action. In Appendix B.1 we will check that regularization A gives a similar result as regularization B without including such a contribution. Therefore, we believe that the codimension-three joint at most shifts the action of an overall constant.

We now build the spacetime region involved in subregion-CA conjecture. The RT surface [9] is given by the spacelike geodesic

$$t = 0\,, \qquad z^2 + x^2 = \left(\frac{l}{2}\right)^2\,, \tag{4.2.3}$$

which is a semicircle of radius $l/2$. It is convenient to parametrize the curve as

$$z_{\rm RT} = \sqrt{\left(\frac{l}{2}\right)^2 - x^2}\,. \tag{4.2.4}$$

The boundaries of the entanglement wedge are formed by null geodesics emanating orthogonally from each point of the RT surface in both the past and

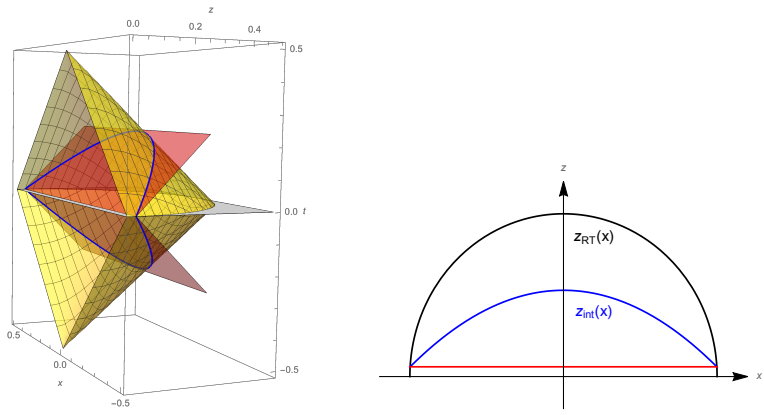

Figure 4.5: On the left: Intersection of the WDW patch with the entanglement wedge in the (x, z, t) space. The boundary of the entanglement wedge is in yellow, while the boundary of the WDW patch is in red. On the right: Joint curves projected in the (x, z) plane, with z_{RT} in black, z_{int} in blue and the cutoff $z = \varepsilon$ in red.

future directions. In AdS$_3$, such null geodesics meet at the past and future tips of the domain of dependence of the boundary subregion. The entanglement wedge is thus a cone, whose null boundaries are parametrized by

$$t_{\rm EW} = \pm\left(\frac{l}{2} - \sqrt{z^2 + x^2}\right) . \tag{4.2.5}$$

The null boundaries of the WDW patch, which is attached to the regulator surface, are instead described by

$$t_{\rm WDW} = \pm\,(z - \varepsilon) . \tag{4.2.6}$$

In the above expressions, the plus and minus sign applies to the future and past boundaries, respectively. The intersection curve between the entanglement wedge and the WDW patch boundaries is

$$z_{\rm int} = \frac{(l+2\varepsilon)^2 - 4x^2}{4(l+2\varepsilon)} \qquad \text{or} \qquad x_{\rm int} = \pm\frac{1}{2}\sqrt{(l+2\varepsilon)(l-4z+2\varepsilon)}\,. \tag{4.2.7}$$

The introduction of the UV cutoff ε restricts the range of allowed values for the x-coordinate over the relevant region to $-x_{\rm max} \le x \le x_{\rm max}$, where

$$x_{\rm max} = x_{\rm RT}(z = \varepsilon) = \sqrt{\left(\frac{l}{2}\right)^2 - \varepsilon^2}\,. \tag{4.2.8}$$

Having identified the region involved in subregion-CA proposal, in the next section we explicitly calculate the gravitational action (4.1.1). Note that our geometric construction is symmetric under the two reflections $t \to -t$ and $x \to -x$. Due to this amount of symmetry, we will restrict our investigation to the spacetime region $t \geq 0, x \geq 0$, and include the proper symmetry factors in the end.

4.2.1 Action computation

Referring to the analysis in Sec. 4.1, the gravitational action of the region shown in Fig. 4.5 has four main contributions:

$$I = I_{\mathcal{W}} + I_{\mathcal{N}} + I_{\mathcal{J}} + I_{ct}\,. \tag{4.2.9}$$

Bulk contribution. The scalar curvature of AdS_3 is constant, so the Einstein-Hilbert action (4.1.2) is proportional to the spacetime volume. As it is clear from the right Fig. 4.5, the bulk contribution can be split into two parts, separated by the joint curve $z_{int}(x)$ of eq. (4.2.7). The first region $\varepsilon \leq z \leq z_{int}(x)$ is delimited by the WDW patch null boundaries, so we have

$$\begin{aligned} I^1_{\mathcal{W}} &= -\frac{L}{4\pi G}\int_0^{x_{max}} dx \int_\varepsilon^{z_{int}} dz \int_0^{t_{WDW}} \frac{dt}{z^3} \\ &= -\frac{L}{16\pi G}\frac{l}{\varepsilon} - \frac{L}{4\pi G}\log\left(\frac{\varepsilon}{l}\right) - \frac{L}{8\pi G}\,. \end{aligned} \tag{4.2.10}$$

The second region $z_{\rm int}(x) \leq z \leq z_{\rm RT}(x)$ is instead delimited by the entanglement wedge null boundaries, thus

$$\begin{aligned} I^2_{\mathcal{W}} &= -\frac{L}{4\pi G}\int_0^{x_{max}} dx \int_{z_{int}}^{z_{RT}} dz \int_0^{t_{EW}} \frac{dt}{z^3} \\ &= \frac{L}{8\pi G}\log\left(\frac{\varepsilon}{l}\right) + \frac{L(\pi^2+8)}{64\pi G}\,. \end{aligned} \tag{4.2.11}$$

The total result of the bulk action is

$$I^{\rm AdS}_{\mathcal{W}} = 4(I^1_{\mathcal{W}} + I^2_{\mathcal{W}}) = -\frac{L}{4\pi G}\frac{l}{\varepsilon} + \frac{L}{2\pi G}\log\left(\frac{l}{\varepsilon}\right) + \frac{L\pi}{16G}\,. \tag{4.2.12}$$

Null boundary terms. A hypersurface $\mathcal{B}$ described by the scalar equation $\Phi(x^a) = 0$ has a normal vector $k_\mu = -\partial_\mu \Phi$. In case $\mathcal{B}$ is null, $k_\mu k^\mu = 0$ and the vector is also tangent to the hypersurface. In particular, it can be shown [135]

that $\mathcal{B}$ is generated by null geodesics which have k^μ as a tangent vector. In our case, the null normals to the WDW patch and entanglement wedge boundaries are given by the following 1-forms

$$\mathbf{k}^\pm = \alpha\,(\pm dt - dz)\,, \qquad \mathbf{w}^\pm = \beta\left(\pm dt + \frac{z dz}{\sqrt{z^2+x^2}} + \frac{x dx}{\sqrt{z^2+x^2}}\right), \quad (4.2.13)$$

where $\alpha, \beta > 0$ are arbitrary constants that will not affect the final result. Denoting by $(k^\pm)^\mu$ and $(w^\pm)^\mu$ the corresponding null vectors, it can be checked that they satisfy the geodesic equations

$$(k^\pm)^\mu \nabla_\mu (k^\pm)^\nu = 0\,, \qquad (w^\pm)^\mu \nabla_\mu (w^\pm)^\nu = 0\,, \quad (4.2.14)$$

meaning that the null surfaces are affinely parametrized. Consequently, the null surfaces contributions (4.1.6) vanish: $I_{\mathcal{N}} = 0$.

Choosing an affine parametrization for the null generators also allows us to express the scalar expansion of the congruence as [135]

$$\Theta = \nabla_\mu k^\mu\,. \quad (4.2.15)$$

Thus, we can readily evaluate the counterterm (4.1.10) on each null boundary:

- In agreement with the calculations in [38], the counterterm on the entanglement wedge boundary vanishes because $\Theta = 0$.
- For the boundary of the WDW patch, we obtain

$$\begin{aligned} I_{\rm ct}^{\rm WDW} &= -\frac{L}{2\pi G}\int_0^{x_{\max}} dx \int_\varepsilon^{z_{\rm int}} \frac{dz}{z^2}\log\left|\alpha\frac{\tilde{L}z}{L^2}\right| \\ &= \frac{L}{4\pi G}\frac{l}{\varepsilon}\left[1+\log\left(\alpha\frac{\tilde{L}\varepsilon}{L^2}\right)\right] + \frac{L}{4\pi G}\log\left(\frac{\varepsilon}{l}\right)\log\left(\alpha^2\frac{\varepsilon l\tilde{L}^2}{L^4}\right) \\ &\quad + \frac{L}{2\pi G}\log\left(\frac{\varepsilon}{l}\right) + \frac{L\pi}{12G}\,. \end{aligned} \quad (4.2.16)$$

Joint terms. In the spacetime region $t \geq 0, x \geq 0$ under consideration there are three joint contributions (4.1.8), all coming from the intersection between two null codimension-one surfaces:

- The first joint is at the cutoff $z = \varepsilon$, where the future and past boundaries of the WDW patch meet. We have

$$\sqrt{\sigma} = \frac{L}{\varepsilon}\,, \qquad \log\left|\frac{\mathbf{k}^-\cdot\mathbf{k}^+}{2}\right| = \log\left|\alpha^2\frac{\varepsilon^2}{L^2}\right|, \quad (4.2.17)$$

so from the general expression (4.1.8)

$$I_{\mathcal{J}}^{\text{cutoff}} = -\frac{L}{8\pi G}\frac{l}{\varepsilon}\log\left(\alpha\frac{\varepsilon}{L}\right). \tag{4.2.18}$$

- The second joint is at the RT surface, where the future and past boundaries of the entanglement wedge intersect. Here we obtain

$$\sqrt{\sigma} = \frac{2lL}{l^2-4x^2}, \qquad \log\left|\frac{\mathbf{w}^+\cdot\mathbf{w}^-}{2}\right| = \log\left|\beta^2\frac{l^2-4x^2}{4L^2}\right|, \tag{4.2.19}$$

  which give

$$I_{\mathcal{J}}^{\text{RT}} = \frac{L}{8\pi G}\log\left(\frac{\varepsilon}{l}\right)\log\left(\frac{\beta^2\varepsilon l}{L^2}\right) + \frac{\pi L}{96G}. \tag{4.2.20}$$

- The last joint term comes from the intersection between the future boundaries of the WDW patch and entanglement wedge, where

$$\sqrt{\sigma} = \frac{4L(l+2\varepsilon)}{(l-2x+2\varepsilon)(l+2x+2\varepsilon)}, \tag{4.2.21}$$

$$\log\left|\frac{\mathbf{k}^+\cdot\mathbf{w}^+}{2}\right| = \log\left|\frac{\alpha\beta(l-2x+2\varepsilon)^2(l+2x+2\varepsilon)^2}{16L^2(4x^2+(l+2\varepsilon)^2)}\right|. \tag{4.2.22}$$

  Therefore, the joint evaluates to

$$I_{\mathcal{J}}^{\text{int}} = -\frac{L}{8\pi G}\log\left(\frac{\varepsilon}{l}\right)\log\left(\frac{\alpha\beta}{2}\frac{\varepsilon l}{L^2}\right) - \frac{5\pi L}{192G}. \tag{4.2.23}$$

Summing up all the joint contributions, we get

$$\begin{aligned} I_{\mathcal{J}}^{\text{tot}} &= 2(I_{\mathcal{J}}^{\text{cutoff}} + I_{\mathcal{J}}^{\text{RT}}) + 4I_{\mathcal{J}}^{\text{int}} \\ &= -\frac{L}{4\pi G}\frac{l}{\varepsilon}\log\left(\alpha\frac{\varepsilon}{L}\right) + \frac{L}{4\pi G}\log\left(\frac{\varepsilon}{l}\right)\log\left(\frac{4L^2}{\alpha^2\varepsilon l}\right) - \frac{\pi L}{12G}. \end{aligned} \tag{4.2.24}$$

As expected, this result is independent of the normalization constant β of the null generators $\mathbf{w}^{\pm}$. Indeed, no counterterm is required to remove the arbitrariness in choosing β, in agreement with the vanishing of the expansion scalar Θ of the corresponding null surfaces. Also, when summing the joint term (4.2.24) with the counterterm contribution (4.2.16) the dependence on α cancels.

4.2.2 Complexities

By adding all the contributions, subregion action complexity is

$$\mathcal{SC}_A^{\text{AdS}} = \frac{I_{\text{tot}}^{\text{AdS}}}{\pi} = \frac{c}{3\pi^2}\left\{\frac{l}{2\varepsilon}\log\left(\frac{\tilde{L}}{L}\right) - \log\left(\frac{2\tilde{L}}{L}\right)\log\left(\frac{l}{\varepsilon}\right) + \frac{\pi^2}{8}\right\}. \quad (4.2.25)$$

Instead, from eq. (4.2.12) spacetime volume complexity is

$$\mathcal{SC}_{V2.0}^{\text{AdS}} = \frac{2}{3}c\left\{\frac{l}{\varepsilon} - 2\log\left(\frac{l}{\varepsilon}\right) - \frac{\pi^2}{4}\right\}. \quad (4.2.26)$$

Such results are in agreement with [35]. In both expressions, we recognize a term proportional to the entanglement entropy of the segment

$$S^{\text{AdS}} = \frac{c}{3}\log\left(\frac{l}{\varepsilon}\right). \quad (4.2.27)$$

We conclude that holographic subregion complexity for a single interval has a leading divergence proportional to the segment length, a subleading divergence proportional to the entanglement entropy, and a constant finite piece. In the following section, we check whether this expression also holds in the BTZ case.

4.3 Subregion complexity for a segment in the BTZ black hole

Likewise AdS_3 spacetime, the BTZ black hole is a solution of gravity in $2+1$ dimensions with bulk action (4.1.2). The metric of the planar BTZ BH with non-compact coordinates (t, z, x) is [41, 42]

$$ds^2 = \frac{L^2}{z^2}\left(-f dt^2 + \frac{dz^2}{f} + dx^2\right), \qquad f = 1 - \left(\frac{z}{z_h}\right)^2, \quad (4.3.1)$$

where L denotes the AdS radius and z_h the (inverse) radius of the event horizon. The mass per unit volume, the temperature, and the entropy density are

$$M = \frac{L^2}{16\pi G z_h^2}, \qquad T = \frac{1}{2\pi z_h}, \qquad S_{BH} = \frac{L^2}{4G z_h}, \quad (4.3.2)$$

respectively. In Fig. 4.6 we show the geometric construction to be considered for the estimation of subregion action complexity for a symmetric boundary strip $x \in \left[-\frac{l}{2}, \frac{l}{2}\right]$ lying at $t = 0$.

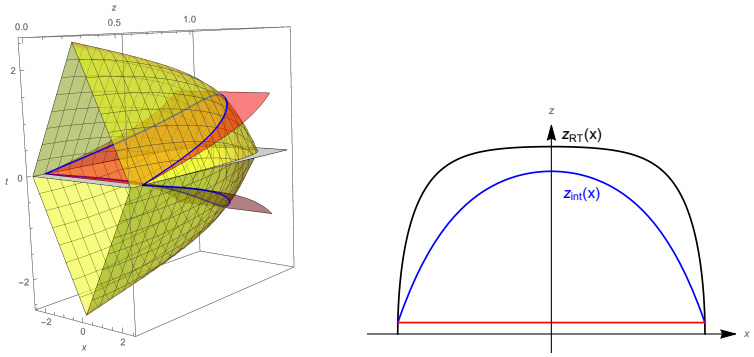

Figure 4.6: Region relevant to the action computation for a segment in the BTZ case, with $l = 5$. On the left: Intersection between the WDW patch and entanglement wedge in the (x, z, t) space. The boundary of the entanglement wedge is in yellow, while the boundary of the WDW patch is in red. On the right: Intersection curves in the (x, z) plane, with z_{RT} in black, z_{int} in blue and the cutoff $z = \varepsilon$ in red.

The RT surface is a spacelike geodesic on the constant time slice $t = 0$ anchored at the edges of the boundary subregion [75]:

$$x_{\pm} = \frac{z_h}{4}\left[\log\left(\frac{J+1}{J-1}\right)^2 + \log\left(\frac{z_h^2 - Jz^2 \pm \sqrt{z_h^4 - (1+J^2)\,z_h^2 z^2 + J^2 z^4}}{z_h^2 + Jz^2 \pm \sqrt{z_h^4 - (1+J^2)\,z_h^2 z^2 + J^2 z^4}}\right)^2\right], \tag{4.3.3}$$

where

$$J = \coth\left(\frac{l}{2z_h}\right). \tag{4.3.4}$$

The geodesic turning point is at $x_{\pm}(z_*) = 0$, with

$$z_* = z_h \tanh\left(\frac{l}{2z_h}\right). \tag{4.3.5}$$

Since $z_* < z_h$ for every value of the segment length l, the geodesic never crosses the BH event horizon. So, contrary to holographic complexity, subregion complexity is not a good candidate to probe the BH interior, at least in the static case. We will see in Ch. 6 that in dynamical backgrounds the HRT surface does explore the BH interior [75].

For later purposes, it is convenient to invert eq. (4.3.3), getting

$$z_{RT} = z_h \sqrt{\frac{\cosh\left(\frac{l}{z_h}\right) - \cosh\left(\frac{2x}{z_h}\right)}{\cosh\left(\frac{l}{z_h}\right) + 1}} \,. \tag{4.3.6}$$

In our static case, the entanglement wedge coincides with the causal wedge [164–166], which can be constructed by sending null geodesics from the boundary causal diamond of the subregion into the bulk. The explicit expressions of such geodesics are [165]

$$\begin{aligned} \tilde{x}_{\rm EW}(z,j) &= \frac{z_h}{2} \log\left(\frac{\sqrt{z_h^2 + j^2(z^2 - z_h^2)} + jz}{\sqrt{z_h^2 + j^2(z^2 - z_h^2)} - jz}\right) , \\ \tilde{t}_{\rm EW}(z,j) &= \pm\left[\frac{l}{2} + \frac{z_h}{2} \log\left(\frac{\sqrt{z_h^2 + j^2(z^2 - z_h^2)} - z}{\sqrt{z_h^2 + j^2(z^2 - z_h^2)} + z}\right)\right] . \end{aligned} \tag{4.3.7}$$

Solving the first eq. (4.3.7) for $j = j(z,x)$ and plugging the result into the second equation, we get the closed-form expression for the entanglement wedge boundary:

$$t_{\rm EW} = \pm\left[\frac{l}{2} - z_h \,\mathrm{arccoth}\left(\frac{\sqrt{2} z_h \cosh\left(\frac{x}{z_h}\right)}{\sqrt{2z^2 + z_h^2 \cosh\left(\frac{2x}{z_h}\right) - z_h^2}}\right)\right] . \tag{4.3.8}$$

On the other hand, the WDW patch is bounded by the radial null geodesics

$$t_{\rm WDW} = \pm\frac{z_h}{4} \log\left(\frac{z_h + z}{z_h - z}\frac{z_h - \varepsilon}{z_h + \varepsilon}\right)^2 . \tag{4.3.9}$$

The intersection between the WDW patch and entanglement wedge boundaries is thus

$$t_{\rm int} = t_{\rm WDW} \,, \qquad z_{\rm int} = z_h \frac{\cosh\left[\frac{l}{2z_h} + \mathrm{arctanh}\left(\frac{\varepsilon}{z_h}\right)\right] - \cosh\left(\frac{x}{z_h}\right)}{\sinh\left[\frac{l}{2z_h} + \mathrm{arctanh}\left(\frac{\varepsilon}{z_h}\right)\right]} . \tag{4.3.10}$$

The resulting spacetime region is located at $-x_{\rm max} \leq x \leq x_{\rm max}$, with

$$x_{\rm max} = x_+(z = \varepsilon) = z_h \,\mathrm{arccosh}\left[\sqrt{1 - \frac{\varepsilon^2}{z_h^2}} \cosh\left(\frac{l}{2z_h}\right)\right] . \tag{4.3.11}$$

We can now move to the computation of the gravitational action, focusing on the $t \geq 0, x \geq 0$ region.

4.3.1 Action computation

The gravitational action of the region in Fig. 4.6 has four main contributions:

$$I = I_{\mathcal{W}} + I_{\mathcal{N}} + I_{\mathcal{J}} + I_{ct}\,. \tag{4.3.12}$$

Bulk contribution. As in the AdS case, we split the integration region into two parts, separated by the intersection curve (4.3.10). In analogy with the first line of eqs. (4.2.10) and (4.2.11), the total bulk action is then $I^{\rm BTZ}_{\mathcal{W}} = 4(I^1_{\mathcal{W}} + I^2_{\mathcal{W}})$, that leads to

$$I^{\rm BTZ}_{\mathcal{W}} = \frac{L}{8\pi G z_h}\int_0^{x_{\max}} dx\left\{\frac{4\sinh\left[\frac{l}{2z_h}+\operatorname{arctanh}\left(\frac{\varepsilon}{z_h}\right)\right]}{\cosh\left(\frac{l}{2z_h}+\operatorname{arctanh}\left(\frac{\varepsilon}{z_h}\right)\right)-\cosh\left(\frac{x}{z_h}\right)}-\frac{4z_h}{\varepsilon}\right.$$
$$\left.+2\coth\left(\frac{x}{z_h}\right)\log\left|\frac{\sinh\left(\frac{l-2x}{2z_h}\right)\sinh^2\left[\frac{l+2x+2z_h\,\operatorname{arctanh}(\varepsilon/z_h)}{4z_h}\right]}{\sinh\left(\frac{l+2x}{2z_h}\right)\sinh^2\left[\frac{l-2x+2z_h\,\operatorname{arctanh}(\varepsilon/z_h)}{4z_h}\right]}\right|\right\}. \tag{4.3.13}$$

The integral can be analytically solved, giving

$$I^{\rm BTZ}_{\mathcal{W}} = -\frac{L}{4\pi G}\frac{l}{\varepsilon}+\frac{L}{2\pi G}\log\left(\frac{2z_h}{\varepsilon}\sinh\left(\frac{l}{2z_h}\right)\right)+\frac{\pi L}{16G}\,. \tag{4.3.14}$$

Null boundary terms. Prior to computing the remaining contributions, we need to determine the null normals to the bounding surfaces. To this purpose, we employ an affine parametrization, which can be found by describing geodesics through the Lagrangian

$$\mathcal{L} = \frac{L^2}{z^2}\left(-f(z)\,\dot{t}^2+\frac{\dot{z}^2}{f(z)}+\dot{x}^2\right), \tag{4.3.15}$$

in which the dot represents a derivative with respect to the affine parameter λ. Since the Lagrangian is independent of t and x, there are two motion constants:

$$E = -\frac{1}{2}\frac{\partial\mathcal{L}}{\partial\dot{t}} = \frac{L^2}{z^2}f(z)\,\dot{t}\,, \qquad J = \frac{1}{2}\frac{\partial\mathcal{L}}{\partial\dot{x}} = \frac{L^2}{z^2}\dot{x}\,. \tag{4.3.16}$$

Also imposing the null condition $\mathcal{L}=0$, we get

$$\dot{z} = \pm\frac{z^2}{L^2}\sqrt{E^2-J^2f(z)}\,. \tag{4.3.17}$$

From eqs. (4.3.16) and (4.3.17), the tangent vector to the null geodesic is

$$V^\mu = (\dot{t},\,\dot{z},\,\dot{x}) = \left(\frac{z^2}{L^2 f(z)}E,\,\pm\frac{z^2}{L^2}\sqrt{E^2-J^2f(z)},\,\frac{z^2}{L^2}J\right). \tag{4.3.18}$$

Lowering the index, we get the normal one-form to the null geodesic

$$\mathbf{V} = V_\mu dx^\mu = -E\,dt \pm \frac{\sqrt{E^2 - J^2 f(z)}}{f(z)}\,dz + J\,dx\,. \tag{4.3.19}$$

The null geodesics bounding the WDW patch are x-constant curves, so they are characterized by $J = 0$. This gives the normals

$$\mathbf{k}^\pm = k^\pm_\mu dx^\mu = \alpha\left(\pm dt - \frac{dz}{f(z)}\right)\,, \tag{4.3.20}$$

where α is an arbitrary positive constant.
On the other hand, the null geodesics bounding the entanglement wedge are normal to the RT surface, i.e.

$$V_\mu \frac{dX^\mu_{RT}(x)}{dx} = 0\,, \qquad X^\mu_{\rm RT}(x) = (0, z_{RT},\, x)\,, \tag{4.3.21}$$

with z_{RT} given in eq. (4.3.6). Combining such a condition with eq. (4.3.19), we find a relation between E and J, which fixes

$$\mathbf{w}^\pm = w^\pm_\mu dx^\mu = \beta\,(\pm dt + a\,dz + b\,dx)\,, \tag{4.3.22}$$

where β is again a positive constant and

$$a = \frac{z\,z_h^2 \cosh\left(\frac{x}{z_h}\right)}{(z_h^2 - z^2)\sqrt{z^2 + z_h^2 \sinh^2\left(\frac{x}{z_h}\right)}}\,, \qquad b = \frac{z\,z_h^2 \sinh\left(\frac{x}{z_h}\right)}{(z_h^2 - z^2)\sqrt{z^2 + z_h^2 \sinh^2\left(\frac{x}{z_h}\right)}}\,. \tag{4.3.23}$$

We are now ready to consider the null surface contributions to the action.
The term in eq. (4.1.6) vanishes because we used an affine parametrization: $I_{\mathcal{N}} = 0$. The counterterm in eq. (4.1.10) comes from two kind of boundaries:

- On the entanglement wedge, since the expansion scalar $\Theta = \nabla_\mu (w^\pm)^\mu$ vanishes, we have $I^{\rm EW}_{ct} = 0$.

- On the WDW patch, a direct calculation gives

$$\begin{aligned} I_{\text{ct}}^{\text{WDW}} &= -\frac{L}{2\pi G}\int_0^{x_{\max}} dx \int_\varepsilon^{z_{\text{int}}} \frac{dz}{z^2}\log\left|\frac{\tilde{L}}{L^2}\,\alpha z\right| \\ &= \frac{L}{2\pi G}\left(1+\log\left|\frac{\tilde{L}}{L^2}\,\alpha\varepsilon\right|\right)\frac{x_{\max}}{\varepsilon} \\ &+ \frac{L}{2\pi G}\int_0^{x_{\max}} dx\,\frac{\sinh\left(\frac{l}{2z_h}+\operatorname{arctanh}\left(\frac{\varepsilon}{z_h}\right)\right)}{z_h\left[\cosh\left(\frac{x}{z_h}\right)-\cosh\left(\frac{l}{2z_h}\right)+\operatorname{arctanh}\left(\frac{\varepsilon}{z_h}\right)\right]}\times \\ &\times\left(1+\log\left|\frac{\tilde{L}z_h\alpha}{L^2}\,\frac{\cosh\left(\frac{l}{2z_h}+\operatorname{arctanh}\left(\frac{\varepsilon}{z_h}\right)\right)-\cosh\left(\frac{x}{z_h}\right)}{\cosh\left(\frac{l}{2z_h}+\operatorname{arctanh}\left(\frac{\varepsilon}{z_h}\right)\right)}\right|\right). \end{aligned} \tag{4.3.24}$$

Joint contributions. In the spacetime region $t \geq 0, x \geq 0$, there are three null-null intersection curves contributing to the joint term of eq. (4.1.8):

- The joint at the cutoff, given by the intersection between the future and past boundaries of the WDW patch, is

$$I_{\mathcal{J}}^{\text{cutoff}} = -\frac{L}{8\pi G}\int_0^{x_{\max}}\frac{dx}{\varepsilon}\log\left|\frac{\alpha^2 z_h^2\,\varepsilon^2}{L^2(z_h^2-\varepsilon^2)}\right|. \tag{4.3.25}$$

- The joint at the RT surface, lying at the intersection between the future and past boundaries of the entanglement wedge, is

$$\begin{aligned} I_{\mathcal{J}}^{\text{RT}} = -\frac{L}{8\pi G z_h}\int_0^{x_{\max}} dx\,&\frac{\sinh\left(\frac{l}{z_h}\right)}{\cosh\left(\frac{l}{z_h}\right)-\cosh\left(\frac{2x}{z_h}\right)}\times \\ &\times\log\left|\frac{\beta^2 z_h^2}{2L^2}\,\frac{\cosh\left(\frac{l}{z_h}\right)-\cosh\left(\frac{2x}{z_h}\right)}{\cosh^2\left(\frac{x}{z_h}\right)}\right|. \end{aligned} \tag{4.3.26}$$

- The joint at the intersection (4.3.10) between the future null boundaries of the WDW patch and entanglement wedge gives

$$I_{\mathcal{J}}^{\text{int}} = \frac{L}{8\pi G z_h}\int_0^{x_{\max}} dx\, \frac{\sinh\left(\frac{l}{2z_h}+\operatorname{arctanh}\left(\frac{\varepsilon}{z_h}\right)\right)}{\cosh\left(\frac{l}{2z_h}+\operatorname{arctanh}\left(\frac{\varepsilon}{z_h}\right)\right)-\cosh\left(\frac{x}{z_h}\right)}\times$$
$$\times\log\left|\frac{e^{x/z_h}\alpha\beta z_h^2}{L^2}\,\frac{\left[\cosh\left(\frac{l}{2z_h}+\operatorname{arctanh}\left(\frac{\varepsilon}{z_h}\right)\right)-\cosh\left(\frac{x}{z_h}\right)\right]^2}{1+e^{2x/z_h}\cosh\left(\frac{l}{2z_h}+\operatorname{arctanh}\left(\frac{\varepsilon}{z_h}\right)\right)-2e^{x/z_h}}\right|. \tag{4.3.27}$$

Adding up all the above expressions, we find the total joint contribution

$$I_{\mathcal{J}}^{\text{tot}} = 2(I_{\mathcal{J}}^{\text{cutoff}} + I_{\mathcal{J}}^{\text{RT}}) + 4I_{\mathcal{J}}^{\text{int}}\,. \tag{4.3.28}$$

4.3.2 Complexities

We have analytically solved all the above-mentioned integrals, the cumbersome results of which we do not write down here. In order to simplify the expressions, we have made use of various dilogarithm identities, including

$$8\,\text{Re}\left[\text{Li}_2\left(\frac{1+ie^{\frac{y}{2}}}{1+e^{\frac{y}{2}}}\right)-\text{Li}_2\left(\frac{1}{1+e^{\frac{y}{2}}}\right)-\text{Li}_2\left(1+ie^{\frac{y}{2}}\right)-\text{Li}_2\left(\frac{e^{\frac{y}{2}}-i}{1+e^{\frac{y}{2}}}\right)\right]$$
$$=-\frac{7\pi^2}{6}+4\log^2\left(1+e^{\frac{y}{2}}\right)+\log\left[4y-8\log\left(\frac{e^y-1}{y}\right)+8\log\left(\frac{2}{y}\sinh\frac{y}{2}\right)\right], \tag{4.3.29}$$

which can be proven by taking a derivative of both sides of the equation with respect to y. Subregion action complexity for a boundary line segment is then

$$\mathcal{SC}_A^{\text{BTZ}} = \frac{c}{3\pi^2}\left\{\frac{l}{2\varepsilon}\log\left(\frac{\tilde{L}}{L}\right)-\log\left(\frac{2\tilde{L}}{L}\right)\log\left(\frac{2z_h}{\varepsilon}\sinh\left(\frac{l}{2z_h}\right)\right)+\frac{\pi^2}{8}\right\}. \tag{4.3.30}$$

Introducing the entanglement entropy for the line segment

$$S^{\text{BTZ}} = \frac{c}{3}\log\left(\frac{2z_h}{\varepsilon}\sinh\left(\frac{l}{2z_h}\right)\right), \tag{4.3.31}$$

we can express subregion action complexity as

$$\mathcal{SC}_A^{\text{BTZ}} = \frac{c}{6\pi^2}\frac{l}{\varepsilon}\log\left(\frac{\tilde{L}}{L}\right)-\log\left(\frac{2\tilde{L}}{L}\right)\frac{S^{\text{BTZ}}}{\pi^2}+\frac{c}{24}\,. \tag{4.3.32}$$

From the bulk contribution to the gravitational action in eq. (4.3.14), we deduce that subregion spacetime volume complexity for a boundary line segment is

$$\mathcal{SC}_{V2.0}^{\mathrm{BTZ}} = \frac{2c}{3}\frac{l}{\varepsilon} - 4S^{\mathrm{BTZ}} - \frac{\pi^2}{6}c\,. \tag{4.3.33}$$

Note that eqs. (4.3.32) and (4.3.33) have the same structure as eqs. (4.2.25) and (4.2.26) of the AdS case, which is recovered for $z_h \to +\infty$.

A useful cross-check can be done in the large subregion limit $l \gg z_h$. Keeping just the terms linear in l in eq. (4.3.30), the expression reproduces subregion action complexity $\mathcal{SC}_A^{\mathrm{BTZ,R}}$ computed for one side of the Kruskal diagram [34, 149]:

$$\mathcal{SC}_A^{\mathrm{BTZ,R}} = \frac{c}{6}\frac{l}{\pi^2}\left[\frac{1}{\varepsilon}\log\left(\frac{\tilde{L}}{L}\right) - \frac{1}{z_h}\log\left(\frac{2\tilde{L}}{L}\right)\right]. \tag{4.3.34}$$

Note that the $\log\varepsilon$ divergence is suppressed by the segment length l.

Subregion volume complexity of a boundary segment for the BTZ BH has been computed in [39, 147]:

$$\mathcal{SC}_V^{\mathrm{BTZ}} = \frac{2\,c}{3}\left(\frac{l}{\varepsilon} - \pi\right), \tag{4.3.35}$$

which is non-trivially independent of temperature. Indeed, subregion $\mathcal{SC}_V$ in BTZ is a topological quantity: for multiple intervals, the authors of [147] found the following result by means of the Gauss-Bonnet theorem

$$\mathcal{SC}_V^{\mathrm{AdS}} = \mathcal{SC}_V^{\mathrm{BTZ}} = \frac{2\,c}{3}\left(\frac{l_{tot}}{\varepsilon} - 2\pi\chi + \frac{\pi}{2}\,m\right). \tag{4.3.36}$$

In this formula, l_{tot} is the total length of the boundary segments, χ is the Euler characteristic of the extremal codimension-one surface involved in subregion-CV, and m is the number of ninety degrees junctions between the RT surface and the boundary segments themselves. It would be interesting to check whether a similar result could be established for subregion-CA and subregion-CV 2.0 for multiple line segments. This motivates us to study the simplest case of two segments in AdS$_3$.

4.4 Subregion complexity for two segments in AdS$_3$

In this section we evaluate subregion action complexity for a disjoint subregion on the AdS$_3$ boundary. In particular, we consider two segments of equal size l with separation d, lying at the constant time slice $t = 0$. For simplicity, we take a symmetric configuration, with the boundary subregion given by

$x \in [-l - d/2, -d/2] \cup [d/2, l + d/2]$. The holographic entanglement entropy is the length of the shortest geodesic anchored at the edges of the subregion. There are two possibilities [81, 90]:

- The minimal geodesic is the union of the RT surfaces for the individual disjoint segments.
- The minimal geodesic connects the two disjoint segments.

The two cases are shown in Fig. 4.7:

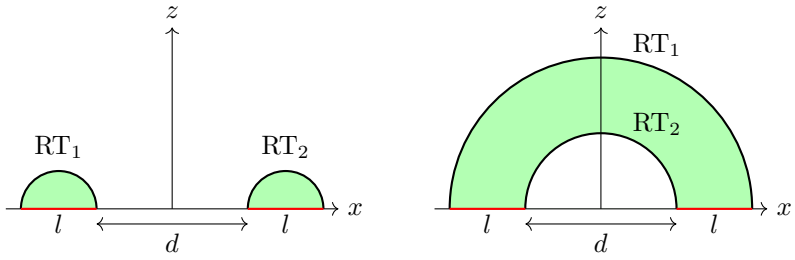

Figure 4.7: The possible RT surfaces for disjoint subregions.

For fixed segments length l, a critical distance d_0 exists for which the two curves have the same length, namely

$$d_0 = (\sqrt{2} - 1)l\,. \tag{4.4.1}$$

For $d > d_0$ the locally minimizing geodesic is given by the configuration in the left Fig. 4.7, whereas for $d < d_0$ by the right one.

For the first configuration we have two non-intersecting entanglement wedges, so

$$\mathcal{SC}^1_A = 2\,\mathcal{SC}^{\text{AdS}}_A\,, \qquad \mathcal{SC}^1_{V2.0} = 2\,\mathcal{SC}^{\text{AdS}}_{V2.0}\,. \tag{4.4.2}$$

For the second configuration a new geometric construction is required, a schematic representation of which is shown in Fig. 4.8. Similarly to the previous calculations, we make use of regularization B (see Fig. 4.4).

As we have seen above, the RT surface is the union of the spacelike geodesics connecting the two boundary segments. Denoting such geodesics by RT$_1$ and RT$_2$, we have

$$z_{RT_1} = \sqrt{\left(\frac{2l+d}{2}\right)^2 - x^2}\,, \qquad z_{RT_2} = \sqrt{\left(\frac{d}{2}\right)^2 - x^2}\,, \tag{4.4.3}$$

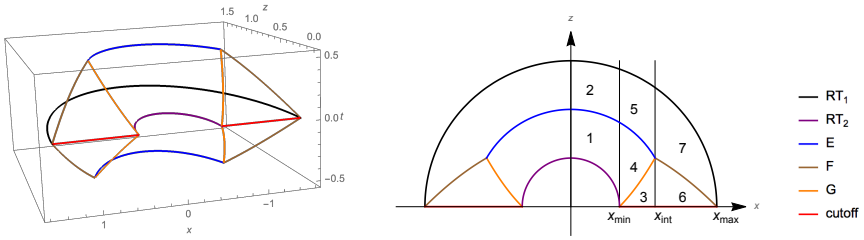

Figure 4.8: On the left: Bulk region relevant to the subregion-CA calculation for two segments in AdS$_3$. On the right: Projection in the (x, z) plane of the codimension-two intersection curves. The regions in which the bulk integral is split are numbered.

respectively. Due to the introduction of the cutoff surface at $z = \varepsilon$, RT$_2$ is truncated at $x = \pm x_{min}$ and RT$_1$ at $x = \pm x_{max}$, which are defined by

$$x_{min} = \sqrt{\left(\frac{d}{2}\right)^2 - \varepsilon^2}\,, \qquad x_{max} = \sqrt{\left(\frac{d+2l}{2}\right)^2 - \varepsilon^2}\,. \tag{4.4.4}$$

All points of the entanglement wedge are causally connected to the RT surface RT$_1 \cup$ RT$_2$ and to the boundary domain of dependence of the subregion [38]. Therefore, the null boundaries of the entanglement wedge, built by sending null geodesics from RT$_1$ and RT$_2$, are

$$t_{EW_1} = \pm\left(\frac{2l+d}{2} - \sqrt{z^2+x^2}\right)\,, \qquad t_{EW_2} = \pm\left(-\frac{d}{2} + \sqrt{z^2+x^2}\right)\,. \tag{4.4.5}$$

The WDW patch, anchored at the cutoff in the present regularization, is bounded by the usual null surfaces

$$t_{WDW} = \pm\,(z - \varepsilon)\,. \tag{4.4.6}$$

Since the resulting spacetime region is symmetric under $t \to -t$ and $x \to -x$, hereinafter we focus on the region $t \geq 0, x \geq 0$. The intersection curve E between the future boundaries of the entanglement wedge (4.4.5) is

$$t_E = \frac{l}{2}\,, \qquad z_E = \frac{1}{2}\sqrt{(d+l)^2 - 4x^2}\,. \tag{4.4.7}$$

The intersection F between the future boundary of the WDW patch (4.4.6) and the future boundary of the entanglement wedge anchored at RT$_1$ is

$$t_F = \frac{1}{4}\left[d + 2\,(l-\varepsilon) - \frac{4x^2}{d + 2\,(l+\varepsilon)}\right]\,, \qquad z_F = t_F + \varepsilon\,. \tag{4.4.8}$$

The intersection G between the future boundary of the WDW patch and the future boundary of the entanglement wedge anchored at RT_2 gives

$$t_G = -\frac{d}{4} + \frac{x^2}{d-2\varepsilon} - \frac{\varepsilon}{2}\,, \qquad z_G = t_G + \varepsilon\,. \tag{4.4.9}$$

Solving the condition $z_E = z_F = z_G$, we find the intersection point among such three curves:

$$x_{int} = \frac{\sqrt{(d-2\varepsilon)\,[d+2\,(l+\varepsilon)]}}{2}\,. \tag{4.4.10}$$

4.4.1 Action computation

The gravitational action of the region in Fig. 4.8 can be computed as

$$I = I_{\mathcal{W}} + I_{\mathcal{N}} + I_{\mathcal{J}} + I_{ct}\,. \tag{4.4.11}$$

Bulk contribution. As shown in Fig. 4.8, the total bulk contribution can be divided into 7 parts:

$$I_{\mathcal{W}} = 4\sum_{i=1}^{7} I^i_{\mathcal{W}}\,, \tag{4.4.12}$$

where

$$\begin{aligned}
I^1_{\mathcal{W}} &= -\frac{L}{4\pi G}\int_0^{x_{min}} dx \int_{z_{RT_2}}^{z_E} dz \int_0^{t_{EW_2}} \frac{dt}{z^3}\,,\\
I^2_{\mathcal{W}} &= -\frac{L}{4\pi G}\int_0^{x_{min}} dx \int_{z_E}^{z_{RT_1}} dz \int_0^{t_{EW_1}} \frac{dt}{z^3}\,,\\
I^3_{\mathcal{W}} &= -\frac{L}{4\pi G}\int_{x_{min}}^{x_{int}} dx \int_{\varepsilon}^{z_G} dz \int_0^{t_{WDW}} \frac{dt}{z^3}\,,\\
I^4_{\mathcal{W}} &= -\frac{L}{4\pi G}\int_{x_{min}}^{x_{int}} dx \int_{z_G}^{z_E} dz \int_0^{t_{EW_2}} \frac{dt}{z^3}\,,\\
I^5_{\mathcal{W}} &= -\frac{L}{4\pi G}\int_{x_{min}}^{x_{int}} dx \int_{z_E}^{z_{RT_1}} dz \int_0^{t_{EW_1}} \frac{dt}{z^3}\,,\\
I^6_{\mathcal{W}} &= -\frac{L}{4\pi G}\int_{x_{int}}^{x_{max}} dx \int_{\varepsilon}^{z_F} dz \int_0^{t_{WDW}} \frac{dt}{z^3}\,,\\
I^7_{\mathcal{W}} &= -\frac{L}{4\pi G}\int_{x_{int}}^{x_{max}} dx \int_{z_F}^{z_{RT_1}} dz \int_0^{t_{EW_1}} \frac{dt}{z^3}\,.
\end{aligned} \tag{4.4.13}$$

Evaluating analytically all the integrals and summing them up, we obtain

$$I_{\mathcal{W}} = -\frac{L}{4\pi G}\left\{\frac{2l}{\varepsilon} - 2\log\frac{d(d+2l)}{\varepsilon^2} + \frac{\pi^2}{2} + 8\,\mathrm{arctanh}\sqrt{\frac{d}{d+2l}} \right. \\ \left. -2\left[\mathrm{Li}_2\left(\frac{\sqrt{d(d+2l)}}{d+l}\right) - \mathrm{Li}_2\left(-\frac{\sqrt{d(d+2l)}}{d+l}\right)\right]\right\} . \tag{4.4.14}$$

Null boundary terms. The null normals to the bounding surfaces can be determined similarly to the case of a single line segment in AdS_3, see Sec. 4.2. The affine parametrization of such normals sets $I_{\mathcal{N}} = 0$ and, as usual, the counterterms for the entanglement wedge boundaries vanish. We are thus left with the counterterm for the boundaries of the WDW patch, which we separate into two contributions:

$$I_{ct,I} = \frac{L}{2\pi G}\int_{x_{min}}^{x_{int}} dx \int_{\varepsilon}^{z_G}\frac{dz}{z^2}\,\log\left(\frac{\tilde{L}\,\alpha\,z}{L^2}\right) , \\ I_{ct,II} = \frac{L}{2\pi G}\int_{x_{int}}^{x_{max}} dx \int_{\varepsilon}^{z_F}\frac{dz}{z^2}\,\log\left(\frac{\tilde{L}\,\alpha\,z}{L^2}\right) . \tag{4.4.15}$$

Joint contributions. We have to include several joint contributions to the action, each of which involves two codimension-one null surfaces:

- The joint at the cutoff $z = \varepsilon$ comes from the intersection between the future and past boundaries of the WDW patch, whose null normals are

$$\mathbf{k}^{\pm} = \alpha\,(\pm dt - dz) . \tag{4.4.16}$$

  The contribution is

$$I_{\varepsilon} = -\frac{L}{4\pi G}\int_{x_{min}}^{x_{max}} dx\,\frac{\log\left(\frac{\alpha^2\varepsilon^2}{L^2}\right)}{\varepsilon} = -\frac{L}{2\pi G}\frac{l\,\log\left(\frac{\alpha\,\varepsilon}{L}\right)}{\varepsilon} . \tag{4.4.17}$$

- The joint at RT_1 is given by the intersection of future and past boundaries of the entanglement wedge with null normals

$$\mathbf{w}_{\mathbf{1}}^{\pm} = \beta\left(\pm dt + \frac{z}{\sqrt{z^2+x^2}}dz + \frac{x}{\sqrt{z^2+x^2}}dx\right) . \tag{4.4.18}$$

This term reads

$$I_{RT_1} = -\frac{L}{2\pi G}\int_0^{x_{max}} dx\,\frac{d+2l}{(d+2l)^2-4x^2}\log\frac{\beta^2\left((d+2l)^2-4x^2\right)}{4L^2}$$
$$= \frac{L}{4\pi G}\log(\varepsilon)\log\left(\frac{\beta^2\varepsilon}{L^2}\right) - \frac{L}{4\pi G}\log(d+2l)\log\frac{(d+2l)\,\beta^2}{L^2} + \frac{L\pi}{48G}\,. \tag{4.4.19}$$

- Similarly, the joint at RT_2 is given by the intersection of future and past boundaries of the entanglement wedge with null normals

$$\mathbf{w_2^{\pm}} = \gamma\left(\pm dt - \frac{z}{\sqrt{z^2+x^2}}dz - \frac{x}{\sqrt{z^2+x^2}}dx\right)\,. \tag{4.4.20}$$

The corresponding contribution is

$$I_{RT_2} = -\frac{L}{2\pi G}\int_0^{x_{min}} dx\,\frac{d}{d^2-4x^2}\log\frac{\gamma^2\left(d^2-4x^2\right)}{4L^2}$$
$$= \frac{L}{4\pi G}\log(\varepsilon)\log\left(\frac{\gamma^2\,\varepsilon}{L^2}\right) - \frac{L}{4\pi G}\log(d)\log\frac{d\,\gamma^2}{L^2} + \frac{L\pi}{48G}\,. \tag{4.4.21}$$

- For the joint at the curve E, the involved null normals are $\mathbf{w_1^+}$ and $\mathbf{w_2^+}$. The contribution reads

$$I_E = \frac{L}{\pi G}\int_0^{x_{int}} dx\,\frac{d+l}{(d+l)^2-4x^2}\log\frac{\beta\,\gamma\left((d+l)^2-4x^2\right)}{4L^2}\,. \tag{4.4.22}$$

- For the joint at the curve F, the involved null normals are $\mathbf{k}^+$ and $\mathbf{w_1^+}$. The term gives

$$I_F = \frac{2L}{\pi G}\int_{x_{int}}^{x_{max}} dx\,\frac{d+2(l+\varepsilon)}{(d+2(l+\varepsilon))^2-4x^2}\log\frac{\alpha\,\beta\left((d+2(l+\varepsilon))^2-4x^2\right)^2}{16L^2\left((d+2(l+\varepsilon))^2+4x^2\right)}\,. \tag{4.4.23}$$

- For the joint at the curve G, the involved null normals are $\mathbf{k}^+$ and $\mathbf{w_2^+}$. The contribution is

$$I_G = \frac{2L}{\pi G}\int_{x_{min}}^{x_{int}} dx\,\frac{d-2\varepsilon}{4x^2-(d-2\varepsilon)^2}\log\frac{\alpha\,\gamma\,(d-2\varepsilon+2x)^2\,(d-2\varepsilon-2x)^2}{16L^2\left[4x^2+(d-2\varepsilon)^2\right]}\,. \tag{4.4.24}$$

4.4.2 Complexities

Adding up all the contributions and using polylogarithm identities, we find

$$\begin{aligned}\mathcal{SC}_A^2 = \frac{c}{3\pi^2}\Bigg\{&\frac{l}{\varepsilon}\log\left(\frac{\tilde{L}}{L}\right) - \log\left(\frac{2\tilde{L}}{L}\right)\log\left(\frac{d(d+2l)}{\varepsilon^2}\right) - \frac{\pi^2}{4} \\ &+\left[\log\left(\frac{\tilde{L}}{L}\right) + \log\left(\frac{2(d+l)}{\sqrt{d(d+2l)}}\right)\right]\log\left(\frac{(d+l+\sqrt{d(d+2l)})^2}{l^2}\right) \\ &+\mathrm{Li}_2\left(\frac{\sqrt{d(d+2l)}}{d+l}\right) - \mathrm{Li}_2\left(-\frac{\sqrt{d(d+2l)}}{d+l}\right)\Bigg\}\,.\end{aligned} \tag{4.4.25}$$

From the bulk contribution (4.4.14) we can instead extract the subregion spacetime volume complexity:

$$\begin{aligned}\mathcal{SC}_{V2.0}^2 = \frac{2\,c}{3}\Bigg\{&\frac{2l}{\varepsilon} - 2\log\frac{d(d+2l)}{\varepsilon^2} + \frac{\pi^2}{2} + 8\,\mathrm{arctanh}\sqrt{\frac{d}{d+2l}} \\ &-2\left[\mathrm{Li}_2\left(\frac{\sqrt{d(d+2l)}}{d+l}\right) - \mathrm{Li}_2\left(-\frac{\sqrt{d(d+2l)}}{d+l}\right)\right]\Bigg\}\,.\end{aligned} \tag{4.4.26}$$

The divergences of eqs. (4.4.25) and (4.4.26) are the same as the corresponding quantities in eq. (4.4.2). In particular, the subleading divergences are still proportional to the entanglement entropy

$$S = \frac{c}{3}\log\frac{d(d+2l)}{\varepsilon^2}\,. \tag{4.4.27}$$

On the other hand, the finite part is a more complicated function of the subregion parameters d, l compared to the single interval case.

4.4.3 Mutual complexity

Let us a consider two subsystems A, B of a physical system. The *mutual information* is defined as

$$I(A|B) = S(A) + S(B) - S(A\cup B)\,, \tag{4.4.28}$$

where $S(A) = -\mathrm{Tr}_A\left(\rho_A \log \rho_A\right)$ denotes the entanglement entropy of the reduced density matrix obtained by tracing over the system external to A. As we have

seen in Sec. 2.2, entanglement entropy is subadditive: $S(A\cup B)\leq S(A)+S(B)$ [81]. As a consequence, mutual information is a positive quantity.

In parallel to entanglement entropy and mutual information, a quantity involving subregion complexity and measuring the correlations between two physical subsystems was introduced in [35, 149] and called *mutual complexity*:

$$\Delta\mathcal{C}=\mathcal{SC}(\rho_A)+\mathcal{SC}(\rho_B)-\mathcal{SC}(\rho_{A\cup B})\,. \tag{4.4.29}$$

In all the three holographic conjectures $\Delta\mathcal{C}$ is a finite quantity, because the divergences appearing in each term exactly cancel out. If mutual complexity is always positive (negative), subregion complexity is *subadditive* (*superadditive*).

By construction, subregion-CV and subregion-CV 2.0 are superadditive, i.e. $\mathcal{SC}(\rho_{A\cup B})\geq\mathcal{SC}(\rho_A)+\mathcal{SC}(\rho_B)$. This is confirmed by the expressions of subregion complexity for two boundary segments in AdS$_3$. In particular, for subregion-CV we can refer to eq. (4.3.36). For distances $d<d_0$ between the two segments we get

$$\Delta\mathcal{C}_V=-\frac{4\,c}{3}\pi\,. \tag{4.4.30}$$

Superadditivity of subregion-CV can be understood from the fact that the volume of codimension-one surfaces is positive, and the disconnected surfaces in the left Fig. 4.7 are contained into the connected surface on the right. Meanwhile, for distances $d>d_0$ the RT surface is disconnected, thus $\Delta\mathcal{C}_V=0$. Note that at the critical distance $d=d_0$ the volume mutual complexity manifests a discontinuous jump, while mutual information vanishes [146, 147]. This observation generically holds for all three holographic conjectures.
Regarding the subregion-CV 2.0 conjecture, from eq. (4.4.26) we find that the mutual complexity for two disjoint intervals at a distance $d<d_0$ is

$$\begin{aligned}\Delta\mathcal{C}_{V2.0}&=\mathcal{SC}^1_{V2.0}-\mathcal{SC}^2_{V2.0}\\&=\frac{4\,c}{3}\left[\log\frac{d(d+2l)}{l^2}-\frac{\pi^2}{2}-4\,\mathrm{arctanh}\sqrt{\frac{d}{d+2l}}\right.\\&\left.+\mathrm{Li}_2\left(\frac{\sqrt{d(d+2l)}}{d+l}\right)-\mathrm{Li}_2\left(-\frac{\sqrt{d(d+2l)}}{d+l}\right)\right]\,,\end{aligned} \tag{4.4.31}$$

see Fig. 4.9 for a plot. Similarly to subregion-CV, $\Delta\mathcal{C}_{V2.0}$ is negative-definite as expected, because the spacetime volume is positive and the bulk region involved in the first configuration of RT surface is smaller than the second one.

Instead, for subregion-CA no general argument is known which fixes the sign of $\Delta\mathcal{C}$. To gain some insights, we exploit the result obtained in the previous

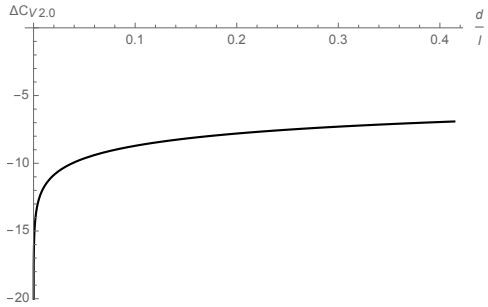

Figure 4.9: Mutual complexity $\Delta\mathcal{C}_{V2.0}$ as a function of $\frac{d}{l} \in [0, \frac{d_0}{l} = \sqrt{2} - 1]$. We have set $c = 1$.

subsection for two boundary segments. For $d < d_0$, we find from eqs. (4.4.2) and (4.4.25) that action mutual complexity is

$$\begin{aligned}\Delta\mathcal{C}_A = \mathcal{SC}_A^1 - \mathcal{SC}_A^2 = \frac{c}{3\pi^2}\Bigg\{&\log\left(\frac{2\tilde{L}}{L}\right)\log\left(\frac{d(d+2l)}{l^2}\right) + \frac{\pi^2}{2} \\ &- \left[\log\left(\frac{\tilde{L}}{L}\right) + \log\left(\frac{2(d+l)}{\sqrt{d(d+2l)}}\right)\right]\log\left(\frac{(d+l+\sqrt{d(d+2l)})^2}{l^2}\right) \\ &-\mathrm{Li}_2\left(\frac{\sqrt{d(d+2l)}}{d+l}\right) + \mathrm{Li}_2\left(-\frac{\sqrt{d(d+2l)}}{d+l}\right)\Bigg\}\,.\end{aligned} \tag{4.4.32}$$

In Fig. 4.10 we plot the function $\Delta\mathcal{C}_A$ for various values of $\eta = \tilde{L}/L$. The figure clearly shows that this quantity can be either positive or negative. In particular, for $\eta = 1/2$ the action mutual complexity of consecutive intervals $d \to 0$ switches from $-\infty$ to $+\infty$, as can be directly deduced by the small d expansion

$$\Delta\mathcal{C}_A \approx \frac{c}{3\pi^2}\log(2\eta)\log\left(\frac{2d}{l}\right)\,. \tag{4.4.33}$$

For $\eta \leq 1/2$ subregion-CA is subadditive for all values of d/l. Conversely, for $\eta > 1/2$ subregion-CA enters a superadditive regime at small enough distances d/l. If we also have $\eta > \eta_0 \approx 2.465$, subregion-CA of two disjoint intervals is always superadditive. It is important to stress that we should require $\eta > 1$ in order to have a positive-definite subregion action complexity. Then, it is not possible to achieve a universally subadditive subregion complexity in a physically consistent setting.

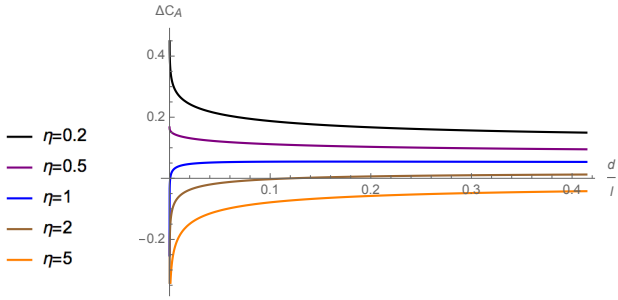

Figure 4.10: Mutual complexity $\Delta\mathcal{C}_A$ for several values of $\eta = \tilde{L}/L$ as a function of $\frac{d}{l} \in [0, \frac{d_0}{l} = \sqrt{2} - 1]$. In order to have a positive-definite subregion action complexity, we must impose $\eta > 1$. The other values of η have been included for completeness. We have set $c = 1$.

A similar behavior of subregion-CA has been found for the thermofield double state, where the subsystems correspond to the whole time-slices in the two disconnected spacetime boundaries. Namely, for asymptotically AdS BHs in D dimensions, it has been shown that subregion-CA is subadditive when $\eta < \hat{\eta}_D$ and superadditive for $\eta > \hat{\eta}_D$ [34, 149]. The critical value $\hat{\eta}_D$ is given by the zero of the function [34]

$$g_D(\eta) = \log((D-2)\eta) + \frac{1}{2}\left(\psi_0(1) - \psi_0\left(\frac{1}{D-1}\right)\right) + \frac{D-2}{D-1}\pi\,, \qquad (4.4.34)$$

where $\psi_0(z) = \Gamma'(z)/\Gamma(z)$ is the digamma function. In our case $D = 3$, we have $\hat{\eta}_3 \approx 0.1$.

4.4.4 Strong sub/superadditivity for overlapping segments

Given two partially overlapping subregions A and B, entanglement entropy satisfies the *strong subadditivity* property [81]

$$\tilde{\Delta}S(A,B) = S(A) + S(B) - S(A\cup B) - S(A\cap B) \geq 0\,. \qquad (4.4.35)$$

Inspired by this relation, a generalization of mutual complexity (4.4.29) to bipartite systems with $A \cap B \neq \emptyset$ has been proposed [35]:

$$\tilde{\Delta}\mathcal{C}(A,B) = \mathcal{SC}(\rho_A) + \mathcal{SC}(\rho_B) - \mathcal{SC}(\rho_{A\cup B}) - \mathcal{SC}(\rho_{A\cap B})\,. \qquad (4.4.36)$$

Divergences in the four contributions cancel, so $\tilde{\Delta}\mathcal{C}$ is a finite quantity. If $\tilde{\Delta}\mathcal{C}$ is always positive (negative), subregion complexity is said to be *strongly*

subadditive (*superadditive*). The sign of mutual complexity is in general non-trivial. To perform a preliminary analysis, we can exploit the results presented in the previous sections.

Let us consider as subregions two line segments of lengths a, b, whose intersection is a segment of length c. The union of these intervals is a segment of total length $a + b - c$. Since $\tilde{\Delta}\mathcal{C}$ is completely determined by subregion complexity of a single segment, we have all the necessary ingredients to investigate strong sub/superadditivity of subregion complexity in BTZ spacetime. Specifically, from eqs. (4.3.32), (4.3.33) and (4.3.35) we find

$$\begin{aligned} \tilde{\Delta}\mathcal{C}_A^{\mathrm{BTZ}} &= -\log(2\eta)\,\frac{\tilde{\Delta}S^{\mathrm{BTZ}}}{\pi^2}\,, \\ \tilde{\Delta}\mathcal{C}_{V2.0}^{\mathrm{BTZ}} &= -4\tilde{\Delta}S^{\mathrm{BTZ}}\,, \\ \tilde{\Delta}\mathcal{C}_V^{\mathrm{BTZ}} &= 0\,, \end{aligned} \tag{4.4.37}$$

where $\tilde{\Delta}S^{\mathrm{BTZ}}$ is the quantity defined in eq. (4.4.35), computed for the two overlapping intervals in the BTZ background. From the strong subadditivity of entanglement entropy (see Sec. 2.2), we deduce that subregion-CV 2.0 is strongly superadditive, while subregion-CA is strongly subadditive for $\eta < 1/2$ and strongly superadditive for $\eta > 1/2$. Finally, subregion-CV saturates strong superadditivity. The same conclusions apply to AdS_3, where $\tilde{\Delta}S^{\mathrm{BTZ}}$ in eq. (4.4.37) is replaced by the corresponding quantity $\tilde{\Delta}S^{\mathrm{AdS}}$.

4.5 Discussion

In this chapter we have studied the subregion-CA and subregion-CV 2.0 conjectures in AdS_3 and in the BTZ background, arguing that:

- For a single segment subsystem, subregion complexity in AdS_3 and BTZ spacetimes is directly related to the entanglement entropy, see eqs. (4.3.32) and (4.3.33).
- For a disconnected two-segments subsystem, subregion complexity in AdS_3 is a more complicated function of the lengths and relative separation of the intervals, see eqs. (4.4.25) and (4.4.26). The takeaway message is that subregion complexity carries a different amount of information compared to entanglement entropy. In particular, mutual complexity (defined in eq. (4.4.29)) for two disjoint segments is not proportional to mutual information.

While subregion-CV and subregion-CV 2.0 are superadditive by construction, we have found that the sign of action mutual complexity $\Delta\mathcal{C}_A$ of a disjoint two-segments subregion in AdS_3 drastically depends on the parameter $\eta = \tilde{L}/L$ (see figure 4.10). After imposing $\eta > 1$ to have a positive-definite subregion action complexity, we are left with two possibilities:

- If $\eta \geq \eta_0 \approx 2.465$, subregion-CA is superadditive.
- If $1 < \eta < \eta_0$, subregion-CA is superadditive for small segments distances d and subadditive for larger $d < d_0 = (\sqrt{2} - 1)l$.

Additionally, we have shown that in both AdS_3 and BTZ spacetimes subregion-CV and subregion-CV 2.0 are strongly superadditive, just as subregion-CA in the physical regime $\eta > 1$. Strictly speaking, subregion-CV saturates strong superadditivity.

Chapter 5

Subregion complexity in warped AdS_3

This chapter is an adaptation of the published article [144].

The AdS/CFT correspondence has unveiled a deep relation between geometry and quantum information: the area of minimal surfaces into asymptotically AdS is proportional to the entanglement entropy of boundary subsystems [9, 167, 168], and geometric quantities exploring the interior of AdS BHs are conjectured to be dual to complexity of the boundary state [11, 13–15, 117]. The question arises whether such a connection extends to different spacetimes. Evidence of this has been found for an ultraviolet modification of the AdS/CFT correspondence, named WAdS/WCFT correspondence [44–46, 48, 49], which posits a duality between $(2+1)$-dimensional gravitational theories in asymptotically *warped anti-de Sitter* (WAdS) *spacetime* and a class of non-relativistic $(1+1)$-dimensional QFTs, called *warped conformal field theories* (WCFTs), living on its boundary. More precisely, a WCFT has as global symmetry group $\mathrm{SL}(2,\mathbb{R}) \times \mathrm{U}(1)$, which contains translations $x^{\pm} \to x^{\pm} + a^{\pm}$ and a chiral scaling transformation $x^{-} \to \lambda\, x^{-}$, where $x^{\pm}$ denote the spacetime coordinates and $a^{\pm}, \lambda$ are constants. The infinite-dimensional local symmetry group is instead given by the Virasoro and the U(1) Kac-Moody algebras [47].

The WAdS/WCFT correspondence mainly relies on the fact that WAdS_3 spacetime is a continuous deformation of AdS_3, with isometry group $\mathrm{SL}(2,\mathbb{R}) \times \mathrm{U}(1)$. In addition, several holographic results can be generalized to this framework. For instance, an analog of the Cardy formula for WCFT_2 reproducing the Bekenstein-Hawking entropy of WAdS_3 BHs was derived in

[48]. Also, agreement has been found between the entanglement entropy in WCFT$_2$ and the holographic counterpart determined by semi-classical particle trajectories in WAdS$_3$ [50–54]. Motivated by these findings, holographic complexity was studied in asymptotically WAdS$_3$ spacetimes by employing CV and CA proposals [116, 119, 169, 170].

In this chapter we compute the divergences of subregion-CA, subregion-CV, and subregion-CV 2.0 for the left (right) factors of the thermofield double state dual to WAdS$_3$ rotating BHs. Then, we investigate the temperature dependence of all the three conjectures and the additivity properties of subregion-CA, also drawing a comparison with the BTZ case presented in the previous chapter. In details, in Sec. 5.1 we start with a review of some basic properties of warped BHs realized as solutions in Einstein gravity. In Sec. 5.2 we compute the divergences of both CA and subregion-CA for warped rotating BHs. In Sec. 5.3 we perform a similar analysis for subregion-CV and subregion-CV 2.0. Calculations for warped non-rotating BHs are deferred to Appendix B.

5.1 Black holes in warped AdS$_3$ spacetime

Warped AdS$_3$ can be obtained by expressing AdS$_3$ as a Hopf fibration of the real line over AdS$_2$, and multiplying the fiber by a warping factor depending on a real parameter ν^2 [43]. For $\nu^2 > 1$ we obtain *stretched* AdS$_3$, whereas for $\nu^2 < 1$ we get *squashed* AdS$_3$. The warping procedure can be accomplished by deforming AdS$_3$ along either timelike or spacelike fibers, providing different classes of WAdS$_3$ spacetimes.

Black hole solutions in asymptotically WAdS$_3$ are known for the spacelike stretched case ($\nu^2 > 1$) [44, 171, 172], and are described by the metric

$$\begin{aligned}\frac{ds^2}{\ell^2} &= dt^2 + \frac{dr^2}{(\nu^2+3)(r-r_+)(r-r_-)} + \frac{r}{4}\Psi(r)d\theta^2 \\ &\quad + \left(2\nu r - \sqrt{r_+ r_-(\nu^2+3)}\right) dt d\theta\,,\end{aligned} \tag{5.1.1}$$

with

$$\Psi(r) = 3(\nu^2-1)r + (\nu^2+3)(r_+ + r_-) - 4\nu\sqrt{r_+ r_-(\nu^2+3)}\,. \tag{5.1.2}$$

Introducing a parameter $\tilde{r}_0$ defined as

$$\tilde{r}_0 = \max(0, \rho_0)\,, \qquad \rho_0 = \frac{4\nu\sqrt{r_+ r_-(\nu^2+3)} - (\nu^2+3)(r_+ + r_-)}{3(\nu^2-1)}\,, \tag{5.1.3}$$

such that $\Psi(\rho_0) = 0$, the coordinates range is: $\tilde{r}_0 \leq r < \infty$, $-\infty < t < \infty$ and $\theta \sim \theta + 2\pi$. In the above expressions, r_- and r_+ denote the radii of the inner and outer event horizon, respectively, so $r_- \leq r_+$. The special case $\nu^2 = 1$ reproduces the BTZ BH [41, 42]. For $\nu^2 < 1$ the metric is instead pathological, because it admits closed timelike curves.

The WAdS$_3$ BHs described by eq. (5.1.1) can be built as solutions of Topological Massive Gravity [171, 172], New Massive Gravity [173], linear combinations of such mass terms [174], and string theory constructions [175–177]. In this thesis we will focus on realizations in Einstein gravity with matter [178, 179], which we illustrate in the next subsection. Regardless of the model in which eq. (5.1.1) is obtained, the temperature and angular velocity of the outer horizon are [44]

$$T = \frac{\nu^2+3}{4\pi\ell}\,\frac{r_+ - r_-}{2\nu r_+ - \sqrt{(\nu^2+3)r_+ r_-}}\,, \qquad \Omega = \frac{2}{(2\nu r_+ - \sqrt{(\nu^2+3)r_+ r_-})\ell}\,. \tag{5.1.4}$$

On the other hand, the entropy and the conserved charges of the BH depend on the gravitational action we choose. In Einstein gravity, the entropy is proportional to the area of the outer event horizon

$$S = \frac{\ell\pi}{4G}(2\nu r_+ - \sqrt{(\nu^2+3)r_+ r_-})\,, \tag{5.1.5}$$

while the mass and angular momentum are [178, 179]

$$M = \frac{1}{16G}(\nu^2+3)\left((r_- + r_+) - \frac{\sqrt{(\nu^2+3)r_+ r_-}}{\nu}\right)\,, \tag{5.1.6}$$

$$J = \frac{\ell}{32G}(\nu^2+3)\left(\frac{r_- r_+(5\nu^2+3)}{2\nu} - (r_+ + r_-)\sqrt{(\nu^2+3)r_+ r_-}\right)\,. \tag{5.1.7}$$

As we will see, these quantities enter the divergences coefficients of holographic (subregion) complexity.

5.1.1 An explicit realization in Einstein gravity

WAdS$_3$ BHs can be realized as solutions in Einstein gravity coupled to matter. Nonetheless, all the known explicit constructions have some pathology in the matter content. For instance, in [180] WAdS$_3$ BHs are obtained as solutions whose sources are perfect fluids with spacelike quadrivelocity. We instead consider the model introduced in [178], namely Maxwell-Chern-Simons electrodynamics coupled to Einstein gravity. For the resulting geometry to be free of closed timelike curves ($\nu^2 \geq 1$), a ghost-like kinetic Maxwell term is

required. One may be wary of results collected in such an unphysical scenario. In this regard, we point out that the same theoretical setting has been studied in [119], where the asymptotic growth of action complexity has been found to be proportional to the product between the Hawking temperature and the Bekenstein-Hawking entropy, as expected. Therefore, the CA conjecture seems solid enough to survive to the existence of ghosts in the theory. Consistent outcomes have also been found for the CV conjecture [116]. In this chapter we will take the same perspective, assuming that the holographic proposals for subregion complexity are not spoiled by the presence of ghost fields.

The model we are going to work with is Einstein gravity in $2+1$ dimensions with a negative cosmological constant. The matter content is a U(1) gauge field with both Maxwell and Chern-Simons terms [178]. The bulk action is

$$\begin{aligned} I_{\mathcal{W}} &= \frac{1}{16\pi G}\int_{\mathcal{W}} d^3x\,\left[\sqrt{-g}\left(R-2\Lambda-\frac{\kappa}{4}F_{\mu\nu}F^{\mu\nu}\right)-\frac{\alpha}{2}\epsilon^{\mu\nu\rho}A_\mu F_{\nu\rho}\right] \\ &\equiv \int_{\mathcal{W}} d^3x\,\sqrt{-g}\,\mathcal{L}\,, \end{aligned} \tag{5.1.8}$$

where the coefficient of the Maxwell kinetic term can take the values $\kappa=\pm 1$. The scalar curvature and cosmological constant are

$$R=-\frac{6}{\ell^2}\,,\qquad \Lambda=-\frac{1}{L^2}\,, \tag{5.1.9}$$

respectively. The equations of motion for the gauge field read [119]

$$D_\mu F^{\nu\mu}=-\frac{\alpha}{\kappa}\frac{\epsilon^{\nu\rho\sigma}}{\sqrt{-g}}F_{\rho\sigma}\,, \tag{5.1.10}$$

while the Einstein's equations are

$$G_{\mu\nu}-\frac{1}{L^2}g_{\mu\nu}=\frac{\kappa}{2}T_{\mu\nu}\,,\qquad T_{\mu\nu}=F_{\mu\sigma}F^{\sigma}_{\nu}-\frac{1}{4}g_{\mu\nu}F^{\rho\sigma}F_{\rho\sigma}\,, \tag{5.1.11}$$

where $G_{\mu\nu}$ is the Einstein tensor and $T_{\mu\nu}$ the energy-momentum tensor. With the gauge choice

$$A=a\,dt+c\,r\,d\theta\,,\qquad F=c\,dr\wedge d\theta\,, \tag{5.1.12}$$

in which a and c are constants, the Maxwell and Einstein's equations fix

$$\alpha=\kappa\frac{\nu}{\ell}\,,\qquad L=\ell\sqrt{\frac{2}{3-\nu^2}}\,,\qquad c=\pm\ell\sqrt{\frac{3(1-\nu^2)}{2\kappa}}\,. \tag{5.1.13}$$

Note that we cannot simultaneously avoid closed timelike curves ($\nu^2\geq 1$) and ghosts ($\kappa=+1$). We will take $\nu^2\geq 1$, causing the kinetic term for the Maxwell

field to have the "wrong" sign ($\kappa = -1$).
Even though the action depends explicitly on a through the Chern-Simons term, such a gauge parameter is not constrained by the equations of motion. By the way, the only value of a for which the mass M is associated to the Killing vector $\partial/\partial t$ and does not depend on the U(1) gauge transformations is [119, 179]

$$a = \frac{\ell}{\nu}\sqrt{\frac{3(\nu^2-1)}{2}}\,. \tag{5.1.14}$$

For this value, the Lagrangian density reads

$$\mathcal{I} \equiv 16\pi G\,\sqrt{-g}\,\mathcal{L} = -\frac{\ell}{2}(\nu^2+3)\,. \tag{5.1.15}$$

5.1.2 Eddington-Finkelstein coordinates

For our purposes, it is convenient to introduce null coordinates. This can be easily accomplished by using the Arnowitt-Deser-Misner (ADM) decomposition of the metric (5.1.1)

$$ds^2 = -N^2dt^2 + \frac{\ell^4 dr^2}{4\Upsilon^2 N^2} + \ell^2\Upsilon^2(d\theta + N^\theta dt)^2\,, \tag{5.1.16}$$

where

$$\Upsilon^2 = \frac{r}{4}\Psi(r)\,, \qquad N^2 = \frac{\ell^2(\nu^2+3)(r-r_+)(r-r_-)}{4\Upsilon^2}\,,$$
$$N^\theta = \frac{2\nu r - \sqrt{r_+ r_-(\nu^2+3)}}{2\Upsilon^2}\,. \tag{5.1.17}$$

The (subregion-)CA computation we will perform in the next section involves the construction of the WDW patch, whose boundaries can be parametrized by the set of null coordinates u, v introduced in [181]. Null geodesics at constant u and v satisfies $(d\theta + N^\theta dt) = 0$, then from the metric (5.1.16) we get

$$du = u_\mu dx^\mu = dt - \frac{\ell^2}{2\Upsilon N^2}dr\,, \qquad dv = v_\mu dx^\mu = dt + \frac{\ell^2}{2\Upsilon N^2}dr\,. \tag{5.1.18}$$

These one-forms are both normal and tangent to the null boundaries of the WDW patch. The integral curves of u^α and v^α are null geodesics in the affine parametrization, thus satisfying

$$u^\alpha\nabla_\alpha u^\beta = 0\,, \qquad v^\alpha\nabla_\alpha v^\beta = 0\,, \tag{5.1.19}$$

where ∇_α is the covariant derivative.
By integrating eq. (5.1.18), we find the Eddington-Finkelstein coordinates

$$u = t - r^*(r)\,, \qquad v = t + r^*(r)\,, \tag{5.1.20}$$

where the tortoise coordinate r^* is

$$r^*(r) = \int^r \frac{dr'}{f(r')}\,, \qquad f(r) = \frac{2\Upsilon N^2}{\ell^2} = \frac{(\nu^2+3)(r-r_-)(r-r_+)}{\sqrt{r\Psi(r)}}\,. \tag{5.1.21}$$

Eq. (5.1.21) can be directly integrated, leading to an explicit expression for r^*. For $r_+ \neq r_-$, corresponding to non-extremal BHs, we have [181]

$$\begin{aligned} r^*(r) = \frac{\sqrt{3\,(\nu^2-1)}}{\nu^2+3}\Bigg\{ & \frac{\sqrt{r_+(r_+-\rho_0)}}{r_+-r_-}\log\left(\frac{|r-r_+|}{\left(\sqrt{r}\sqrt{r_+-\rho_0}+\sqrt{r-\rho_0}\sqrt{r_+}\right)^2}\right) \\ & -\frac{\sqrt{r_-(r_--\rho_0)}}{r_+-r_-}\log\left(\frac{|r-r_-|}{\left(\sqrt{r}\sqrt{r_--\rho_0}+\sqrt{r-\rho_0}\sqrt{r_-}\right)^2}\right) \\ & +2\log(\sqrt{r}+\sqrt{r-\rho_0})\Bigg\}\,. \end{aligned} \tag{5.1.22}$$

Note that the tortoise coordinate r^* is divergent at the spacetime boundary $r \to \infty$, with leading behavior

$$\lim_{r\to\infty} r^*(r) \approx \frac{\sqrt{3(\nu^2-1)}}{\nu^2+3}\log r\,. \tag{5.1.23}$$

Generic values (r_+, r_-) describes a rotating BH, whose Penrose diagram is the same as the one of the Reissner-Nordström BH [181], see Fig. 5.2. In the extremal limit $r_+ = r_-$, the BH temperature is zero and there is no thermofield double. Consequently, the Penrose diagram has just one boundary. In this thesis we will not consider this case. Non-rotating BHs have vanishing angular momentum $J = 0$, and are obtained by one of the following conditions:

$$r_- = 0\,, \qquad \frac{r_+}{r_-} = \frac{4\nu^2}{\nu^2+3}\,. \tag{5.1.24}$$

The corresponding Penrose diagram is the same as the one for the Schwarzschild BH in $3+1$ dimensions [181], see Fig. B.2. Since the two conditions in eq. (5.1.24) can be mapped into each other by an isometry [181], we will always consider the simpler one $r_- = 0$, $r_+ = r_h$ when referring to non-rotating BHs. The holographic conjectures for such solutions are extensively studied in Appendix B.2.

5.2 Subregion action complexity

5.2.1 Comments on regularization

In this section we determine the divergences of (subregion-)action complexity for a two-sided rotating WAdS BH, deferring the analog computation for the non-rotating case to Appendix B.2. To this purpose, we introduce a UV cutoff close to the spacetime boundary at $r = \Lambda$.

As we have seen in Ch. 4, in asymptotically AdS two different regularizations can be used [40] for the CA conjecture, see Fig. 4.4. In regularization A the WDW patch is anchored at the spacetime boundary, whereas in regularization B the WDW is attached to the cutoff surface. By an explicit computation performed in BTZ spacetime, in Appendix B.1 we have shown that the two regularizations lead to the same divergences of subregion-CA, provided that in regularization A appropriate counterterms are introduced at the cutoff surface [182].

In Fig. 5.1 we show the Penrose diagram for a two-sided WAdS rotating BH, but the following discussion also applies to the case of WAdS non-rotating BHs. As it is clear from the picture, the Penrose diagram structure of asymptotically WAdS resembles that of asymptotically Minkowski spacetime, and is thus radically different from AdS. In particular, the 45 degrees boundaries correspond to the future null infinity and past null infinity. The right (left) corner, representing spacelike infinity, corresponds to $r \to \infty$ and arbitrary t. Generalizing regularization A in WAdS is not straightforward, since this would cause the corner of the WDW patch to be located at the spacelike infinity for all values of the boundary time, thus making complexity an unphysical time-independent quantity. Therefore, in order to compute (subregion) action complexity, we employ regularization B. The works [119, 169, 170], in which the CA conjecture in asymptotically WAdS is investigated, make use of regularization B as well. With this choice, the expected result for the complexity rate at late time $\dot{\mathcal{C}}_A \propto TS$ is obtained in Einstein gravity [119].

5.2.2 Action complexity for rotating WAdS black holes

The spacetimes we are dealing with in this chapter have a left and a right boundary, where two copies of WCFTs are located. The time coordinates on each boundary, denoted by t_L and t_R, are defined at the cutoff surface $r = \Lambda$, where the limit $\Lambda \to +\infty$ is understood. As explained in Subsec. 2.3.2, we assume the boundary times to increase upward at both the left and right

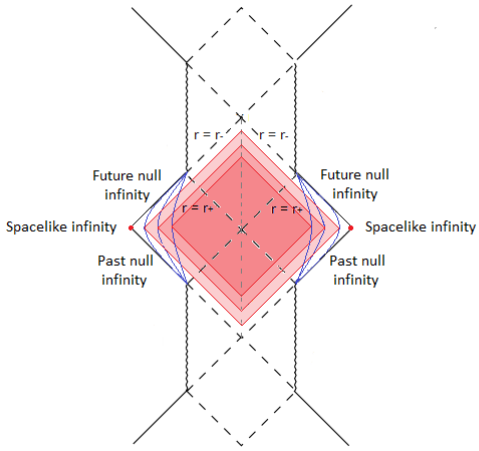

Figure 5.1: In WAdS, the causal structure is similar to asymptotically Minkowski spacetime. Regularization A would give a WDW patch whose corner is located at the spacelike infinity, thus providing a time-independent complexity. We point out that in regularization B the WDW patch covers the entire BH interior in the limit of infinite cutoff Λ.

boundaries, so that the thermofield double state (TFD) dual to the two-sided BH geometry is time-dependent [101]. It is not restrictive to consider the symmetric configuration

$$t_L = t_R = \frac{t_b}{2}\,. \tag{5.2.1}$$

Furthermore, we focus on the TFD state at zero boundary time $t_b = 0$, which, bearing in mind that the action growth rate has been found to be positive [119], has the minimum action complexity by time reflection symmetry.

In this section we compute the divergences of the total action of the WDW patch in the rotating WAdS BH geometry. The calculation for the non-rotating WAdS BH involves slightly different details that are sketched in Appendix B.2.1. By the way, the result is recovered in the $r_- \to 0$ limit of the rotating case as expected.

The Penrose diagram and the corresponding WDW patch for the rotating WAdS BH are depicted in Fig. 5.2. We indicate with r_{m1} and r_{m2} the position of the null joints at the top and bottom vertices of the WDW patch, respectively. In

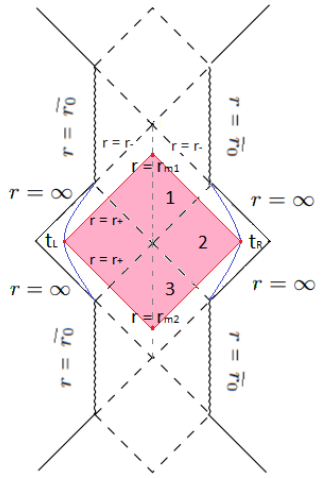

Figure 5.2: Penrose diagram and WDW patch at $t_b = 0$ for the rotating WAdS BH.

terms of the tortoise coordinate, such joints are described by

$$\frac{t_b}{2} + r^*_\Lambda - r^*(r_{m1}) = 0\,, \qquad \frac{t_b}{2} - r^*_\Lambda + r^*(r_{m2}) = 0\,, \tag{5.2.2}$$

where $r^*_\Lambda = r^*(\Lambda)$. At $t_b = 0$, we get

$$r^*_\Lambda = r^*(r_{m1}) = r^*(r_{m2}) \equiv r^*(r_m)\,. \tag{5.2.3}$$

From the picture we note that the configuration is transparently symmetric, so the actions of the future and past BH interiors are equal.
Unfortunately, eq. (5.2.3) cannot be solved exactly. Since the tortoise coordinate $r^* \to +\infty$ at both $r = \Lambda \to \infty$ and $r \to r_-$, we study the behavior in their neighborhood:

- Nearby $r = r_-$, we find

$$r^*(r_m) = -\frac{\sqrt{3(\nu^2-1)}}{\nu^2+3}\tilde{A}\log|r_m - r_-| + \tilde{B} + \mathcal{O}(r_m - r_-)\,, \tag{5.2.4}$$

  where $\tilde{B}$ is a constant and

$$\tilde{A} = \frac{\sqrt{r_-\Psi(r_-)}}{(r_+ - r_-)\sqrt{3(\nu^2-1)}} > 0\,. \tag{5.2.5}$$

- Around $r = \Lambda$,

$$r^*_\Lambda = \frac{\sqrt{3(\nu^2-1)}}{\nu^2+3}\log\Lambda + \tilde{C} + \mathcal{O}(\Lambda^{-1})\,, \tag{5.2.6}$$

  where $\tilde{C}$ does not depend on Λ.

Putting all together, eq. (5.2.3) implies

$$r_m - r_- \approx \Lambda^{-1/\tilde{A}}\,\exp\left[\frac{(\tilde{B}-\tilde{C})(\nu^2+3)}{\tilde{A}\sqrt{3(\nu^2-1)}}\right]. \tag{5.2.7}$$

The action of the WDW patch has several contributions, which we have thoroughly illustrated in Sec. 4.1:

$$I = I_{\mathcal{W}} + I_{\mathcal{B}} + I_{\mathcal{J}} + I_{ct}\,. \tag{5.2.8}$$

The only difference lies in the bulk contribution $I_{\mathcal{W}}$, which contains additional terms due to the matter fields, see eq. (5.1.8). We now individually evaluate each contribution.

Bulk contributions. We follow the calculation in [119]. The integrand of the bulk action is constant, implying that this contribution is proportional to the spacetime volume enclosed in the WDW patch. It is convenient to separate this bulk region into three parts, as indicated in Fig. 5.2:

$$\begin{aligned} I^1_{\mathcal{W}} &= \frac{\mathcal{I}}{8G}\int_{r_{m1}}^{r_+} dr\left(\frac{t_b}{2} + r^*_\Lambda - r^*(r)\right), \\ I^2_{\mathcal{W}} &= \frac{\mathcal{I}}{4G}\int_{r_+}^{\Lambda} dr\,(r^*_\Lambda - r^*(r))\,, \\ I^3_{\mathcal{W}} &= \frac{\mathcal{I}}{8G}\int_{r_{m2}}^{r_+} dr\left(-\frac{t_b}{2} + r^*_\Lambda - r^*(r)\right), \end{aligned} \tag{5.2.9}$$

where $\mathcal{I}$ is defined in eq. (5.1.15). A factor of 2π comes from the integration over the angular coordinate θ, by exploiting the spherical symmetry of the region of interest. For future purposes, we distinguish between the bulk terms in the BH interior and in the exterior region. Namely, the interior bulk term is given by

$$I^{\text{int}}_{\mathcal{W}} = 2(I^1_{\mathcal{W}} + I^3_{\mathcal{W}}) = -\frac{\ell}{4G}(\nu^2+3)\left[(r_+ - r_m)r^*_\Lambda - \int_{r_m}^{r_+} dr\, r^*(r)\right]. \tag{5.2.10}$$

The last integral in eq. (5.2.10) is finite, because the function $r^*(r)$ has integrable singularities in $r \approx r_-, r_+$. So, the divergent part of the internal bulk action comes from the first contribution and reads:

$$I_{\mathcal{W}}^{\text{int}} = -\frac{\ell}{4G}\sqrt{3(\nu^2-1)}(r_+ - r_-)\log\Lambda + \mathcal{O}(\Lambda^0)\,. \tag{5.2.11}$$

On the other hand, the external bulk term is

$$I_{\mathcal{W}}^{\text{ext}} = 2\, I_{\mathcal{W}}^2 = -\frac{\ell}{4G}(\nu^2+3)\int_{r_+}^{\Lambda} dr\ (r_\Lambda^* - r^*(r))\ . \tag{5.2.12}$$

Expanding eq. (5.1.22), we get the behavior of $r^*(r)$ at large r:

$$r^*(r) = \tilde{\alpha}\log(4r) + \tilde{\beta} + \frac{\tilde{\gamma}}{r} + \mathcal{O}(r^{-2})\,, \tag{5.2.13}$$

where

$$\tilde{\beta} = -2\frac{\sqrt{r_+\Psi(r_+)}\log\left(\sqrt{r_+}+\sqrt{r_+-\rho_0}\right) - \sqrt{r_-\Psi(r_-)}\log\left(\sqrt{r_-}+\sqrt{r_--\rho_0}\right)}{(\nu^2+3)(r_+-r_-)}\,,$$

$$\tilde{\alpha} = \frac{\sqrt{3(\nu^2-1)}}{\nu^2+3}\,, \qquad \tilde{\gamma} = \frac{\sqrt{3(\nu^2-1)}}{2(\nu^2+3)}\,(\rho_0 - 2r_+ - 2r_-)\,. \tag{5.2.14}$$

The divergences of (5.2.12) are then

$$\begin{aligned} I_{\mathcal{W}}^{\text{ext}} &= \frac{\ell}{4G}(\nu^2+3)\left[-\tilde{\alpha}\Lambda + (\tilde{\alpha}r_+ + \tilde{\gamma})\log\Lambda\right] + \mathcal{O}(\Lambda^0) \\ &= -\frac{\ell}{4G}\sqrt{3(\nu^2-1)}\ \Lambda + \frac{\ell}{8G}\sqrt{3(\nu^2-1)}(\rho_0 - 2r_-)\ \log\Lambda + \mathcal{O}(\Lambda^0)\,. \end{aligned} \tag{5.2.15}$$

Null boundary terms. In principle we have to take into account the surface terms coming from the null boundaries of the WDW patch. However, these can be set to zero by employing an affine parametrization for the boundary geodesics, as in eq. (5.1.19).

Joint terms. The action of the WDW patch has four null-null joint contributions: two on the cutoff surface $r = \Lambda$ and two in the region inside the black and white hole at $r = r_m$. They can all be directly evaluated from eq. (4.1.8):

$$I_{\mathcal{J}} = \frac{\zeta}{8\pi G}\int_{\mathcal{J}} d\theta\,\sqrt{\sigma}\,\log\left|\frac{\mathbf{k}_L\cdot\mathbf{k}_R}{2}\right|\,, \qquad \sqrt{\sigma} = \ell\,\Upsilon(r) = \ell\sqrt{\frac{r}{4}\Psi(r)}\,, \tag{5.2.16}$$

where $\mathbf{k}_L$ and $\mathbf{k}_R$ are normal one-forms defined on the boundaries meeting at the joint. The joints at the cutoff surface have $\zeta = -1$, while the ones in the

interior of the black and white holes have $\zeta = +1$. The null normals are given in eq. (5.1.18), that leads to

$$\frac{\mathbf{k}_L \cdot \mathbf{k}_R}{2} = \frac{u^\mu v_\mu}{2} = \frac{\alpha^2}{\ell^2}\frac{2\Upsilon(r)}{f(r)}\,, \tag{5.2.17}$$

where α is the arbitrary constant arising from the ambiguity in normalizing the null normals. From eq. (5.2.16), we get a general expression for the null-null joint in the radial position $r = r_k$:

$$I_{\mathcal{J}}^{r_k} = -\zeta_k \frac{\ell}{4G}\sqrt{\frac{r_k}{4}\Psi(r_k)}\,\log\left|\frac{\ell^2}{\alpha^2}\frac{f(r_k)}{2\Upsilon(r_k)}\right|\,. \tag{5.2.18}$$

The joint inside the black (white) hole, located at $r = r_m$, gives

$$\begin{aligned} I_{\mathcal{J}}^{r_m} &= -\frac{\ell}{8G}\sqrt{r_m\Psi(r_m)}\,\log\left|\frac{\ell^2}{\alpha^2}\frac{\left(\nu^2+3\right)(r_m-r_-)(r_m-r_+)}{r_m\Psi(r_m)}\right| \\ &= \frac{\ell}{8G}\sqrt{3\left(\nu^2-1\right)}\,(r_+-r_-)\,\log\Lambda + \mathcal{O}\left(\Lambda^0\right)\,. \end{aligned} \tag{5.2.19}$$

Each joint nearby the cutoff surface reads

$$\begin{aligned} I_{\mathcal{J}}^{\Lambda} &= \frac{\ell}{8G}\sqrt{\Lambda\Psi\left(\Lambda\right)}\,\log\left|\frac{\ell^2}{\alpha^2}\frac{\left(\nu^2+3\right)(\Lambda-r_-)(\Lambda-r_+)}{\Lambda\Psi\left(\Lambda\right)}\right| \\ &= \Lambda\frac{\ell}{8G}\sqrt{3\left(\nu^2-1\right)}\,\log\left|\frac{\ell^2}{\alpha^2}\frac{\nu^2+3}{3\left(\nu^2-1\right)}\right| + \mathcal{O}\left(\Lambda^0\right)\,. \end{aligned} \tag{5.2.20}$$

Summing the contributions of the four joints, we obtain

$$\begin{aligned} I_{\mathcal{J}}^{tot} &= 2\left(I_{\mathcal{J}}^{r_m} + I_{\mathcal{J}}^{\Lambda}\right) \\ &= \frac{\ell}{4G}\sqrt{3\left(\nu^2-1\right)}\left[\Lambda\log\left|\frac{\ell^2}{\alpha^2}\frac{\nu^2+3}{3\left(\nu^2-1\right)}\right| + (r_+-r_-)\log\Lambda\right] + \mathcal{O}\left(\Lambda^0\right)\,. \end{aligned} \tag{5.2.21}$$

Counterterm for null boundaries. The counterterm in eq. (4.1.10) must be included for each null boundary, in order to render the action reparametrization invariant:

$$I_{ct} = \frac{\ell}{8\pi G}\int_{\mathcal{B}} d\theta\, d\lambda\,\sqrt{\sigma}\,\Theta\,\log\left|\tilde{L}\,\Theta\right|\,. \tag{5.2.22}$$

To evaluate the counterterm for the future right boundary of the WDW patch along the null lines described by the Eddington-Finkelstein coordinates (u, v), it is convenient to perform the change of variable $\lambda \to r$, using

$$\frac{\partial r}{\partial\lambda} = \alpha\, v^r = \frac{2\alpha}{\ell^2}\Upsilon(r)\,. \tag{5.2.23}$$

Therefore, the integral becomes

$$\begin{aligned} I_{ct} &= \frac{\ell}{4G}\int_{r_m}^{\Lambda} dr\, \frac{\partial\sqrt{\sigma}}{\partial r}\log\left|\frac{\tilde{L}}{\sqrt{\sigma}}\frac{\partial\sqrt{\sigma}}{\partial r}\frac{2\alpha}{\ell^2}\Upsilon(r)\right| \\ &= \frac{\ell}{16G}\int_{r_m}^{\Lambda} dr\, \frac{\partial_r(r\Psi(r))}{\sqrt{r\,\Psi(r)}}\log\left|\frac{\alpha\tilde{L}}{2\ell^2}\frac{\partial_r(r\,\Psi(r))}{\sqrt{r\Psi(r)}}\right| . \end{aligned} \tag{5.2.24}$$

By symmetry, the counterterms for the four null boundaries of the WDW patch are the same. By the fact that $\Psi(r)$ is linear in r, we deduce that the only divergence arises from $r=\Lambda$:

$$I_{ct}^{\rm tot} = 4I_{ct} = \Lambda\frac{\ell}{4G}\sqrt{3\left(\nu^2-1\right)}\log\left|\frac{\alpha^2\tilde{L}^2}{\ell^4}3\left(\nu^2-1\right)\right| + \mathcal{O}\left(\Lambda^0\right) . \tag{5.2.25}$$

Total action. Summing up all the contributions, the divergences of the total action are

$$\begin{aligned} I^{\rm tot} &= \frac{\ell}{4G}\sqrt{3(\nu^2-1)}\left[\log\left(\frac{\tilde{L}^2}{\ell^2}(\nu^2+3)\right)-1\right]\Lambda \\ &+ \frac{\ell}{4G}\sqrt{3(\nu^2-1)}\left(\frac{\rho_0}{2}-r_-\right)\log\Lambda + \mathcal{O}\left(\Lambda^0\right) . \end{aligned} \tag{5.2.26}$$

Similarly to the AdS case, the divergent contribution in the counterterm exactly washes away the dependence on the ambiguous constant α appearing in the divergent contribution of the joints.

5.2.3 Action of internal regions and subregion complexity

We now investigate the divergences of subregion-CA for the left (right) factor of the thermofield double state, taking as a subregion the whole left (right) boundary time-slice. Choosing as a boundary time $t_b = 0$, subregion action complexity is given by the gravitational action of the portion of WDW patch external to the BH, namely region 2 shown in Fig. 5.2. Subregion-CA can thus be found by subtracting from the total action (5.2.26) the contributions of the interior of the black and white holes. We emphasize that the external action obtained by this subtraction procedure has to be interpreted as *twice* the subregion action complexity of the left (right) factor of the thermofield double state at $t_b = 0$. Therefore, a factor $1/2$ is intended when referring to the holographic interpretation. With this purpose in mind, we start by evaluating the gravitational action of the internal regions. Again, we focus on the rotating WAdS BH, relegating the non-rotating case to Appendix B.2.2.

Bulk contribution. The bulk part of the internal action has already been computed in eq. (5.2.11).

Joint terms. In the BH (white hole) interior, there are four null-null joints of the form (5.2.18). As shown in Fig. 5.3, one is located at $r = r_m$, and three lie at the event horizon $r = r_+$:

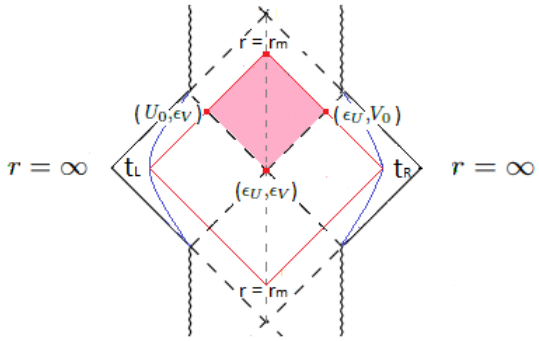

Figure 5.3: Joints involved in the computation of the WAdS BH interior action.

By symmetry, the same joints can be found inside the white hole. In the $\Lambda \to +\infty$ limit, in which $r_m \to r_-$, all these contributions are in principle divergent since $f(r_+) = f(r_-) = 0$. As it happens in AdS [34], we will see that due to the opposite sign of nearby joints these divergences partially cancel.

To perform the calculation of the joint terms on the horizon, it is useful to introduce the Kruskal coordinates (U, V) defined for $r > r_-$ as in [181]

$$\begin{aligned} U &= \text{sign}(r - r_+)\, e^{b_*(r^*(r)-t)} = \text{sign}(r - r_+)\, e^{-b_* u}\,, \\ V &= e^{b_*(r^*(r)+t)} = e^{b_* v}\,, \end{aligned} \tag{5.2.27}$$

where

$$b_* = \frac{f'(r_+)}{2} = \frac{(\nu^2+3)(r_+ - r_-)}{2\sqrt{r_+ \Psi(r_+)}}\,. \tag{5.2.28}$$

Below, we will make use of the relation

$$\log|UV| = 2b_* r^*(r) = f'(r_+) r^*(r)\,. \tag{5.2.29}$$

We point out that, since $r_* \to -\infty$ for $r \to r_+$ (see eq. (5.1.22)), the external BH horizon for the right boundary corresponds to $U = 0$, whereas the external white hole horizon for the right boundary corresponds to $V = 0$.

In order to regularize the divergence of joint terms at the horizon, we follow the prescription given in [34]. The idea is to move the joints off the horizon by introducing the infinitesimal regulators $\varepsilon_U, \varepsilon_V$. Then, we evaluate the total contribution of two joints with the same coordinate $V = \varepsilon_V$. Given that such terms have opposite signs ζ_k, from eq. (5.2.18) we get a resulting contribution proportional to

$$\begin{aligned}
&\log\left|\frac{\ell^2}{\alpha^2}\frac{f(r_{U_1,\varepsilon_V})}{2\Upsilon(r_+)}\right| - \log\left|\frac{\ell^2}{\alpha^2}\frac{f(r_{U_2,\varepsilon_V})}{2\Upsilon(r_+)}\right| = \int_{r_{U_2,\varepsilon_V}}^{r_{U_1,\varepsilon_V}} \frac{dr}{f(r)} f'(r) \\
&\approx f'(r_+)\int_{r_{U_2,\varepsilon_V}}^{r_{U_1,\varepsilon_V}} \frac{dr}{f(r)} = f'(r_+)\left[r^*(r_{U_1,\varepsilon_V}) - r^*(r_{U_2,\varepsilon_V})\right] \qquad (5.2.30)\\
&= \log|U_1\varepsilon_V| - \log|U_2\varepsilon_V| = \log\left|\frac{U_1}{U_2}\right|,
\end{aligned}$$

where in the last line use has been made of eq. (5.2.29).
This expression tells us that in the limit $\varepsilon_V \to 0$, the sum of two consecutive joints at the horizon is regular. By symmetry of the manipulations we have performed, the same argument applies if we exchange $U \leftrightarrow V$. Combining such results, we conclude that

$$\log\left|\frac{\ell^2}{\alpha^2}\frac{f(r_{U,V})}{2\Upsilon(r_+)}\right| = \log|UV| + F(r_+)\,, \qquad (5.2.31)$$

where the function $F(r)$ is regular at the horizon and reads

$$F(r) = \log\left|\frac{\ell^2}{\alpha^2}\frac{f(r)}{2\Upsilon(r)}\right| - f'(r_+)r^*(r)\,. \qquad (5.2.32)$$

Exploiting the symmetry of the geometry, the total joint contribution for the internal action is twice the contribution from the BH interior:

$$\begin{aligned}
I_{\mathcal{J}}^{\text{int}} = -2\times\frac{\ell}{4G}\Bigg\{&\Upsilon(r_m)\log\left|\frac{\ell^2}{\alpha^2}\frac{f(r_m)}{2\Upsilon(r_m)}\right| \\
&+\Upsilon(r_+)\left[\log\left|\frac{\ell^2}{\alpha^2}\frac{f(r_{\epsilon_U,\epsilon_V})}{2\Upsilon(r_+)}\right| - \log\left|\frac{\ell^2}{\alpha^2}\frac{f(r_{U_0,\epsilon_V})}{2\Upsilon(r_+)}\right| - \log\left|\frac{\ell^2}{\alpha^2}\frac{f(r_{\epsilon_U,V_0})}{2\Upsilon(r_+)}\right|\right]\Bigg\}\,. \qquad (5.2.33)
\end{aligned}$$

This expression simplifies to

$$\begin{aligned}
I_{\mathcal{J}}^{\text{int}} &= \frac{\ell}{2G}\Upsilon(r_+)\left[2b_*r_\Lambda^* + F(r_+)\right] - \frac{\ell}{2G}\Upsilon(r_m)\log\left|\frac{\ell^2}{\alpha^2}\frac{f(r_m)}{2\Upsilon(r_m)}\right| \qquad (5.2.34)\\
&= \frac{\ell}{2G}\sqrt{3(\nu^2-1)}(r_+ - r_-)\log\Lambda + \mathcal{O}(\Lambda^0)\,.
\end{aligned}$$

Counterterm for null boundaries. The counterterm for the internal action is the same as eq. (5.2.24), with the integral running from $r = r_m$ to $r = r_+$. Possible dependence on the UV cutoff Λ can arise only from the lower endpoint of integration $r = r_m$. However, putting the expansion (5.2.7) inside the integral, we explicitly checked that no divergent pieces appear.

Internal and external action. Putting together all the terms contributing to the internal action, we obtain

$$\begin{aligned} I^{\text{int}} &= \frac{\ell}{4G}\sqrt{3(\nu^2-1)}(r_+ - r_-)\log\Lambda + \mathcal{O}(\Lambda^0) \\ &= \frac{4\sqrt{3(\nu^2-1)}}{\nu^2+3}\,\ell\, TS\,\log\Lambda + \mathcal{O}(\Lambda^0)\,, \end{aligned} \tag{5.2.35}$$

where in the second line we have expressed the result in terms of the BH temperature (5.1.4) and entropy (5.1.5). Contrary to the AdS case [34, 149], the internal action is divergent. To explain this outcome, we again refer to Fig. 5.1. When in regularization B we send the UV cutoff Λ to infinity, the WDW patch include all the BH interior. Such a region is responsible for the linear growth of action complexity at large time [119]. Therefore, we deduce that taking the $\Lambda \to +\infty$ limit is equivalent to sending the boundary time to infinity with finite cutoff, which gives a divergent internal action.

Subtracting the result (5.2.35) from the total action (5.2.26), we find the divergences of the external action, which is interpreted as twice subregion complexity:

$$\begin{aligned} I^{\text{ext}} &= \frac{\ell}{4G}\sqrt{3(\nu^2-1)}\left[\log\left(\frac{\tilde{L}^2}{\ell^2}(\nu^2+3)\right) - 1\right]\Lambda \\ &+ \frac{\ell}{4G}\sqrt{3(\nu^2-1)}\left(\frac{\rho_0}{2} - r_+\right)\log\Lambda + \mathcal{O}(\Lambda^0)\,. \end{aligned} \tag{5.2.36}$$

We will extensively comment this outcome in Sec. 5.4.

5.3 Subregion volume and spacetime volume complexity

5.3.1 Volume complexity for rotating WAdS black holes

In this section we compute the divergences of (subregion-)volume complexity for the rotating WAdS BH. The corresponding analysis for the non-rotating WAdS

BH is addressed in Appendix B.2.3, where the finite part is also evaluated. In [116] the finite part of volume complexity has been found to grow in time, with a late time rate proportional to the product between the Hawking temperature and Bekenstein-Hawking entropy of the BH. We here focus on the thermofield double state at time $t_b = 0$, whose volume complexity is thus minimal.

The extremal codimension-one surface anchored at $t_b = 0$ lies at constant time $t = 0$ into the bulk and connects the whole left and right boundary time-slices at $t_L = 0$ and $t_R = 0$. The RT surface lies on the outer event horizon $r = r_+$, corresponding to the bifurcation surface in the Penrose diagram of Fig. 5.2. The bifurcation surface splits the extremal codimension-one surface into a left and right part, whose volume we denote by $V(L)$ and $V(R)$, respectively. By symmetry such volumes are equal, then

$$V^{\text{out}} = V(L) + V(R) = 2V(L)\,. \tag{5.3.1}$$

According to subregion-CV, $V(L)$ ($V(R)$) is interpreted as the subregion complexity of the left (right) factor of the thermofield double state at $t_b = 0$.

The volume can be directly computed from the determinant of the induced metric on the $t = 0$ bulk slice:

$$\begin{aligned} V(L) &= 2\pi\ell^2 \int_{r_+}^{\Lambda} dr\, G(r)\,, \\ G(r) &= \sqrt{\frac{r\left(3(\nu^2-1)r + (\nu^2+3)(r_+ + r_-) - 4\nu\sqrt{r_+ r_-(\nu^2+3)}\right)}{4(\nu^2+3)(r-r_-)(r-r_+)}}\,. \end{aligned} \tag{5.3.2}$$

Nearby the outer horizon $r \to r_+$, the function $G(r)$ can be approximated as

$$\begin{aligned} G(r) &= \frac{g}{\sqrt{r-r_+}} + \mathcal{O}\left(\sqrt{r-r_+}\right)\,, \\ g &= \sqrt{\frac{r_+\left(4\nu^2 r_+ + (\nu^2+3)r_- - 4\nu\sqrt{r_+ r_-(\nu^2+3)}\right)}{4(\nu^2+3)(r_+ - r_-)}}\,. \end{aligned} \tag{5.3.3}$$

Inserting such an expansion into the integral we get

$$2\pi\ell^2 \int_{r_+}^{r_+ + \varepsilon} dr\, G(r) \approx 2\pi\ell^2 \int_{r_+}^{r_+ + \varepsilon} dr\, \frac{g}{\sqrt{r-r_+}} \approx 4\pi\ell^2 g\sqrt{\epsilon}\,. \tag{5.3.4}$$

Therefore, there is no divergence arising at the horizon.
At $r \to \infty$, the function $G(r)$ behaves as

$$G(r) = \sqrt{\frac{3(\nu^2-1)}{4(\nu^2+3)}} + \frac{\nu\left(\nu(r_+ + r_-) - \sqrt{r_+ r_-(\nu^2+3)}\right)}{\sqrt{3(\nu^2-1)(\nu^2+3)}}\frac{1}{r} + \mathcal{O}\left(\frac{1}{r^2}\right)\,. \tag{5.3.5}$$

Upon integration, the first two terms give rise to a linear and a logarithmic divergence. So, we conclude that

$$V(L) = \pi\ell^2\sqrt{\frac{3(\nu^2-1)}{\nu^2+3}}\,\Lambda + \frac{32\pi G\ell^2\nu^2}{(\nu^2+3)^{3/2}\sqrt{3(\nu^2-1)}}M\log\Lambda + \mathcal{O}\left(\Lambda^0\right)\,. \quad (5.3.6)$$

Interestingly, the logarithmically divergent term is proportional to the BH mass M, expressed in eq. (5.1.6).

5.3.2 Spacetime volume complexity for rotating WAdS black holes

According to subregion-CV 2.0 conjecture, mixed state complexity is related to the spacetime volume of the intersection between the WDW patch and the entanglement wedge of the boundary subregion. For the left (right) factor of the thermofield double state at $t_b = 0$, the bulk region of interest coincides with the left (right) portion of WDW patch external to the black and white holes. Since the integrand in the bulk contribution (5.1.8) to the gravitational action is a constant, (twice) the result can be directly borrowed from eq. (5.2.15):

$$V^{\text{ext}}_{\text{bulk}} = 4\pi\ell^3\frac{\sqrt{3(\nu^2-1)}}{\nu^2+3}\,\Lambda - 4\pi\ell^3\frac{\sqrt{3(\nu^2-1)}}{\nu^2+3}\left(\frac{\rho_0}{2}-r_-\right)\log\Lambda + \mathcal{O}(\Lambda^0)\,. \quad (5.3.7)$$

The contribution to the spacetime volume from the interior of the black and white holes can be similarly obtained from eq. (5.2.11):

$$V^{\text{int}}_{\text{bulk}} = 4\pi\ell^3\frac{\sqrt{3(\nu^2-1)}}{\nu^2+3}(r_+ - r_-)\log\Lambda + \mathcal{O}(\Lambda^0)\,, \quad (5.3.8)$$

which added to the external contribution gives the spacetime volume complexity of the thermofield double state at $t_b = 0$.

5.4 Discussion

In this chapter we have computed the divergences of subregion complexity for the left (right) factor of the thermofield double state dual to (non-)rotating WAdS BHs, by employing subregion-CA, subregion-CV, and subregion-CV 2.0 conjectures. We now examine the main features of these results, focusing on the differences with the asymptotically AdS case $\nu^2 = 1$.

Structure of divergences. For the BTZ BH, all the notions of holographic subregion complexity present a linear divergence in the cutoff Λ [34, 149].

For WAdS BHs, we have found that all the versions of holographic subregion complexity have a linear and a logarithmic divergence in Λ. Regarding subregion action complexity, the coefficient of the linear divergence, as in the BTZ case, can be either positive or negative depending on the value of the length scale $\tilde{L}$. On the other hand, the coefficient of the logarithmic divergence is just a function of the BH parameters $F(r_+, r_-)$, or equivalently $F(T, J)$. Such a function changes from case to case, namely:

- For $\mathcal{SC}_A$ (5.2.36), $F(r_+, r_-) \propto K_+ = \frac{\rho_0}{2} - r_+$ with a positive coefficient.
- For $\mathcal{SC}_V$ (5.3.6), $F(r_+, r_-) \propto M$ with a positive coefficent.
- For $\mathcal{SC}_{V2.0}$ (5.3.7), $F(r_+, r_-) \propto K_- = \frac{\rho_0}{2} - r_-$ with a negative coefficient.

Sub/superadditivity. Taking as a subsystem the whole left (right) boundary at $t_b = 0$, the mutual complexity defined in eq. (4.4.29) reads

$$\Delta\mathcal{C} = \mathcal{SC}(L) + \mathcal{SC}(R) - \mathcal{C}^{\text{tot}} = \mathcal{SC}^{\text{ext}} - \mathcal{C}^{\text{tot}} = -\mathcal{SC}^{\text{int}} \,. \tag{5.4.1}$$

For AdS BHs the internal action I^{int} at $t_b = 0$ is finite [34, 149] and its sign depends on the value of the length scale $\tilde{L}$. In turn, depending on the sign of I^{int}, subregion action complexity $\mathcal{SC}_A$ can be either subadditive or superadditive, see the analog discussion in Sec. 4.4.3.
Instead, for WAdS BHs the internal action I^{int} in eq. (5.2.35) is always positive and independent of the counterterm length scale $\tilde{L}$. Consequently, $\Delta\mathcal{C}_A$ is negative, and $\mathcal{SC}_A$ of the left and right factors of the thermofield double state is superadditive. By construction, $\mathcal{SC}_V$ and $\mathcal{SC}_{V2.0}$ are also superadditive. However, $\mathcal{SC}_V$ for the left and right factors of the thermofield double state saturates superadditivity at $t_b = 0$, whereas $\mathcal{SC}_{V2.0}$ does not, see eqs. (5.3.1) and (5.3.8), respectively.

Temperature behavior. For neutral AdS BHs, $\mathcal{SC}_{V2.0}$ decreases with temperature. $\mathcal{SC}_A$ does the same if $\tilde{L} > L/2$, otherwise it increases with temperature. Instead, in $2+1$ bulk dimensions $\mathcal{SC}_V$ is a topological quantity independent of temperature [147].
For WAdS BHs, the leading dependence of subsystem complexity on temperature is governed by the coefficient of the $\log\Lambda$ term. It is thus convenient to define

$$H_J = \frac{\partial M}{\partial T}\Big|_J \,, \qquad H_+ = \frac{\partial K_+}{\partial T}\Big|_J \,, \qquad H_- = \frac{\partial K_-}{\partial T}\Big|_J \,. \tag{5.4.2}$$

Introducing the parameter

$$\varepsilon = r_-/r_+, \qquad 0 \leq \varepsilon < 1 \,, \tag{5.4.3}$$

the specific heat at constant angular momentum H_J can be directly calculated from eqs. (5.1.4), (5.1.6) and (5.1.7) as

$$\begin{aligned} H_J &= \frac{\partial M}{\partial r_+}\frac{\partial r_+}{\partial T} + \frac{\partial M}{\partial r_-}\frac{\partial r_-}{\partial T} \\ &= \frac{\pi \ell r_+}{4G}\,\frac{\nu(\varepsilon-1)\left(\varepsilon\left(-3\nu^2+2\nu\sqrt{(\nu^2+3)\,\varepsilon}+3\right)-2\nu\sqrt{(\nu^2+3)\,\varepsilon}\right)}{\varepsilon\left(\nu^2(4\varepsilon-1)-3\right)}\,, \end{aligned} \tag{5.4.4}$$

where the quantities $\frac{\partial r_+}{\partial T}$ and $\frac{\partial r_-}{\partial T}$ have been computed from the inverse of the matrix

$$\begin{pmatrix} \frac{\partial T}{\partial r_+} & \frac{\partial T}{\partial r_-} \\ \frac{\partial J}{\partial r_+} & \frac{\partial J}{\partial r_-} \end{pmatrix}. \tag{5.4.5}$$

Similarly, H_+ and H_- turn out to be

$$H_+ = \frac{\hat{a}}{\hat{b}}\,, \qquad H_- = \frac{\hat{c}}{\hat{b}}\,, \tag{5.4.6}$$

with

$$\begin{aligned} \hat{a} &= 2\pi\ell r_+\left(\sqrt{(\nu^2+3)\,r_+^2\varepsilon}-2\nu r_+\right)^2\left[\nu\left(\nu^2((\varepsilon-18)\varepsilon-7)+3\varepsilon(\varepsilon+6)+3\right)\right. \\ &\quad\left.\times\sqrt{(\nu^2+3)\,r_+^2\varepsilon}-r_+\varepsilon\left(-31\nu^4+6\nu^2+\left(\nu^2+3\right)^2\varepsilon+9\right)\right], \\ \hat{b} &= 3\left(\nu^2-1\right)\sqrt{(\nu^2+3)\,r_+^2\varepsilon}\left(4\nu\sqrt{(\nu^2+3)\,r_+^2\varepsilon}+\left(\nu^2+3\right)r_+(-\varepsilon-1)\right) \\ &\quad\times\left(2\nu(\varepsilon+1)\sqrt{(\nu^2+3)\,r_+^2\varepsilon}-\left(5\nu^2+3\right)r_+\varepsilon\right), \\ \hat{c} &= 2\pi\ell r_+\left(\sqrt{(\nu^2+3)\,r_+^2\varepsilon}-2\nu r_+\right)^2\left[\nu\left(\nu^2(\varepsilon(7\varepsilon+18)-1)-3(\varepsilon(\varepsilon+6)+1)\right)\right. \\ &\quad\left.\times\sqrt{(\nu^2+3)\,r_+^2\varepsilon}+r_+\varepsilon\left(\left(\nu^2+3\right)^2+\left(-31\nu^4+6\nu^2+9\right)\varepsilon\right)\right]. \end{aligned} \tag{5.4.7}$$

To study the sign of the quantities (5.4.2) as functions of (ϵ, ν), we define (see Fig. 5.4)

$$\begin{aligned} &\text{Region A}: \qquad 0 < \varepsilon < \frac{\nu^2+3}{4\nu^2} \equiv \varepsilon_c(\nu)\,, \\ &\text{Region B}: \qquad \varepsilon_c(\nu) < \varepsilon < 1\,. \end{aligned} \tag{5.4.8}$$

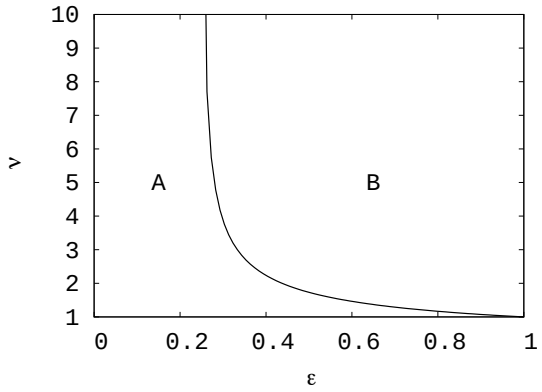

Figure 5.4: Regions of parameter space (ε, ν) with different temperature behavior of $\mathcal{SC}_V$ and $\mathcal{SC}_A$.

The angular momentum J (5.1.7) is negative (positive) in region A (B), while it vanishes along the two curves $\varepsilon = 0$ and $\varepsilon = \varepsilon_c(\nu)$. Interestingly, the quantities (H_J, H_+) change sign together with the angular momentum:

- H_J is negative in region A and positive in region B.
- H_+ is positive in region A and negative in region B.

Consequently, in the region where $H_J > 0$, $\mathcal{SC}_V$ increases with temperature at constant J, whereas $\mathcal{SC}_A$ decreases. Conversely, in the thermodynamically unstable region where $H_J < 0$, $\mathcal{SC}_V$ decreases with temperature, while $\mathcal{SC}_A$ increases.

To determine the sign of H_- we have to distinguish among three regions, which are shown in Fig. 5.5. In particular, region A, in which H_- is positive, is still the one defined in eq. (5.4.8), while region B splits into regions B_1, where H_- is negative, and B_2, where H_- is again positive. Therefore, $\mathcal{SC}_{V2.0}$ decreases with temperature at constant J in regions A and B_2, whereas it increases in region B_1.

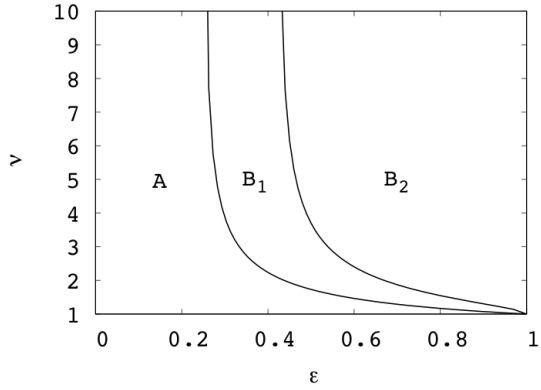

Figure 5.5: Regions of parameter space (ε, ν) with different temperature behavior of $\mathcal{SC}_{V2.0}$.

Finally, we observe that the three quantities (H_J, H_+, H_-) all diverge along the curves $\varepsilon = 0$ and $\varepsilon = \varepsilon_c(\nu)$. The divergence of H_J suggest a second order phase transition, similar to the one occurring for Kerr and Reissner-Nordström BHs in flat spacetime [183].

Chapter 6

Subregion complexity in a holographic global quench

This chapter is an adaptation of the published article [156].

So far, we have explored holographic mixed state complexity in static backgrounds, namely neutral BHs in AdS_3 and $WAdS_3$ spacetimes. In these cases subregion complexity is time-independent, due to the fact that the RT surface, which delimits the relevant spacetime regions involved in the holographic conjectures, always lies outside the BH. This does not happen in dynamical backgrounds, where subregion complexity manifests a non-trivial time evolution.

In this last part of the thesis we focus on *quantum quenches*, extensively studied out-of-equilibrium processes modeling the evolution of perturbed systems towards a new equilibrium condition. Such processes can be divided into two main classes: *global quenches*, in which the perturbation interests the whole system, and *local quenches*, in which the initial perturbation is localized in a finite region. In the context of the AdS/CFT correspondence, gravitational realizations are known for both kinds of quenches. In particular, a CFT global quench is holographically represented by the Vaidya geometry [75], describing the formation of an AdS BH due to the gravitational collapse of matter. On the other hand, a CFT local quench is equivalent to the free fall of a particle-like object in AdS spacetime [76], a model which we will thoroughly study in Ch. 7.

By exploiting the gravitational description of CFT quenches, holographic complexity has been investigated for both the global [68–70, 184] and local case [71, 72]. In this chapter we address the problem of determining the time

evolution of subregion-CV for a boundary segment in $(2+1)$-dimensional Vaidya spacetime. This analysis was initiated in [155] for generic spacetime dimensions, and was also performed for solutions of modified gravity [185, 186]. However, in all these works a translation-invariant ansatz for the codimension-one extremal surface involved in subregion-CV conjecture is advocated. While this assumption is correct in time-independent geometries, we argue that it is in general not consistent in Vaidya spacetime. We thus compute the extremal surface numerically and we investigate how its volume changes as a function of the boundary time at which the subregion lies.

The chapter is organized as follows: in Sec. 6.1 we describe the Vaidya geometry and we review the analytic HRT surface in case the shell of collapsing matter has zero thickness. In Sec. 6.2 we show that the translation-invariant ansatz for the codimension-one extremal surface is inconsistent and we numerically compute subregion-CV for a boundary segment. We finally comment the result in Sec. 6.3. Some technical details are collected in Appendix C.

6.1 Spacelike geodesics in Vaidya spacetime

According to the subregion-CV proposal, mixed state complexity of a time-dependent boundary state is related to the volume of a codimension-one extremal bulk surface anchored at the HRT surface [96] of the boundary state itself. In $2+1$ bulk dimensions, the HRT surface is simply a spacelike geodesic attached to a boundary line segment. Following [75], in this section we review how to build this kind of geodesics in $(2+1)$-dimensional Vaidya spacetime.

The spacetime metric is

$$\begin{aligned} ds^2 &= -r^2 f(v,r)\, dv^2 + 2\, dv\, dr + r^2\, dx^2 \\ &= \frac{1}{z^2}\left[-f\,(v,z)\, dv^2 - 2\, dv\, dz + dx^2\right] , \end{aligned} \tag{6.1.1}$$

in which we have set the AdS radius $L=1$ and

$$f = 1 - \frac{m(v)}{r^2} = 1 - m(v)\, z^2 . \tag{6.1.2}$$

We will interchangeably use r or $z=1/r$ as a radial coordinate. As usual, the coordinate v is constant along infalling null rays and its value at the spacetime boundary $r\to\infty$ (equivalently, $z\to 0$) coincides with the boundary time.
For $m(v)=M$, by expressing the metric (6.1.1) in the time coordinate t, given

by $dv = dt - dz/f$, we get the BTZ BH in Schwarzschild coordinates (4.3.1):

$$ds^2 = \frac{1}{z^2}\left(-f dt^2 + \frac{dz^2}{f} + dx^2\right), \qquad f = 1 - Mz^2 . \tag{6.1.3}$$

For $m(v) = 0$, we instead recover vacuum AdS_3 (4.2.1). For the Vaidya metric to describe the formation of a BTZ BH triggered by the collapse of null matter, we are thus interested in functions $m(v)$ interpolating between $m = 0$ and $m = M$. Such a geometry models a CFT_2 global quench.

Concretely, in the numerical calculations we will take

$$m(v) = \frac{M}{2}\left(1 + \tanh\frac{v}{\tilde{v}}\right), \tag{6.1.4}$$

where $\tilde{v}$ parametrizes the thickness of the shell. In the zero thickness limit $\tilde{v} \to 0$, $m(v)$ can be written in terms of the Heaviside step function $\vartheta(v)$ as

$$m(v) = M\,\vartheta(v) . \tag{6.1.5}$$

With this choice, the spacetime metric (6.1.1) interpolates between vacuum AdS_3 for $v < 0$ and the BTZ BH for $v > 0$. The infinitesimally thick shell of collapsing null dust falls from the spacetime boundary at time $t = 0$ and follows the null trajectory $v = 0$ into the bulk. In the situation described by eq. (6.1.5), analytical solutions for the spacelike geodesics are available.

We are interested in spacelike geodesics anchored at the boundary subregion, which we consider as a segment of length l lying at constant time t on the boundary. In particular, we adopt the symmetric configuration $x \in \left[-\frac{l}{2}, \frac{l}{2}\right]$. Therefore, parametrizing the HRT geodesic as $v(x), r(x)$, the boundary conditions at $r = +\infty$ are

$$x(r = \infty) = \pm\frac{l}{2}, \qquad v(r = \infty) = t . \tag{6.1.6}$$

By symmetry, the geodesic turning point $r = r_*$ is at $x = 0$, i.e.

$$x(r = r_*) = 0, \qquad v(r = r_*) = v_* . \tag{6.1.7}$$

Note that both r_* and v_* are functions of the boundary time t.

Since the spacetime (6.1.5) is characterized by a junction between AdS_3 and BTZ at $v = 0$, the general HRT geodesic can be obtained by gluing at $v = 0$ the HRT geodesic for the BTZ BH and the one for AdS_3. We denote by $r = r_s$ the position of such gluing points.

6.1.1 AdS_3 geodesics

For $v < 0$, the Vaidya spacetime is the vacuum AdS_3

$$ds^2 = -r^2 dv^2 + 2\, dv\, dr + r^2\, dx^2 \ . \tag{6.1.8}$$

The corresponding portion of the HRT surface is given by the spacelike geodesic at constant bulk time

$$x_\pm(r) = \pm \frac{\sqrt{r^2 - r_*^2}}{r_* r}\,, \qquad v_\pm(r) = \frac{1}{r_s} - \frac{1}{r}\,, \tag{6.1.9}$$

where (r_*, r_s) are functions of the boundary time t and the subregion length l. We refer to $(x_+(r), v_+(r))$ and $(x_-(r), v_-(r))$ as branches 1 and 2, respectively. At initial time $t = 0$, the geodesic is entirely in AdS_3, so a comparison with eq. (4.2.4) gives

$$r_*(t=0) = \frac{2}{l}\,. \tag{6.1.10}$$

6.1.2 BTZ geodesics

For $v > 0$, the Vaidya spacetime is the BTZ BH

$$\begin{aligned} ds^2 &= -r^2 \left(1 - \frac{r_h^2}{r^2}\right) dv^2 + 2\, dv\, dr + r^2\, dx^2 \\ &= -\left(r^2 - r_h^2\right) dt^2 + \frac{dr^2}{r^2 - r_h^2} + r^2 dx^2\,. \end{aligned} \tag{6.1.11}$$

The BH event horizon is located at $r = r_h = \sqrt{M}$ and the Hawking temperature is $T = r_h/(2\pi)$. Following [75], the geodesic equations are

$$\begin{aligned} -r_h E &= -\left(r^2 - r_h^2\right) \dot{t}\,, \qquad r_h J = r^2 \dot{x}\,, \\ 1 &= -\left(r^2 - r_h^2\right) \dot{t}^2 + \frac{\dot{r}^2}{r^2 - r_h^2} + r^2 \dot{x}^2\,, \end{aligned} \tag{6.1.12}$$

where the dot denotes a derivative with respect to the affine parameter λ. The constants of motion E and J are associated to the invariance under t and x translations, and can thus be interpreted as the energy and angular momentum of the geodesic, respectively. Requiring the solution to be invariant under

$x \to -x$, the spacelike geodesics satisfying eqs. (6.1.12) can be expressed as [75]

$$x_{\pm}(r) = \frac{1}{2r_h} \ln \left| \frac{r^2 - J\, r_h^2 \pm \sqrt{r^4 + (E^2 - J^2 - 1)\, r_h^2\, r^2 + J^2\, r_h^4}}{r^2 + J\, r_h^2 \pm \sqrt{r^4 + (E^2 - J^2 - 1)\, r_h^2\, r^2 + J^2\, r_h^4}} \right| + \frac{1}{4r_h} \ln \left| \frac{(J+1)^2 - E^2}{(J-1)^2 - E^2} \right| , \tag{6.1.13}$$

$$v_{\pm}(r) = \frac{1}{2r_h} \ln \left| \frac{r^2 - (E+1)\, r_h^2 \pm \sqrt{r^4 + (E^2 - J^2 - 1)\, r_h^2\, r^2 + J^2\, r_h^4}}{r^2 + (E-1)\, r_h^2 \pm \sqrt{r^4 + (E^2 - J^2 - 1)\, r_h^2\, r^2 + J^2\, r_h^4}} \right| + \frac{1}{2r_h} \ln \left| \frac{r - r_h}{r + r_h} \right| + t\,. \tag{6.1.14}$$

Such geodesics represent the portion of the HRT surface in the Vaidya spacetime for $v > 0$.

According to the values of E, J in eqs. (6.1.13) and (6.1.14), the geodesics can be divided into four classes, as shown in Fig. 6.1:

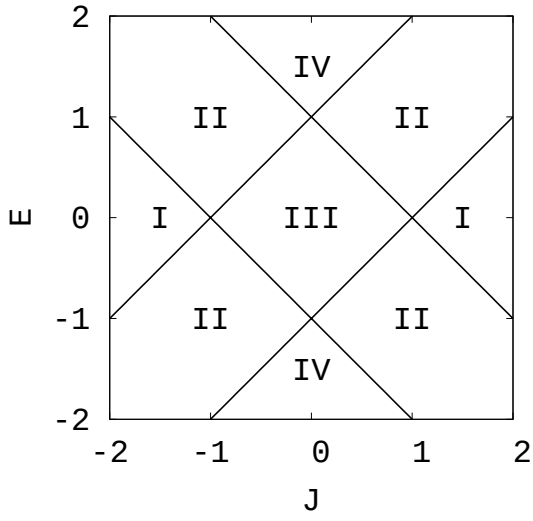

Figure 6.1: The four classes of BTZ spacelike geodesics in the parameter space (J, E). The figure is a reproduction of a picture taken from [75].

Geodesics with $E = 0$ lies on t-constant slices into the bulk. Without loss of generality, let us suppose that $J > 0$. As it is clear from Fig. 6.1, there are only

two kinds of geodesics, characterized by $J > 1$ (region I) and $J < 1$ (region III).[1] We show plots of such geodesics in Fig. 6.2:

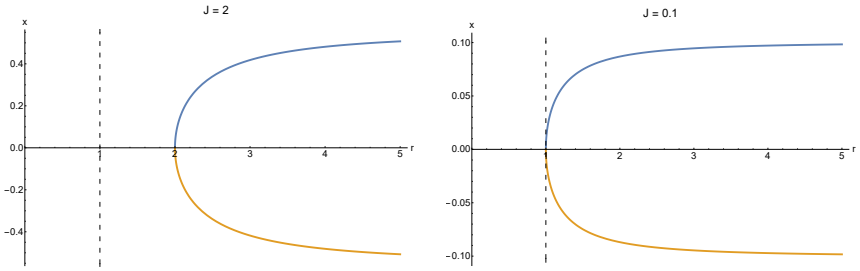

(I) (III)

Figure 6.2: Spacelike geodesics (6.1.13) in BTZ spacetime with $E = 0$ and different values of the parameter J. The blue curve represents $x_+(r)$, while the yellow one represents $x_-(r)$. The dotted line represents the BH event horizon, which we set to $r_h = 1$.

By direct calculation, we find that the turning point $r_* = r_0$ is

$$r_0 = \begin{cases} J\, r_h\,, & J > 1\,, \\ r_h\,, & J < 1\,. \end{cases} \tag{6.1.15}$$

The geodesics in region I have minimal length compared to geodesics in region III, so the former are eligible as RT surfaces in the static BTZ BH. As we have already argued in Sec. 4.3, the RT surface in this scenario never penetrates inside the BH, being $r_0 > r_h$. For $J > 1$, the angular momentum J is related to the boundary subregion length l by

$$\frac{l}{2} = \frac{1}{4r_h} \ln\left(\frac{J+1}{J-1}\right)^2 , \qquad \text{or} \qquad J = \coth\left(\frac{r_h\, l}{2}\right) . \tag{6.1.16}$$

Therefore, the turning point position can be expressed in terms of l as

$$r_0 = r_h \coth\left(\frac{r_h\, l}{2}\right) . \tag{6.1.17}$$

For generic E, there are in principle four classes of geodesics, which are shown in Fig. 6.3. Contrary to the equal-time geodesics with $E = 0$, these curves cross the BH event horizon. Moreover, if $E \neq 0$ the spacelike geodesics in eqs. (6.1.13) and (6.1.14) connect points on the spacetime boundary at different

[1] In the special case $E = 0$ and $J = 1$, the geodesic is singular. We shall see that this value will be never attained in our context.

values of the time coordinate t. Even though the subregions we are interested in lies at t-constant slices on the spacetime boundary, solutions with $E \neq 0$ are allowed in Vaidya spacetime, since they can be part of full geodesics with equal-time endpoints.

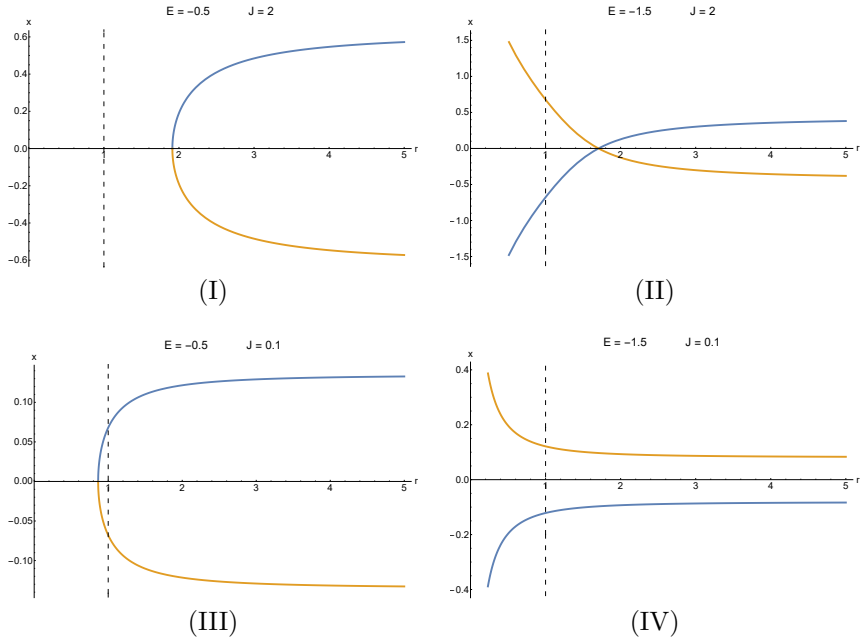

Figure 6.3: Spacelike geodesics (6.1.13) in BTZ spacetime with different values of the parameters (E, J). The blue curve represents $x_+(r)$, while the yellow one represents $x_-(r)$. The BH event horizon $r_h = 1$ is represented by the dotted line.

6.1.3 Joining geodesics

The HRT surface in Vaidya spacetime can be obtained by gluing together the AdS_3 geodesic (6.1.9) and the BTZ one (6.1.13,6.1.14) at $r = r_s$. Following [75], the requirement that the length of the full geodesic is minimal fixes the two constants of motion of the BTZ portion:

$$E = -\frac{r_h\sqrt{r_s^2 - r_*^2}}{2r_s^2}\,, \qquad J = \frac{r_*}{r_h}\,. \tag{6.1.18}$$

It is important to note that (E, J) depend on the boundary time t and on the subregion length l. For fixed length l, their time dependence can thus be

determined by two constraints on the parameters (r_s, r_*). The first constraint fixes the subregion length l to be the sum of the AdS (6.1.9) and BTZ (6.1.13) contributions. Expressing the condition as $f_l(r_s, r_*) = 0$, we have

$$f_l(r_s, r_*) = \frac{1}{r_h} \ln \frac{2r_s \left(r_s^2 + r_* r_h\right) + \left(2r_s^2 - r_h^2\right) \sqrt{r_s^2 - r_*^2}}{2r_s \left(r_s^2 - r_* r_h\right) + \left(2r_s^2 - r_h^2\right) \sqrt{r_s^2 - r_*^2}} + 2\frac{\sqrt{r_s^2 - r_*^2}}{r_s r_*} - l \,. \tag{6.1.19}$$

The second constraint is determined from eq. (6.1.14) by imposing $v(r_s) = 0$, and reads

$$\frac{r_s}{r_h} = \frac{1}{2} \left(\coth(r_h t) + \sqrt{\coth^2(r_h t) - \frac{2\sqrt{1 - \frac{r_*^2}{r_s^2}}}{1 + \sqrt{1 - \frac{r_*^2}{r_s^2}}}} \right) . \tag{6.1.20}$$

Unfortunately, the system of eqs. (6.1.19) and (6.1.20) cannot be solved in closed-form. In Appendix C.1 we provide analytic approximations for (r_s, r_*) at small and large times t. Numerical results for given values of the boundary subregion size l are shown in Fig. 6.4:

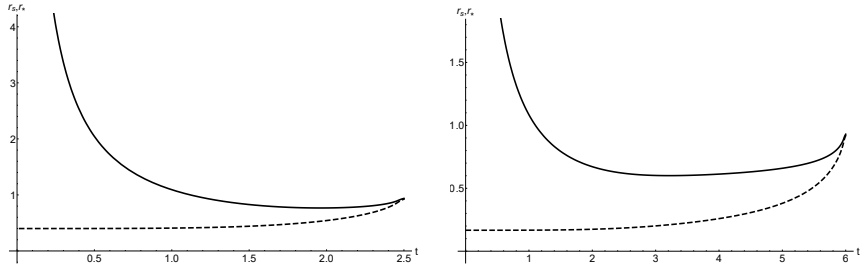

Figure 6.4: Junction point position r_s (solid line) and turning point r_* (dashed line) of the HRT geodesic in Vaidya spacetime as functions of the boundary time t. The subregion length is $l = 5$ on the left and $l = 12$ on the right, and we have set $r_h = 1$.

At initial boundary time $t = 0$, the HRT geodesic entirely lies in the AdS part of the full spacetime, so $r_s \to \infty$ and $r_*(0) = 2/l$. We define as *thermalization time* t_* the value of the boundary time at which the whole HRT geodesic enters the BTZ part of spacetime, namely $r_s = r_*$. For $t > t_*$, the HRT geodesic entirely lies in BTZ, so subregion volume complexity drops to the constant thermal value (4.3.35). Eqs. (6.1.19) and (6.1.20) give

$$t_* = l/2 \,, \qquad r_*(t_*) = r_s(t_*) = r_0 \,, \tag{6.1.21}$$

see eq. (6.1.17). For $l \gg 1/r_h$, we have $r_0 \to r_h$.

At intermediate times $0 < t < t_*$, the HRT geodesic crosses the shell of null dust. It is useful to define:

$$\begin{aligned}
\chi^{\pm}(r) &= \frac{1}{2r_h} \ln \left| \frac{r^2 - J\, r_h^2 \pm \sqrt{r^4 + (-1 + E^2 - J^2)\, r_h^2\, r^2 + J^2\, r_h^4}}{r^2 + J\, r_h^2 \pm \sqrt{r^4 + (-1 + E^2 - J^2)\, r_h^2\, r^2 + J^2\, r_h^4}} \right| + \frac{l}{2}\,, \\
\nu^{\pm}(r) &= \frac{1}{2r_h} \ln \left| \frac{r^2 - (E+1)\, r_h^2 \pm \sqrt{r^4 + (E^2 - J^2 - 1)\, r_h^2\, r^2 + J^2\, r_h^4}}{r^2 + (E-1)\, r_h^2 \pm \sqrt{r^4 + (E^2 - J^2 - 1)\, r_h^2\, r^2 + J^2\, r_h^4}} \right| \\
&\quad + \frac{1}{2r_h} \ln \left| \frac{r - r_h}{r + r_h} \right| + t\,,
\end{aligned} \tag{6.1.22}$$

in which the values of E and J are given by eq. (6.1.18). The sign of (E, J) implies that if $r_s \geq r_h/\sqrt{2}$ we have to consider only branch 1, whereas if $r_s \leq r_h/\sqrt{2}$ also branch 2 comes into play [75]. In the latter case, a part of branch 2 connects the AdS_3 geodesic to the full branch 1, which is anchored at the spacetime boundary.

To be more precise, let us denote by r_m the minimal value of the r-coordinate on the BTZ part of the HRT geodesic, namely

$$r_m^2 = \frac{r_h^2}{2} \left(1 - E^2 + J^2 + \sqrt{(1 - E^2 + J^2)^2 - 4J^2} \right)\,, \tag{6.1.23}$$

where E, J are again given by eq. (6.1.18).
In the case $r_s \geq r_h/\sqrt{2}$, the full Vaidya geodesic is

$$\begin{aligned}
\hat{x}_{\pm}(r) &= \begin{cases} \pm \frac{\sqrt{r^2 - r_*^2}}{r_*\, r} & \text{if} \quad r \leq r_s,\ v \leq 0\,, \\ \pm \chi^{+}(r) & \text{if} \quad r > r_s,\ v > 0\,, \end{cases} \\
\hat{v}_{\pm}(r) &= \begin{cases} \frac{1}{r_s} - \frac{1}{r} & \text{if} \quad r \leq r_s,\ v \leq 0\,, \\ \nu^{+}(r) & \text{if} \quad r > r_s,\ v > 0\,. \end{cases}
\end{aligned} \tag{6.1.24}$$

Instead, in the case $r_s \leq r_h/\sqrt{2}$, the full geodesic is

$$\begin{aligned}
\hat{x}_{\pm}(r) &= \begin{cases} \pm \frac{\sqrt{r^2 - r_*^2}}{r_*\, r} & \text{if} \quad r \leq r_s,\ v \leq 0\,, \\ \pm \chi^{+}(r) & \text{if} \quad r \geq r_m,\ v > 0\,, \\ \pm \chi^{-}(r) & \text{if} \quad r_m \leq r < r_s,\ v > 0\,, \end{cases} \\
\hat{v}_{\pm}(r) &= \begin{cases} \frac{1}{r_s} - \frac{1}{r} & \text{if} \quad r \leq r_s,\ v \leq 0\,, \\ \nu^{+}(r) & \text{if} \quad r \geq r_m,\ v > 0\,, \\ \nu^{-}(r) & \text{if} \quad r_m \leq r < r_s,\ v > 0\,. \end{cases}
\end{aligned} \tag{6.1.25}$$

An example of time evolution of the HRT geodesic in Vaidya spacetime is shown in Fig. 6.5, where the radial coordinate $z = 1/r$ is adopted:

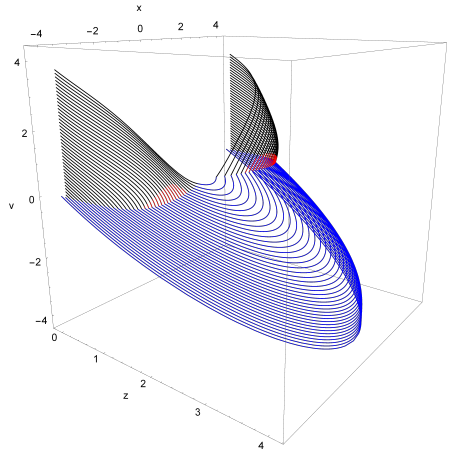

Figure 6.5: Time evolution of the HRT geodesic in Vaidya spacetime for $l = 8, r_h = 1$. The black and red curves represent branch 1 and 2 in the BTZ portion of spacetime, respectively. The blue curve denotes the AdS part of the full geodesic.

6.1.4 Numerical geodesics

In order to render the problem of solving the partial differential equations for the codimension-one extremal surface more tractable, it is useful to consider a non-zero shell thickness $\tilde{v}$ in eq. (6.1.4). Such a choice spoils the analytic solution for the HRT geodesic expressed in eqs. (6.1.24) and (6.1.25), so we have to numerically solve the geodesic equations:

$$\ddot{z} + \left(z\, m(v) - \frac{2 + z^3 m'(v)}{2z} \right) \dot{v}^2 - \frac{2}{z}\dot{z}^2 - \frac{2}{z}\dot{z}\dot{v} + \left(\frac{1}{z} - z m(v) \right) \dot{x}^2 = 0\,,$$

$$\ddot{v} + \frac{\dot{v}^2}{z} - \frac{\dot{x}^2}{z} = 0\,, \qquad \ddot{x} - 2\frac{\dot{x}\dot{z}}{z} = 0\,, \tag{6.1.26}$$

where the dot denotes a derivative with respect to the affine parameter λ and the prime a derivative with respect to the coordinate v. The geodesics we are interested in satisfy the boundary conditions in eq. (6.1.6), and are determined by solving the geodesic equations (6.1.26) by means of a shooting method implemented in Wolfram Mathematica. We have checked that in the $\tilde{v} \to 0$ limit the analytic geodesics described in Sec. 6.1.3 are recovered.

6.2 Subregion volume complexity

In this section we investigate the time evolution of the volume of the codimension-one extremal surface anchored at the boundary segment of length l and at the corresponding HRT geodesic. According to subregion-CV, such a volume is conjectured to be dual to mixed state complexity in the boundary CFT_2 [39].

6.2.1 Volume in AdS_3 and BTZ

As the HRT geodesic, in the initial stage $t \leq 0$ the extremal codimension-one surface is entirely in AdS_3, whereas in the final stage $t \geq l/2$ the surface is entirely in the BTZ part of spacetime. In this section, we will regularize the UV divergent volume by subtracting its initial value V_{AdS}. In vacuum AdS_3, the RT surface is given by eq. (4.2.3)

$$z^2 + x^2 = \left(\frac{l}{2}\right)^2 , \tag{6.2.1}$$

and the codimension-one extremal surface is simply

$$z = t - v \, , \tag{6.2.2}$$

with t the boundary time. So, introducing a UV cutoff at $z = 1/\Lambda$, we get

$$V_{AdS} = 2 \int_{1/\Lambda}^{l/2} \frac{\sqrt{(l/2)^2 - z^2}}{z^2} dz = l\,\Lambda - \pi \, . \tag{6.2.3}$$

As we have discussed in Sec. 4.3, after thermalization the volume is exactly the same, i.e.

$$V_{BTZ} = V_{AdS} \, . \tag{6.2.4}$$

This outcome is a hallmark of the $(2+1)$-dimensional case, and is a consequence of the Gauss-Bonnet theorem [147]. As a result, after thermalization subregion volume complexity returns to its initial value.

6.2.2 Inconsistency of the x-independent ansatz

We now focus on volume subregion complexity at intermediate times $0 < t < l/2$. We start by parametrizing the extremal codimension-one surface as $v(x, r)$ in the full Vaidya spacetime. Thus, the volume functional can be written as

$$V = \int dr\, dx\, \mathcal{V} \, , \qquad \mathcal{V} = \sqrt{r^2(2 - r^2 f \partial_r v)\partial_r v - (\partial_x v)^2} \, , \tag{6.2.5}$$

where $f = f(r, v)$. Defining

$$v_x = \partial_x v\,, \qquad v_r = \partial_r v\,, \tag{6.2.6}$$

the Euler-Lagrange equation for the volume functional reads

$$\partial_x \left(\frac{\partial \mathcal{V}}{\partial v_x} \right) + \partial_r \left(\frac{\partial \mathcal{V}}{\partial v_r} \right) - \frac{\partial \mathcal{V}}{\partial v} = 0\,. \tag{6.2.7}$$

Since the functional (6.2.5) is invariant under translations in x, it is reasonable to look for x-independent solutions of eq. (6.2.7), characterized by

$$v_x = 0\,, \qquad \partial_x v_r = 0\,. \tag{6.2.8}$$

With this ansatz, if we restrict to the BTZ portion of spacetime, where $f = f_{BTZ}(r)$, the equation of motion (6.2.7) reduces to the ordinary differential equation

$$\left(3r_h^2 - 6r^2\right) v'(r)^2 + \left(-3r^2 r_h^2 + r_h^4 + 2r^4\right) v'(r)^3 - r v''(r) + 2v'(r) = 0\,, \tag{6.2.9}$$

in which the prime denotes a derivative with respect to the coordinate r.

In the BTZ portion of spacetime, the extremal codimension-one surface we are looking at must be attached to the spacelike geodesic (6.1.13,6.1.14). Consequently, in order for the x-independent ansatz to be consistent, eq. (6.2.9) must be satisfied by the geodesic itself. This is correct just for $E = 0$, which holds in static BTZ. Therefore, in the time-dependent background where $E \neq 0$, the x-independent ansatz considered in [155] is not a solution to the equation of motion (6.2.9) and cannot be regarded as the extremal codimension-one surface.

By the way, in the full Vaidya spacetime, the x-independent ansatz is exact both in the initial stage $t \leq 0$ and in the final stage $t \geq l/2$. Moreover, we will provide numerical evidence that nearby these two time regimes such an ansatz is a good approximation to the actual solution of eq. (6.2.7). So, we refer to the configuration $v(r)$ attached to the HRT geodesic (6.1.24,6.1.25) as the *pseudosolution*. Since the actual solution is expected to be a local maximum of the volume functional, we also expect the volume of the pseudosolution to constitute a lower bound for the volume of the solution. We will check this expectation by explicit numerical examples.

6.2.3 Volume of the pseudosolution

To attain an analytic lower bound to the volume subregion complexity, we consider the x-independent ansatz for the codimension-one extremal surface.

The total volume of the pseudosolution $\hat{V}$ is the sum of the AdS and BTZ contributions:

$$\hat{V} = \hat{V}_{AdS} + \hat{V}_{BTZ}\,. \tag{6.2.10}$$

The AdS_3 part gives

$$\hat{V}_{AdS} = -\pi + 2\frac{\sqrt{r_s^2 - r_*^2}}{r_*} + 2\arcsin\frac{r_*}{r_s}\,. \tag{6.2.11}$$

In the BTZ part of spacetime, the pseudosolution is given by eq. (6.1.14), in which the plus sign corresponds to branch 1 and the minus sign to branch 2. For both branches, the square root of the induced metric determinant reads

$$\psi(r) = r\sqrt{\frac{(r-r_*)\,(r+r_*)}{r^4 + \left[-1 + \frac{r_h^2(r_s^2-r_*^2)}{4r_s^4} - \frac{r_*^2}{r_h^2}\right] r_h^2\, r^2 + r_*^2\, r_h^2}}\,, \tag{6.2.12}$$

where we have plugged in the values for E and J given in eq. (6.1.18). Therefore, from eqs. (6.1.24) and (6.1.25) we get

$$\begin{aligned}\hat{V}_{BTZ} = {} & 2\,\vartheta\left(r_s - \frac{r_h}{\sqrt{2}}\right)\int_{r_s}^{\Lambda} dr\,\psi(r)\int_0^{\chi^+(r)} dx \\ & + 2\,\vartheta\left(\frac{r_h}{\sqrt{2}} - r_s\right)\left\{\int_{r_m}^{\Lambda} dr\,\psi(r)\int_0^{\chi^+(r)} dx + \int_{r_m}^{r_s} dr\,\psi(r)\int_0^{\chi^-(r)} dx\right\}\,,\end{aligned} \tag{6.2.13}$$

in which $r = \Lambda$ is the UV cutoff.

Summing up the two contributions, we find a closed-form expression for the volume of the pseudosolution:

$$\begin{aligned}\hat{V} = {} & -\pi + 2\frac{\sqrt{r_s^2 - r_*^2}}{r_*} + 2\arcsin\frac{r_*}{r_s} + l\int_{r_s}^{\Lambda} dr\,\psi(r) \\ & + \frac{1}{r_h}\int_{r_s}^{\Lambda} dr\,\psi(r)\,\ln\frac{r^2 - r_*\,r_h + \sqrt{r^4 + \left[-1 + \frac{r_h^2(r_s^2-r_*^2)}{4r_s^4} - \frac{r_*^2}{r_h^2}\right] r_h^2\, r^2 + r_*^2\, r_h^2}}{r^2 + r_*\,r_h + \sqrt{r^4 + \left[-1 + \frac{r_h^2(r_s^2-r_*^2)}{4r_s^4} - \frac{r_*^2}{r_h^2}\right] r_h^2\, r^2 + r_*^2\, r_h^2}} \\ & + \vartheta\left(\frac{r_h}{\sqrt{2}} - r_s\right)\left\{\frac{1}{r_h}\ln\frac{1 - \frac{r_h^2(r_s^2-r_*^2)}{4r_s^4} + \frac{r_*^2}{r_h^2} - 2\frac{r_*}{r_h}}{1 - \frac{r_h^2(r_s^2-r_*^2)}{4r_s^4} + \frac{r_*^2}{r_h^2} + 2\frac{r_*}{r_h}} + 2\,l\right\}\int_{r_m}^{r_s} dr\,\psi(r)\,.\end{aligned} \tag{6.2.14}$$

When the subregion length is such that $l >> 1/r_h$, the time evolution of the volume of the pseudosolution (6.2.14) is characterized by three stages. We here summarize the main features of each regime, deferring the details of the computations to Appendix C.

Early times. In this regime we have

$$r_* = \frac{2}{l}\,, \qquad r_s = \frac{r_h}{2}\coth\left(\frac{r_h t}{2}\right)\,. \tag{6.2.15}$$

Plugging eq. (6.2.15) into the volume (6.2.14), we obtain

$$\frac{\hat{V}}{l} = \Lambda + r_h\,\tanh\frac{r_h t}{2} + \mathcal{O}(1/l)\,. \tag{6.2.16}$$

Such an expression suitably describes the pseudosolution volume for both $r_s > r_h/\sqrt{2}$ and $r_s < r_h/\sqrt{2}$, provided that eq. (6.2.15) can be trusted. From numerical evidence, it turns out that this is true up to a time of $\mathcal{O}(\log(r_h l))$.

As we will see by comparison with the numerical result, at early times the pseudosolution is a good approximation of the actual solution. In particular, we can rely on the first order Taylor expansion of eq. (6.2.16), which leads to

$$\frac{V}{l} = \Lambda + \frac{r_h^2\,t}{2} + \mathcal{O}(1/l)\,. \tag{6.2.17}$$

Such an outcome is further supported by the inequality $\tanh x \leq x$, in agreement with the fact that the volume of the pseudosolution provides a lower bound to the extremal volume. Furthermore, eq. (6.2.17) reproduces the same growth rate of volume complexity obtained in [69] for a one-sided Vaidya BH

$$\frac{dV}{dt} = \Omega_0\frac{r_h^2}{2}\,. \tag{6.2.18}$$

In our case, the divergent quantity Ω_0 corresponds to the boundary subregion length l in the limit $l \to +\infty$, describing a dual pure state.

Intermediate times, $\mathcal{O}(\log r_h l) < t < \frac{l}{2} - \frac{0.53}{r_h}$. The volume of the pseudosolution is

$$\frac{\hat{V}}{l} \approx \Lambda + \frac{\hat{V}_1}{l} + (\varpi - 1)\eta(r_s) - \varpi\,\eta(r_m)\,, \tag{6.2.19}$$

where $\hat{V}_1$, ϖ, and $\eta(r)$ are defined in Appendix C.2. Unfortunately, at large l we expect a significant deviation between the pseudosolution volume and the extremal one. Nonetheless, the estimate (6.2.19) bounds the extremal volume from below.

Late times, $\frac{l}{2} - \frac{0.53}{r_h} < t < \frac{l}{2}$. The volume of the pseudosolution is estimated to be

$$\frac{\hat{V}}{l} = \Lambda + \frac{r_h^2\, l}{4} \frac{\sqrt{r_s r_h (r_h - r_s)(2r_s - r_h)}}{(r_s - r_h)^2 + r_s^2} + \mathcal{O}(l^0)\,, \tag{6.2.20}$$

see Appendix C.2 for a derivation. The volume $\hat{V}$ attains its maximum value at $r_s = r_h/\sqrt{2}$, where it scales as

$$\max\left(\frac{\hat{V}}{l}\right) = \Lambda + \frac{r_h^2\, l}{8}\,. \tag{6.2.21}$$

By means of eq. (C.1.7), we find the following behavior nearby the thermalization time $t \approx l/2$:

$$r_s \approx r_h \left(1 - \sqrt{\frac{r_h}{2}\left(\frac{l}{2} - t\right)}\right), \qquad \frac{\hat{V}}{l} \approx \Lambda + l\left(\frac{r_h}{2}\right)^{9/4}\left(\frac{l}{2} - t\right)^{1/4}. \tag{6.2.22}$$

We expect the pseudosolution volume to satisfactorily approximate the extremal volume in this time regime too, as can be directly checked from the numerical solution which we present in the next subsection.

6.2.4 Numerical solution

Unfortunately, we do not have an analytic expression for the actual solution which extremizes the volume functional. Therefore, in order to compute the extremal volume involved in subregion-CV, we have to perform a numerical analysis. For convenience, we parametrize the extremal surface as $z(x, v)$, which we expect to be a single-valued function.[2] The new volume functional is

$$V = \int dv\, dx\, \mathcal{V}\,, \qquad \mathcal{V} = \frac{\sqrt{-(2\partial_v z + f(v,z)) - (\partial_x z)^2}}{z^2}\,, \tag{6.2.23}$$

where

$$z_x = \partial_x z\,, \qquad z_v = \partial_v z\,. \tag{6.2.24}$$

The Euler-Lagrange equation for the volume functional is

$$\partial_x\left(\frac{\partial \mathcal{V}}{\partial z_x}\right) + \partial_v\left(\frac{\partial \mathcal{V}}{\partial z_v}\right) - \frac{\partial \mathcal{V}}{\partial z} = 0\,. \tag{6.2.25}$$

[2] The solution expressed as $v(z, x)$ is not single-valued nearby the regions where branch 1 is attached to branch 2. This is not convenient for numerical calculations.

More explicitly, the differential equation for the extremal solution $z(x, v)$ reads

$$\begin{aligned} &- z_{vv} + z_{xx}(2z_v + f) - 2z_{vx}z_x + (z_x)^2 \frac{(2f - z\partial_z f + 2z_v)}{z} \\ &+ 4\frac{(z_v)^2}{z} + 3z_v \frac{(4f - z\partial_z f)}{2z} + 2\frac{f^2}{z} - \frac{1}{2} f\partial_z f - \frac{1}{2}\partial_v f = 0\,, \end{aligned} \tag{6.2.26}$$

with boundary condition specified by the HRT geodesic.

We have solved eq. (6.2.26) numerically using both the analytic and numerical geodesics found in Sec. 6.1, and we have checked that all results match when $\tilde{v}$ is small enough for the numerical solution of eqs. (6.1.26) to represent a good approximation of the analytic solution in the $\tilde{v} \to 0$ limit.
Specifically, we have used the finite-element method implemented in Wolfram Mathematica to solve the equations in an adaptive triangulation of the HRT geodesic, the discretization consisting of cells with maximum size $\mathcal{O}(10^{-4})$ in units of $r_h = 1$. To check that our results are robust, we reproduced them independently with a linearized iterative solver working on a regular rectangular grid meshing the HRT geodesic.

We have numerically solved the volume equations up to $r_h\, l = 6$. Higher values of l are numerically challenging, because the geodesics develop sharp kinks requiring very fine-grained discretizations in order to obtain reliable results. An example of numerical solution is shown in Fig. 6.6:

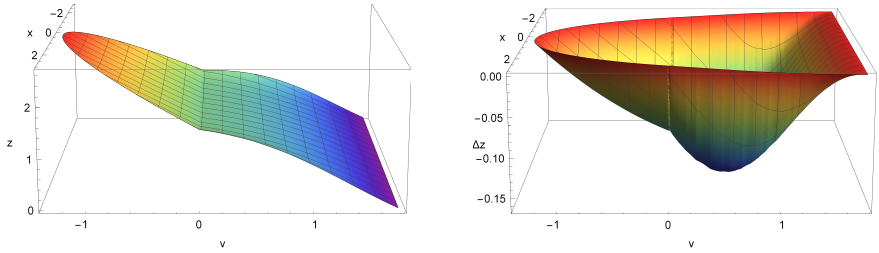

Figure 6.6: On the left: Extremal codimension-one surface computed numerically. On the right: Difference Δz between the actual solution and the pseudosolution. We have set $l = 6$, $t = 1.75$ and $r_h = 1$.

The extremal surface is not smooth at the shell, as expected from the curves shown in Fig. 6.5. As it can be seen in the right part of Fig. 6.6, there are significant differences between the numerical solution and the pseudosolution.

We can now study the time evolution of the on shell volume functional (6.2.23), which we denote by V. As already discussed, we regularize the UV divergences by subtracting the vacuum AdS volume of eq. (6.2.3). Since the volume

divergences are time-independent, the resulting quantity is finite for every value of the boundary time t. Some plots of the regularized extremal volume are shown in Fig. 6.7, where, by comparison, the regularized volume of the pseudosolution is also displayed. As expected, the solution has a bigger volume. Moreover, Fig. 6.7 confirms that the volume of the pseudosolution is a good approximation both at early $t \approx 0$ and late $t \approx l/2$ times. At intermediate times, the discrepancy with the extremal volume tends to increase with l. Additionally, as it can be seen from the picture, the extremal volume appears to be smoother than the volume of the pseudosolution as a function of t. In particular, the slope variation of the former is less pronounced than the slope variation of the latter.

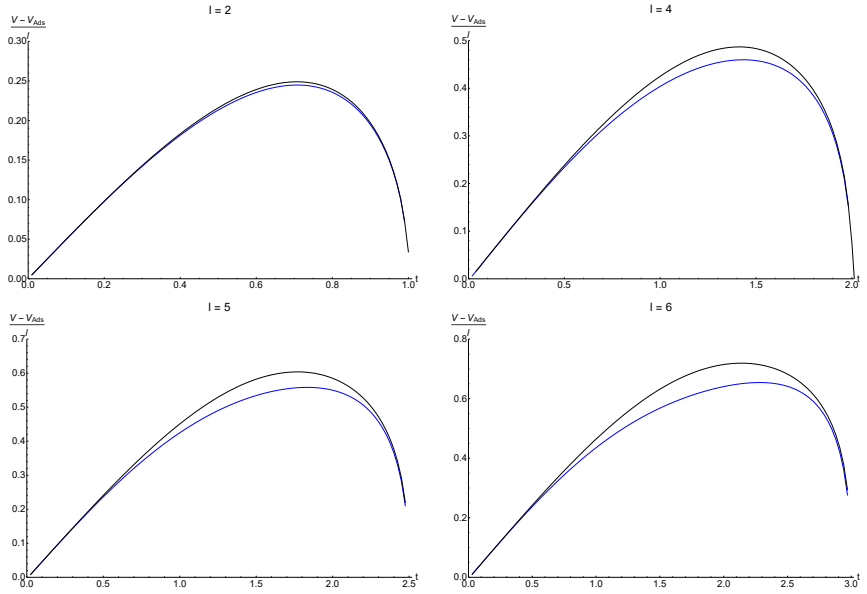

Figure 6.7: Time dependence of the extremal volume V (in black), compared to the volume $\hat{V}$ of the pseudosolution (in blue) for $l = 2, 4, 5, 6$. We have set $r_h = 1$.

6.3 Discussion

In this chapter we have investigated subregion volume complexity for a boundary line segment of length l in $(2 + 1)$-dimensional Vaidya spacetime with an infinitesimally thick shell of null matter. In order to express the holographic

result in terms of boundary CFT quantities, we employ the relations

$$c = \frac{3}{2G}\,, \qquad T = \frac{r_h}{2\pi}\,, \qquad S_{BH} = \frac{r_h}{4G}\,, \qquad \mathcal{SC}_V = \frac{V}{G}\,, \tag{6.3.1}$$

denoting the central charge, the final temperature and the entropy density of the system, and subregion volume complexity, respectively. In such expressions, the AdS radius has been set to $L = 1$, like throughout all this chapter. The regularized subregion volume complexity, defined by $\Delta\mathcal{SC}_V = \mathcal{SC}_V - \mathcal{SC}_V^{AdS}$, is thus given by

$$\frac{\Delta\mathcal{SC}_V}{l} = \frac{4\pi}{3}\, c\, T\, W_\lambda(\tau)\,, \tag{6.3.2}$$

where

$$\tau = 2\pi T\, t\,, \qquad \lambda = 2\pi T\, l\,, \qquad W_\lambda(\tau) = \frac{V - V_{\text{AdS}}}{\lambda}\,. \tag{6.3.3}$$

The function $W_\lambda(\tau)$ is plotted in Fig. 6.8 for a few values of the parameter λ:

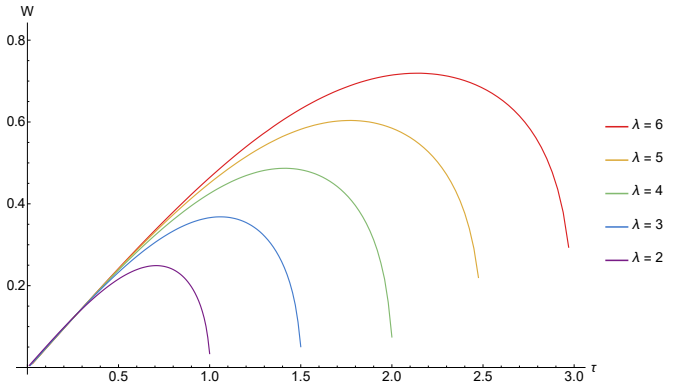

Figure 6.8: Numerical result for W_λ as a function of τ for some values of λ.

As we have argued, both at early times $\tau \approx 0$ and late times $\tau \approx \lambda/2$, subregion volume complexity is well-approximated by the pseudosolution volume, analytic expressions of which are given in Subsec. 6.2.3. In the final stage of the evolution, the maximum value of W_λ is expected to scale at least as the maximum volume of the pseudosolution (6.2.21), namely l^2.
For small τ, eq. (6.2.17) implies that $W_\lambda \approx \tau/2$. In this regime the boundary effects are negligible, so we expect subregion complexity to coincide with pure state complexity. Consequently, the Lloyd's bound [108] on the growth rate of complexity should apply. In fact, at early times we recover the result of eq. (6.2.18)

$$\frac{d\mathcal{C}_V}{dt} = 8\pi M\,, \qquad M = \frac{r_h^2}{16\pi G}\,, \tag{6.3.4}$$

where M is the BH mass per unit volume. This rate matches the asymptotic growth rate of time-independent BHs, thus it saturates the conjectured Lloyd's bound. Moreover, Fig. 6.8 clearly shows that in the early stage the complexity growth rate is a decreasing function of time. Therefore, subregion volume complexity never violates the Lloyd's bound.

As we will see in the next chapter, entanglement entropy plays a main role in capturing the thermalization process of a system. According to the Ryu-Takayanagi prescription, the entanglement entropy of a boundary subregion can be holographically computed by the area of the corresponding RT surface [9, 81]. In dynamical backgrounds, a covariant version of holographic entanglement entropy is given by the area of the HRT surface [96]

$$S = \frac{\mathcal{A}_{\text{HRT}}}{4G} \,. \tag{6.3.5}$$

It is interesting to compare the time evolutions of this quantity and subregion volume complexity. Holographic entanglement entropy has been computed in [74, 75], and a plot is shown in Fig. 6.9 for various segment lengths l:

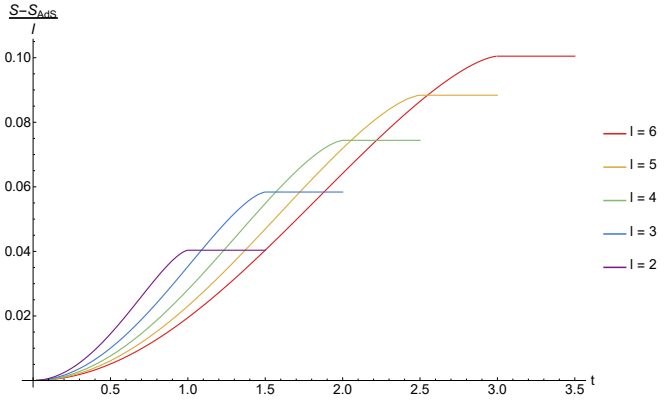

Figure 6.9: Holographic entanglement entropy of the line segment as a function of time for different lengths l. The entanglement entropy has been regularized by subtracting the diverging entropy S_{AdS} of the vacuum AdS. We have set $G = 1$ and $r_h = 1$ for illustrative purposes.

While entanglement entropy monotonically interpolates between the value in vacuum AdS and the thermal one, subregion volume complexity grows up to a maximum scaling at least as l^2 before going back to its initial value. This remarkable feature, which directly follows from the Gauss-Bonnet theorem, see eq. (6.2.4), looks rather counterintuitive from the boundary field theory perspective and is a peculiarity of the $(2+1)$-dimensional case. Indeed, for black

branes in asymptotically AdS_d with $d > 3$ this property does not hold [146]. A thermalization value different from the initial one has also been found in Vaidya spacetime for $d > 3$ in [155], where the pseudosolution has been employed. We expect that in the small $l\,T$ regime these calculations are correct. Therefore, we guess that in general spacetime dimensions subregion volume complexity grows at initial times, prior to decreasing down to a thermal value which is much closer to the initial one than to the maximum. A possibility to heuristically justify this behavior in the dual field theory is to interpret subregion volume complexity as purification complexity, introduced at the beginning of Ch. 4. Statistically, the mixed macrostate at the thermal equilibrium has a maximal amount of associated pure microstates. Thus, having at our disposal a big community of target states, it is reasonable that the minimal complexity is small, due to the large number of samples. By contrast, far away from the thermal equilibrium the number of microstates describing the target density matrix is much smaller, so it is not surprising that the minimal complexity is larger.

We conclude by remarking that we were able to numerically compute subregion volume complexity just for $r_h l \leq 6$. However, Fig. 6.7 shows that the discrepancy with the pseudosolution volume becomes increasingly important as l grows. Therefore, we were not able to check a property conjectured in [155, 187], according to which at intermediate times and large l subregion volume complexity linearly grows with a lower slope compared to the early times one. Since such a behavior is displayed by the volume of the pseudosolution, which provides an unreliable approximation at intermediate times and large l, this proposal should be revisited.

Chapter 7

A falling magnetic monopole as a holographic local quench

This chapter is mainly an adaptation of the published article [188]. *Some details are taken from* [189], *such as Fig.* 7.14.

Quantum quenches are well-known examples of out-of-equilibrium processes, allowing us to investigate the thermalization of quantum systems following an injection of energy or a change of coupling constants. In the previous chapter we have focused on global quenches, characterized by a spatially homogeneous perturbation. By considering their gravitational realization, corresponding to the formation of a BH in AdS, we have studied the time evolution of holographic quantities such as the entanglement entropy and subregion volume complexity.

Due to the homogeneity of the perturbation, it is unclear how entanglement spreads during a global quench. A more transparent model in which to address the problem is a local quench, triggered by a perturbation localized in a finite region. In CFTs, a local perturbation can be concretely introduced by joining two initially decoupled field theories and evolving with a translation-invariant Hamiltonian [58, 190] or by splitting the initial system into two disconnected pieces [191]. Alternatively, one can act with local operators on the vacuum state and study the evolution of the excited state [60, 192–194].

In this chapter we focus on the last sort of quench, which is known to be holographically equivalent to the free fall of a massive particle-like object in higher dimensional AdS [76]. In particular, we look at the fall of 't Hooft-Polyakov monopole [195] in AdS_4 as a model of CFT_3 local quench induced by

the insertion of a condensate, which breaks the SU(2) global symmetry of the theory. In order to build the falling solution, in Sec. 7.1 we start from a static monopole in global AdS_4. Then, in Sec. 7.2 we map the static configuration in global AdS_4 to a dynamic one in Poincaré AdS_4. To unveil the dynamics of the process, in Sec. 7.3 we compute the expectation value of some local operators, including the holographic energy-momentum tensor, and in Sec. 7.4 we evaluate the holographic entanglement entropy. Drawing a comparison with the same quantities characterizing the quench dual to a falling BH [76, 196, 197], we discuss to which extent the quench physics is affected by the choice of the falling particle. Some technical details are addressed in Appendix D.

7.1 A static monopole in global AdS_4

Prior to describing a falling monopole in AdS spacetime, we build a static solution in asymptotically global AdS. As in [198], we consider a $(3+1)$-dimensional theory of gravity coupled to an SU(2) gauge field and a massive adjoint scalar, with action

$$S = \int d^4x\sqrt{-g}\left[\frac{1}{16\pi G}\left(R - 2\Lambda\right) + \mathcal{L}_M\right], \tag{7.1.1}$$

in which $\mathcal{L}_M$ is the matter Lagrangian

$$\mathcal{L}_M = -\frac{1}{4}F^a_{\mu\nu}F^{a\,\mu\nu} - \frac{1}{2}D_\mu\phi^a D^\mu\phi^a - \frac{m_\phi^2}{2}\phi^a\phi^a\,. \tag{7.1.2}$$

The cosmological constant and the scalar mass are given by

$$\Lambda = -\frac{3}{L^2}\,, \qquad m_\phi^2 = -\frac{2}{L^2}\,, \tag{7.1.3}$$

where the mass is chosen ad-hoc for reasons that will be clear later. In eq. (7.1.2), $F_{\mu\nu} = F^a_{\mu\nu}\,\sigma_a/2$[1] represents the non-abelian field strength of the SU(2) gauge field $A_\mu = A^a_\mu\,\sigma_a/2$, i.e.

$$F^a_{\mu\nu} = \partial_\mu A^a_\nu - \partial_\nu A^a_\mu + e\,\epsilon^{abc}A^b_\mu A^c_\nu\,, \tag{7.1.4}$$

with e the Yang-Mills coupling.
The covariant derivative acts on the adjoint scalar as

$$D_\mu\phi_a = \partial_\mu\phi_a + e\,\epsilon_{abc}A^b_\mu\phi^c\,. \tag{7.1.5}$$

[1] We denote by σ_a the SU(2) Pauli matrices.

The gauge field, scalar field and Einstein's equations are

$$\begin{gathered} D^\mu F^a_{\mu\nu} - e\,\epsilon^{abc}\phi^b D_\nu \phi^c = 0\,, \qquad g^{\mu\nu} D_\mu D_\nu \phi^a - m^2_\phi \phi^a = 0\,, \\ R_{\mu\nu} - \frac{1}{2} R g_{\mu\nu} + \Lambda g_{\mu\nu} = 8\pi G\, T_{\mu\nu}\,, \end{gathered} \tag{7.1.6}$$

where D_μ is the combination of the gravitational and SU(2) gauge covariant derivatives, and $T_{\mu\nu}$ is the bulk energy-momentum tensor

$$T_{\mu\nu} = D_\mu \phi^a D_\nu \phi^a + F_{a\mu\alpha} F_{a\nu}{}^{\alpha} + g_{\mu\nu} \mathcal{L}_M\,. \tag{7.1.7}$$

We take as a background global AdS_4, whose metric can be read from eq. (2.1.5):

$$ds^2 = L^2 \left[-\left(1 + r^2\right) d\tau^2 + \frac{dr^2}{1 + r^2} + r^2 \left(d\theta^2 + \sin^2\theta d\varphi^2 \right) \right]. \tag{7.1.8}$$

According to the AdS/CFT correspondence, the gravitational theory in global AdS_4 is dual to a CFT_3 living at the spacetime boundary $r \to +\infty$. Each bulk field is associated to a boundary operator, whose VEV and source are dictated by the boundary expansion of the bulk fields themselves. In this setup, the bulk scalar field ϕ^a is dual to a global SU(2) triplet of operators O^a, while the bulk gauge field A^a_μ is dual to the global SU(2) currents J^a_μ, see eq. (2.1.29).

First, let us consider the scalar bulk field ϕ^a. At large r, the field has the following expansion

$$\phi^a = \frac{\alpha^a}{r^{\Delta_1}} + \frac{\beta^a}{r^{\Delta_2}} + \dots\,. \tag{7.1.9}$$

In the holographic framework, the parameters $\Delta_{1,2}$ are interpreted as the dimensions of the VEVs and sources of the operators O^a dual to the scalar triplet ϕ^a. For our choice of mass in eq. (7.1.3), we have

$$\Delta_1 = 1\,, \qquad \Delta_2 = 2\,. \tag{7.1.10}$$

In accordance to Fig. 2.3 for $d = 3$, for a scalar mass $m^2_\phi = -2/L^2$ both Δ_1 and Δ_2 are above the unitarity bound. For this reason, we have at our disposal several valid boundary conditions:[2]

- The *Dirichlet quantization*, where α^a corresponds to the source and β^a to the VEV of the boundary field:

$$J^a_D = \alpha^a\,, \qquad \langle O^a_2 \rangle = \beta^a\,. \tag{7.1.11}$$

[2]The subscript in the operator O^a refers to its dimension.

- The *Neumann quantization*, where $-\beta^a$ corresponds to the source and α^a to the VEV:
$$J_N^a = -\beta^a\,, \qquad \langle O_1^a \rangle = \alpha^a\,. \tag{7.1.12}$$
- The *multitrace deformation* [199–203], where $\langle O_1^a \rangle = \alpha^a$ and the boundary field theory is deformed by the action term
$$S_{\mathcal{F}} = \int d^3x\sqrt{-h}\,[J_{\mathcal{F}}^a\,\alpha^a + \mathcal{F}(\alpha^a)]\,, \qquad J_{\mathcal{F}}^a = -\beta^a - \frac{\partial \mathcal{F}}{\partial \alpha^a}\,, \tag{7.1.13}$$
with $\mathcal{F}$ an arbitrary function. Requiring the theory to be isolated, or equivalently $J_{\mathcal{F}}^a = 0$, we get
$$\beta^a = -\frac{\partial \mathcal{F}}{\partial \alpha^a}\,. \tag{7.1.14}$$

We point out that, among the three possibilities, the only way to obtain a non-trivial monopole solution with no source for the dual operator is the multitrace deformation satisfying eq. (7.1.14).

Regarding the gauge field A_μ^a, the large-r expansion modes have dimensions $\Delta_{1,2}^A = 0, 1$. In this case, we can only interpret the source for the dual SU(2) currents to be the coefficient of the leading-order mode, which we set to zero. Such a condition, together with eq. (7.1.14), is necessary for the boundary CFT to manifest a spontaneous, rather than explicit, breaking of the SU(2) global symmetry.

7.1.1 Monopole solution in the probe limit

Global AdS_4 solves the Einstein's equations (7.1.6) in vacuum. However, the matter fields backreact on the geometry, spoiling the vacuum solution. As a preliminary step, we can neglect the effects of backreaction working in the $G \to 0$ limit, which decouples the Einstein-Hilbert action from the matter contribution in eq. (7.1.1). In this approximation, a monopole solution can be built by a generalization of 't Hooft-Polyakov ansatz in global AdS_4 [198, 204, 205]:
$$\phi^a = \frac{1}{L} H(r) n^a\,, \qquad A_l^a = F(r) r\,\epsilon^{aik} n^k \partial_l\, n^i\,, \tag{7.1.15}$$
where $x^l = (r, \theta, \varphi)$ and n^k is the unit vector in S^2 spherical coordinates:
$$n^k = (\sin\theta\cos\varphi, \sin\theta\sin\varphi, \cos\theta)\,. \tag{7.1.16}$$

Plugging the ansatz into the equations of motion (7.1.6), we obtain

$$\begin{aligned} F'' &= -F'\frac{2(1+2r^2)}{r(1+r^2)} - F\frac{-2+2r^2+3erF-e^2r^2F^2}{r^2(1+r^2)} - H^2\frac{e(1-erF)}{r(1+r^2)}\,, \\ H'' &= -H'\frac{2(1+2r^2)}{r(1+r^2)} + 2H\,\frac{(1-erF)^2}{r^2(1+r^2)} - \frac{2H}{1+r^2}\,. \end{aligned} \tag{7.1.17}$$

Regularity of the solution requires that both $H(r), F(r) \sim r$ at $r = 0$. On the other hand, the boundary conditions at $r \to +\infty$ can be fixed depending on the dual CFT we want to describe. Such a choice is encoded in the coefficients $(\alpha_H, \beta_H, \alpha_F, \beta_F)$ appearing in the near-boundary expansion of the scalar and gauge fields:

$$H(r) = \frac{\alpha_H}{r} + \frac{\beta_H}{r^2} + \dots\,, \qquad F(r) = \frac{\alpha_F}{r} + \frac{\beta_F}{r^2} + \dots\,. \tag{7.1.18}$$

As we have argued above, we set $\alpha_F = 0$ in order to avoid an explicit breaking of the $SU(2)$ global symmetry in the dual CFT, as in [198]. Instead, to obtain a non-empty AdS background, we look for solutions with non-vanishing α_H and β_H. Once that α_H is fixed, β_H is determined by imposing the solution to be smooth. We stress that the monopole magnetic flux is independent of the boundary conditions, see Appendix D.1.

At the leading order in the gauge coupling e, eqs. (7.1.17) are solved by

$$\begin{aligned} H(r) &= \frac{\alpha_H}{r}\left[1 - \frac{\tan^{-1} r}{r}\right]\,, \\ F(r) &= \frac{e\,\alpha_H^2}{16r^3}\left[\pi^2 r^2 - 4\left(r^2+1\right)(\tan^{-1} r)^2 - \left(\pi^2-4\right) r \tan^{-1} r\right]\,, \end{aligned} \tag{7.1.19}$$

which entails the following coefficients

$$\beta_H = -\frac{\pi}{2}\alpha_H\,, \qquad \beta_F = e\,\alpha_H^2\,\frac{12\pi - \pi^3}{32}\,. \tag{7.1.20}$$

The solution (7.1.19) is also valid for arbitrary e, provided that α_H is sufficiently small.

At higher order in e, we must solve eqs. (7.1.17) numerically. To this purpose, it is convenient to introduce the compact variable ψ defined by

$$r = \tan\psi\,. \tag{7.1.21}$$

The resulting equations of motion are

$$F'' = \frac{e^2F^3 + F\left(e^2H^2 + 2\cot^2(\psi) - 2\right) - 3eF^2\cot(\psi) - \cot(\psi)\left(eH^2 + 2F'\right)}{\cos^2\psi},$$
$$H'' = 4\,\frac{H\left(e^2F^2\tan(\psi) - 2eF + 2\cot(2\psi)\right) - H'}{\sin(2\psi)}. \tag{7.1.22}$$

In Fig. 7.1 we show an example of numerical solution, while in Fig. 7.2 we plot the values (α_H, β_H) for various numerical solutions:

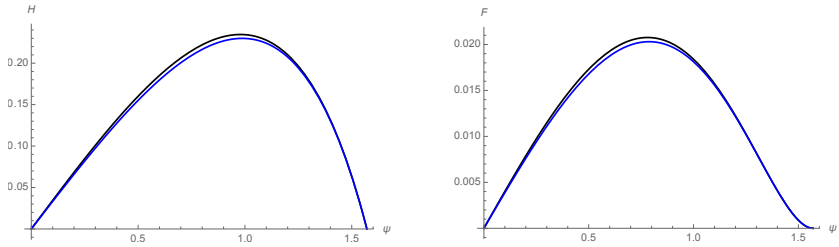

Figure 7.1: Numerical solutions for $H(\psi)$ and $F(\psi)$ are shown in black. As a comparison, the analytic approximations in eq. (7.1.19) are shown in blue. We have set $e = 1$, $\alpha_H = 1$.

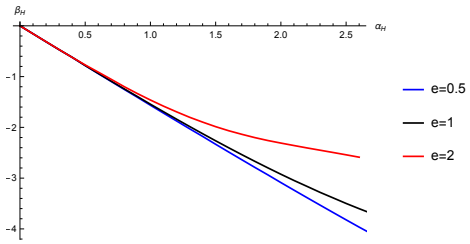

Figure 7.2: Allowed values of the coefficients (α_H, β_H) for different values of e. The relation in eq. (7.1.20) is satisfied for small e.

7.1.2 Monopole backreaction

Considering the monopole backreaction, we can take the spherically symmetric solution to the Einstein's equations

$$ds^2 = L^2\left[-\left(1+r^2\right)h(r)g(r)d\tau^2 + \frac{h(r)}{g(r)}\frac{dr^2}{1+r^2} + r^2\left(d\theta^2+\sin^2\theta d\varphi^2\right)\right]. \tag{7.1.23}$$

In order to recover asymptotically global AdS$_4$, we require that

$$\lim_{r\to\infty} h(r) = \lim_{r\to\infty} g(r) = 1\,. \tag{7.1.24}$$

The full set of equations of motion in this background is

$$F'' = -F'\frac{2(1+2r^2)}{r(1+r^2)} - \frac{g'}{g}\left(\frac{F}{r}+F'\right) - H^2\frac{e(1-erF)}{r(1+r^2)}\frac{h}{g}$$
$$- F\frac{1}{r^2(1+r^2)}\left[2r^2 + \frac{h}{g}\left(-2+3erF-e^2r^2F^2\right)\right],$$
$$H'' = -H'\left(\frac{2(1+2r^2)}{r(1+r^2)}+\frac{g'}{g}\right) - \frac{h}{g}\left(-2H\,\frac{(1-erF)^2}{r^2(1+r^2)} + \frac{2H}{1+r^2}\right),$$
$$g' = \frac{4\pi G}{L^2}\,\frac{2H^2\left[(2-erF)erF+r^2-1\right] - F^2(2-erF)^2}{r(1+r^2)}\,h + \frac{1+3r^2}{r(r^2+1)}(h-g),$$
$$h' = \frac{8\pi G}{L^2}h\left(\frac{r}{2}(H')^2 + \frac{(F+rF')^2}{r}\right).$$

The asymptotic form of the equations of motion fixes the large r expansions

$$h(r) = 1+\frac{h_2}{r^2}+\frac{h_3}{r^3}+\mathcal{O}(1/r^4)\,, \qquad g(r) = 1+\frac{g_2}{r^2}+\frac{g_3}{r^3}+\mathcal{O}(1/r^4)\,, \tag{7.1.25}$$

with

$$g_2 = -h_2 = \frac{2\pi G\alpha_H^2}{L^2}\,, \qquad h_3 = -\frac{16\pi G}{3L^2}\alpha_H\beta_H\,. \tag{7.1.26}$$

The unfixed parameter g_3 can be found by requiring the solution to be smooth.

To analytically solve the equations of motion, it is useful to introduce the expansion parameter

$$\epsilon = \frac{\pi\, G\,\alpha_H^2}{L^2}\,. \tag{7.1.27}$$

At the leading order in e and ϵ, the $H(r)$ and $F(r)$ solutions are still given by eq. (7.1.19). The leading order backreaction on the metric instead gives

$$h(r) = 1+\epsilon\, h_\epsilon + \mathcal{O}(\epsilon^2)\,, \qquad g(r) = 1+\epsilon\, g_\epsilon + \mathcal{O}(\epsilon^2)\,, \tag{7.1.28}$$

where

$$
\begin{aligned}
h_\epsilon &= \pi^2 - \frac{4}{r^2} - \frac{2}{r^2+1} - 4\frac{2\left(r^2-1\right) r \arctan r + \left(r^4+1\right)\arctan^2 r}{r^4}\,, \\
g_\epsilon &= \pi^2 + \frac{1}{r^2} - \frac{2r\arctan r + 3}{r^2}\left(1 - \frac{2}{1+r^2}\right) \\
&\quad - 2\arctan r\,\frac{2\left(r^4-1\right)\arctan r + r\left(3r^2+4\right)}{r^4}\,.
\end{aligned}
\tag{7.1.29}
$$

These solutions set

$$
g_3 = -\frac{10\,\pi^2\,G\,\alpha_H^2}{3\,L^2}\,. \tag{7.1.30}
$$

The profile functions at higher order in e and ϵ are again accessible by numerically solving the equations of motion. As in the probe limit, it is convenient to introduce the variable $\psi = \arctan r$, getting the following equations of motion

$$
\begin{aligned}
F'' &= \frac{1}{g}\left[-e\csc\psi\sec\psi\left(3F^2+H^2\right)h + e^2\sec^2\psi\,F^3 h - F'\left(2g\,\csc\psi\sec\psi + g'\right)\right. \\
&\quad \left. + F\left(h\left(2\csc^2\psi + e^2H^2\sec^2\psi\right) - \sec\psi\left(2g\,\sec\psi + g'\,\csc\psi\right)\right)\right]\,, \\
H'' &= \frac{1}{g}\left[2hH\left(\csc^2\psi - 2eF\,\csc\psi\sec\psi + \sec^2\psi\left(-1+e^2F^2\right)\right)\right. \\
&\quad \left. - \left(2g\,\csc\psi\sec\psi + g'\right)H'\right]\,, \\
h' &= \frac{2\pi G}{L^2}h\left[2\left(F\,\csc\psi\sec\psi + F'\right)^2 + H'^2\right]\sin 2\psi\,, \\
g' &= \tan\psi\left(3+\cot^2\psi\right)(h-g) + \frac{4\pi G}{L^2}h\tan\psi\left[-F^2(-2\cot\psi + eF)^2\right. \\
&\quad \left. + 2H^2 - 2(\cot\psi - eF)^2H^2\right]\,.
\end{aligned}
\tag{7.1.31}
$$

In Fig. 7.3 we show a comparison between the numerical and the analytic solutions.

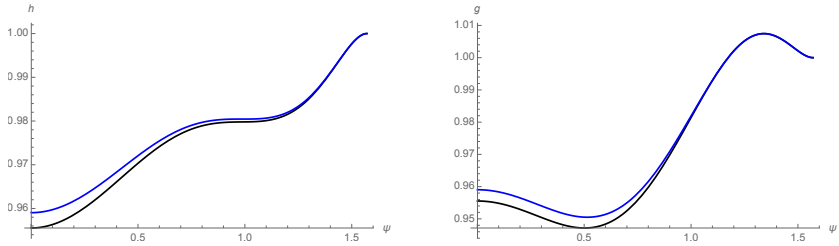

Figure 7.3: Numerical solutions for the metric functions $h(\psi)$ and $g(\psi)$ are shown in black. As a comparison, the analytic approximations in eq. (7.1.29) are shown in blue. We have set $e = 1$, $\alpha_H = 1$, $L = 1$ and $G = 0.1$.

7.2 A falling monopole in Poincaré AdS$_4$

The gravity dual of a CFT local quench is the free fall of a particle in AdS [76]. To obtain such a solution, we employ the nice trick introduced in [206]. The idea is to map a spherically symmetric asymptotically global AdS geometry to a time-dependent asymptotically Poincaré AdS geometry by performing a change of coordinates.

The empty Poincaré AdS$_4$ metric with coordinates (t, z, x, φ) is

$$ds^2 = \frac{L^2}{z^2}\left(dz^2 - dt^2 + dx^2 + x^2 d\varphi^2\right) . \tag{7.2.1}$$

The metric in eq. (7.2.1) and the global AdS metric in eq. (7.1.8) can be mapped into each other via the coordinate transformation

$$\begin{aligned} \sqrt{1+r^2}\,\cos\tau &= \frac{A^2+z^2+x^2-t^2}{2A\,z}\,, \qquad \sqrt{1+r^2}\,\sin\tau = \frac{t}{z}\,, \\ r\,\sin\theta &= \frac{x}{z}\,, \qquad r\,\cos\theta = \frac{z^2+x^2-t^2-A^2}{2A\,z}\,, \end{aligned} \tag{7.2.2}$$

leaving the angular coordinate φ unchanged. The transformation can be inverted, leading to

$$\begin{aligned} r &= \frac{\sqrt{A^4+2A^2(t^2+x^2-z^2)+(z^2+x^2-t^2)^2}}{2A\,z}\,, \\ \tau &= \arctan\left(\frac{2A\,t}{z^2+x^2-t^2+A^2}\right)\,, \\ \theta &= \arctan\left(\frac{2A\,x}{z^2+x^2-t^2-A^2}\right)\,. \end{aligned} \tag{7.2.3}$$

As a result of the change of variables in eq. (7.2.3), a static particle centered at $r = 0$ in global AdS is mapped to a falling configuration in Poincaré AdS, following the curve

$$x = 0\,, \qquad z = \sqrt{t^2 + A^2}\,. \tag{7.2.4}$$

In the point-like approximation, eq. (7.2.4) represents the particle trajectory. Note that this holographic model is symmetric under time reversal $t \to -t$: for $t < 0$ the particle approaches the spacetime boundary $z = 0$, whereas for $t > 0$ it moves towards the bulk interior. From the CFT perspective, the initial condition at $t = 0$ corresponds to the initially perturbed state prepared by the insertion of an appropriate operator. The parameter A, which on the gravity side specifies the initial position of the falling particle along the z-direction, fixes the size of the perturbed region in the boundary field theory.

In the remainder of this chapter, we apply this general setup to the monopole solution discussed in Sec. 7.1.

7.2.1 Bulk energy density of the falling monopole

Based on the above discussion, one may be tempted to treat the magnetic monopole obtained by the mapping (7.2.3) as a point-like particle falling along the trajectory of eq. (7.2.4). The bulk energy-momentum tensor (7.1.7) helps us out in checking this intuition.

For simplicity, we neglect the monopole backreaction and we perform the coordinate change (7.2.3)

$$x^\mu = (\tau\,, r\,, \theta\,, \varphi) \to x'^\mu = (t\,, z\,, x\,, \varphi)\,. \tag{7.2.5}$$

After the mapping, the energy-momentum tensor in Poincaré AdS is given by

$$T'_{\alpha\beta}\,(x') = \frac{\partial x^\mu}{\partial x'^\alpha}\,\frac{\partial x^\nu}{\partial x'^\beta}\,T_{\mu\nu}\,(x)\,. \tag{7.2.6}$$

To extract physical quantities from the tensor, we express it in the vierbein basis e^μ_m:

$$T'_{mn}\,(x') = e^\mu_m e^\nu_n\,T'_{\mu\nu}\,(x')\,, \qquad e^\mu_m\,e^\nu_n\,g'_{\mu\nu} = \eta_{mn}\,, \tag{7.2.7}$$

where $g'_{\mu\nu}$ and η_{mn} are the Poincaré AdS and the Minkowski metric tensors, respectively. We specialize to[3]

$$e^\mu_0 = \left(\frac{z}{L}\,, 0\,, 0\,, 0\right)\,, \qquad e^\mu_1 = \left(0\,, \frac{z}{L}\,, 0\,, 0\right)\,, \qquad e^\mu_2 = \left(0\,, 0\,, \frac{z}{L}\,, 0\right)\,. \tag{7.2.8}$$

[3]In this section, the Minkowski indices m, n take the values $0, 1, 2, 3$, while the curved spacetime indices are t, z, x, φ.

The energy density measured in such an orthonormal frame is

$$\rho = T'^{00} = \frac{z^2}{L^2}\, T'_{tt}\,, \tag{7.2.9}$$

and the components of the Poynting vector $\vec{s} = (s_z, s_x, s_\varphi)$ are

$$s_z = T'^{01} = -\frac{z^2}{L^2}\, T'_{tz}\,, \qquad s_x = T'^{02} = -\frac{z^2}{L^2}\, T'_{tx}\,, \qquad s_\varphi = 0\,. \tag{7.2.10}$$

Figs. 7.4 and 7.5 display numerical results for the energy density and the energy flux into the bulk spacetime at fixed time.

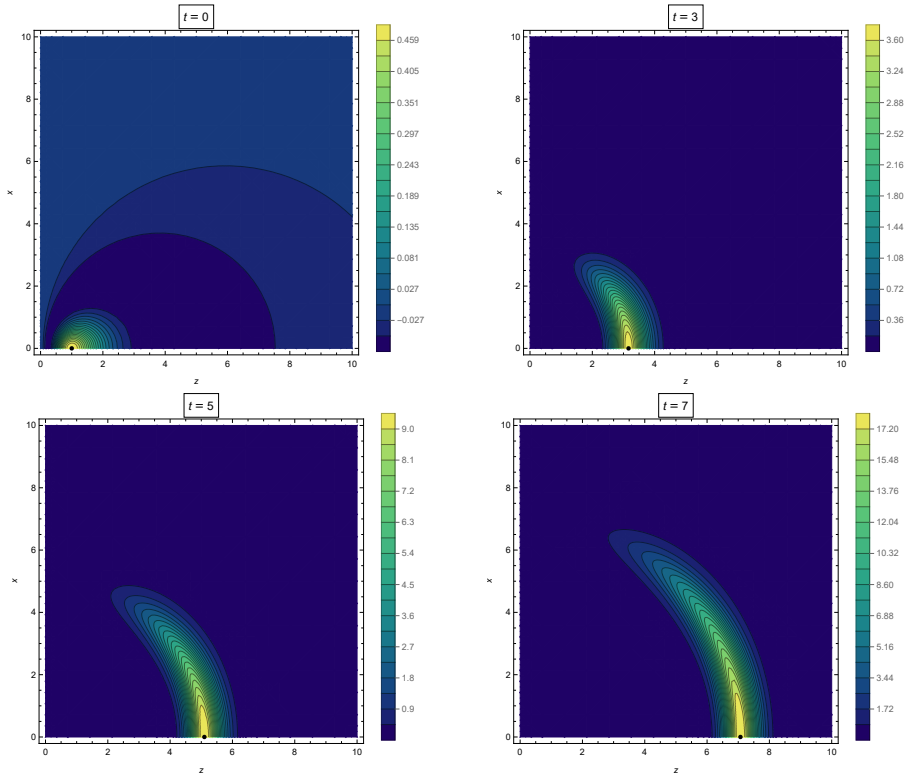

Figure 7.4: Contour lines of constant energy density for fixed time. The monopole center is represented by the black spot. The numerical values $A = 1$ and $L = 1$ have been chosen.

The pictures clearly show that the monopole behaves as a point-like particle only at early times. Namely, at $t = 0$, as all the components of the Poynting

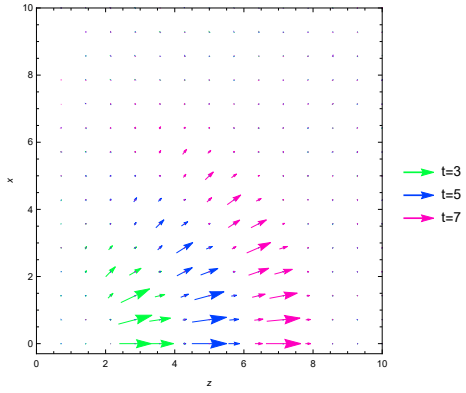

Figure 7.5: Direction of the bulk Poynting vector for fixed time. The numerical values $A = 1$ and $L = 1$ have been chosen.

vector vanish, there is no energy flux. Then the energy density, initially localized nearby the AdS boundary, propagates along a spherical wavefront. We will shortly see that this mimics the spread of the perturbation from the excited region in the boundary CFT.

7.3 A holographic local quench

Having established the gravitational model for a local quench, we now turn to the boundary CFT interpretation. In particular, we exploit the AdS/CFT correspondence to investigate the expectation values of local operators such as the scalar triplet O^a, the global SU(2) currents J^a_μ, and the holographic energy-momentum tensor. As we will discuss, the physics of the boundary CFT is crucially influenced by the choice of boundary conditions on the bulk scalar field ϕ^a.

7.3.1 Boundary conditions for the scalar

We start our analysis by exploring the near-boundary behavior of the bulk scalar field. In global AdS, the direction n^a of ϕ^a in the internal SU(2) space is given in eq. (7.1.16): $n^a = (\sin\theta\cos\varphi, \sin\theta\sin\varphi, \cos\theta)$. Upon performing the coordinate transformation (7.2.3), the direction of the bulk scalar nearby the

Poincaré AdS boundary $z = 0$ becomes

$$n^a = \frac{1}{\omega^{1/2}} \left(-2Ax\cos\varphi, -2Ax\sin\varphi, A^2 + t^2 - x^2\right) + O(z^2)\,, \tag{7.3.1}$$

where we have defined the quantity

$$\omega(x,t) = A^4 + 2A^2\left(t^2 + x^2\right) + \left(t^2 - x^2\right)^2\,. \tag{7.3.2}$$

To get an idea of the spread of the perturbation, we can think of the quench as having an expanding core located at

$$x = \sqrt{t^2 + A^2}\,, \tag{7.3.3}$$

which, at late times, can be appreciably approximated by the lightcone of the origin $x = t$. At the core of the quench (7.3.3), the bulk scalar field $\phi = \phi^a\sigma^a$ points in the direction

$$n = n^a\sigma^a = -(\sigma_1\cos\varphi + \sigma_2\sin\varphi)\,. \tag{7.3.4}$$

So, at late times the n^3 component vanishes on top of the lightcone. From Fig. 7.6, bearing in mind that $n^a n^a = 1$, we deduce that the scalar field points along the σ_3 direction inside the lightcone and along the $-\sigma_3$ one outside the lightcone. Therefore, at large time we end up with two regions of vacuum (inside and outside the lightcone) separated by an expanding shell of energy. From the boundary expansion of ϕ^a, we will see that the absolute value of the scalar field is peaked at the core (7.3.3) and is almost zero both inside and outside the lightcone.

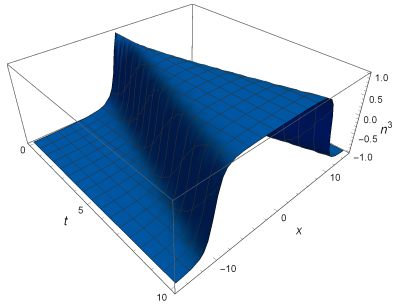

Figure 7.6: Near-boundary value of n^3 as a function of (t, x) for $A = 1$. Negative values of the radial cylindrical coordinate x correspond to $\varphi \to -\varphi$.

Let us now investigate the VEV and source of the local operator O^a, which can be extracted from the boundary expansion of the bulk scalar field ϕ^a. From eq.

(7.2.3), the global AdS radial coordinate at $z \approx 0$ reads

$$r = \frac{a}{z} + \mathcal{O}(z)\,, \qquad a = \frac{\omega^{1/2}}{2A}\,. \tag{7.3.5}$$

Consequently, the boundary expansion of $H(r)$ is

$$H = \frac{\alpha_H}{r} + \frac{\beta_H}{r^2} + \mathcal{O}(r^{-3}) = \tilde{\alpha}_H\, z + \tilde{\beta}_H\, z^2 + \mathcal{O}(z^3)\,, \tag{7.3.6}$$

where

$$\tilde{\alpha}_H = \frac{\alpha_H}{a} = \alpha_H\, \frac{2A}{\omega^{1/2}}\,, \qquad \tilde{\beta}_H = \frac{\beta_H}{a^2} = \beta_H\, \frac{4A^2}{\omega}\,. \tag{7.3.7}$$

A plot of $\tilde{\alpha}_H$ and $\tilde{\beta}_H$ is shown in Fig. 7.7:

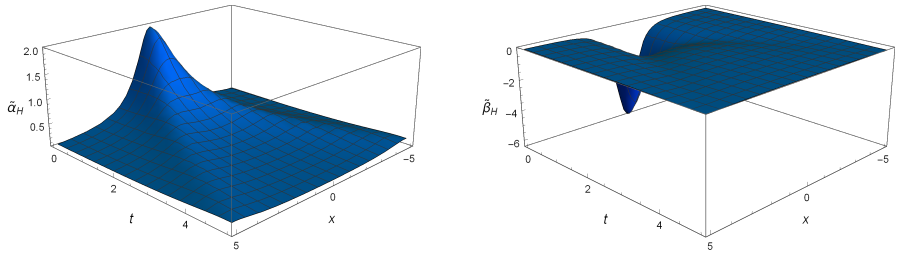

Figure 7.7: The quantities $\tilde{\alpha}_H$ (on the left) and $\tilde{\beta}_H$ (on the right) as functions of (t, x) in the small backreaction limit (7.1.20). Negative values of x correspond to $\varphi \to -\varphi$. We have set $A = 1$, $\alpha_H = 1$.

Interestingly,

$$\frac{\tilde{\beta}_H}{\tilde{\alpha}_H^2} = \frac{\beta_H}{\alpha_H^2} = \kappa\,, \tag{7.3.8}$$

where κ is a constant. In the limit of negligible backreaction, the value of such a constant can be directly read from eq. (7.1.20)

$$\kappa = -\frac{\pi}{2\alpha_H}\,. \tag{7.3.9}$$

Combining eqs. (7.3.1) and (7.3.6), the expansion of ϕ^a nearby the Poincaré AdS boundary is

$$\phi^a = \frac{H(z)}{L} n^a = \frac{1}{L}\left(\tilde{\alpha}^a\, z + \tilde{\beta}^a\, z^2 + \mathcal{O}(z^3)\right)\,, \tag{7.3.10}$$

with $\tilde{\alpha}^a = n^a \tilde{\alpha}_H$ and $\tilde{\beta}^a = n^a \tilde{\beta}_H$. As for the global AdS case, the scalar field ϕ^a admits several boundary conditions:

- The Dirichlet quantization, where $\tilde{\alpha}^a$ corresponds to the source and $\tilde{\beta}^a$ to the VEV of the boundary field:

$$J_D^a = \tilde{\alpha}^a\,, \qquad \langle O_2^a \rangle = \tilde{\beta}^a\,. \tag{7.3.11}$$

- The Neumann quantization, where $-\tilde{\beta}^a$ corresponds to the source and $\tilde{\alpha}^a$ to the VEV:

$$J_N^a = -\tilde{\beta}^a\,, \qquad \langle O_1^a \rangle = \tilde{\alpha}^a\,. \tag{7.3.12}$$

- The multitrace deformation, where $\langle O_1^a \rangle = \tilde{\alpha}^a$ and the boundary field theory is deformed by the action term

$$S_{\mathcal{F}} = \int d^3x\sqrt{-h}\,[J_{\mathcal{F}}^a\,\tilde{\alpha}^a + \mathcal{F}(\tilde{\alpha}^a)]\,, \qquad J_{\mathcal{F}}^a = -\tilde{\beta}^a - \frac{\partial \mathcal{F}}{\partial \tilde{\alpha}^a}\,, \tag{7.3.13}$$

  with $\mathcal{F}$ an arbitrary function.

In general, all quantization choices enforce external time-dependent sources. However, for the multitrace deformation with

$$\mathcal{F}_\kappa(\tilde{\alpha}^a) = -\frac{\kappa}{3}\,(\tilde{\alpha}^a\tilde{\alpha}^a)^{3/2} = -\frac{\kappa}{3}\tilde{\alpha}_H^3 \tag{7.3.14}$$

the boundary field has no source, since

$$\tilde{\beta}^a = -\frac{\partial \mathcal{F}_\kappa}{\partial \tilde{\alpha}^a}\,, \tag{7.3.15}$$

as can be checked from eq. (7.3.8).

7.3.2 The boundary global currents

The boundary expansion of the bulk gauge field (7.1.15) contains

$$F(r)\,r = \alpha_F + \frac{\beta_F}{r} + \mathcal{O}(r^{-2}) = \alpha_F + \frac{\beta_F}{a}\,z + \mathcal{O}(z^2) \tag{7.3.16}$$

Thus, setting $\alpha_F = 0$ as in Sec. 7.1 causes the gauge field A_l^a to vanish at the Poincaré boundary $z = 0$. In other words, if the sources for the global symmetries are set to zero in global AdS, they still vanish after the change of coordinates leading to Poincaré AdS.

From the order z terms in the boundary expansion of A_l^a we extract the following expectation values of the three global currents J_l^a:

$$\langle J_l^1 \rangle = \frac{8A^2\beta_F}{\omega^{3/2}} \left(tx\sin\varphi, -\frac{1}{2}\left(A^2+t^2+x^2\right)\sin\varphi, -\frac{1}{2}x\left(A^2+t^2-x^2\right)\cos\varphi \right) ,$$

$$\langle J_l^2 \rangle = \frac{8A^2\beta_F}{\omega^{3/2}} \left(-tx\cos\varphi, \frac{1}{2}\left(A^2+t^2+x^2\right)\cos\varphi, -\frac{1}{2}x\left(A^2+t^2-x^2\right)\sin\varphi \right) ,$$

$$\langle J_l^3 \rangle = \frac{8A^2\beta_F}{\omega^{3/2}} \left(0, 0, -Ax^2\right) , \tag{7.3.17}$$

where $x^l = (t, x, \varphi)$ are the boundary coordinates, and $a = 1, 2, 3$ is the $SU(2)$ global index. A plot of the charge density component J_t^2 is shown in Fig. 7.8:

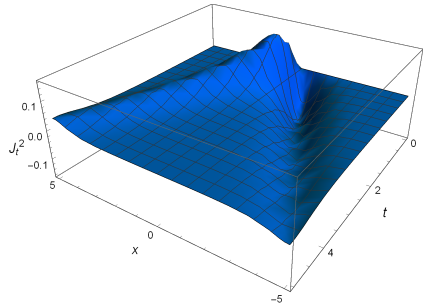

Figure 7.8: Charge density of the second component in the SU(2) space J_t^2 as a function of (t, x) for $\varphi = 0$ (positive x) and $\varphi = \pi$ (negative x), in the small backreaction limit of eq. (7.1.20). The peak and the pit correspond to positive and negative global charges, which are taken apart from each other by the quench. We have set $A = 1$, $\alpha_H = 1$ and $e = 1$.

Remarkably, in the SU(2) space the expectation value of the global current is always orthogonal to the direction n^a of the scalar field expectation value:

$$\langle J_l^a \rangle \, n^a = 0 \, . \tag{7.3.18}$$

So, the quench breaks all the three global symmetry group generators. This happens just on top of the approximate lightcone of eq. (7.3.3). Inside and outside the lightcone both the scalar and the current expectation values tend to zero, thus the SU(2) global symmetry of the boundary theory is unbroken.

7.3.3 The boundary energy-momentum tensor

One of our purposes is to probe how the features of the falling particle in the bulk spacetime influence the boundary quench. To get an insight, we will compare the holographic model of a falling monopole with the model of a falling BH studied in [76]. From now on, we refer to the former as *monopole quench* and to the latter as *BH quench*. In this subsection, we compute the holographic energy-momentum tensors in both models, finding out that proper boundary conditions on bulk fields exist for which they coincide up to a scaling factor.

We first consider the BH quench. A BH in global AdS_4 can be seen as a static particle located at $r = 0$, whose effect on the background geometry is known exactly. In particular, the spacetime metric with backreaction is

$$ds^2 = L^2 \left[-\left(1 + r^2 - \frac{M}{r}\right) d\tau^2 + \frac{dr^2}{1 + r^2 - \frac{M}{r}} + r^2 \left(d\theta^2 + \sin^2\theta d\varphi^2\right) \right], \tag{7.3.19}$$

in which M is a dimensionless parameter proportional to the BH mass

$$m_{BH} = \frac{1}{2}\frac{ML}{G}. \tag{7.3.20}$$

As usual, by applying the change of variables in eq. (7.2.3) the static BH in global AdS is mapped to a falling BH in Poincaré AdS. Then, the holographic energy-momentum tensor [207] can be obtained by putting the resulting metric in the *Fefferman-Graham* (FG) *form*. Details of the calculation are deferred to Appendix D.2.1, where expressions for all the components of the holographic energy-momentum tensor are also given, see eq. (D.2.7). The energy density is

$$T_{tt}^{(BH)} = \frac{A^3 L^2 M}{\pi G} \frac{\omega + 6t^2 x^2}{\omega^{5/2}}, \tag{7.3.21}$$

a plot of which is represented in Fig. 7.9. The picture reveals that at time $t = 0$ energy is injected in a spherical region of radius A centered in $x = 0$. As time passes, the perturbation propagates into the system while being quenched. The energy-momentum tensor turns out to be conserved and traceless, and the total energy of the boundary system is

$$\mathcal{E}^{(BH)} = 2\pi \int_0^{+\infty} T_{tt}^{(BH)} x\, dx = \frac{L}{A} m_{BH}. \tag{7.3.22}$$

The monopole quench requires a more accurate discussion, since the holographic energy-momentum tensor depends on the boundary conditions on bulk fields. Let us treat the problem in the Dirichlet quantization, covered in [208]. Starting

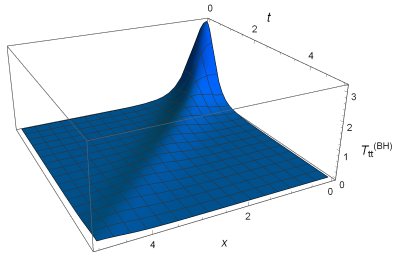

Figure 7.9: Energy density of the CFT_3 interested by the local quench dual to a falling BH. We have set $A = L = M = 1$ and $G = 0.1$.

from the backreacted metric (7.1.23), we perform the coordinate change of eq. (7.2.3). The expression of the intermediate metric is a bit cumbersome, so in Appendix D.2.2 we just specify the coordinates expansion that puts it in the FG form. All the non-vanishing components of the energy-momentum tensor $T_{mn}^{(D)}$ extracted from this metric are given in eq. (D.2.10). The energy density is

$$\begin{aligned} T_{tt}^{(D)} &= \frac{A^3}{3\pi G\,\omega^{5/2}}\left[48\pi G\alpha_H\beta_H\,x^2t^2 + (8\pi G\alpha_H\beta_H - 3g_3L^2)(\omega + 6t^2x^2)\right] \\ &\approx 2\pi\alpha_H^2A^3\,\frac{\omega + 2t^2x^2}{\omega^{5/2}}\,, \end{aligned} \tag{7.3.23}$$

where in the second line we have inserted the analytic approximations of eqs. (7.1.20) and (7.1.30), which are valid for small backreaction. In this limit, the total energy is

$$\mathcal{E}^{(D)} = 2\pi\int_0^{+\infty} T_{tt}^{(D)}\,x\,dx = \frac{\pi^2\alpha_H^2}{A}\left(1 - \frac{2}{3}\frac{t^2}{A^2 + t^2}\right)\,, \tag{7.3.24}$$

which decreases in time. The non-conservation of energy motivates us to investigate a different quantization.

A change of the quantization condition produces a shift of $T_{mn}^{(D)}$ by finite parts [203]. Here we specialize to a class of multitrace deformations that do not break the SU(2) global symmetry. Recalling that $\tilde{\alpha}^a = n^a\tilde{\alpha}_H$ and $\tilde{\beta}^a = n^a\tilde{\beta}_H$, we can express the source as

$$J_{\mathcal{F}}^a = n^a J_{\mathcal{F}}\,. \tag{7.3.25}$$

As a function $\mathcal{F}$ parametrizing the multitrace deformation we choose

$$\mathcal{F}(\tilde{\alpha}^a) = \mathcal{F}(\tilde{\alpha}^a\tilde{\alpha}^a) = \mathcal{F}(\tilde{\alpha}_H)\,. \tag{7.3.26}$$

The current can be written in terms of $\tilde{\alpha}_H$ and $\tilde{\beta}_H$ as

$$J_{\mathcal{F}} = -\tilde{\beta}_H - \mathcal{F}'(\tilde{\alpha}_H)\,. \tag{7.3.27}$$

The energy-momentum tensor is (see Appendix D.2.3 for further details)

$$T_{ij}^{(\mathcal{F})} = T_{ij}^{(D)} + \eta_{ij}[\mathcal{F}(\tilde{\alpha}_H) - \tilde{\alpha}_H\tilde{\beta}_H - \mathcal{F}'(\tilde{\alpha}_H)\tilde{\alpha}_H]\,, \tag{7.3.28}$$

with η_{ij} the metric tensor at the spacetime boundary. This result also applies to the Neumann quantization, which can be realized as a multitrace deformation with $\mathcal{F} = 0$. If we instead specialize to $\mathcal{F} = \mathcal{F}_\kappa$, see eq. (7.3.14), the external source vanishes and the energy-momentum tensor is conserved. Moreover, an explicit computation reveals that the energy-momentum tensor has the same functional form as the one for the BH quench:

$$T_{ij}^{(\kappa)} = \frac{m_M}{m_{BH}}\,T_{ij}^{(BH)}\,, \qquad m_M = \frac{16\pi G\alpha_H\beta_H - 3L^2 g_3}{6LG}\,, \tag{7.3.29}$$

where m_M is the monopole mass. In the space of parameters we have explored, m_M turns out to be positive. Thus, the spreading of the perturbation in the dual CFT_3 is still described by Fig. 7.9. In the small backreaction limit, inserting the analytical values of eqs. (7.1.20) and (7.1.30) we find

$$m_M = \frac{\pi^2}{3}\frac{\alpha_H^2}{L} = \frac{\pi}{3}\frac{L}{G}\epsilon\,. \tag{7.3.30}$$

The total energy is

$$\mathcal{E}^{(\kappa)} = 2\pi\int_0^{+\infty} T_{tt}^{(\kappa)}\,x\,dx = \frac{L}{A}m_M\,. \tag{7.3.31}$$

As apparent from eq. (7.3.29), the energy-momentum tensor is not a probe enough precise to distinguish between a falling monopole and a falling BH into the bulk. In the next section, we will see that the holographic entanglement entropy does the job.

7.4 Holographic entanglement entropy

In this section we examine the holographic entanglement entropy, which turns out to be a better non-local probe of the bulk geometry. To study the effect of the leading order backreaction on this quantity, it is convenient to use the ϵ defined in eq. (7.1.27) as an expansion parameter. We will find that the

corrections to the entanglement entropy due to the classical backreaction are of order α_H^2, where

$$\alpha_H^2 = \epsilon \frac{L^2}{G} \frac{1}{\pi} \,. \tag{7.4.1}$$

In the limit of extremely small ϵ, bulk quantum corrections [209] can be of the same order of magnitude as the ones due to classical backreaction (see for example [210]). In this section we will focus on a regime in which quantum corrections are negligible. For this to be true, we first fix a sufficiently small ϵ in order to justify the leading order calculation of the backreaction. Then, we choose

$$\frac{L^2}{G} \gg \frac{1}{\epsilon} \tag{7.4.2}$$

in such a way that the classical bulk contributions dominate over the quantum ones, which are of order $(L^2/G)^0$. This implies a large monopole mass, i.e. $m_M \gg 1/L$, see eq. (7.3.30). Equivalently, the dual local operator triggering the quench has a large operator dimension, as in [60]. In order to trust our analytic approximation for a sufficiently large α_H^2, we need to pick a sufficiently small gauge coupling e, as discussed below eq. (7.1.20).

The asymptotically global AdS metric at the leading order in ϵ is

$$\begin{aligned} \frac{ds^2}{L^2} = &- (1+r^2)\left[1+\epsilon\left(h_\epsilon + g_\epsilon\right)\right] d\tau^2 + \left[1+\epsilon\left(h_\epsilon - g_\epsilon\right)\right] \frac{dr^2}{1+r^2} \\ &+ r^2 (d\theta^2 + \sin^2\theta d\varphi^2) \,, \end{aligned} \tag{7.4.3}$$

where h_ϵ and g_ϵ are defined in eq. (7.1.28). To investigate the evolution of holographic entanglement entropy during a local quench, we apply the change of variables in eq. (7.2.3), obtaining a time-dependent background. The resulting metric tensor can be written as

$$g_{\mu\nu} = g^{(0)}_{\mu\nu} + \epsilon\, g^{(1)}_{\mu\nu} + \mathcal{O}(\epsilon^2) \,, \qquad \epsilon = \frac{\pi G\, \alpha_H^2}{L^2} \,. \tag{7.4.4}$$

The RT prescription teaches us that holographic entanglement entropy for boundary subregions is related to the area of extremal codimension-two bulk surfaces, which can be parametrized as $x^\mu(y^\alpha)$. The induced metric on such surfaces is

$$G_{\alpha\beta} = \frac{\partial x^\mu}{\partial y^\alpha} \frac{\partial x^\nu}{\partial y^\beta} g_{\mu\nu} \,. \tag{7.4.5}$$

Expanding as a power series in ϵ we get

$$G_{\alpha\beta} = G^{(0)}_{\alpha\beta} + \epsilon\, G^{(1)}_{\alpha\beta} + O(\epsilon^2) \,, \qquad G^{(k)}_{\alpha\beta} = \frac{\partial x^\mu}{\partial y^\alpha} \frac{\partial x^\nu}{\partial y^\beta} g^{(k)}_{\mu\nu} \,, \qquad k = 0, 1 \,. \tag{7.4.6}$$

It is important to note that, at first order, it is enough to work with the unperturbed RT surface $x^\mu(y^\alpha)$, which simplifies the computation a lot. The change of area of the RT surface due to the leading order backreaction can be calculated by expanding the induced metric determinant in the area functional. The first order term of this expansion is [76]

$$\Delta\mathcal{A} = \frac{\epsilon}{2}\int d^2y\,\sqrt{G^{(0)}}\,\mathrm{Tr}\left[G^{(1)}(G^{(0)})^{-1}\right]\,. \tag{7.4.7}$$

From the boundary theory perspective, the leading order difference in entanglement entropy between the perturbed state and the vacuum is proportional to eq. (7.4.7)

$$\Delta S = \frac{\Delta\mathcal{A}}{4G}\,. \tag{7.4.8}$$

We will explore this quantity for various subregions in the boundary system.

7.4.1 Disk centered at the origin

We start by taking a spherically symmetric boundary subregion, namely a disk of radius l centered at $x = 0$ and lying at constant time t. The corresponding RT surface in unperturbed Poincaré AdS_4 is the half sphere

$$z = \sqrt{l^2 - x^2}\,, \tag{7.4.9}$$

at constant bulk time t. From eq. (7.4.7) we obtain

$$\Delta S(l,t) = \frac{\pi^2\,\alpha_H^2}{4}\,\frac{1}{l}\int_0^l \frac{(h_\epsilon - g_\epsilon)\,x^3}{(l^2-x^2)^{3/2}}\,\frac{\omega(l,t)}{(A^2-l^2+t^2)^2+4A^2x^2}\,dx\,, \tag{7.4.10}$$

where ω is defined in eq. (7.3.2). The functions h_ε and g_ε depend on the coordinate r, which on top of the RT surface reads

$$r = \frac{1}{2A}\sqrt{\frac{(A^2-l^2+t^2)^2+4A^2x^2}{l^2-x^2}}\,. \tag{7.4.11}$$

The A dependence of the entropy can be completely reabsorbed by rescaling the quantities l, x, t as

$$l \to \frac{l}{A}\,, \qquad x \to \frac{x}{A}\,, \qquad t \to \frac{t}{A}\,. \tag{7.4.12}$$

For this reason, the numerical analysis has been performed for $A = 1$ without loss of generality. Some results are shown in Fig. 7.10. We find that ΔS is

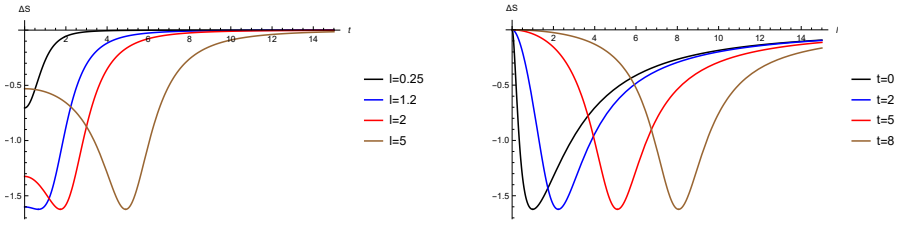

Figure 7.10: On the left: Time dependence of ΔS for a spherical subregion with fixed radius l centered at the origin of the quench. On the right: ΔS as a function of l at fixed time t. The numerical values $\alpha_H = 1$, $A = 1$ are used.

always negative, meaning that the perturbed entanglement entropy is always smaller than its vacuum value. This counter-intuitive property can be explained by thinking of the quench as a process triggering the condensation of the scalar operator (thus breaking a global symmetry on the boundary, as in holographic superconductors [8]) in an expanding spacetime region. A lower entropy fits with the intuition that, due to condensation, the number of degrees of freedom decreases compared to the vacuum [211], for which the expectation value of the scalar operator vanishes.

Analytic expressions for ΔS can be found in some regimes. Nearby the boundary $r \to +\infty$, we can employ the expansions

$$h_\epsilon = -\frac{2}{r^2} + \dots , \qquad g_\epsilon = \frac{2}{r^2} + \dots . \tag{7.4.13}$$

Since the minimal value of r on the RT surface is given by eq. (7.4.11) evaluated at $x = 0$, the approximation (7.4.13) is valid in the whole integration region involved in the ΔS computation if

$$|A^2 + t^2 - l^2| \gg 2lA\,. \tag{7.4.14}$$

With this assumption, eq. (7.4.10) explicitly gives

$$\Delta S = -\pi^2\,\alpha_H^2 \left[\left(\frac{Al}{\sqrt{\omega(l,t)}} + \frac{\sqrt{\omega(l,t)}}{4Al} \right) \operatorname{arctanh}\left(\frac{2Al}{\sqrt{\omega(l,t)}} \right) - \frac{1}{2} \right] . \tag{7.4.15}$$

The condition (7.4.14) is satisfied in various situations:

- Small radius, $l \ll A$:

$$\Delta S = -\frac{8}{3}\pi^2\,\alpha_H^2\,\frac{A^2\,l^2}{(A^2+t^2)^2}\,. \tag{7.4.16}$$

- Large time, $t \gg A$ and $t \gg l$:

$$\Delta S = -\frac{8}{3}\pi^2\,\alpha_H^2\,\frac{l^2\,A^2}{t^4}\,. \tag{7.4.17}$$

- $t = 0$ and $l \gg A$:

$$\Delta S = -\frac{8}{3}\pi^2\,\alpha_H^2\,\frac{A^2}{l^2}\,. \tag{7.4.18}$$

Remarkably, for given (l, t), the RT surfaces (7.4.9) in Poincaré AdS are mapped by the transformation (7.2.3) to τ-constant surfaces in global AdS. Such surfaces are attached at the boundary $r \to \infty$ to a circle with constant $\theta = \theta_0$, with

$$\theta_0(l,t) = \arctan\left(\frac{2A\,l}{l^2 - t^2 - A^2}\right)\,, \tag{7.4.19}$$

corresponding to a parallel on the S^2 boundary. Consequently, the RT surface is uniquely fixed by the combination of parameters appearing in eq. (7.4.19), and the same holds for $\Delta S(l, t)$.

Among the RT surfaces obtained by a mapping to global AdS, the ones satisfying

$$l = l_0 = \sqrt{t^2 + A^2} \tag{7.4.20}$$

are special, since they lie at constant $\theta = \pi/2$ and at $r \to \infty$ are attached at the equator of S^2. Due to symmetry, we conclude that such surfaces has either the maximal or the minimal area variation $\Delta\mathcal{A}$. In the monopole quench, we know that ΔS is negative and close to zero for both small and large l. So, we expect that $l = l_0$ is a minimum of ΔS, as confirmed by the numeric plots in Fig. 7.10. For $l = l_0$, the exact value of ΔS is

$$\Delta S_0 = \Delta S(l_0) = \frac{\pi^2\,\alpha_H^2}{4}\int_0^\infty (h_\epsilon - g_\epsilon)\,\frac{r}{\sqrt{1+r^2}}\,dr \approx -\Upsilon\,\frac{\pi^2\,\alpha_H^2}{4}\,, \tag{7.4.21}$$

where the last equality is valid for small backreaction and

$$\Upsilon = 6\pi - 12 - 8\pi\,\beta(2) + 14\,\zeta(3) \approx 0.658\,. \tag{7.4.22}$$

In this expression, $\beta(2) \approx 0.916$ is the *Catalan's constant* and ζ is the *Riemann zeta function*. At $t = 0$, the disk with radius $l = l_0$ coincides with the region perturbed by the operator insertion. Then, the disk expands as the core of the quench, see eq. (7.3.3). At large t, the causality bound on the speed of entanglement is met, and both the disk and the perturbation expand at approximately the speed of light. Such a picture heuristically explains why this particular subregion has a time-independent and maximal deviation of entanglement entropy with respect to vacuum: entanglement spreads with matter.

7.4.2 Translated disk

We now translate the disk subregion, shifting its center from the initially perturbed region. For convenience, we introduce Cartesian coordinates

$$\vec{x} = (x_1, x_2) = (x\cos\varphi, x\sin\varphi)\ . \tag{7.4.23}$$

The subregion we look at is a disk of radius l centered at $(x_1, x_2) = (\xi, 0)$ and lying at constant time t. The corresponding RT surface in unperturbed Poincaré AdS_4 is the translated half sphere

$$z = \sqrt{l^2 - (x_1 - \xi)^2 - x_2^2}\,. \tag{7.4.24}$$

In Appendix D.3.1 we write down the integral expressing the first-order correction to the holographic entanglement entropy. Again, the result is invariant under the scaling of spatial and time coordinates in eq. (7.4.12), with $\xi \to \xi/A$ as well. In Fig. 7.11 numerical plots for arbitrary radius l are displayed:

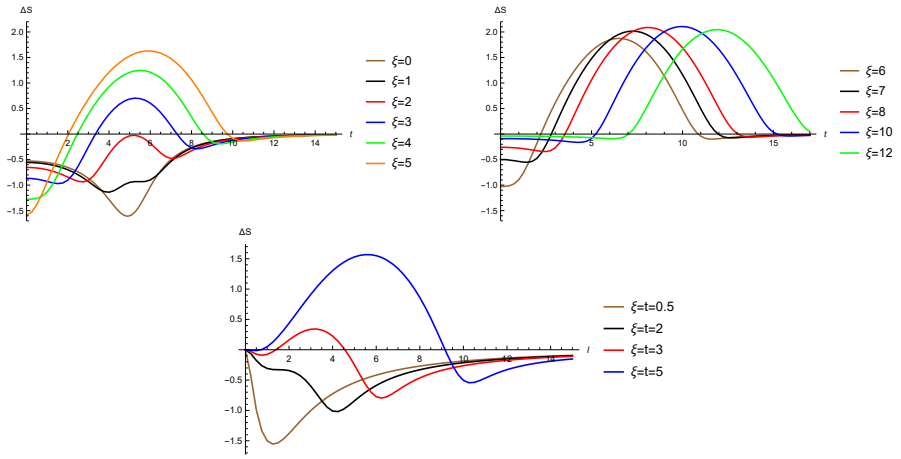

Figure 7.11: Top: Time dependence of ΔS for a disk-shaped subregion of radius $l = 5$ centered at $(x_1, x_2) = (\xi, 0)$ for different values of ξ. For large ξ, the maximum is reached for $t \approx \xi$. Bottom: ΔS as a function of l for a translated disk-shaped subregion, for various values of $t = \xi$. Numerical values $\alpha_H = 1$, $A = 1$ have been fixed.

For small l, the RT surface remains at large r. So, the expansion (7.4.13) can be used, leading to the compact expression

$$\Delta S(l, t, \xi) = -\frac{8}{3}\pi^2\,\alpha_H^2\,\frac{A^2\,l^2}{A^4 + 2A^2\,(\xi^2 + t^2) + (t^2 - \xi^2)^2}\,. \tag{7.4.25}$$

Clearly, such a ΔS is always negative. For large $l \gg \xi$, the subregion can be regarded with good approximation as a disk centered at $\xi \approx 0$. From the results of the previous subsection, we thus expect a negative ΔS. For intermediate l, the quantity ΔS can instead become positive, as shown in Fig. 7.11.

The sign of ΔS for the translated disk can be justified by invoking the simple model of free quasiparticles propagation [57]. In this picture, the excitation is assumed to create many copies of Einstein-Podolsky-Rosen (EPR) pairs, which then propagate without interactions as in Fig. 7.12:

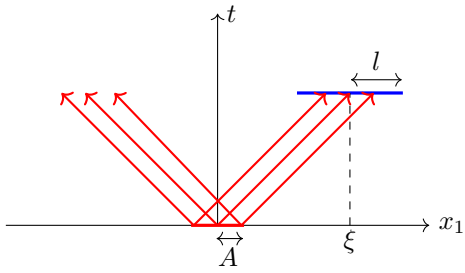

Figure 7.12: Sketch of quasiparticle propagating at the speed of light in the spacetime sectional plane (t, x_1). The entangled quasiparticles in an EPR pair move without interactions in opposite directions. When just one of the quasiparticles belonging to an EPR pair is inside the blue region, the entanglement entropy of the region itself increases.

When just one of the entangled quasiparticles in an EPR pair enters a given region, the entanglement with the outside increases, giving a positive contribution to ΔS. It has been shown that this model reproduces several aspects of the spread of entanglement in global and local quenches [55, 57, 59, 93]. Models with interacting quasiparticles have also been studied [212]. In all these examples, the contribution of the excitations to the entanglement entropy is positive. In the monopole quench, there is also a negative contribution to the entanglement entropy due to the scalar condensate. In general, we expect a competition between the quasiparticle and the condensate contribution, which is responsible for the change of sign of the entanglement entropy variation for the translated disk. It is reasonable to suppose that the translation of the disk from the originally perturbed region enhances the quasiparticles contribution at the expenses of the condensate one. This would explain the absence of positivity regimes of ΔS for the centered disk.

7.4.3 Half-plane

Finally, we take as a boundary subregion the half-plane $x_1 \geq 0$ at constant time t. The unperturbed RT is the bulk surface at $x_1 = 0$ and constant time t. A convenient choice of parameters is

$$y^\alpha = (z, x_2) \, . \tag{7.4.26}$$

Details of the calculations are given in Appendix D.3.2. From the closed-form expression, we deduce that the entropy variation ΔS is a function of t/A. Therefore, it is not restrictive to set $A = 1$. The numerical result is shown in Fig. 7.13:

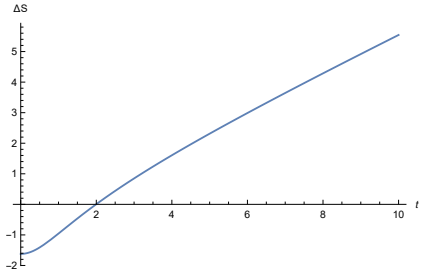

Figure 7.13: Time dependence of ΔS for the half-plane. The numerical values $\alpha_H = 1$, $A = 1$ have been chosen.

At $t = 0$ the entanglement entropy variation is negative, in agreement with the expectation that the condensate reduces the entanglement entropy with respect to vacuum. After an initial transient time, ΔS enters a linear growth regime and becomes positive around $t \approx 2A$. From this time on, we expect the quasiparticles contribution to dominate over the condensate one.

For $t = 0$, the entropy variation is given by the same value ΔS_0 as in eq. (7.4.21). This can be computed by mapping the $t = 0, x_1 = 0$ plane to global AdS by means of the transformation (7.2.3). The resulting RT surface in global AdS lies at $\tau = 0$ and $\varphi = \pm\pi/2$, so from the metric (7.4.3) we can easily compute

$$\Delta S = \frac{\epsilon L^2}{4G} \int_{-\pi/2}^{\pi/2} d\theta \int_0^{+\infty} (h_\epsilon - g_\epsilon) \, \frac{r}{\sqrt{1+r^2}} \, dr = \Delta S_0 \, . \tag{7.4.27}$$

At large t, from the analysis in Appendix D.3.2 we find that ΔS increases linearly in time:

$$\Delta S = K \, \alpha_H^2 \, \frac{t}{A} \, , \qquad K \approx 0.636 \, , \tag{7.4.28}$$

where the constant K is defined in eq. (D.3.13). Such a linear growth agrees with the numerical plot shown in Fig. 7.13. We emphasize that eq. (7.4.28) is valid only in the regime where we can trust our perturbative calculation in the parameter ϵ. At very large t, we expect the large backreaction effects to spoil this result. We point out that a constant growth rate of ΔS at large t has also been found in the $(3+1)$-dimensional BH quench [196].

7.4.4 The first law of entanglement entropy

A formula similar to the first law of thermodynamics is believed to hold for the entanglement entropy under certain assumptions. This so-called *first law of entanglement entropy* (FLEE) can be derived from the *relative entropy* [81, 213], a quantity measuring how distinguishable a density matrix ρ is from a reference density matrix σ:

$$S(\rho||\sigma) = \mathrm{Tr}(\rho \log \rho) - \mathrm{Tr}(\rho \log \sigma)\,. \tag{7.4.29}$$

As a direct consequence of this definition, we always have

$$S(\rho||\sigma) \geq 0\,, \qquad S(\rho||\sigma) = 0 \;\Leftrightarrow\; \rho = \sigma\,. \tag{7.4.30}$$

The relative entropy can be written as

$$S(\rho||\sigma) = \Delta\langle \mathcal{K}_\sigma \rangle - \Delta S\,, \tag{7.4.31}$$

where $\mathcal{K}_\sigma$ is the *modular Hamiltonian* of the density matrix σ

$$\mathcal{K}_\sigma = -\log \sigma\,, \tag{7.4.32}$$

and S is the entanglement entropy $S(\rho) = -\mathrm{Tr}(\rho \log \rho)$. The Δ denotes the difference between a quantity computed for ρ and the same quantity computed for σ. The positivity of relative entropy directly implies

$$\Delta\langle \mathcal{K}_\sigma \rangle \geq \Delta S\,. \tag{7.4.33}$$

If we now specialize to two nearby density matrices, i.e.

$$\sigma = \rho_0\,, \qquad \rho = \rho_0 + \varepsilon \rho_1 + O(\varepsilon^2)\,, \tag{7.4.34}$$

with ε an expansion parameter, the relative entropy scales as

$$S(\rho||\sigma) = O(\varepsilon^2)\,. \tag{7.4.35}$$

Since at $O(\varepsilon)$ the relative entropy vanishes, there is a general expectation [213] that for small deformations eq. (7.4.33) is saturated, leading to the FLEE:

$$\Delta\langle \mathcal{K}_\sigma \rangle = \Delta S\,. \tag{7.4.36}$$

The question if FLEE is satisfied in QFTs is subtle. Indeed, in that case the density matrix ρ is infinite dimensional and, in principle, it is not clear when a perturbation might be considered small.

We now specialize to ball-shaped subsystems, as in Subsecs. 7.4.1 and 7.4.2. The modular Hamiltonian $\mathcal{K}_\sigma$ for the density matrix of a $(2+1)$-dimensional CFT on a spherical region can be expressed in terms of the energy density operator as [167]

$$\mathcal{K}_\sigma = 2\pi \int_{\text{sphere}} d^2\vec{x}\ \frac{l^2 - |\vec{x}|^2}{2l} T_{tt}(\vec{x})\,. \tag{7.4.37}$$

Taking as ρ the density matrix of the state prepared by the operator insertion and as σ the vacuum state, in the limit of small l we get

$$\Delta\langle \mathcal{K}_\sigma \rangle = \frac{\pi l}{2} \Delta E\,, \tag{7.4.38}$$

with ΔE the energy variation between the two states. From the holographic perspective, the RT surface for small radius l is located nearby the AdS boundary, so that the area variation due to backreaction is tiny. It is thus reasonable to suppose the FLEE to be valid in this regime. Plugging eq. (7.4.38) into eq. (7.4.36), the FLEE for small spherical subregions can be written as [214]

$$\Delta S = \frac{\Delta E}{T_E}\,, \qquad T_E = \frac{2}{\pi l}\,, \tag{7.4.39}$$

where T_E is named *entanglement temperature* by virtue of the analogy with the first law of thermodynamics.

Let us come back to the physical system we are examining. In the BH quench, for $l << \sqrt{t^2 + A^2}$ the energy variation between the perturbed and the vacuum state is

$$\Delta E^{(BH)} = 2\pi \int_0^l T_{tt}^{(BH)}\, x\, dx = \frac{M A^3 L^2 l^2}{G(t^2 + A^2)^3}\,, \tag{7.4.40}$$

where eq. (7.3.21) has been used. In this regime, the FLEE (7.4.39) has been found to be satisfied [76]. As we have discussed, for the multitrace deformation in eq. (7.3.14) the holographic energy density for the monopole and the BH quenches are the same up to a scale, see eq. (7.3.29). Therefore, for $l << \sqrt{t^2 + A^2}$ we get

$$\Delta E^{(\kappa)} = \frac{m_M}{m_{BH}}\, \Delta E^{(BH)}\,. \tag{7.4.41}$$

Comparing with eq. (7.4.25), the FLEE is evidently violated in the monopole quench. In particular:

- ΔS is negative, whereas $\Delta E^{(\kappa)}$ is positive.
- ΔS scales as l^2, and not as l^3 as predicted by the FLEE.
- There is no choice of boundary conditions for which the energy $\Delta E^{(\kappa)}$ is proportional to ΔS.

In agreement with our result, the FLEE is generally invalidated in holographic models with scalar fields, in which the FG expansion of the bulk metric does not start at order z^d [213, 215], with d the dimension of the spacetime boundary. The violation of the FLEE in the monopole quench can be understood from the fact that the monopole and vacuum belong to different topological sectors. Consequently, for a fixed value of the multitrace coupling κ the dual states cannot be continuously deformed into each other as required by eq. (7.4.34).

7.5 Discussion

In this chapter we have explored the model of a falling magnetic monopole in Poincaré AdS_4, which is dual to a local quench triggered by the insertion of a local operator in the boundary CFT_3. Starting from the static configuration in the global AdS_4 setup introduced in [198], we have provided an analytic monopole solution including the leading-order backreaction in the regime of small gauge coupling. Then, we have obtained the holographic model of local quench by mapping the static monopole in global AdS_4 to a falling monopole in Poincaré AdS_4, following the trick presented in [206].

By exploiting the AdS/CFT dictionary, we have collected the expectation values of local operators in the dual CFT_3 interested by the local quench. With Dirichlet and Neumann quantizations, the scalar operator has a time-dependent source, which leads to the non-conservation of the energy-momentum tensor. Instead, for the multitrace deformation of eq. (7.3.14), the source for the scalar operator vanishes and the energy of the system is conserved. Remarkably, the energy-momentum tensor for this choice has the same functional form as the energy-momentum tensor for the BH quench studied in [76].

Looking for a better probe of the bulk geometry, we have investigated the variation of holographic entanglement entropy due to the leading-order classical backreaction. Contrary to the energy-momentum tensor, the entropy variation in the monopole quench is in fact different compared to the BH quench one. The latter can be computed as in Sec. 7.4, by setting in eq. (7.4.3)

$$h_\epsilon = 0\,, \qquad g_\epsilon = -\frac{1}{r+r^3}\,, \qquad \epsilon = M\,, \tag{7.5.1}$$

which come from the first-order exact BH metric of eq. (7.3.19) with M regarded as a backreaction parameter. In Fig. 7.14 we show the holographic entanglement entropy variation for the BH and the monopole quenches in the case of translated disk-subregions with fixed radius:

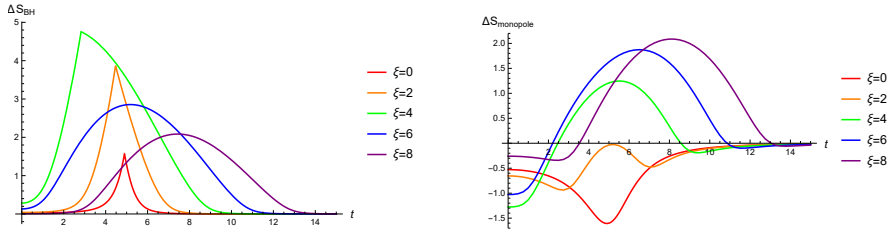

Figure 7.14: Time dependence of the entanglement entropy variation due to backreaction for disk-shaped subregions centered at $(x_1, x_2) = (\xi, 0)$ in the BH (left) and monopole (right) quenches. Plots for fixed subregion radius $l = 5$ and different values of ξ are displayed. We have set $A = L = G = M = \alpha_h = 1$.

For both quenches the positive contribution to ΔS can be ascribed to the free propagation of EPR pairs of entangled quasiparticles [57]. For the monopole quench, an additional negative contribution due to the presence of a condensate at the core of the local quench [211] can cause ΔS to become negative. When the subregion is highly translated with respect to the core of the local quench, such a contribution is dominated by the quasiparticles one.
For a half-plane subregion in the monopole quench, the condensate contribution to ΔS dominates at early times, whereas the quasiparticles contribution dominates at late times, when the entanglement entropy variation manifests a constant growth rate, see Fig. 7.13. The same late time behavior has also been found for the BH quench [196].

The FLEE, relating the variation of entanglement entropy to the variation of energy under small perturbations [214], has been found to hold for small subregions in the BH quench. The similarities between the energy-momentum tensors for the BH and monopole quenches, accompanied by the radically different behaviors of entanglement entropy in the two processes, are responsible for the violation of the FLEE in the latter model. The same outcome is shared with other AdS backgrounds involving the backreaction of scalar bulk fields, see [213, 215]. Whether a given deformation in a QFT obeys the FLEE is still an open question [215]. It would be interesting to further test its validity in different non-equilibrium systems.

Chapter 8

Conclusions and outlook

In this thesis we have investigated different facets of the interconnection between quantum information and gravity. The two key players have been entanglement entropy and (subregion) complexity. While the former is a well-established quantum information quantity holographically interpreted as the area of extremal surfaces into AdS spacetime, the latter is still object of research both in the quantum information and in the gravitational realms.

In the context of computer science, complexity is defined as the minimum number of elementary gates needed to build up a circuit which accomplishes a given computational task. For random circuits, it is now proven that complexity grows linearly for a time exponential in the number of qubits involved by the circuit, prior to saturating to an exponential value [12]. Moreover, when subject to a perturbation triggered by a gate acting on a single qubit, complexity presents a delay in the linear growth known as switchback effect.
A demanding challenge is to extend complexity to quantum mechanical systems, where a continuous definition is prompted. A promising option is represented by the Nielsen's geometrical approach, which replaces the counting of discrete gates forming a circuit with the length of a continuous path representing a unitary operator. Obviously, one would expect complexity geometry to reproduce the same features as circuit complexity. In Ch. 3 we have addressed this question for a system of n qubits, finding some particular regimes in which complexity geometry is compatible with an exponential lower bound and the switchback effect. For the holographic purposes, rather than complexity of unitary operators, we should look at complexity of quantum states. To tackle the issue, we have observed that unitary and state complexity are related by a particular map which goes under the name of Riemannian submersion.

We have then shifted the focus to the holographic interpretation of state complexity as the (spacetime) volume or gravitational action of proper bulk regions. The conjectured gravitational counterparts of complexity can be suitably adapted to deal with mixed states of subsystems, and then turned into holographic proposals for subregion complexity. With the motivation of analyzing the properties of these gravitational quantities, we have explored subregion complexity = volume (subregion-CV), subregion complexity = action (subregion-CA), and subregion complexity = spacetime volume (subregion-CV 2.0) conjectures in diverse spacetimes.

In Ch. 4 we have computed subregion-CA and subregion-CV 2.0 in AdS_3 and the Banados-Teitelboim-Zanelli (BTZ) spacetimes for a boundary line segment. The logarithmically divergent contribution appearing in the results reconstructs the holographic entanglement entropy of the boundary subregion, suggesting a connection with subregion complexity. However, an analogous computation for two disjoint segments in AdS_3 has revealed that subregion complexity and entanglement entropy carry different information.

Another intriguing playground in which to study the gravitational proposals for subregion complexity is the WAdS/WCFT correspondence, which may play a role in the program of generalizing the gauge/gravity duality to non-asymptotically AdS spacetimes. The bulk side is represented by a gravitational theory in asymptotically warped AdS (WAdS), attained as a continuous deformation of AdS_3 spacetime. The boundary side is given by a class of two-dimensional non-relativistic field theories referred to as warped conformal field theories (WCFTs). In Ch. 5 we have studied all the three proposals for a subregion extending to the whole (left) right boundary of WAdS containing a (non-)rotating black hole (BH) in WAdS. With respect to the AdS case, some differences arise in the divergences structure, additivity properties and temperature dependence, which we thoroughly describe below.

The interrelation between gravity and quantum information plays a pivotal role in the analysis of out-of-equilibrium physics in strongly coupled CFTs. On the one hand, quantum information concepts are valuable probes of thermalization. On the other hand, by virtue of the AdS/CFT correspondence, phenomena far from equilibrium at strong coupling admit a gravitational description in terms of time-dependent processes taking place in higher-dimensional AdS spacetime. In this thesis we have considered quantum quenches, which describe thermalization of systems following a global or a local perturbation. A CFT global quench corresponds to the formation of an AdS BH by the gravitational collapse of matter, depicted by Vaidya spacetime, whereas a CFT local quench is dual to the free fall of a massive particle-like object in AdS.
Exploiting holography, we have inspected some aspects of the quench physics by means of quantum information tools. In Ch. 6 we have applied subregion-CV

conjecture for a boundary line segment in three-dimensional Vaidya spacetime, addressing the time evolution of mixed state complexity during a global quench. Instead, in Ch. 7 we have employed holographic entanglement entropy as a probe to distinguish between local quenches realized by the falling of different bulk objects.

In the following, we go into details of the main results of the thesis and we draw the general conclusions of our analysis. We also propose some future directions of related research.

Complexity geometry. For a system of n qubits we can distinguish between two kinds of complexity: unitary complexity, quantifying the difficulty of implementing a unitary operator, and state complexity, measuring how hard it is to prepare a state from a reference one. By employing the geometrical toolkit proposed by Nielsen, we have studied both notions.

Regarding unitary complexity, we have discussed two penalization schemes for the generators of the $\mathfrak{su}(2^n)$ algebra: the draconian model, equally penalizing generators acting on more than two qubits, and the progressive model, in which penalty factors scale as a power of the number of qubits simultaneously entangled by the corresponding generator. We have argued that progressive penalties smoothly reproduce two fundamentals properties in the limit of large n and penalties. Firstly, the unitary manifold has a negative curvature, a condition compatible with ergodicity of geodesics and the switchback effect. Secondly, an etude of conjugate points strongly indicates that maximal unitary complexity scales exponentially with n. Both features are necessary for the quantum system to manifest a chaotic behavior, which in turn is required for complexity to mimic the physics of BH interiors.

Our argument for bounding complexity geometry offers a strong evidence, but not a rigorous proof. Recently, exponential lower bounds on maximal unitary complexity has been shown to hold with two distinct methods: a geometric approach based on the Bishop-Gromov bound on the volume of geodesic balls [140], and a quantum circuit approach based on the counting of gates approximating a unitary operator path [142]. The result extends to a large family of penalization schemes, including the draconian and the progressive models we have investigated. In light of this, one may be worried about the huge arbitrariness in the choice of penalties. In [24], the authors have conjectured that a broad class of high-dimensional geometries exists whose members share the same effective description at long-distances. In other words, while these geometries are highly sensitive to the change of penalties at small scales, they are appreciably the same at large scale (read, from one member to another, large complexities of unitary operators differ at-worst polynomially in the number of qubits n and in the length of the corresponding paths [142]). The exponential

lower bound on maximal complexity common to many penalized geometries can be deemed as a consistency check of this equivalence.

State complexity is defined as the lowest complexity of any operator building the target state from the reference one. The minimization is made trivial by the formalism of Riemannian submersions, which are particular maps from the manifold of unitary operators to the Hilbert space of states. The submersion approach has two main advantages. First, by O'Neill's formula we can compute the sectional curvatures on the state manifold starting from the sectional curvatures on the unitary manifold and the algebra of the $\mathfrak{su}(2^n)$ generators. Second, the geodesics on the state manifold can be built as projections through the Riemannian submersion of horizontal geodesics on the unitary manifold. In principle, both these properties allows us to reveal the geometric structure of the state manifold regardless of its metric. By the way, we have also provided a general closed-form expression for the penalized metric on the state manifold, which we have explicitly used to examine the instructive one-qubit and one-qutrit systems.

The geometric approach to complexity opens to many future directions. We list some of them:

- Penalty factors dramatically affects the properties of complexity geometry, at least at small distances. It would be valuable to figure out how this reflects on complexity in QFT. Studies along these lines have been initiated in [27, 216], where uniform penalties for the entangling gates (resembling the draconian model) have been employed.
- Our results applies to pure states. It would be interesting to extend the geometric approach to putative definitions of mixed state complexity, such as purification and basis complexity [34]. Properties like sub/superadditivity could guide us towards a matching with the holographic results.

Holographic subregion complexity. We now sketch a comparison of subregion-CV ($\mathcal{SC}_V$), subregion-CA ($\mathcal{SC}_A$), and subregion-CV 2.0 ($\mathcal{SC}_{V2.0}$) for a BH in AdS_3 and in $WAdS_3$ spacetimes, concentrating on the divergence structure, additivity properties, and temperature dependence. Once we have a comprehensive view, we look for a match of the holographic results with the putative definitions of mixed state complexity. Before starting, we point out that at the state of the art a firm conclusion is lacking.

In BTZ, subregion complexity has been computed for a mixed state localized on a boundary line segment of length l, while in asymptotically $WAdS_3$ it has been calculated for the left (right) factor of the thermofield double (TFD)

state, which is located on the whole left (right) boundary time-slice. So, for a consistent comparison, in BTZ we take the limit of infinitely long boundary segment. In this limit, our results match $\mathcal{SC}_A$ and $\mathcal{SC}_{V2.0}$ for the left (right) factor of the TFD state dual to a two-sided BTZ BH, which was previously computed in [34, 149]. In particular, the logarithmic divergence appearing in $\mathcal{SC}_A$ (4.3.32) and $\mathcal{SC}_{V2.0}$ (4.3.33) for finite l gets suppressed, and only the linear divergence is left.
The divergence structure of $\mathcal{SC}_A$ and $\mathcal{SC}_{V2.0}$ for the left (right) factor of the TFD state dual to a two-sided WAdS_3 BH is richer, presenting also a logarithmically divergent term. Similar observations hold for $\mathcal{SC}_V$.
In Table 8.1 we summarize these findings for non-rotating BTZ and WAdS_3 BHs, recalling that the divergence structure for rotating WAdS_3 BHs is analogous to the non-rotating case. Contrary to eqs. (4.0.1) and (4.0.2), not knowing the details of the WAdS/WCFT dictionary we do not normalize the bulk quantities:

	BTZ	**Non-rotating WAdS_3 BH**
V	$\frac{Ll}{\varepsilon}$	$\frac{\pi\ell^2}{\varepsilon}\sqrt{\frac{3(\nu^2-1)}{\nu^2+3}} - \frac{2\pi\ell^2\nu^2 r_h \log\varepsilon}{\sqrt{3(\nu^2-1)(\nu^2+3)}}$
I	$\frac{l}{4\pi G}\left(\frac{\log\eta}{\varepsilon} - r_h\log(2\eta)\right)$	$\frac{\ell\sqrt{3(\nu^2-1)}\left(\log\left\lvert\eta^2(\nu^2+3)\right\rvert-1\right)}{8G\varepsilon} + \frac{\ell r_h(7\nu^2-3)\log\varepsilon}{16G\sqrt{3(\nu^2-1)}}$
V_{bulk}	$L^2 l\left(\frac{1}{\varepsilon} - r_h\right)$	$\frac{2\pi\ell^3}{\varepsilon}\frac{\sqrt{3(\nu^2-1)}}{\nu^2+3} - \frac{\pi\ell^3 r_h\log\varepsilon}{\sqrt{3(\nu^2-1)}}$

Table 8.1: Divergence structure of holographic subregion complexity for the left (right) factor of the TFD states dual to the non-rotating BTZ BH with flat horizon and the non-rotating WAdS_3 BH. In the above expressions, r_h is the dimensionless radius of the BH event horizon, ε denotes the dimensionless UV cutoff, $\nu^2 > 1$ represents the warping parameter, L and ℓ are the curvature radii of AdS_3 and WAdS_3, respectively. In the BTZ case, we have taken the limit $l\, r_h >> L$ of the results of Sec. 4.3, reproducing the findings in [34].

For convenience, we have introduced

$$\eta = \begin{cases} \tilde{L}/L & \text{for } \text{AdS}_3\,, \\ \tilde{L}/\ell & \text{for } \text{WAdS}_3\,. \end{cases} \tag{8.0.1}$$

The length scale $\tilde{L}$ arises from the counterterm of eq. (4.1.10), which ensures reparametrization invariance of the total gravitational action. At first sight, the dependence of the action on an arbitrary scale may undermine its physical interpretation. By the way, we should keep in mind that (subregion) complexity itself is affected by a huge degree of arbitrariness, due to the choice of reference state and elementary gates. One possibility is that the ambiguities on both

sides of the correspondence are related to each other. Nevertheless, we can attempt to restrict the allowed values of η. To this purpose, we appeal to the positivity of subregion complexity, which requires the leading divergence in $\mathcal{SC}_A$ to be positive-definite. This is accomplished for $\eta > 1$ in BTZ, and for $\eta > \sqrt{e/(\nu^2+3)}$ in WAdS_3.

Let us now look at the additivity of holographic subregion complexity. Given any two subsystems A and B, we recall that subregion complexity is said to be superadditive whether

$$\mathcal{SC}(A) + \mathcal{SC}(B) \leq \mathcal{SC}(A \cup B)\,, \tag{8.0.2}$$

otherwise it is said to be subadditive.
Considering two identical line segments of length l and distance d on the boundary of AdS_3, we have found that if $d > d_0 = \left(\sqrt{2}-1\right) l$, the three holographic quantities saturates superadditivity, see Fig. 4.7. Below the critical distance d_0, while $\mathcal{SC}_V$ and $\mathcal{SC}_{V2.0}$ are trivially superadditive, the superadditivity of $\mathcal{SC}_A$ can be influenced by the value of η. In particular, as shown in Fig. 4.10, $\mathcal{SC}_A$ is always superadditive for $\eta \geq \eta_0 \approx 2.465$, whereas it is superadditive only at small distances between the two segments for $1 < \eta < \eta_0$.

To compare the BTZ and WAdS_3 BH cases, we specialize to boundary time $t_b = 0$, when the spacetime respects the time-reflection symmetry. In [34, 149], $\mathcal{SC}_V$ for the left (right) factor of the TFD state dual to the non-rotating BTZ BH has been found to saturate superadditivity, contrary to $\mathcal{SC}_{V2.0}$, which is strictly superadditive. Similarly to the two-segments subregion, $\mathcal{SC}_A$ has been observed to be superadditive for $\eta > \eta_D \approx 0.1$ and subadditive for $\eta < \eta_D$.
Remarkably, we have seen that $\mathcal{SC}_A$ for the left (right) factor of the TFD state dual to the WAdS_3 BH is always superadditive, regardless of the value of η. We summarize such properties in Table 8.2:

	BTZ	**WAdS_3 BH**
V	saturates superadditivity	saturates superadditivity
I	superadditive for $\eta > \eta_D \approx 0.1$	superadditive
V_{bulk}	superadditive	superadditive

Table 8.2: Additivity properties of holographic subregion complexity at time $t_b = 0$ for the left (right) factor of the TFD states dual to the BTZ and the WAdS_3 BH. The value of η_D has been computed from [34].

In BTZ, the temperature behavior of the three holographic quantities can be read off from the dependence of the expressions in Table 8.1 on the radius of the BH event horizon r_h. In fact, the temperature of the BTZ BH is given by $T = r_h/(2\pi L)$. We readily note that $\mathcal{SC}_V$ is temperature-independent, $\mathcal{SC}_{V2.0}$ decreases with temperature, and $\mathcal{SC}_A$ decreases with temperature too, but only if $\eta > 1/2$. Remarkably, the positivity constraint $\eta > 1$ forces $\mathcal{SC}_A$ for the left (right) factor of the TFD state dual to the BTZ BH to be superadditivite and to decrease with temperature.
For a rotating BH in WAdS_3, we have instead found that the temperature behavior is non-trivially correlated with the sign of specific heat at constant angular momentum H_J. In details, in the thermodinamically stable region $H_J > 0$, $\mathcal{SC}_V$ increases with temperature, $\mathcal{SC}_A$ decreases with temperature, while the behavior of $\mathcal{SC}_{V2.0}$ depends on the value of the warping parameter ν, and on the radii of the outer and inner event horizons, see Figs. 5.4 and 5.5.

Similarly to other quantum information quantities such as the entanglement entropy, it would be interesting to understand whether subregion complexity could also serve as a probe of out-of-equilibrium physics. With this in mind, we have examined the time evolution of $\mathcal{SC}_V$ for a boundary line segment in three-dimensional Vaidya spacetime, which can be viewed as a holographic model of CFT_2 global quench triggered by an injection of energy in the whole system. Our analysis reveals that soon after the global perturbation, $\mathcal{SC}_V$ grows at a constant rate proportional to the segment length l. Then, $\mathcal{SC}_V$ reaches a maximum value scaling at least as l^2, prior to returning to the initial vacuum value at the thermalization time, after which it remains constant.

The collected information on holographic subregion complexity can serve as a guide to determine the dual CFT quantity. So far, the main proposals quantifying the difficulty of building mixed states are purification complexity $\mathcal{C}_P$ and basis complexity $\mathcal{C}_B$, which we have introduced at the beginning of Ch. 4. The former is defined as the lowest complexity of all purifications of the target state, while the latter is identified with the complexity of preparing the target state ρ from the less complex pure state with the same spectrum as ρ.
A preliminary analysis on the temperature behavior of purification and basis complexity is drawn in [34] on the basis of the limits of vanishing and infinite temperature. To gain some intuition, let us consider the problem of building the thermal state of an n-qubits system. When $T = 0$ the state of our system is pure, so its spectrum is trivial. Supposing that a quantum circuit exists which prepares the state, we have $\mathcal{C}_P = \mathcal{C}_B \sim n$. Instead, when $T \to \infty$ the state is maximally mixed, in which case building the spectrum is enough to fully determine the state, leading to $\mathcal{C}_B = 0$. Also, a purification of the maximally mixed state can be constructed by a circuit of $\mathcal{O}(n)$ gates, giving $\mathcal{C}_P \sim n$. Putting all together and assuming that subregion complexity is a monotonic

function of T, we deduce that $\mathcal{C}_B$ decreases with temperature, while $\mathcal{C}_P$ should weakly depend on temperature.
Following [34], let us now investigate the additivity of purification and basis complexity taking as a bipartition the left ρ_L and right ρ_R factors of the TFD state $|TFD\rangle$. It is here useful to recall that the TFD state is a purification of both the thermal states ρ_L and ρ_R (though, in general, not the optimal one [35]), see Subsec. 2.3.1. Now, building the spectra of two copies of the thermal state clearly costs more than preparing the spectrum of the TFD state. Therefore, roughly estimating purification complexity as the sum of the complexities in constructing the spectrum and the basis of the target state, we conclude that $\mathcal{C}_P$ is subadditive: $\mathcal{C}_P(\rho_L) + \mathcal{C}_P(\rho_R) = 2\,\mathcal{C}_P(\rho_R) > \mathcal{C}(|TFD\rangle)$. On the other hand, the effort in constructing the basis of the TFD state is twice that of preparing the basis of each factor. Since complexity of the TFD state is approximately the sum of the costs of constructing the spectrum and the basis, we deduce that $\mathcal{C}_B$ is superadditive: $\mathcal{C}_B(\rho_L) + \mathcal{C}_B(\rho_R) = 2\,\mathcal{C}_B(\rho_R) < \mathcal{C}(|TFD\rangle)$.

Complexity of mixed states have been later deepened, see e.g. [35, 37, 66, 150]. The conjecture about subadditivity of purification complexity have been explicitly checked and slightly modified. In principle, it is possible to work with two distinct bases for the fundamental gates: a *physical basis*, which distinguishes the physical degrees of freedom of the original mixed state from the artificial degrees of freedom introduced for the purification procedure, and a *diagonal basis*, which shuffles the two sets. An analysis performed in free QFTs have emphasized that the choice of basis affects the properties of purification complexity [35, 217]. In particular, $\mathcal{C}_P$ for the left and right bipartition of the TFD state is subadditive in the diagonal basis, whereas it is superadditive in the physical basis only for particular choices of reference state [35]. We try to sketch the current situation in Table 8.3:

	Additivity	**Temperature dependence**
$\mathcal{C}_P$	depends on the basis and reference state	weakly depends on T
$\mathcal{C}_B$	superadditive	decreases with T

Table 8.3: Properties of purification complexity $\mathcal{C}_P$ and basis complexity $\mathcal{C}_B$. Additivity refers to the bipartition of the TFD state in left and right factors. For $\mathcal{C}_P$, additivity has been explicitly evaluated in free QFTs [35].

Let us finally draw a tentative parallel between the holographic proposals and mixed state complexity of the thermal state.
In BTZ spacetime, $\mathcal{SC}_A$ and $\mathcal{SC}_{V2.0}$ seem to qualitatively match the additivity properties of $\mathcal{C}_P$ in the physical basis, even if only for specific choices of the reference state [35]. An additional clue of the matching comes from the UV divergence, which for the holographic conjectures and $\mathcal{C}_P$ in free QFTs is linear in the cutoff ε and proportional to the subregion length [35], see Table 8.1. Watching at the holographic global quench that we have investigated, interpretation of $\mathcal{C}_P$ as the field theory counterpart of $\mathcal{SC}_V$ could provide us with an heuristic explanation to the presence of a maximum prior to saturation. Indeed, the decreasing of $\mathcal{SC}_V$ shortly before the thermalization can be attributed to the increasing of the number of pure microstates corresponding to the mixed target state. In such a big family of microstates, it should not be hard to find a purification of the target state which is close (in the complexity sense) to the reference state. A local maximum preceding a saturation regime has also been found in the time evolution of mixed state circuit complexity for a line segment in a harmonic chain after a global quench of the mass parameter [218]. Anyway, we stress that for a conclusive comparison we should look at mixed state complexity in strongly coupled CFTs. We mention that some work in this direction has been done. For instance, in two-dimensional CFTs, $\mathcal{C}_P$ has been shown to reproduce subregion-CV, subregion-CA, and subregion-CV 2.0 mutual complexity for adjacent segment-subregions of the vacuum state [36].
In asymptotically WAdS$_3$, Tables 8.2 and 8.3 seem to teach us that $\mathcal{C}_B$ matches $\mathcal{SC}_A$ in the thermodynamically stable region with $H_J > 0$. On the contrary, $\mathcal{C}_B$ seems to match $\mathcal{SC}_V$ in the unstable region with $H_J < 0$. However, we emphasize that the properties of $\mathcal{C}_P$ and $\mathcal{C}_B$ may drastically change in WCFTs. We leave this issue as an interesting future development. We list some other open questions calling for further investigation:

- One of the obscure aspects of (subregion-)CA conjecture is the appearance of the arbitrary scale $\tilde{L}$, arising from the gravitational action counterterm for null boundaries. As we have seen, the value of $\tilde{L}$ considerably affects the physical properties of holographic complexity, thus it requires a physical interpretation from the field theory side of the AdS/CFT correspondence. By comparing the UV divergences of holographic complexity with the QFT results, this bulk length scale has been suggested to be related to the arbitrariness in defining the reference state and the elementary gates in the boundary field theory [27, 28]. The authors of [219, 220] have instead proposed to give up the reparametrization invariance of the gravitational action in favor of a special parametrization which sets to zero the action complexity in vacuum AdS. Consequently, the dual vacuum state is regarded as the reference one. It would be worth clarifying which

picture leads to a better matching between holographic and field theory results.

- The $WAdS_3$ BHs we have considered can also be built as solutions of Topological Massive Gravity and New Massive Gravity. In the presence of additional terms in the gravitational action of the model, the holographic proposals must be modified [221, 222]. The CA conjecture in theories of modified gravity has been studied for several backgrounds [222–224], also including $WAdS_3$ BHs [169]. A possible direction would be to study how holographic subregion complexity for $WAdS_3$ BHs changes with the introduction of new terms in the gravitational action.

- In this thesis we have examined the time evolution of $\mathcal{SC}_V$ during a holographic global quench. It would be interesting to conduct an analogous analysis for $\mathcal{SC}_A$ and $\mathcal{SC}_{V2.0}$. In several cases the three holographic quantities are qualitatively similar, so it is hard to discriminate between them. It would be valuable to test if dynamical processes as the global quench allow for a distinction, also comparing the holographic and QFT outcomes [66, 67, 218].

- In [17] an infinite class of observables localized on codimension-one bulk surfaces has been found to provide viable substitutes for the maximal volume as the holographic dual of complexity. Later, in [18] the result has been generalized to observables living on bulk spacetime regions, also including the gravitational action and the spacetime volume of the WDW patch. All these quantities share two universal features: a linear growth at late time and the switchback effect. A way to prefer an observable of the infinite class would be to look for further features that (subregion) complexity is expected to display. For instance, from the outcomes presented in Chs. 4 and 5 we deduce that additivity properties and temperature dependence discriminate between volume, action, and spacetime volume subregion complexity. In this perspective, it would be helpful to investigate such properties from the field theory side of the AdS/CFT correspondence and to exploit them to skim the putative gravitational duals.

Holographic local quench. Likewise global quenches, local quenches in CFTs can be realized by holographic models. As a starting point, we have found an explicit magnetic monopole solution in global AdS_4 which includes the backreaction of matter fields at the leading order. The analytic solution is valid in the regime of small gauge coupling, while out of this domain we have provided numerical results. By mapping the static configuration in global AdS_4 to a dynamical one in Poincaré AdS_4, we have obtained a free falling magnetic

monopole, which shares the same dynamics as a local quench triggered by the insertion of a condensate in the boundary CFT_3.
We have then drawn a comparison between our setup and a falling BH, wondering how the dual quenches differ. With boundary conditions on bulk fields for which the energy of the dual system is conserved, we have shown that the holographic energy-momentum tensors of the two models have the same functional form, whereas the holographic entanglement entropy evolution is drastically different, to the extent that the first law of entanglement entropy (FLEE) is violated in the monopole case. Basically, the FLEE relates the variation of energy resulting from a continuous deformation of a quantum state to the variation of entanglement entropy. To put it differently, an increasing of the energy should be accompanied by an increasing of the entanglement entropy. This has been shown to be true for the BH quench [76], contrary to the monopole quench, in which case the excitation of the vacuum state due to the condensate insertion causes a decreasing of the entanglement entropy: the degrees of freedom diminish with respect to vacuum because of condensation [211]. The invalidation of the FLEE in the monopole quench can be grasped from topological arguments. Namely, since the monopole and vacuum belong to distinct topological sectors, the dual states are not continuously deformable into each others, which is necessary for the FLEE to hold. The takeaway message is that entanglement entropy, a quantum information concept, can act as a probe for gravitational systems.
We point out some possible future developments:

- The monopole solution with backreaction that we have discussed can be the starting point to study other solitonic objects in AdS. For instance, a falling vortex in AdS_3 could be regarded as a holographic model of CFT_2 local quench. Since AdS_3 is locally equivalent to the BTZ spacetime, a coordinate transformation exists that maps the former into the latter [72, 225]. Upon the application of this map to the static vortex, the resulting configuration is a vortex falling into the BTZ BH, which is the gravitational equivalent to a local quench at finite temperature. We can exploit this setup to check whether the conclusions we have drawn for the monopole quench are solid enough to survive to different spacetime dimensions and non-zero temperature.

- Holographic complexity for local quenches dual to falling particles has been studied in [71, 72]. Along these lines, to gain an insight into the impact of condensates on the evolution of quantum complexity, it could be worth investigating holographic (subregion) complexity for the local quench dual to the falling magnetic monopole. This would also tell us whether this quantity, similarly to holographic entanglement entropy, makes a distinction between different falling objects. To this regard, it would be interesting to look at the *first law of complexity* [226, 227], which

argues that under a perturbation of the target state, the variation of circuit complexity only depends on the endpoint of the optimal circuit. In holographic settings where the target state is well-represented by a dual bulk geometry, the first law of complexity can represent an efficient diagnostic tool. Analysis of the first law of complexity for perturbations triggered by the introduction of bulk scalar fields, in the same spirit as our asymptotically AdS geometry with monopole backreaction, has been performed in [226, 227].

- In [228] (subsystem) circuit complexity for a local quench obtained by suddenly joining two harmonic chains has been studied. The temporal evolution of subsystem complexity for the mixed state localized on a segment has been found to depend on the position of the joining point with respect to the segment itself. However, the quantity generally manifests a local maximum. It would be interesting to compare these findings with holographic results. It is important to stress that the gravitational model described in Ch. 7 is the holographic dual of a local quench triggered by an operator insertion. The joining of two subsystems is instead a different quench protocol, whose gravitational counterpart has been discussed in [191, 229].

Appendix A

Counting out sectional curvatures

A.1 Derivation of the general counting formula

A generalized Pauli matrix ρ of weight $w_\rho = M$ is a tensor product of M SU(2) Pauli matrices σ_i $(i = x, y, z)$ and $n - M$ identity operators $\mathbb{1}_2$. We are here interested in counting the number of generalized Pauli matrices σ of weight $w_\sigma = N$ which anti-commute with ρ and whose commutator has a given weight $w_{[\rho,\sigma]}$. According to eq. (3.1.26), the sectional curvatures $K(\rho, \sigma)$ have the same value for all these generators.

Let us define d as the number of qubits to which ρ and σ assign a *different* SU(2) Pauli matrix. From eq. (3.1.17), we recall that d must necessarily be odd for ρ and σ to anti-commute. Similarly, we define s as the number of qubits to which ρ and σ assign the *same* SU(2) Pauli matrix. We provide an example:

$$\rho = \sigma_x \otimes \mathbb{1}_2 \otimes \sigma_z \otimes \sigma_y \otimes \mathbb{1}_2 \otimes \sigma_z \otimes \sigma_x$$

$$\sigma = \sigma_x \otimes \sigma_y \otimes \mathbb{1}_2 \otimes \sigma_z \otimes \mathbb{1}_2 \otimes \sigma_z \otimes \mathbb{1}_2$$

Figure A.1: Example of anti-commuting generalized Pauli matrices ρ and σ of weight $M = 5$ and $N = 4$ for a system of $n = 7$ qubits. In this case we have $d = 1$ (red entries) and $s = 2$ (blue entries).

By definition, the constraint $d + s \leq \min(M, N)$ must be satisfied.
As a consequence of the SU(2) Pauli matrices algebra, we easily deduce that the commutator $[\rho, \sigma]$ has weight

$$w_{[\rho,\sigma]} = M + N - d - 2s\,. \tag{A.1.1}$$

Note that the weight of the commutator is completely determined by the odd integer $c_{sd} = d + 2s$. For illustrative purposes, we show the allowed values of (s, d) for an odd and even value of $\min(M, N)$:

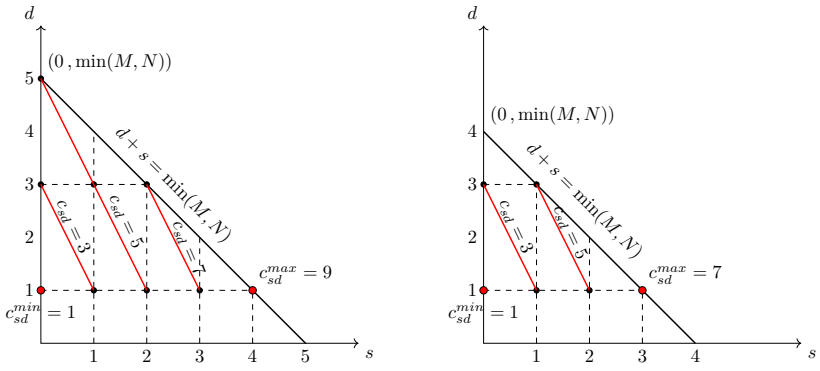

Figure A.2: Black dots represent allowed values of $(s\,, d)$ for odd (on the left) and even (on the right) value of $\min(M, N)$. The pairs $(s\,, d)$ for which we get the minimum and the maximum values of c_{sd} are represented by red dots.

All the pairs providing the same $w_{[\rho,\sigma]}$ are joined by red lines. Clearly, for fixed M and N the value of $w_{[\rho,\sigma]}$ decreases as we move from left to right in the picture. Therefore, the maximum weight is realized for $d = 1$ and $s = 0$, whereas the minimum weight is realized for $d = 1$ and $s = \min(M - 1, N - 1)$. It is thus convenient to introduce an integer label r, such that the possible values of the weight $w_{[\rho,\sigma]}$ are

$$w_r = |M - N| + 1 + 2r\,, \tag{A.1.2}$$

where

$$\begin{aligned} &\text{for} \quad M \geq N: \qquad r = N - \frac{d + 2s + 1}{2}\,, \qquad r = 0, \ldots, N - 1\,, \\ &\text{for} \quad M < N: \qquad r = M - \frac{d + 2s + 1}{2}\,, \qquad r = 0, \ldots, M - 1\,. \end{aligned} \tag{A.1.3}$$

So far, we have not taken into account that the weight of a generator cannot exceed the number of qubits, i.e. $w_r \leq n$. This upper bound can be specified

by restricting the integer r to the range

$$\begin{aligned} 0 \leq r \leq \min\left(N-1, \left[\frac{n-(M-N)-1}{2}\right]\right) \qquad & \text{for} \quad M \geq N\,, \\ 0 \leq r \leq \min\left(M-1, \left[\frac{n-(N-M)-1}{2}\right]\right) \qquad & \text{for} \quad M < N\,, \end{aligned} \tag{A.1.4}$$

where $[\dots]$ denotes the integer part.

We now focus on a generator ρ of weight M. Such a generator acts on M qubits with an SU(2) Pauli matrix and leaves the remaining $n-M$ qubits invariant. For computational purposes, we address the issue of determining the number $\mathcal{R}(M,N,r)$ of generators σ with weight N whose commutator $[\rho,\sigma]$ has weight w_r, as in eq. (A.1.2). In order to derive an explicit expression for $\mathcal{R}(M,N,r)$, we first count the generators σ for a given value of (s,d). Then, we sum over all the allowed values of (s,d).

Let us discuss how to build a generator σ with fixed value of (s,d). We start by considering d out of the M qubits on which ρ acts, and require σ to assign to each of them an SU(2) Pauli matrix different than the one assigned by ρ. This can be achieved in $2^d\binom{M}{d}$ ways. Next, we choose s out of the remaining $M-d$ qubits involved by ρ, and demand σ to assign to each of them the same SU(2) Pauli matrix assigned by ρ. This choice can be performed in $\binom{M-d}{s}$ ways. Then, since σ has weight N, we are left with $N-d-s$ arbitrary one-qubit Pauli matrices to be distributed among the $n-M$ qubits untouched by ρ. This can be accomplished in $3^{N-d-s}\binom{n-M}{N-d-s}$ ways. Finally, we fill out the remaining entries in the σ tensor product with identity operators. Putting all together, the number of generators σ satisfying the required properties is thus

$$\mathcal{R}_{sd}(M,N,r) = 2^d \binom{M}{d}\binom{M-d}{s}\binom{n-M}{N-d-s} 3^{N-d-s}\,. \tag{A.1.5}$$

The number $\mathcal{R}(M,N,r)$ we are interested in is obtained by summing over all the allowed values of (s,d) providing the same weight w_r:

$$\mathcal{R}(M,N,r) = \sum_{(s,d)\in L_r^{(M,N)}} \mathcal{R}_{sd}(M,N,r)\,, \tag{A.1.6}$$

where

$$\begin{aligned} L_r^{(M,N)} &= \left\{(s,d)\,|\, s = N-r-\frac{d+1}{2},\, d\,\text{odd},\, d \leq 2r+1\right\} \qquad \text{for} \quad M \geq N\,, \\ L_r^{(M,N)} &= \left\{(s,d)\,|\, s = M-r-\frac{d+1}{2},\, d\,\text{odd},\, d \leq 2r+1\right\} \qquad \text{for} \quad M < N\,, \end{aligned} \tag{A.1.7}$$

see eq. (A.1.3) and Fig. A.2. Defining $d = 2k + 1$ with k a positive integer, we get for $M \geq N$:

$$\mathcal{R}(M,N,r) = \sum_{k=0}^{r} 2^{2k+1} \binom{M}{2k+1} \binom{M-2k-1}{N-r-k-1} \binom{n-M}{r-k} 3^{r-k}\,, \quad \text{(A.1.8)}$$

and for $M < N$:

$$\mathcal{R}(M,N,r) = \sum_{k=0}^{r} 2^{2k+1} \binom{M}{2k+1} \binom{M-2k-1}{M-r-k-1} \binom{n-M}{N-M+r-k} 3^{N-M+r-k}\,. \quad \text{(A.1.9)}$$

Note that in these expressions we should not worry about negative values of $N-r-k-1$ and $M-r-k-1$, respectively, which indeed may occur.[1] In fact, the corresponding terms into the sum vanish, as can be seen by analytically continuing the binomial coefficient with the Γ function.

We can now determine the number $\mathcal{N}(M,N,r)$ of sectional curvatures with value $K(M,N,r)$ given in eq. (3.3.4). This is simply

$$\mathcal{N}(M,N,r) = \mathcal{N}_M\, \mathcal{R}(M,N,r) = \mathcal{N}_N\, \mathcal{R}(N,M,r)\,, \quad \text{(A.1.10)}$$

where $\mathcal{N}_M$ and $\mathcal{N}_N$ denote the number of generators with weight M and N respectively, see eq. (3.3.1).

A.2 Counting arguments in the progressive model

We now apply the general counting formula to the progressive schedule (3.3.11): $q_w = \alpha^{w-1}$. Starting from eq. (3.3.4), we compute the values of sectional curvatures $K(M,N,r)$ associated to two generalized Pauli matrices with weight M and N. A direct calculation gives, for $M \geq N$:

$$K(M,N,r) = -3\alpha^{2(r+1-N)} + 2\alpha^{1-N} + 2\alpha^{1-M} + \alpha^{-2r}(1-\alpha^{-(M-N)})^2\,, \quad \text{(A.2.1)}$$

and, for $M < N$:

$$K(M,N,r) = -3\alpha^{2(r+1-M)} + 2\alpha^{1-N} + 2\alpha^{1-M} + \alpha^{-2r}(1-\alpha^{-(N-M)})^2\,. \quad \text{(A.2.2)}$$

Note that, at large α, sectional curvatures scale at most as $\alpha^0 + \mathcal{O}(\alpha^{-1})$.

[1] This happens because we have just imposed $d + s \leq \min(M,N)$ as an upper bound to the value of k into the sum. However, for $2r \geq \min(M,N) - 1$ a tighter bound is given by $s = \min(M,N) - r - k - 1 \geq 0$, see Fig. A.2.

Leading order

Let us consider the α^0 contributions to eqs. (A.2.1,A.2.2). For $r = 0$, the only non-vanishing sectional curvatures at this order are for $M = N = 1$ and

$$M, N > 1\,, \qquad M \neq N\,, \tag{A.2.3}$$

in which cases $K = 1$. For $r \geq 1$, that is allowed only for $M, N > 1$, we have

$$K\left(M, N, r\right) = \begin{cases} -3\alpha^{2(r+1-N)} + O\left(\alpha^{-1}\right) & \text{for } \; M \geq N\,, \\ -3\alpha^{2(r+1-M)} + O\left(\alpha^{-1}\right) & \text{for } \; M < N\,. \end{cases} \tag{A.2.4}$$

In both cases, the α^0 order is non-vanishing only for the maximum value $r = \min(M-1, N-1)$, for which $K = -3$.

We can now compute the Ricci tensor contracted with a unit vector $u\left(\sigma\right)$ with weight $w_\sigma = M$, defined in eq. (3.5.6):

$$R_M = \sum_N \sum_r K\left(M, N, r\right)\, \mathcal{R}\left(M, N, r\right)\,. \tag{A.2.5}$$

For $M = 1$, the only leading-order contribution is for $M = N = 1$:

$$R_1 = \mathcal{R}\left(1, 1, 0\right) = 2\,. \tag{A.2.6}$$

For $1 < M \leq n$, there are both positive and negative contributions to R_M. The positive leading-order contributions are given by the sectional curvatures with $r = 0$, whose value is $K = 1$:

$$\begin{aligned} R_M^+ &= \sum_{N=2}^{M-1} \mathcal{R}\left(M, N, 0\right) + \sum_{N=M+1}^{n} \mathcal{R}\left(M, N, 0\right) \\ &= 2M\left(2^{M-1} - 3 + 2^{2(n-M)}\right)\,. \end{aligned} \tag{A.2.7}$$

The negative leading-order contributions to R_M are given by the sectional curvatures with $r = N - 1$ if $M \geq N$ and $r = M - 1$ if $M < N$, all equal to $K = -3$. The multiplicity of such sectional curvatures turns out to be the same in both cases:

$$\begin{aligned} \mathcal{R}\left(M, N, N-1\right) &= 2M \binom{n-M}{N-1} 3^{N-1} \qquad \text{for } \; M \geq N\,, \\ \mathcal{R}\left(M, N, M-1\right) &= 2M \binom{n-M}{N-1} 3^{N-1} \qquad \text{for } \; M < N\,. \end{aligned} \tag{A.2.8}$$

From here we get

$$R_M^- = -3 \sum_{N=2}^{N_{\max}} 2M \binom{n-M}{N-1} 3^{N-1} = -6M \left[2^{2(n-M)} - 1 \right] . \tag{A.2.9}$$

The maximum value of N into the sum, $N_{\max} = 1 + n - M$, ensures that $r = \min(M-1, N-1)$ is allowed, as can be deduced from eq. (A.1.4).
Finally, the leading-order result for R_M with $1 < M \leq n$ is

$$R_M = R_M^+ + R_M^- = 2M \left(2^{M-1} - 2^{2(n-M)+1} \right) . \tag{A.2.10}$$

Using eq. (3.3.1) and this result, the scalar curvature is computed as

$$R = \sum_{M=1}^{n} \mathcal{N}_M \, R_M = 3n \left(4^n - 2 \times 7^{n-1} \right) . \tag{A.2.11}$$

Next-to-leading order

We can systematically improve the previous calculation order by order in the expansion parameter α. For example, at order α^{-1}, the only non-zero contributions $\delta K^{(1)}(M, N, r)$ to the sectional curvatures (A.2.1,A.2.2) are

$$M = N = 2 , \qquad r = 0, 1 , \qquad \delta K^{(1)} = \frac{4}{\alpha} ,$$

$$M = N - 1 , \qquad N \geq 4 , \qquad r = 0 , \qquad \delta K^{(1)} = -\frac{2}{\alpha} ,$$

$$M = 2 , \qquad N \geq 4 , \qquad r = 0 , \qquad \delta K^{(1)} = \frac{2}{\alpha} ,$$

$$M = 2 , \qquad N \geq 3 , \qquad r = 1 , \qquad \delta K^{(1)} = \frac{2}{\alpha} ,$$

and the ones obtained by exchanging M and N.
Due to non-trivial cancellations, the only correction to R_M is for $M = 2$:

$$\delta R_2^{(1)} = \sum_N \sum_r \delta K^{(1)}(2, N, r) \, \mathcal{R}(2, N, r) = \frac{4^n}{\alpha} . \tag{A.2.12}$$

This gives the following correction to the curvature:

$$\delta R^{(1)} = \mathcal{N}_2 \, \delta R_2^{(1)} = \frac{9}{2} n(n-1) \frac{4^n}{\alpha} . \tag{A.2.13}$$

Appendix B

Alternative computations of the action

B.1 Another regularization for the action of one segment in BTZ

In this Appendix we repeat the calculation of subregion-CA for a line segment in BTZ applying regularization A of Fig. 4.4. In particular, the null boundaries of the WDW patch are attached to the spacetime boundary $z = 0$ and a timelike regularizing surface $z = \varepsilon$ cuts the bulk region we integrate over. The resulting geometry is shown in figure B.1.

The geometric data are slightly different from the ones introduced in Sec. 4.3. The RT surface and the entanglement wedge are the same as eqs. (4.3.3) and (4.3.8), but the WDW patch boundaries are now

$$t_{\text{WDW}} = \pm \frac{z_h}{4} \log \left(\frac{z_h + z}{z_h - z} \right)^2 , \tag{B.1.1}$$

where the plus and minus sign refers to the future and negative boundaries, respectively. The null normals to the WDW patch and entanglement wedge boundaries are unchanged, while the intersection curve between the WDW patch and entanglement wedge boundaries becomes

$$z_{\text{int}} = z_h \coth \left(\frac{l}{2z_h} \right) - z_h \cosh \left(\frac{x}{z_h} \right) \operatorname{csch} \left(\frac{l}{2z_h} \right) . \tag{B.1.2}$$

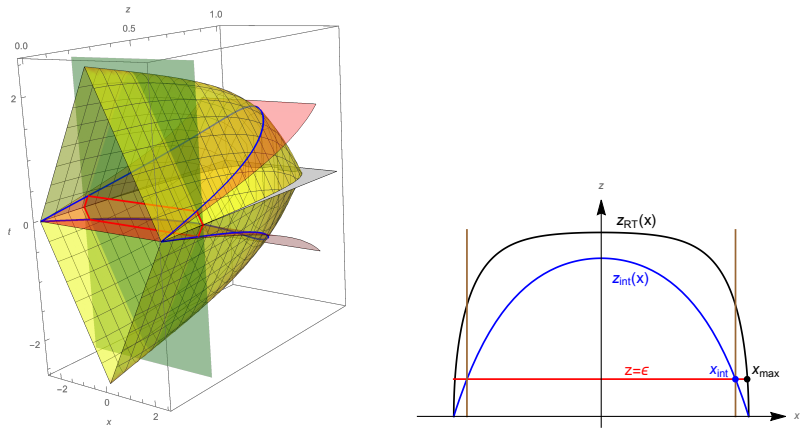

Figure B.1: Bulk region involved in the action computation for a segment in the BTZ case, with $l = 5$. Left: Intersection between the WDW patch and entanglement wedge in the (x, z, t) space. The boundary of the entanglement wedge is in yellow, while the boundary of the WDW patch is in red. Right: Intersections in the (x, z) plane, with z_{RT} in black, z_{int} in blue and the cutoff $z = \varepsilon$ in red.

Contrary to regularization B, such an intersection curve and the RT surface do not meet at the cutoff $z = \varepsilon$, but at the boundary $z = 0$. For this reason, there are no codimension-three joints. The meeting points between the intersection curve and the cutoff are located at $x = \pm x_{\text{int}}$, with

$$x_{\text{int}} = z_h \operatorname{arccosh}\left(\cosh\left(\frac{l}{2z_h}\right) - \frac{\varepsilon}{z_h}\sinh\left(\frac{l}{2z_h}\right)\right) . \tag{B.1.3}$$

As usual, exploiting the invariance of the bulk region under $t \to -t$ and $x \to -x$, we restrict the action computation to $t \geq 0, x \geq 0$.

B.1.1 Action computation

The contributions to the gravitational action are

$$I = I_{\mathcal{W}} + I_{\text{GHY}} + I_{\mathcal{N}} + I_{\mathcal{J}} + I_{ct} , \tag{B.1.4}$$

where the appearance of the GHY term is due to the regularization choice.

Bulk contribution. Following the right Fig. B.1, we split the bulk term into three contributions:

$$
\begin{aligned}
I^1_{\mathcal{W}} &= -\frac{L}{4\pi G}\int_0^{x_{\rm int}} dx \int_\varepsilon^{z_{\rm int}} dz \int_0^{t_{\rm WDW}} \frac{dt}{z^3}\,,\\
I^2_{\mathcal{W}} &= -\frac{L}{4\pi G}\int_0^{x_{\rm int}} dx \int_{z_{\rm int}}^{z_{\rm RT}} dz \int_0^{t_{\rm EW}} \frac{dt}{z^3}\,,\\
I^3_{\mathcal{W}} &= -\frac{L}{4\pi G}\int_{x_{\rm int}}^{x_{\rm max}} dx \int_\varepsilon^{z_{\rm RT}} dz \int_0^{t_{\rm EW}} \frac{dt}{z^3}\,.
\end{aligned}
\tag{B.1.5}
$$

A direct evaluation conveys

$$
\begin{aligned}
I^1_{\mathcal{W}} + I^2_{\mathcal{W}} =& \frac{L}{16\pi G z_h}\int_0^{x_{\rm int}} dx \left\{ \coth\left(\frac{x}{z_h}\right) \log\left| \frac{\sinh\left(\frac{l-2x}{2z_h}\right)\sinh^2\left[\frac{l+2x}{4z_h}\right]}{\sinh\left(\frac{l+2x}{2z_h}\right)\sinh^2\left[\frac{l-2x}{4z_h}\right]}\right| \right.\\
&\left. + \frac{2\sinh\left(\frac{l}{2z_h}\right)}{\cosh\left(\frac{l}{2z_h}-\cosh\left(\frac{x}{z_h}\right)\right)} - \frac{2z_h}{\varepsilon} + \left(\frac{z_h^2}{\varepsilon^2}-1\right)\log\left|\frac{z_h-\varepsilon}{z_h+\varepsilon}\right| \right\}\,,
\end{aligned}
$$

$$
I^3_{\mathcal{W}} = -\frac{L}{16\pi G}\,. \tag{B.1.6}
$$

The total bulk contribution is thus given by

$$
I_{\mathcal{W}} = 4\left(I^1_{\mathcal{W}} + I^2_{\mathcal{W}} + I^3_{\mathcal{W}}\right)\,. \tag{B.1.7}
$$

Gibbons-Hawking-York contribution. The GHY surface term in the action is expressed in eq. (4.1.5). The only contribution of this kind comes from the timelike regularizing surface at $z=\varepsilon$, and can be separated into two parts:

$$
\begin{aligned}
I^1_{\rm GHY} &= \left[\frac{L}{8\pi G}\int_0^{x_{\rm int}} dx \int_0^{t_{\rm WDW}} dt \left(\frac{2}{z^2}-\frac{1}{z_h^2}\right)\right]_{z=\varepsilon} = \frac{L}{8\pi G}\frac{l}{\varepsilon} - \frac{L}{4\pi G}\,,\\
I^2_{\rm GHY} &= \left[\frac{L}{8\pi G}\int_{x_{\rm int}}^{x_{max}} dx \int_0^{t_{\rm EW}} dt \left(\frac{2}{z^2}-\frac{1}{z_h^2}\right)\right]_{z=\varepsilon} = \frac{L}{8\pi G}\,.
\end{aligned}
\tag{B.1.8}
$$

The total GHY contribution then reads

$$
I_{\rm GHY} = 4\left(I^1_{\rm GHY} + I^2_{\rm GHY}\right) = \frac{L}{2\pi G}\left(\frac{l}{\varepsilon}-1\right)\,. \tag{B.1.9}
$$

Null boundary terms. The details of the null boundaries contributions are very similar to regularization B. Namely, $I_{\mathcal{N}}$ and the counterterm on the

entanglement wedge boundaries vanish. The counterterm on the boundary of the WDW patch is instead

$$
\begin{aligned}
I_{ct}^{\mathrm{WDW}} &= -\frac{L}{2\pi G}\int_0^{x_{\mathrm{int}}} dx \int_\varepsilon^{z_{\mathrm{int}}} \frac{dz}{z^2}\log\left|\frac{\tilde{L}}{L^2}\,\alpha z\right| = \\
&= \frac{L}{2\pi G}\int_0^{x_{\max}} dx \left\{ \frac{1+\log\left|\frac{\tilde{L}}{L^2}\,\alpha\varepsilon\right|}{\varepsilon} + \frac{\sinh\left(\frac{l}{2z_h}\right)}{z_h\left[\cosh\left(\frac{x}{z_h}\right)-\cosh\left(\frac{l}{2z_h}\right)\right]}\times \right. \\
&\left. \times\left(1+\log\left|\frac{\tilde{L}z_h\alpha}{L^2}\,\frac{\cosh\left(\frac{l}{2z_h}\right)-\cosh\left(\frac{x}{z_h}\right)}{\cosh\left(\frac{l}{2z_h}\right)}\right|\right)\right\}.
\end{aligned}
\tag{B.1.10}
$$

Joint terms. Besides the null-null joints at the RT surface and at the intersection curve between the future boundaries of the WDW patch and entanglement wedge, that we have already met in regularization B, timelike-null joints rise at the cutoff surface. To deal with such contributions, described in eq. (4.1.8), we introduce the outward-directed normal one-form $\mathbf{s}$ to the $z=\varepsilon$ surface

$$
\mathbf{s} = -\frac{L}{\varepsilon\sqrt{f(\varepsilon)}}dz\,. \tag{B.1.11}
$$

Summarizing, there are four terms:

- The timelike-null joint at the intersection between the future boundary of the WDW patch and the regulator surface, giving

$$
\begin{aligned}
I_{\mathcal{J}}^{\mathrm{cutoff1}} &= -\frac{L}{8\pi G}\int_0^{x_{\mathrm{int}}}\frac{dx}{\varepsilon}\log\left(\frac{\alpha\,\varepsilon}{L\sqrt{f(\varepsilon)}}\right) \\
&= -\frac{L}{16\pi G}\frac{l}{\varepsilon}\log\left(\frac{\alpha\varepsilon}{L}\right)+\frac{L}{8\pi G}\log\left(\frac{\alpha\varepsilon}{L}\right).
\end{aligned}
\tag{B.1.12}
$$

- The timelike-null joint at the intersection between the future boundary of the entanglement wedge and the regulator surface, reading

$$
I_{\mathcal{J}}^{\mathrm{cutoff2}} = \mathcal{O}\left(\varepsilon\log\varepsilon\right). \tag{B.1.13}
$$

- The null-null joint at the RT surface, which is the same as in regularization B, see eq. (4.3.26).

- The null-null joint at the intersection curve between the future boundaries of the WDW patch and entanglement wedge, leading to

$$I_{\mathcal{J}}^{\text{int}} = \frac{L}{8\pi G z_h}\int_0^{x_{\text{int}}} dx\, \frac{\sinh\left(\frac{l}{2z_h}\right)}{\cosh\left(\frac{l}{2z_h}\right)-\cosh\left(\frac{x}{z_h}\right)}\times \\ \times \log\left|\frac{\alpha\beta z_h^2}{2L^2}\frac{\left(\cosh\left(\frac{l}{2z_h}\right)-\cosh\left(\frac{x}{z_h}\right)\right)^2}{\cosh\left(\frac{x}{z_h}\right)\cosh\left(\frac{l}{2z_h}\right)-1}\right| . \tag{B.1.14}$$

The total joint contribution yields

$$I_{\mathcal{J}} = 4(I_{\mathcal{J}}^{\text{cutoff1}} + I_{\mathcal{J}}^{\text{cutoff2}} + I_{\mathcal{J}}^{\text{int}}) + 2I_{\mathcal{J}}^{\text{RT}} . \tag{B.1.15}$$

B.1.2 Complexity

Summing up all the contributions and performing the integrals, we finally get

$$\mathcal{SC}_A^{\text{BTZ}} = \frac{c}{6\pi^2}\frac{l}{\varepsilon}\left(1+\log\left(\frac{\tilde{L}}{L}\right)\right) - \log\left(\frac{2\tilde{L}}{L}\right)\frac{S^{\text{BTZ}}}{\pi^2} - \frac{c}{3\pi^2}\left(\frac{1}{2}+\log\left(\frac{\tilde{L}}{L}\right)\right)+\frac{c}{24} . \tag{B.1.16}$$

The only differences with eq. (4.3.32), obtained through regularization B, are in the coefficient of the linear divergence and in a finite piece dependent on the counterterm scale $\tilde{L}$.

Recently, in order to obtain a universal divergences structure of the gravitational action, independently of the adopted regularization scheme, counterterms on timelike boundaries have been proposed. In regularization A, the counterterm for the timelike cutoff surface reads [182]

$$I_{\text{ct}}^{\text{cutoff}} = -\frac{1}{16\pi G}\int d^{D-2}x\, dt\, \sqrt{-h}\left(\frac{2(D-2)}{L}+\frac{L}{D-3}\tilde{R}\right) , \tag{B.1.17}$$

being $\tilde{R}$ the Ricci scalar on the codimension-one surface $z=\varepsilon$.[1] Adding the extra counterterm with $D=3$ to eq. (B.1.17), we find

$$\mathcal{SC}_A^{\text{BTZ}} = \frac{c}{6\pi^2}\frac{l}{\varepsilon}\log\left(\frac{\tilde{L}}{L}\right) - \log\left(\frac{2\tilde{L}}{L}\right)\frac{S^{\text{BTZ}}}{\pi^2} - \frac{c}{3\pi^2}\log\left(\frac{\tilde{L}}{L}\right)+\frac{c}{24} . \tag{B.1.18}$$

As a result, the numerical coefficient of all the divergences is the same as in eq. (4.3.32), and the two regularizations differ just by a finite piece dependent on the counterterm length scale $\tilde{L}$.

[1] The Ricci scalar on the cutoff surface $z=\varepsilon$ reads $\tilde{R} = (D-2)(D-3)\varepsilon^2/L^4$.

B.2 Holographic conjectures for warped non-rotating black holes

In this Appendix we focus on the non-rotating WAdS BH with $r_+ = r_h$ and $r_- = 0$. By adapting the calculations described in Secs. 5.2 and 5.3, we check that the divergences of holographic (subregion-)complexity reproduce the limit $r_- \to 0$ of the rotating case.

B.2.1 Total action

We start by computing the CA conjecture, relating complexity to the gravitational action of the WDW patch. The Penrose diagram and the WDW patch for the non-rotating WAdS BH are illustrated in Fig. B.2. In the following, we determine each contribution to the gravitational action.

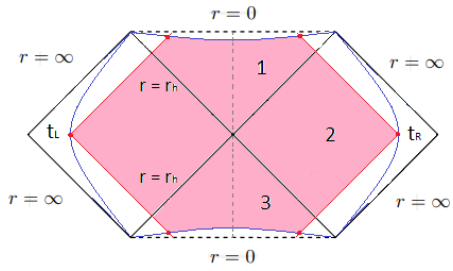

Figure B.2: Penrose diagram and WDW patch at $t_L = t_R = \frac{t_b}{2} = 0$ for the non-rotating WAdS BH.

Bulk contributions. As shown in Fig. B.2, the bulk contribution can be partitioned into three terms:

$$
\begin{aligned}
I^1_{\mathcal{W}} &= \frac{\mathcal{I}}{8G} \int_{\varepsilon_0}^{r_h} dr \left(\frac{t_b}{2} + r^*_\Lambda - r^*(r) \right) , \\
I^2_{\mathcal{W}} &= \frac{\mathcal{I}}{4G} \int_{r_h}^{\Lambda} dr \left(r^*_\Lambda - r^*(r) \right) , \\
I^3_{\mathcal{W}} &= \frac{\mathcal{I}}{8G} \int_{\varepsilon_0}^{r_h} dr \left(-\frac{t_b}{2} + r^*_\Lambda - r^*(r) \right) ,
\end{aligned}
\tag{B.2.1}
$$

with $\mathcal{I}$ given in eq. (5.1.15) and $\epsilon_0 \to 0$ an IR cutoff. The sum of eqs. (B.2.1) provides the total bulk action

$$\begin{aligned} I_{\mathcal{W}}^{\text{tot}} &= \frac{\mathcal{I}}{2G}\int_0^{\Lambda} dr\,(r_\Lambda^* - r^*(r)) \\ &= -\frac{\ell}{4G}(\nu^2+3) r_\Lambda^*\,\Lambda + \frac{\ell}{4G}(\nu^2+3)\int_0^{\Lambda} dr\, r^*(r)\,. \end{aligned} \tag{B.2.2}$$

Boundary terms. Contrary to the rotating case, we have here to include the GHY term (4.1.5) for the two spacelike boundaries at $r = \varepsilon_0$. This evaluates to [119]

$$\begin{aligned} I_{\text{GHY}} &= -\frac{\ell(\nu^2+3)}{4G}(2\varepsilon_0 - r_h)(r_\Lambda^* - r^*(\varepsilon_0)) \\ &= \frac{\ell(\nu^2+3)}{4G} r_h\,(r_\Lambda^* - r^*(0))\,, \end{aligned} \tag{B.2.3}$$

where in the last step we have taken the limit $\varepsilon_0 \to 0$. Due to the near-boundary behavior of the tortoise coordinate, the expression is divergent for $\Lambda \to \infty$. As in the rotating case, the contributions from null boundaries vanish because we are using an affine parametrization for the null geodesics congruence, see eq. (5.1.19).

Joint contributions. We have two classes of joints: null-null joints at the UV cutoff $r = \Lambda$ and spacelike-null joints at the IR cutoff $r = \varepsilon_0$. The latter vanish when we perform the limit $\varepsilon_0 \to 0$. The former are instead given by eq. (5.2.18) with $r_k = \Lambda$ and $\zeta_k = -1$:

$$\begin{aligned} I_{\mathcal{J}}^{\text{tot}} &= 2 \times \frac{\ell}{4G}\sqrt{\frac{\Lambda}{4}\Psi(\Lambda)}\,\log\left|\frac{\ell^2}{\alpha^2}\frac{f(\Lambda)}{2\Upsilon(\Lambda)}\right| \\ &= \frac{\ell}{4G}\sqrt{\Lambda\Psi(\Lambda)}\,\log\left|\frac{\ell^2}{\alpha^2}\frac{(\nu^2+3)(\Lambda - r_h)}{\Psi(\Lambda)}\right|. \end{aligned} \tag{B.2.4}$$

Counterterm for null boundaries. Similarly to eq. (5.2.24), the counterterm which renders the action invariant under diffeomorphisms is

$$I_{\text{ct}}^{\text{tot}} = 4\times\frac{\ell}{4G}\int_{\varepsilon_0}^{\Lambda} dr\,\frac{6(\nu^2-1)r + (\nu^2+3)r_h}{4\sqrt{r\Psi(r)}}\,\log\left|\frac{\alpha\tilde{L}}{2\ell^2}\frac{6(\nu^2-1)r + (\nu^2+3)r_h}{\sqrt{r\Psi(r)}}\right|. \tag{B.2.5}$$

Analytically solving the integral and taking $\varepsilon_0 \to 0$, we find

$$I_{ct}^{\rm tot} = \frac{\ell}{4G}\left[\frac{2(\nu^2+3)r_h}{\sqrt{3(\nu^2-1)}}\arctan\left(\frac{\sqrt{3(\nu^2-1)\Lambda}}{\sqrt{(\nu^2+3)r_h+3(\nu^2-1)\Lambda}}\right)\right.$$
$$\left.-\sqrt{\Lambda\Psi(\Lambda)}\log\left|\frac{4\ell^4}{\alpha^2\tilde{L}^2}\frac{\Lambda\Psi(\Lambda)}{\left[(\nu^2+3)r_h+6(\nu^2-1)\Lambda\right]^2}\right|\right] .$$

Total action. Putting all the results together, we obtain the expression for the total action of the WDW patch

$$I^{\rm tot} = \frac{\ell}{4G}(\nu^2+3)\int_0^\Lambda dr\, r^*(r) - \frac{\ell}{4G}(\nu^2+3)r_\Lambda^*\,\Lambda + \frac{\ell(\nu^2+3)}{4G}r_h\,(r_\Lambda^* - r^*(0))$$
$$+\frac{\ell}{4G}\sqrt{\Lambda\Psi(\Lambda)}\log\left|\frac{\tilde{L}^2}{4\ell^2}\frac{(\nu^2+3)(\Lambda-r_h)\left[(\nu^2+3)r_h+6(\nu^2-1)\Lambda\right]^2}{\Lambda\Psi^2(\Lambda)}\right|$$
$$+\frac{\ell}{2G}\frac{(\nu^2+3)r_h}{\sqrt{3(\nu^2-1)}}\arctan\left(\frac{\sqrt{3(\nu^2-1)\Lambda}}{\sqrt{(\nu^2+3)r_h+3(\nu^2-1)\Lambda}}\right) . \tag{B.2.6}$$

The divergent terms in the total gravitational action are thus

$$I^{\rm tot} = \frac{\ell}{4G}\sqrt{3(\nu^2-1)}\left(\log\left|\frac{\tilde{L}^2}{\ell^2}(\nu^2+3)\right| - 1\right)\Lambda$$
$$-\frac{\ell}{8G}\frac{\nu^2+3}{\sqrt{3(\nu^2-1)}}\,r_h\log\Lambda + \mathcal{O}(\Lambda^0)\,, \tag{B.2.7}$$

which reproduce the result (5.2.26) for the rotating BH in the $r_- \to 0$ limit.

B.2.2 External action

In this section we directly compute the gravitational action of the portion of WDW patch external to the black and white holes, without passing from the internal action.

Bulk contribution. The bulk contribution can be easily read from eq. (B.2.1):

$$I_{\mathcal{W}}^{\rm ext} = 2\,I_{\mathcal{W}}^2 = -\frac{\ell}{4G}\sqrt{3(\nu^2-1)}\,\Lambda - \frac{\ell}{8G}\frac{\nu^2+3}{\sqrt{3(\nu^2-1)}}\,r_h\log\Lambda + \mathcal{O}(\Lambda^0)\,, \tag{B.2.8}$$

which gives twice the spacetime volume complexity:

$$V^{\rm ext}_{\rm bulk} = 4\pi\ell^3 \frac{\sqrt{3(\nu^2-1)}}{\nu^2+3}\,\Lambda + \frac{2\pi\ell^3}{\sqrt{3(\nu^2-1)}}\, r_h \log\Lambda + \mathcal{O}(\Lambda^0)\,. \tag{B.2.9}$$

This expression coincides with (twice) the spacetime volume complexity for the rotating case in eq. (5.3.7) for $r_- \to 0$.

Joint terms. As in the rotating case, we need to be careful with the regularization of the joints at the horizon. To circumvent this issue, we again follow the procedure described in [34]. From eq. (5.2.18), in the present situation we get

$$\begin{aligned} I^{\rm ext}_{\mathcal{J}} = -\frac{\ell}{4G}\Bigg\{ & -2\Upsilon(\Lambda)\log\left|\frac{\ell^2}{\alpha^2}\frac{f(\Lambda))}{2\Upsilon(\Lambda)}\right| \\ & +2\Upsilon(r_h)\left[-\log\left|\frac{\ell^2}{\alpha^2}\frac{f(r_{\epsilon_U,\epsilon_V})}{2\Upsilon(r_h)}\right| + \log\left|\frac{\ell^2}{\alpha^2}\frac{f(r_{U_0,\epsilon_V})}{2\Upsilon(r_h)}\right| + \log\left|\frac{\ell^2}{\alpha^2}\frac{f(r_{\epsilon_U,V_0})}{2\Upsilon(r_h)}\right|\right]\Bigg\}\,. \end{aligned} \tag{B.2.10}$$

It is convenient to add and subtract the first term in the second line and to use the relation (5.2.30) to get

$$\begin{aligned} I^{\rm ext}_{\mathcal{J}} = & \frac{\ell}{2G}\Upsilon(\Lambda)\log\left|\frac{\ell^2}{\alpha^2}\frac{f(\Lambda)}{2\Upsilon(\Lambda)}\right| \\ & -\frac{\ell}{2G}\Upsilon(r_h)\left[\log(U_0V_0) + \log\left|\frac{\ell^2}{\alpha^2}\frac{f(r_{\epsilon_U,\epsilon_V})}{2\Upsilon(r_h)}\right| - \log(\epsilon_U\epsilon_V)\right]\,. \end{aligned} \tag{B.2.11}$$

Finally, the expression simplifies by means of eqs. (5.2.29) and (5.2.31):

$$I^{\rm ext}_{\mathcal{J}} = -\frac{\ell}{2G}\left[\nu r_h\left(\frac{\nu^2+3}{2\nu}r^*_\Lambda + F(r_h)\right) - \Upsilon(\Lambda)\log\left|\frac{\ell^2}{\alpha^2}\frac{(\nu^2+3)(\Lambda-r_h)}{\Psi(\Lambda)}\right|\right]\,. \tag{B.2.12}$$

The function $F(r)$, given by eq. (5.2.32), is finite and does not contribute to the divergences of the external action.

Counterterm for null boundaries. The counterterm contribution can be obtained similarly to eq. (B.2.5), by performing the integral from r_h to Λ. This leads to

$$I^{\rm ext}_{\rm ct} = -\frac{\ell}{2G}\Upsilon(\Lambda)\log\left|\frac{4\ell^4}{\alpha^2\tilde{L}^2}\frac{\Lambda\Psi(\Lambda)}{\left[6(\nu^2-1)\Lambda + (\nu^2+3)r_h\right]^2}\right| + \mathcal{O}(\Lambda^0)\,. \tag{B.2.13}$$

External action. Adding all the terms, we finally obtain

$$I^{\text{ext}} = \frac{\ell}{4G}\sqrt{3(\nu^2-1)}\left(\log\left|\frac{\tilde{L}^2}{\ell^2}(\nu^2+3)\right|-1\right)\Lambda - \frac{\ell}{8G}\frac{7\nu^2-3}{\sqrt{3(\nu^2-1)}}\, r_h \log\Lambda + \mathcal{O}(\Lambda^0)\,, \tag{B.2.14}$$

which reproduces the rotating BH result of eq. (5.2.36) in the $r_- \to 0$ limit.

B.2.3 Volume

As in the rotating case, for $t_b = 0$ the extremal codimension-one surface involved in subregion-CV conjecture is the bulk slice at $t = 0$ extending from the bifurcation surface $r = r_h$ to the left (right) boundary. Its volume is simply given by the integral of the induced metric:

$$V(L) = 2\pi\int_{r_h}^{\Lambda} dr\, G(r) = 2\pi\ell^2\int_{r_h}^{\Lambda} dr\,\sqrt{\frac{3(\nu^2-1)r+(\nu^2+3)r_h}{4(\nu^2+3)(r-r_h)}}\,. \tag{B.2.15}$$

Performing the variable change $R = r/r_h$, we obtain

$$V(L) = 2\pi\ell^2 r_h\int_1^{\Lambda/r_h} dR\,\sqrt{\frac{3(\nu^2-1)R+(\nu^2+3)}{4(\nu^2+3)(R-1)}}\,. \tag{B.2.16}$$

The integral can be analytically solved, giving

$$V(L) = \pi\ell^2\sqrt{\frac{3(\nu^2-1)}{\nu^2+3}}\Lambda + \frac{2\pi\ell^2\nu^2 r_h}{\sqrt{3(\nu^2-1)(\nu^2+3)}}\log\left(\frac{\Lambda}{r_h}\right) + \\ + \pi\ell^2 r_h\frac{(3-\nu^2)+2\nu^2\log\left[\frac{3(\nu^2-1)}{\nu^2}\right]}{2\sqrt{3(\nu^2-1)(\nu^2+3)}}\,. \tag{B.2.17}$$

As expected, the divergent part of this expression reproduces the rotating BH result of eq. (5.3.6) in the $r_- \to 0$ limit.

Appendix C

Approximations for the pseudosolution volume

C.1 Approximations for the constraint equations

The constraints in eqs. (6.1.19) and (6.1.20)

$$0 = \frac{1}{r_h} \ln \frac{2r_s \left(r_s^2 + r_* r_h\right) + \left(2r_s^2 - r_h^2\right) \sqrt{r_s^2 - r_*^2}}{2r_s \left(r_s^2 - r_* r_h\right) + \left(2r_s^2 - r_h^2\right) \sqrt{r_s^2 - r_*^2}} + 2\frac{\sqrt{r_s^2 - r_*^2}}{r_s r_*} - l\,,$$

$$\frac{r_s}{r_h} = \frac{1}{2}\left(\coth(r_h t) + \sqrt{\coth^2(r_h t) - \frac{2\sqrt{1 - \frac{r_*^2}{r_s^2}}}{1 + \sqrt{1 - \frac{r_*^2}{r_s^2}}}}\right)$$

cannot be solved in closed-form for (r_s, r_*), and are also rather tricky to be solved numerically, due to the exponential accuracy which is needed at large l and t. However, in the early and late time regimes, some useful approximations are available.

Early times. At early times $t \approx 0$, the HRT geodesic mainly lies in the AdS part of spacetime. Therefore, $r_s \to \infty$ and $r_* \approx 2/l$, so we can use the $r_* \ll r_s$ approximation in eqs. (6.1.19) and (6.1.20). This leads to

$$r_* = \frac{2}{l}\,, \qquad r_s = \frac{r_h}{2} \coth\left(\frac{r_h t}{2}\right)\,, \tag{C.1.1}$$

which provides a good description of the geodesic early evolution.

Late times. Formally setting $t \to \infty$ in eq. (6.1.20), we get

$$\hat{r}_* = r_h \frac{r_s(2r_s - r_h)}{(r_h - r_s)^2 + r_s^2} \,. \tag{C.1.2}$$

The function $\hat{r}_*(r_s)$ (C.1.2) is shown in Fig. C.1 together with several l-constant curves solving the constraint in eq. (6.1.19):

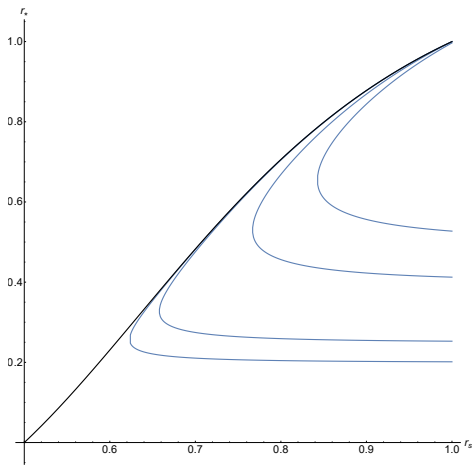

Figure C.1: Plot of the $t \to \infty$ limit curve $\hat{r}_*(r_s)$ (black line). The blue lines correspond to l-constant curves in the (r_s, r_*) plane satisfying eq. (6.1.19) for $l = 4, 5, 8, 10$ from top to bottom. We have set $r_h = 1$.

The physical accessible region in the parameter plane (r_s, r_*) is below the curve $\hat{r}_*(r_s)$. In other words, we necessarily have $r_s > r_h/2$.
In the late time regime, we can introduce a small parameter $\epsilon_* \geq 0$, which parametrizes the deviation from the curve (C.1.2) as

$$r_* = \hat{r}_* - r_h \, \epsilon_* \,. \tag{C.1.3}$$

We can then solve eq. (6.1.19) at the leading order in ϵ_*, getting

$$\epsilon_* = \frac{8(1-\rho_s)(2\rho_s - 1)\rho_s^3}{(1 - 2\rho_s + 2\rho_s^2)^2} \frac{1}{\exp\left(r_h l - \frac{4(1-\rho_s)}{2\rho_s - 1}\right) - \frac{8\rho_s^5 - 20\rho_s^4 + 18\rho_s^3 - 7\rho_s + 2}{(1-\rho_s)(2\rho_s^2 - 2\rho_s + 1)}} \,, \tag{C.1.4}$$

where we have introduced $\rho_s = r_s/r_h$. We are here interested in exploring the behavior of the HRT geodesic shortly before the thermalization, which takes place at $t = l/2$. Therefore, the $t \to \infty$ limit is related to the large l case. At

the leading order in l, we find the simpler expression

$$\epsilon_* \approx \frac{8(1-\rho_s)(2\rho_s-1)\rho_s^3}{(1-2\rho_s+2\rho_s^2)^2}\exp\left(-r_h l+\frac{4(1-\rho_s)}{2\rho_s-1}\right), \tag{C.1.5}$$

which is a good approximation when ρ_s is not so close to $1/2$, a condition that is true at large times.

Plugging the expansion (C.1.3) into the time constraint of eq. (6.1.20), we find

$$r_h t = \frac{1}{2}\ln\left(\frac{8\,(1-\rho_s)\,\rho_s^3}{\epsilon_*\,(2\rho_s-1)\,(2\rho_s^2-2\rho_s+1)^{\,2}}\right). \tag{C.1.6}$$

Inserting the value of ϵ_* (C.1.5), we get

$$r_h t = \frac{1}{2}\left(r_h l-\frac{4\,(1-\rho_s)}{2\rho_s-1}-\ln\,(2\rho_s-1)^2\right). \tag{C.1.7}$$

Note that the condition $\rho_s = 1/\sqrt{2}$ is equivalent to

$$r_h \bar{t} = \frac{r_h l}{2}-\sqrt{2}-\ln\left(\sqrt{2}-1\right) \approx \frac{r_h l}{2}-0.53\,. \tag{C.1.8}$$

Therefore, for $t < \bar{t}$ we have $\rho_s < 1/\sqrt{2}$, whereas for $t > \bar{t}$ we get $\rho_s > 1/\sqrt{2}$.

C.2 The pseudosolution volume at late times

In this section we compute the volume of the pseudosolution $\hat{V}$ shortly before the thermalization. In particular, we work in the limit $l, t \gg 1/r_h$ and in the regime in which $r_* \approx \hat{r}_*$, extensively using the results of Appendix C.1. By notational convenience, we split the volume of the pseudosolution into four contributions:

$$\hat{V} = \hat{V}_1 + \hat{V}_2 + \hat{V}_3 + \hat{V}_4\,. \tag{C.2.1}$$

Referring to eq. (6.2.14) we have

$$\hat{V}_1 = -\pi + 2\frac{\sqrt{r_s^2-r_*^2}}{r_*} + 2\arcsin\frac{r_*}{r_s}\,, \qquad \hat{V}_2 = l\int_{r_s}^{\Lambda}\psi(r)dr\,, \tag{C.2.2}$$

$$\hat{V}_3 = \int_{r_s}^{\Lambda}\psi(r)\,\kappa(r)dr\,, \qquad \hat{V}_4 = \vartheta\left(\frac{r_h}{\sqrt{2}}-r_s\right)l\,\varpi\int_{r_m}^{r_s}\psi(r)\,dr\,, \tag{C.2.3}$$

where

$$\kappa(r) = \frac{1}{r_h} \ln \frac{r^2 - r_* r_h + \sqrt{r^4 + \left[-1 + \frac{r_h^2(r_s^2 - r_*^2)}{4r_s^4} - \frac{r_*^2}{r_h^2}\right] r_h^2 r^2 + r_*^2 r_h^2}}{r^2 + r_* r_h + \sqrt{r^4 + \left[-1 + \frac{r_h^2(r_s^2 - r_*^2)}{4r_s^4} - \frac{r_*^2}{r_h^2}\right] r_h^2 r^2 + r_*^2 r_h^2}}\,,$$

$$\varpi = 2 + \frac{1}{r_h l} \ln \frac{1 - \frac{r_h^2(r_s^2 - r_*^2)}{4r_s^4} + \frac{r_*^2}{r_h^2} - 2\frac{r_*}{r_h}}{1 - \frac{r_h^2(r_s^2 - r_*^2)}{4r_s^4} + \frac{r_*^2}{r_h^2} + 2\frac{r_*}{r_h}}\,. \tag{C.2.4}$$

Recalling that at late times $r_s > r_h/2$, from eq. (C.1.3) we derive the following approximation:

$$r_m \approx \sqrt{\hat{r}_* r_h} + \sqrt{\epsilon_*} \sqrt{\frac{r_h^3(r_h^2 - 2r_s^2)}{8r_s^3}} + \mathcal{O}(\epsilon_*)\,. \tag{C.2.5}$$

We now proceed with the calculation of the various terms in $\hat{V}$.

$\hat{V}_4$ **contribution.** Due to the Heaviside function, this term is non-vanishing just in the time window

$$t < \bar{t} = \frac{l}{2} - \frac{0.53}{r_h}\,, \tag{C.2.6}$$

see eq. (C.1.8). By means of the expansion in eq. (C.1.3), we can approximate

$$\begin{aligned} \varpi &= 2 + \frac{1}{r_h l} \ln \frac{\epsilon_*(r_h^2 - 2r_s^2) r_h^2}{8\hat{r}_* r_s^3} + \mathcal{O}(\epsilon_*) \\ &\approx 1 + \frac{1}{r_h l} \left(\frac{4(1-\rho_s)}{2\rho_s - 1} + \ln \frac{(1-\rho_s)(1-2\rho_s^2)}{\rho_s(1 - 2\rho_s + 2\rho_s^2)} \right)\,, \end{aligned} \tag{C.2.7}$$

where in the second line we have used eq. (C.1.5). We also have

$$\psi(r) = r \frac{\sqrt{r^2 - \hat{r}_*^2}}{\sqrt{(r^2 - \hat{r}_* r_h)^2 + \mathcal{O}(\epsilon_*)}}\,. \tag{C.2.8}$$

Since this function must be integrated down to $r_m \approx \sqrt{r_h \hat{r}_*} + \mathcal{O}(\sqrt{\epsilon_*})$, for our purposes we can safely drop the $\mathcal{O}(\epsilon_*)$ term in the denominator. Thus, defining

$$\begin{aligned} \eta(r) &= \int dr\, r \frac{\sqrt{r^2 - \hat{r}_*^2}}{(r^2 - \hat{r}^* r_h)} \\ &= \sqrt{r^2 - \hat{r}_*^2} + \frac{1}{2}\sqrt{(r_h - \hat{r}_*)\hat{r}_*} \ln \left| \frac{\sqrt{(r_h - \hat{r}_*)\hat{r}_*} - \sqrt{r^2 - \hat{r}_*^2}}{\sqrt{(r_h - \hat{r}_*)\hat{r}_*} + \sqrt{r^2 - \hat{r}_*^2}} \right|\,, \end{aligned} \tag{C.2.9}$$

we finally get

$$\hat{V}_4 \approx \vartheta\left(\frac{r_h}{\sqrt{2}} - r_s\right) l\, \varpi\left(\eta(r_s) - \eta(r_m)\right) . \tag{C.2.10}$$

$\hat{V}_2$ **contribution.** At late times, this term can be approximated as

$$\begin{aligned} \hat{V}_2 &\approx l \int_{r_s}^{\Lambda} dr\, r \sqrt{\frac{r^2 - \hat{r}_*^2}{(r^2 - \hat{r}_* r_h)^2 + \epsilon_* A(r)}} , \\ A(r) &= \frac{\hat{r}_* \left(r^2 \left(4 r_s^4 r_h^2 + r_h^6\right) - 4 r_s^4 r_h^4\right)}{2 r_h r_s^4} . \end{aligned} \tag{C.2.11}$$

It is important to note that if $r_s < r_h/\sqrt{2}$ branch 2 comes into play, so $r_s > r_m$. Conversely, if $r_s > r_h/\sqrt{2}$ we necessarily have $r_s < r_m$. Moreover, in the special case $r_s = r_h$, from eq. (C.1.2) we get $\hat{r}_*(r_h) = r_h$. Putting all together, we deduce that

$$r_s \begin{cases} = \sqrt{\hat{r}_* r_h} & \text{for } r_s = \frac{r_h}{\sqrt{2}} \text{ and } r_s = r_h , \\ > \sqrt{\hat{r}_* r_h} & \text{for } r_s < \frac{r_h}{\sqrt{2}} , \\ < \sqrt{\hat{r}_* r_h} & \text{for } \frac{r_h}{\sqrt{2}} < r_s < r_h . \end{cases} \tag{C.2.12}$$

Therefore, we need to distinguish between two cases:

- For $r_s < r_h/\sqrt{2}$ we have $r_s > \sqrt{\hat{r}_* r_h}$, so the ϵ_* term at the denominator is negligible:
$$\hat{V}_2 \approx l\left(\Lambda - \eta(r_s)\right) . \tag{C.2.13}$$
- For $r_s > r_h/\sqrt{2}$ it is convenient to split $\hat{V}_2 = \hat{V}_2^a + \hat{V}_2^b$, with
$$\begin{aligned} \hat{V}_2^a &= l \int_{r_s}^{\sqrt{\hat{r}_* r_h}} dr\, r \frac{\sqrt{r^2 - \hat{r}_*^2}}{\sqrt{(r^2 - \hat{r}_* r_h)^2 + \epsilon_* A}} , \\ \hat{V}_2^b &= l \int_{\sqrt{\hat{r}_* r_h}}^{\Lambda} dr\, r \frac{\sqrt{r^2 - \hat{r}_*^2}}{\sqrt{(r^2 - \hat{r}_* r_h)^2 + \epsilon_* A(r)}} . \end{aligned} \tag{C.2.14}$$
As we will see below, $\hat{V}_2^a$ will be canceled by a term in $\hat{V}_3$, thus we do not evaluate it explicitly. Instead, an approximation for $\hat{V}_2^b$ can be found by noting that the $\mathcal{O}(\epsilon_*)$ term at the denominator acts as an effective cutoff:
$$\hat{V}_2^b \approx l \int_{\tilde{r}}^{\Lambda} dr\, r \frac{\sqrt{r^2 - \hat{r}_*^2}}{(r^2 - \hat{r}_* r_h)} , \qquad \tilde{r} = \sqrt{r_* r_h + \sqrt{\epsilon_* A(\sqrt{\hat{r}_* r_h})}} . \tag{C.2.15}$$
Using eqs. (C.2.9) and (C.1.4), we find the leading l behavior
$$\hat{V}_2^b \approx l\Lambda + \frac{\sqrt{r_s r_h \left(-2 r_s^2 + 3 r_s r_h - r_h^2\right)}}{4\left(2 r_s^2 - 2 r_s r_h + r_h^2\right)} r_h^2 l^2 + \mathcal{O}(l) . \tag{C.2.16}$$

$\hat{V}_3$ **contribution.** In the limit $r_* \to \hat{r}_*$, we find that:

$$\kappa(r) = \frac{1}{r_h} \ln \frac{\rho^2 \left(2\rho_s^2 - 2\rho_s + 1\right) - 2\rho_s^2 + \rho_s + \left|\rho^2 \left(2\rho_s^2 - 2\rho_s + 1\right) - 2\rho_s^2 + \rho_s\right|}{\rho^2 \left(2\rho_s^2 - 2\rho_s + 1\right) + 2\rho_s^2 - \rho_s + \left|\rho^2 \left(2\rho_s^2 - 2\rho_s + 1\right) - 2\rho_s^2 + \rho_s\right|}\,, \tag{C.2.17}$$

in which $\rho = r/r_h$. Again, we need to distinguish between the following two cases:

- If $r_s < r_h/\sqrt{2}$,
$$\rho^2 \left(2\rho_s^2 - 2\rho_s + 1\right) - 2\rho_s^2 + \rho_s > 0 \tag{C.2.18}$$
for every $r_s < r < \Lambda$. The factor $\kappa(r)$ in the integrand is finite and gets suppressed in the large l limit.

- If $r_s > r_h/\sqrt{2}$, eq. (C.2.18) is valid just for $r > \sqrt{r_* r_h}$, and again gives a negligible contribution. Instead, for $r < \sqrt{r_* r_h}$ we have to consider the subleading term in $\kappa(r)$, which reads
$$\kappa(r) = \frac{1}{r_h} \ln \left(-\frac{\epsilon_* \left(\rho^2 \left(4\rho_s^5 - 2\rho_s^3 + 2\rho_s - 1\right) + 2\left(1 - 2\rho_s\right)\rho_s^4\right)}{4\rho_s^4 \left(2\rho_s - 1\right)\left(\rho^2 \left(2\rho_s^2 - 2\rho_s + 1\right) - 2\rho_s^2 + \rho_s\right)} \right). \tag{C.2.19}$$
Plugging in the expansion for ϵ_* given in eq. (C.1.5), we find that
$$\kappa(r) \approx -l + \mathcal{O}(l^0)\,, \tag{C.2.20}$$
so the integral exactly cancels with $\hat{V}_2^a$.

Total volume. Adding up all the contributions, we obtain

$$\frac{\hat{V}}{l} \approx \begin{cases} \Lambda + \frac{\hat{V}_1}{l} + (\varpi - 1)\eta(r_s) - \varpi\eta(r_m) & \text{for } r_s < r_h/\sqrt{2}\,, \\ \Lambda + \frac{r_h^2 l}{4} \frac{\sqrt{r_s r_h (r_h - r_s)(2r_s - r_h)}}{(r_s - r_h)^2 + r_s^2} + \mathcal{O}(l^0) & \text{for } r_s > r_h/\sqrt{2}\,. \end{cases} \tag{C.2.21}$$

Recalling the comment around eq. (C.1.8), the first solution holds at intermediate times $t < \bar{t}$, while the second one at late times $\bar{t} < t < l/2$.

Appendix D

Details of the falling monopole computations

D.1 Abelian field strength and magnetic flux

The abelian field strength and its dual are [195]

$$\mathcal{F}_{\mu\nu} = n^a F^a_{\mu\nu} - \frac{1}{e}\epsilon^{abc} n^a D_\mu n^b D_\nu n^c \,, \qquad \tilde{\mathcal{F}}^{\mu\nu} \equiv \frac{1}{2}\frac{\epsilon^{\mu\nu\alpha\beta}}{\sqrt{-g}}\mathcal{F}_{\alpha\beta} \,. \tag{D.1.1}$$

The latter satisfies

$$D_\mu \tilde{\mathcal{F}}^{\mu\nu} = \frac{4\pi}{e} k^\nu \,, \qquad k_\mu = \frac{1}{8\pi}\epsilon_{\mu\nu\rho\sigma}\epsilon_{abc}\partial^\nu n^a \partial^\rho n^b \partial^\sigma n^c \,, \tag{D.1.2}$$

with k_μ the topological current. The only non-vanishing components of the dual electromagnetic tensor $\tilde{\mathcal{F}}^{\mu\nu}$ are

$$\tilde{\mathcal{F}}^{tr} = -\tilde{\mathcal{F}}^{rt} = -\frac{1}{er^2} \,. \tag{D.1.3}$$

By the Stokes theorem, the magnetic flux on a sphere of radius r is

$$Q = \int_{S^2} \tilde{\mathcal{F}}^{\mu\nu} dS_{\mu\nu} \,, \qquad dS_{\mu\nu} = n_{[\mu} r_{\nu]}\, r^2 \sin\theta \, d\theta d\varphi \,, \tag{D.1.4}$$

where n_μ and r_ν are the unit vectors pointing in the time and radial direction, respectively. A direct computation gives

$$Q = -\frac{8\pi}{e} \,. \tag{D.1.5}$$

Remarkably, the magnetic flux is topological and independent of the boundary coefficients of the bulk fields.

D.2 Calculation of the boundary energy-momentum tensor

D.2.1 Black hole quench

A metric in FG coordinates has the following form

$$\hat{x}^\mu = (\hat{z}, \hat{t}, \hat{x}, \hat{\varphi})\,, \qquad ds^2 = L^2 \left(\frac{d\hat{z}^2}{\hat{z}^2} + \frac{1}{\hat{z}^2} g_{ab}(\hat{z}, \hat{x}^a) d\hat{x}^a d\hat{x}^b \right)\,, \tag{D.2.1}$$

where the index a runs over boundary coordinates

$$\hat{x}^a = (\hat{t}, \hat{x}, \hat{\varphi})\,. \tag{D.2.2}$$

We take $\hat{\varphi} = \varphi$. Nearby the boundary, the FG coordinates can be built perturbatively by means of

$$z = \hat{z} + \sum_{k=2}^{\infty} a_k(\hat{x}, \hat{t}) \hat{z}^k\,, \qquad x = \hat{x} + \sum_{k=1}^{\infty} b_k(\hat{x}, \hat{t}) \hat{z}^k\,, \qquad t = \hat{t} + \sum_{k=1}^{\infty} c_k(\hat{x}, \hat{t}) \hat{z}^k\,. \tag{D.2.3}$$

Plugging into the metric in Poincaré coordinates and comparing with the FG metric order by order, we get:

$$b_1 = c_1 = 0\,, \qquad a_2 = b_2 = c_2 = 0\,, \qquad a_3 = b_3 = c_3 = 0\,, \qquad b_4 = c_4 = 0\,,$$

$$a_4 = -\frac{4\,A^3 M}{3\left(A^4 + 2A^2\hat{t}^2 + 2A^2\hat{x}^2 + \hat{t}^4 - 2\hat{t}^2\hat{x}^2 + \hat{x}^4\right)^{3/2}}\,. \tag{D.2.4}$$

The energy-momentum tensor can be obtained from the results of [207]:

$$T_{ij}^{(BH)} = \frac{L}{8\pi G} \lim_{\hat{z}\to 0} \frac{1}{\hat{z}} \left(K_{ij} - \gamma_{ij} K - \frac{2}{L} \gamma_{ij} \right)\,. \tag{D.2.5}$$

In this expression γ_{ij} is the induced metric on a $\hat{z}$-constant surface nearby the boundary, K_{ij} denotes the extrinsic curvature tensor calculated with an inward unit vector normal to the $\hat{z}$-constant surface, and $K = \gamma^{ij} K_{ij}$ is the trace of the extrinsic curvature tensor.

To explicitly write the components of the energy-momentum tensor, it is convenient to introduce the lightcone coordinates[1]

$$u^i = (u, v, \varphi)\,, \qquad u = t - x\,, \qquad v = t + x\,. \tag{D.2.6}$$

In this coordinate system, the non-vanishing elements of $T_{ij}^{(BH)}$ are

$$\begin{aligned}
T_{uu}^{(BH)} &= \frac{A^3 L^2 M}{8\pi G} \frac{3}{\left(A^2+u^2\right)^{5/2}\left(A^2+v^2\right)^{1/2}}\,,\\
T_{vv}^{(BH)} &= \frac{A^3 L^2 M}{8\pi G} \frac{3}{\left(A^2+v^2\right)^{5/2}\left(A^2+u^2\right)^{1/2}}\,,\\
T_{uv}^{(BH)} &= \frac{A^3 L^2 M}{8\pi G} \frac{1}{\left(A^2+u^2\right)^{3/2}\left(A^2+v^2\right)^{3/2}}\,,\\
T_{\varphi\varphi}^{(BH)} &= \frac{A^3 L^2 M}{8\pi G} \frac{(u-v)^2}{\left(A^2+u^2\right)^{3/2}\left(A^2+v^2\right)^{3/2}}\,.
\end{aligned} \tag{D.2.7}$$

D.2.2 Monopole quench with Dirichlet boundary conditions

In order to put the metric with monopole backreaction in the FG form, we consider the expansion (7.1.25) of h and g nearby the boundary, setting $h_2 = -g_2$. Then, performing the change of variables of eq. (D.2.3) and solving order by order, we obtain

$$\begin{aligned}
&b_1 = c_1 = 0\,, \qquad a_2 = b_2 = c_2 = 0\,, \qquad b_3 = c_3 = 0\,,\\
&a_3 = \frac{2A^2\, g_2}{A^4 + 2A^2\hat{t}^2 + 2A^2\hat{x}^2 + \hat{t}^4 - 2\hat{t}^2\hat{x}^2 + \hat{x}^4}\,,\\
&a_4 = \frac{4A^3\,(g_3 - h_3)}{3\left(A^4 + 2A^2\hat{t}^2 + 2A^2\hat{x}^2 + \hat{t}^4 - 2\hat{t}^2\hat{x}^2 + \hat{x}^4\right)^{3/2}}\,,\\
&b_4 = -\frac{2A^2\, g_2 \hat{x}\left(A^2 - \hat{t}^2 + \hat{x}^2\right)}{\left(A^4 + 2A^2\hat{t}^2 + 2A^2\hat{x}^2 + \hat{t}^4 - 2\hat{t}^2\hat{x}^2 + \hat{x}^4\right)^2}\,,\\
&c_4 = \frac{2A^2\, g_2 \hat{t}\left(A^2 + \hat{t}^2 - \hat{x}^2\right)}{\left(A^4 + 2A^2\hat{t}^2 + 2A^2\hat{x}^2 + \hat{t}^4 - 2\hat{t}^2\hat{x}^2 + \hat{x}^4\right)^2}\,.
\end{aligned} \tag{D.2.8}$$

[1] At the leading order in $\hat{z}$ the FG coordinates coincide with the Poincaré ones: $\hat{t} = t\,, \hat{x} = x$.

We can now use the generalization of eq. (D.2.5) involving scalar fields with Dirichlet boundary conditions [208] to extract the energy-momentum tensor

$$T_{ij}^{(D)} = \frac{L}{8\pi G} \lim_{\hat{z}\to 0} \frac{1}{\hat{z}} \left(K_{ij} - \gamma_{ij} K - \frac{2}{L}\gamma_{ij} - 4\pi G \frac{\gamma_{ij}}{L} \phi^a \phi^a \right) . \tag{D.2.9}$$

The components of the energy-momentum tensor in lightcone coordinates look qualitatively similar to the corresponding components computed in the BH background, see eq. (D.2.7):

$$\begin{aligned}
T_{uu}^{(D)} &= T_{uu}^{(BH)} \left(\frac{16\pi G \alpha_H \beta_H - 3L^2 g_3}{3L^2 M} \right) , \\
T_{vv}^{(D)} &= T_{vv}^{(BH)} \left(\frac{16\pi G \alpha_H \beta_H - 3L^2 g_3}{3L^2 M} \right) , \\
T_{uv}^{(D)} &= T_{uv}^{(BH)} \left(\frac{-16\pi G \alpha_H \beta_H - 3L^2 g_3}{3L^2 M} \right) , \\
T_{\varphi\varphi}^{(D)} &= T_{\varphi\varphi}^{(BH)} \left(\frac{32\pi G \alpha_H \beta_H - 3L^2 g_3}{3L^2 M} \right) .
\end{aligned} \tag{D.2.10}$$

The Ward identity for $T_{ij}^{(D)}$ reflecting diffeomorphism-invariance gives [203, 208]

$$\partial^i T_{ij}^{(D)} = \tilde{\beta}_H \partial_j \tilde{\alpha}_H = \langle O_2 \rangle \partial_j J_D \, , \tag{D.2.11}$$

and the trace of the energy-momentum tensor is

$$\eta^{ij} T_{ij}^{(D)} = \tilde{\alpha}_H \tilde{\beta}_H = \langle O_2 \rangle J_D \, . \tag{D.2.12}$$

So, in the presence of sources for the scalar operators the holographic energy-momentum tensor is neither conserved nor traceless.

D.2.3 Monopole quench with Neumann and multitrace boundary conditions

We follow the approach in [203] to determine the boundary energy-momentum tensor for multitrace deformations. This choice of boundary conditions correspond to adding to the renormalized action $S_{\rm ren}$ the finite boundary action

$$S_{\mathcal{F}} = \int d^3x \, \sqrt{-g_0} \, (J_F \, \tilde{\alpha}_H + \mathcal{F}(\tilde{\alpha}_H)) \, , \qquad J_{\mathcal{F}} = -\tilde{\beta}_H - \mathcal{F}'(\tilde{\alpha}_H) \, , \tag{D.2.13}$$

where g_0 is the determinant of the boundary metric (at the end of the calculation we will specialize to the Minkowski metric $(g_0)_{ij} = \eta_{ij}$). The variations of the action functionals are

$$\begin{aligned} \delta S_{\rm ren} &= \int d^3x\,\sqrt{-g_0}\left(\frac{1}{2}T^{ij}(\delta g_{(0)})_{ij} + \tilde{\beta}_H\delta\tilde{\alpha}_H\right)\,, \\ \delta S_{\mathcal{F}} &= \int d^3x\,\sqrt{-g_0}\left(-\tilde{\alpha}_H\delta\tilde{\beta}_H - \tilde{\alpha}_H\mathcal{F}''(\tilde{\alpha}_H)\delta\tilde{\alpha}_H - \tilde{\beta}_H\delta\tilde{\alpha}_H\right)\,, \end{aligned} \tag{D.2.14}$$

so the total variation is

$$\begin{aligned} \delta S &= \delta S_{\rm ren} + \delta S_{\mathcal{F}} \\ &= \int d^3x\sqrt{-g_0}\left(\frac{1}{2}T^{ij}(\delta g_{(0)})_{ij} - \tilde{\alpha}_H\delta\tilde{\beta}_H - \tilde{\alpha}_H\mathcal{F}''(\tilde{\alpha}_H)\delta\tilde{\alpha}_H\right) \\ &= \int d^3x\sqrt{-g_0}\left(\frac{1}{2}T^{ij}(\delta g_{(0)})_{ij} + \tilde{\alpha}_H\delta J_{\mathcal{F}}\right)\,. \end{aligned} \tag{D.2.15}$$

The shift of the action by $S_{\mathcal{F}}$ causes the following shift of the energy-momentum tensor:

$$\begin{aligned} T^{(\mathcal{F})}_{ij} &= T^{(D)}_{ij} + \eta_{ij}[\mathcal{F}(\tilde{\alpha}_H) + \tilde{\alpha}_H J_F] \\ &= T^{(D)}_{ij} + \eta_{ij}[\mathcal{F}(\tilde{\alpha}_H) - \tilde{\alpha}_H\tilde{\beta}_H - \mathcal{F}'(\tilde{\alpha}_H)\tilde{\alpha}_H]\,. \end{aligned} \tag{D.2.16}$$

The divergence of the energy-momentum tensor is

$$\begin{aligned} \partial^i T^{(\mathcal{F})}_{ij} &= \partial^i T^{(D)}_{ij} + \partial_j[\mathcal{F}(\tilde{\alpha}_H) - \tilde{\alpha}_H\tilde{\beta}_H - \mathcal{F}'(\tilde{\alpha}_H)\tilde{\alpha}_H] \\ &= -\tilde{\alpha}_H(\partial_j\tilde{\beta}_H + \mathcal{F}''(\tilde{\alpha}_H)\,\partial_j\tilde{\alpha}_H)\,, \end{aligned} \tag{D.2.17}$$

while the trace is

$$\begin{aligned} \eta^{ij}T^{(\mathcal{F})}_{ij} &= (T^{(D)})^i_i + 3[\mathcal{F}(\tilde{\alpha}_H) - \tilde{\alpha}_H\tilde{\beta}_H - \mathcal{F}'(\tilde{\alpha}_H)\tilde{\alpha}_H] \\ &= -2\tilde{\alpha}_H\tilde{\beta}_H + 3\mathcal{F}(\tilde{\alpha}_H) - 3\tilde{\alpha}_H\mathcal{F}'(\tilde{\alpha}_H)\,, \end{aligned} \tag{D.2.18}$$

where use has been made of eqs. (D.2.11) and (D.2.12).
Setting to zero the source $J_{\mathcal{F}}$ corresponds to

$$\tilde{\beta}_H = -\mathcal{F}'(\tilde{\alpha}_H)\,. \tag{D.2.19}$$

Note that in this case $T^{(\mathcal{F})}_{ij}$ is conserved, i.e. $\partial^i T^{(\mathcal{F})}_{ij} = 0$, whereas the trace reads

$$\eta^{ij}T^{(\mathcal{F})}_{ij} = -\tilde{\alpha}_H\mathcal{F}'(\tilde{\alpha}_H) + 3\mathcal{F}(\tilde{\alpha}_H)\,, \tag{D.2.20}$$

which vanishes for the triple trace deformation $\mathcal{F} = \mathcal{F}_\kappa$ of eq. (7.3.14).

D.3 Calculation of the holographic entanglement entropy

D.3.1 Translated disk

Defining the polar-like coordinates

$$x_1 = \xi + p\,\cos\vartheta\,, \qquad x_2 = p\,\sin\vartheta\,, \tag{D.3.1}$$

the entanglement entropy variation for the translated disk is given by

$$\begin{aligned}\Delta S = \frac{\pi\alpha_H^2}{2l}\int_0^l dp \frac{p}{\left(l^2-p^2\right)^{3/2}}\int_0^{2\pi} d\vartheta \Bigg[&\frac{\left(h_\varepsilon+g_\varepsilon\right)\left(p^2\cos^2\vartheta - l^2\right)\xi^2 t^2}{\omega_\xi} \\ &+\frac{\left(h_\varepsilon-g_\varepsilon\right)}{4}\frac{\left[p\,\omega_\xi + 2\xi\cos\vartheta\left(l^2-p^2\right)\left(l^2-t^2+A^2+\xi^2+2\xi p\cos\vartheta\right)\right]^2}{\omega_\xi\left[\omega_\xi+4A^2\left(p^2-l^2\right)\right]} \\ &+\frac{\left(h_\varepsilon-g_\varepsilon\right)l^2\xi^2\sin^2\vartheta\left(l^2-p^2\right)\left(l^2-t^2+A^2+\xi^2+2\xi p\cos\vartheta\right)^2}{\omega_\xi\left[\omega_\xi+4A^2\left(p^2-l^2\right)\right]}\Bigg]\,,\end{aligned} \tag{D.3.2}$$

where

$$\omega_\xi \equiv \omega(\sqrt{l^2+\xi^2+2\,\xi\,p\cos\left(2\vartheta\right)}, t)\,, \tag{D.3.3}$$

and ω is defined in eq. (7.3.2). In the above integral, both h_ε and g_ε are functions of

$$r = \frac{1}{2A}\sqrt{\frac{\omega_\xi+4A^2\left(p^2-l^2\right)}{l^2-p^2}}\,. \tag{D.3.4}$$

D.3.2 Half-plane

The closed-form expression for the entropy variation of the half-plane is

$$\begin{aligned}\Delta S = &\frac{\pi\alpha_H^2}{8}\int_0^{+\infty} dz \int_{-\infty}^{+\infty}\frac{\left(h_\epsilon-g_\epsilon\right)\left(C^2+4z^2x_2^2\,D^2\right)}{z^2\left(D^2+4A^2\,t^2\right)^2}\,dx_2 \\ &-\frac{\pi\alpha_H^2}{2}\,t^2\int_0^{+\infty} dz\int_{-\infty}^{+\infty}\frac{\left(h_\epsilon+g_\epsilon\right)\left(x_2^2+z^2\right)}{z^2\left(D^2+4A^2\,t^2\right)}\,dx_2\,,\end{aligned} \tag{D.3.5}$$

with

$$C \equiv t^4 - z^4 - 2t^2\left(x_2^2-A^2\right)+\left(x_2^2+A^2\right)^2\,, \qquad D \equiv -t^2+x_2^2+z^2+A^2\,. \tag{D.3.6}$$

In the above expression, $h_\epsilon(r)$ and $g_\epsilon(r)$ are defined in eq. (7.1.28), with

$$r = \frac{\sqrt{A^4 + 2A^2\,(t^2 + x_2^2 - z^2) + (z^2 + x_2^2 - t^2)^2}}{2A\,z}\,. \tag{D.3.7}$$

We note that the A dependence can be completely reabsorbed by the scaling

$$z \to \frac{z}{A}\,, \qquad x_2 \to \frac{x_2}{A}\,, \qquad t \to \frac{t}{A}\,. \tag{D.3.8}$$

Consequently, from now on we set $A = 1$ without loss of generality.

In order to explore the large t behavior of ΔS, we introduce the variables $\hat\rho, \gamma$ defined by

$$z = \hat\rho \cos\gamma\,, \qquad x_2 = \hat\rho \sin\gamma\,. \tag{D.3.9}$$

At large t, the two integrands in eq. (D.3.5) are non-vanishing just in the region $\hat\rho = t \pm \mu$, with μ of order 1. For convenience, we define

$$\hat\rho = t + \delta\,. \tag{D.3.10}$$

It turns out that, at large t, the term proportional to $(h_\epsilon - g_\epsilon)$ in eq. (D.3.5) is much smaller than the one proportional to $(h_\epsilon + g_\epsilon)$. Moreover, in this regime, we can use the approximation

$$r = \frac{\sqrt{\delta^2 + \sin^2\gamma}}{\cos\gamma} + O(1/t)\,. \tag{D.3.11}$$

At the leading order in t, we find

$$\Delta S = K\,\alpha_H^2\,t\,, \tag{D.3.12}$$

with

$$K = -\frac{\pi}{2}\int_0^\infty \frac{r}{1+r^2}\,\mathbb{E}(-r^2)[h_\epsilon(r) + g_\epsilon(r)]\,dr\,. \tag{D.3.13}$$

$\mathbb{E}$ is the *complete elliptic integral of the second kind*, defined as

$$\mathbb{E}(m) = \int_0^{\pi/2} d\gamma\,\sqrt{1 - m\sin^2\gamma}\,. \tag{D.3.14}$$

Considering the analytic solutions in eq. (7.1.29), we get the approximate numerical value $K \approx 0.636$.

Bibliography

[1] J. M. Maldacena, "The Large N limit of superconformal field theories and supergravity," *Adv. Theor. Math. Phys.*, vol. 2, pp. 231–252, 1998.

[2] A. M. Polyakov, "The Wall of the cave," *Int. J. Mod. Phys. A*, vol. 14, pp. 645–658, 1999.

[3] S. W. Hawking, "Particle Creation by Black Holes," *Commun. Math. Phys.*, vol. 43, pp. 199–220, 1975. [Erratum: Commun.Math.Phys. 46, 206 (1976)].

[4] J. D. Bekenstein, "Black holes and entropy," *Phys. Rev. D*, vol. 7, pp. 2333–2346, 1973.

[5] G. 't Hooft, "Dimensional reduction in quantum gravity," *Conf. Proc. C*, vol. 930308, pp. 284–296, 1993.

[6] L. Susskind, "The World as a hologram," *J. Math. Phys.*, vol. 36, pp. 6377–6396, 1995.

[7] P. Kovtun, D. T. Son, and A. O. Starinets, "Viscosity in strongly interacting quantum field theories from black hole physics," *Phys. Rev. Lett.*, vol. 94, p. 111601, 2005.

[8] S. A. Hartnoll, C. P. Herzog, and G. T. Horowitz, "Building a Holographic Superconductor," *Phys. Rev. Lett.*, vol. 101, p. 031601, 2008.

[9] S. Ryu and T. Takayanagi, "Holographic derivation of entanglement entropy from AdS/CFT," *Phys. Rev. Lett.*, vol. 96, p. 181602, 2006.

[10] S. Ryu and T. Takayanagi, "Aspects of Holographic Entanglement Entropy," *JHEP*, vol. 08, p. 045, 2006.

[11] L. Susskind, "Computational Complexity and Black Hole Horizons," *Fortsch. Phys.*, vol. 64, pp. 24–43, 2016. [Addendum: Fortsch.Phys. 64, 44–48 (2016)].

[12] J. Haferkamp, P. Faist, N. B. T. Kothakonda, J. Eisert, and N. Y. Halpern, "Linear growth of quantum circuit complexity," *Nature Phys.*, vol. 18, no. 5, pp. 528–532, 2022.

[13] D. Stanford and L. Susskind, "Complexity and Shock Wave Geometries," *Phys. Rev. D*, vol. 90, no. 12, p. 126007, 2014.

[14] L. Susskind, "Entanglement is not enough," *Fortsch. Phys.*, vol. 64, pp. 49–71, 2016.

[15] A. R. Brown, D. A. Roberts, L. Susskind, B. Swingle, and Y. Zhao, "Holographic Complexity Equals Bulk Action?," *Phys. Rev. Lett.*, vol. 116, no. 19, p. 191301, 2016.

[16] J. Couch, W. Fischler, and P. H. Nguyen, "Noether charge, black hole volume, and complexity," *JHEP*, vol. 03, p. 119, 2017.

[17] A. Belin, R. C. Myers, S.-M. Ruan, G. Sárosi, and A. J. Speranza, "Does Complexity Equal Anything?," *Phys. Rev. Lett.*, vol. 128, no. 8, p. 081602, 2022.

[18] A. Belin, R. C. Myers, S.-M. Ruan, G. Sárosi, and A. J. Speranza, "Complexity Equals Anything II," 10 2022.

[19] M. A. Nielsen, "A geometric approach to quantum circuit lower bounds," *Quantum Information and Computation*, vol. 6, pp. 213–262, 2006.

[20] A. R. Brown and L. Susskind, "Complexity geometry of a single qubit," *Phys. Rev. D*, vol. 100, no. 4, p. 046020, 2019.

[21] M. A. Nielsen, M. R. Dowling, M. Gu, and A. C. Doherty, "Quantum computation as geometry," *Science*, vol. 311, pp. 1133–1135, 2006.

[22] A. R. Brown, L. Susskind, and Y. Zhao, "Quantum Complexity and Negative Curvature," *Phys. Rev. D*, vol. 95, no. 4, p. 045010, 2017.

[23] A. R. Brown and L. Susskind, "Second law of quantum complexity," *Phys. Rev. D*, vol. 97, no. 8, p. 086015, 2018.

[24] A. R. Brown, M. H. Freedman, H. W. Lin, and L. Susskind, "Effective Geometry, Complexity, and Universality," 11 2021.

[25] B. O'Neill, "The fundamental equations of a submersion," *Michigan Math. J.*, vol. 13, pp. 459–469, 1966.

[26] B. O'Neill, "Submersions and geodesics," *Duke Math. J.*, vol. 34, no. 2, pp. 363–373, 1967.

[27] R. Jefferson and R. C. Myers, "Circuit complexity in quantum field theory," *JHEP*, vol. 10, p. 107, 2017.

[28] S. Chapman, M. P. Heller, H. Marrochio, and F. Pastawski, "Toward a Definition of Complexity for Quantum Field Theory States," *Phys. Rev. Lett.*, vol. 120, no. 12, p. 121602, 2018.

[29] L. Hackl and R. C. Myers, "Circuit complexity for free fermions," *JHEP*, vol. 07, p. 139, 2018.

[30] R. Khan, C. Krishnan, and S. Sharma, "Circuit Complexity in Fermionic Field Theory," *Phys. Rev. D*, vol. 98, no. 12, p. 126001, 2018.

[31] M. Flory and M. P. Heller, "Geometry of Complexity in Conformal Field Theory," *Phys. Rev. Res.*, vol. 2, no. 4, p. 043438, 2020.

[32] M. Flory and M. P. Heller, "Conformal field theory complexity from Euler-Arnold equations," *JHEP*, vol. 12, p. 091, 2020.

[33] N. Chagnet, S. Chapman, J. de Boer, and C. Zukowski, "Complexity for Conformal Field Theories in General Dimensions," *Phys. Rev. Lett.*, vol. 128, no. 5, p. 051601, 2022.

[34] C. A. Agón, M. Headrick, and B. Swingle, "Subsystem Complexity and Holography," *JHEP*, vol. 02, p. 145, 2019.

[35] E. Caceres, S. Chapman, J. D. Couch, J. P. Hernandez, R. C. Myers, and S.-M. Ruan, "Complexity of Mixed States in QFT and Holography," *JHEP*, vol. 03, p. 012, 2020.

[36] H. A. Camargo, L. Hackl, M. P. Heller, A. Jahn, T. Takayanagi, and B. Windt, "Entanglement and complexity of purification in (1+1)-dimensional free conformal field theories," *Phys. Rev. Res.*, vol. 3, no. 1, p. 013248, 2021.

[37] G. Di Giulio and E. Tonni, "Complexity of mixed Gaussian states from Fisher information geometry," *JHEP*, vol. 12, p. 101, 2020.

[38] M. Headrick, V. E. Hubeny, A. Lawrence, and M. Rangamani, "Causality & holographic entanglement entropy," *JHEP*, vol. 12, p. 162, 2014.

[39] M. Alishahiha, "Holographic Complexity," *Phys. Rev. D*, vol. 92, no. 12, p. 126009, 2015.

[40] D. Carmi, R. C. Myers, and P. Rath, "Comments on Holographic Complexity," *JHEP*, vol. 03, p. 118, 2017.

[41] M. Banados, C. Teitelboim, and J. Zanelli, "The Black hole in three-dimensional space-time," *Phys. Rev. Lett.*, vol. 69, pp. 1849–1851, 1992.

[42] M. Banados, M. Henneaux, C. Teitelboim, and J. Zanelli, "Geometry of the (2+1) black hole," *Phys. Rev. D*, vol. 48, pp. 1506–1525, 1993. [Erratum: Phys.Rev.D 88, 069902 (2013)].

[43] I. Bengtsson and P. Sandin, "Anti de Sitter space, squashed and stretched," *Class. Quant. Grav.*, vol. 23, pp. 971–986, 2006.

[44] D. Anninos, W. Li, M. Padi, W. Song, and A. Strominger, "Warped AdS(3) Black Holes," *JHEP*, vol. 03, p. 130, 2009.

[45] D. Anninos, "Hopfing and Puffing Warped Anti-de Sitter Space," *JHEP*, vol. 09, p. 075, 2009.

[46] D. M. Hofman and B. Rollier, "Warped Conformal Field Theory as Lower Spin Gravity," *Nucl. Phys. B*, vol. 897, pp. 1–38, 2015.

[47] D. M. Hofman and A. Strominger, "Chiral Scale and Conformal Invariance in 2D Quantum Field Theory," *Phys. Rev. Lett.*, vol. 107, p. 161601, 2011.

[48] S. Detournay, T. Hartman, and D. M. Hofman, "Warped Conformal Field Theory," *Phys. Rev. D*, vol. 86, p. 124018, 2012.

[49] K. Jensen, "Locality and anomalies in warped conformal field theory," *JHEP*, vol. 12, p. 111, 2017.

[50] D. Anninos, J. Samani, and E. Shaghoulian, "Warped Entanglement Entropy," *JHEP*, vol. 02, p. 118, 2014.

[51] A. Castro, D. M. Hofman, and N. Iqbal, "Entanglement Entropy in Warped Conformal Field Theories," *JHEP*, vol. 02, p. 033, 2016.

[52] W. Song, Q. Wen, and J. Xu, "Generalized Gravitational Entropy for Warped Anti–de Sitter Space," *Phys. Rev. Lett.*, vol. 117, no. 1, p. 011602, 2016.

[53] W. Song, Q. Wen, and J. Xu, "Modifications to Holographic Entanglement Entropy in Warped CFT," *JHEP*, vol. 02, p. 067, 2017.

[54] T. Azeyanagi, S. Detournay, and M. Riegler, "Warped Black Holes in Lower-Spin Gravity," *Phys. Rev. D*, vol. 99, no. 2, p. 026013, 2019.

[55] P. Calabrese and J. L. Cardy, "Time-dependence of correlation functions following a quantum quench," *Phys. Rev. Lett.*, vol. 96, p. 136801, 2006.

[56] P. Calabrese and J. Cardy, "Quantum Quenches in Extended Systems," *J. Stat. Mech.*, vol. 0706, p. P06008, 2007.

[57] P. Calabrese and J. L. Cardy, "Evolution of entanglement entropy in one-dimensional systems," *J. Stat. Mech.*, vol. 0504, p. P04010, 2005.

[58] P. Calabrese and J. Cardy, "Quantum quenches in 1 + 1 dimensional conformal field theories," *J. Stat. Mech.*, vol. 1606, no. 6, p. 064003, 2016.

[59] C. T. Asplund and A. Bernamonti, "Mutual information after a local quench in conformal field theory," *Phys. Rev. D*, vol. 89, no. 6, p. 066015, 2014.

[60] C. T. Asplund, A. Bernamonti, F. Galli, and T. Hartman, "Holographic Entanglement Entropy from 2d CFT: Heavy States and Local Quenches," *JHEP*, vol. 02, p. 171, 2015.

[61] J. Abajo-Arrastia, J. Aparicio, and E. Lopez, "Holographic Evolution of Entanglement Entropy," *JHEP*, vol. 11, p. 149, 2010.

[62] T. Albash and C. V. Johnson, "Evolution of Holographic Entanglement Entropy after Thermal and Electromagnetic Quenches," *New J. Phys.*, vol. 13, p. 045017, 2011.

[63] V. Balasubramanian, A. Bernamonti, N. Copland, B. Craps, and F. Galli, "Thermalization of mutual and tripartite information in strongly coupled two dimensional conformal field theories," *Phys. Rev. D*, vol. 84, p. 105017, 2011.

[64] H. Liu and S. J. Suh, "Entanglement Tsunami: Universal Scaling in Holographic Thermalization," *Phys. Rev. Lett.*, vol. 112, p. 011601, 2014.

[65] H. Liu and S. J. Suh, "Entanglement growth during thermalization in holographic systems," *Phys. Rev. D*, vol. 89, no. 6, p. 066012, 2014.

[66] H. A. Camargo, P. Caputa, D. Das, M. P. Heller, and R. Jefferson, "Complexity as a novel probe of quantum quenches: universal scalings and purifications," *Phys. Rev. Lett.*, vol. 122, no. 8, p. 081601, 2019.

[67] D. W. F. Alves and G. Camilo, "Evolution of complexity following a quantum quench in free field theory," *JHEP*, vol. 06, p. 029, 2018.

[68] M. Moosa, "Evolution of Complexity Following a Global Quench," *JHEP*, vol. 03, p. 031, 2018.

[69] S. Chapman, H. Marrochio, and R. C. Myers, "Holographic complexity in Vaidya spacetimes. Part I," *JHEP*, vol. 06, p. 046, 2018.

[70] S. Chapman, H. Marrochio, and R. C. Myers, "Holographic complexity in Vaidya spacetimes. Part II," *JHEP*, vol. 06, p. 114, 2018.

[71] D. S. Ageev, I. Y. Aref'eva, A. A. Bagrov, and M. I. Katsnelson, "Holographic local quench and effective complexity," *JHEP*, vol. 08, p. 071, 2018.

[72] D. Ageev, "Holographic complexity of local quench at finite temperature," *Phys. Rev. D*, vol. 100, no. 12, p. 126005, 2019.

[73] S. Bhattacharyya and S. Minwalla, "Weak Field Black Hole Formation in Asymptotically AdS Spacetimes," *JHEP*, vol. 09, p. 034, 2009.

[74] V. Balasubramanian, A. Bernamonti, J. de Boer, N. Copland, B. Craps, E. Keski-Vakkuri, B. Muller, A. Schafer, M. Shigemori, and W. Staessens, "Thermalization of Strongly Coupled Field Theories," *Phys. Rev. Lett.*, vol. 106, p. 191601, 2011.

[75] V. Balasubramanian, A. Bernamonti, J. de Boer, N. Copland, B. Craps, E. Keski-Vakkuri, B. Muller, A. Schafer, M. Shigemori, and W. Staessens, "Holographic Thermalization," *Phys. Rev. D*, vol. 84, p. 026010, 2011.

[76] M. Nozaki, T. Numasawa, and T. Takayanagi, "Holographic Local Quenches and Entanglement Density," *JHEP*, vol. 05, p. 080, 2013.

[77] M. Ammon and J. Erdmenger, *Gauge/Gravity Duality: Foundations and Applications*. Cambridge University Press, 2015.

[78] A. Zee, *Einstein Gravity in a Nutshell*. New Jersey: Princeton University Press, 5 2013.

[79] P. Di Francesco, P. Mathieu, and D. Sénéchal, *Conformal field theory*. Graduate texts in contemporary physics, New York, NY: Springer, 1997.

[80] M. Natsuume, *AdS/CFT Duality User Guide*, vol. 903. 2015.

[81] M. Rangamani and T. Takayanagi, *Holographic Entanglement Entropy*, vol. 931. Springer, 2017.

[82] L. Susskind, "Three Lectures on Complexity and Black Holes," SpringerBriefs in Physics, Springer, 10 2018.

[83] S. Chapman and G. Policastro, "Quantum computational complexity from quantum information to black holes and back," *Eur. Phys. J. C*, vol. 82, no. 2, p. 128, 2022.

[84] Y. Nakayama, "Scale invariance vs conformal invariance," *Phys. Rept.*, vol. 569, pp. 1–93, 2015.

[85] J. Polchinski, "Scale and Conformal Invariance in Quantum Field Theory," *Nucl. Phys. B*, vol. 303, pp. 226–236, 1988.

[86] S. S. Gubser, I. R. Klebanov, and A. M. Polyakov, "Gauge theory correlators from noncritical string theory," *Phys. Lett. B*, vol. 428, pp. 105–114, 1998.

[87] E. Witten, "Anti-de Sitter space and holography," *Adv. Theor. Math. Phys.*, vol. 2, pp. 253–291, 1998.

[88] P. Breitenlohner and D. Z. Freedman, "Positive Energy in anti-De Sitter Backgrounds and Gauged Extended Supergravity," *Phys. Lett. B*, vol. 115, pp. 197–201, 1982.

[89] I. R. Klebanov and E. Witten, "AdS / CFT correspondence and symmetry breaking," *Nucl. Phys. B*, vol. 556, pp. 89–114, 1999.

[90] M. Headrick, "Lectures on entanglement entropy in field theory and holography," 7 2019.

[91] C. Holzhey, F. Larsen, and F. Wilczek, "Geometric and renormalized entropy in conformal field theory," *Nucl. Phys. B*, vol. 424, pp. 443–467, 1994.

[92] P. Calabrese and J. L. Cardy, "Entanglement entropy and quantum field theory," *J. Stat. Mech.*, vol. 0406, p. P06002, 2004.

[93] P. Calabrese and J. Cardy, "Entanglement entropy and conformal field theory," *J. Phys. A*, vol. 42, p. 504005, 2009.

[94] M. Srednicki, "Entropy and area," *Phys. Rev. Lett.*, vol. 71, pp. 666–669, 1993.

[95] L. Susskind and E. Witten, "The Holographic bound in anti-de Sitter space," 5 1998.

[96] V. E. Hubeny, M. Rangamani, and T. Takayanagi, "A Covariant holographic entanglement entropy proposal," *JHEP*, vol. 07, p. 062, 2007.

[97] J. M. Maldacena, "Eternal black holes in anti-de Sitter," *JHEP*, vol. 04, p. 021, 2003.

[98] M. Van Raamsdonk, "Building up spacetime with quantum entanglement," *Gen. Rel. Grav.*, vol. 42, pp. 2323–2329, 2010.

[99] A. Einstein, B. Podolsky, and N. Rosen, "Can quantum-mechanical description of physical reality be considered complete?," *Phys. Rev.*, vol. 47, pp. 777–780, May 1935.

[100] J. Maldacena and L. Susskind, "Cool horizons for entangled black holes," *Fortsch. Phys.*, vol. 61, pp. 781–811, 2013.

[101] T. Hartman and J. Maldacena, "Time Evolution of Entanglement Entropy from Black Hole Interiors," *JHEP*, vol. 05, p. 014, 2013.

[102] V. E. Hubeny, "Extremal surfaces as bulk probes in AdS/CFT," *JHEP*, vol. 07, p. 093, 2012.

[103] L. Susskind, "The Typical-State Paradox: Diagnosing Horizons with Complexity," *Fortsch. Phys.*, vol. 64, pp. 84–91, 2016.

[104] L. Susskind, "Black Holes at Exp-time," 6 2020.

[105] L. Susskind and Y. Zhao, "Switchbacks and the Bridge to Nowhere," 8 2014.

[106] Y. Sekino and L. Susskind, "Fast Scramblers," *JHEP*, vol. 10, p. 065, 2008.

[107] P. Hayden and J. Preskill, "Black holes as mirrors: Quantum information in random subsystems," *JHEP*, vol. 09, p. 120, 2007.

[108] S. Lloyd, "Ultimate physical limits to computation," *Nature*, vol. 406, pp. 1047–1054, 2000.

[109] R.-G. Cai, S.-M. Ruan, S.-J. Wang, R.-Q. Yang, and R.-H. Peng, "Action growth for AdS black holes," *JHEP*, vol. 09, p. 161, 2016.

[110] S. H. Shenker and D. Stanford, "Black holes and the butterfly effect," *JHEP*, vol. 03, p. 067, 2014.

[111] D. A. Roberts, D. Stanford, and L. Susskind, "Localized shocks," *JHEP*, vol. 03, p. 051, 2015.

[112] S. H. Shenker and D. Stanford, "Multiple Shocks," *JHEP*, vol. 12, p. 046, 2014.

[113] D. Carmi, S. Chapman, H. Marrochio, R. C. Myers, and S. Sugishita, "On the Time Dependence of Holographic Complexity," *JHEP*, vol. 11, p. 188, 2017.

[114] A. Bernamonti, F. Bigazzi, D. Billo, L. Faggi, and F. Galli, "Holographic and QFT complexity with angular momentum," *JHEP*, vol. 11, p. 037, 2021.

[115] N. Engelhardt and r. Folkestad, "General bounds on holographic complexity," *JHEP*, vol. 01, p. 040, 2022.

[116] R. Auzzi, S. Baiguera, and G. Nardelli, "Volume and complexity for warped AdS black holes," *JHEP*, vol. 06, p. 063, 2018.

[117] A. R. Brown, D. A. Roberts, L. Susskind, B. Swingle, and Y. Zhao, "Complexity, action, and black holes," *Phys. Rev. D*, vol. 93, no. 8, p. 086006, 2016.

[118] A. Al Balushi, R. A. Hennigar, H. K. Kunduri, and R. B. Mann, "Holographic complexity of rotating black holes," *JHEP*, vol. 05, p. 226, 2021.

[119] R. Auzzi, S. Baiguera, M. Grassi, G. Nardelli, and N. Zenoni, "Complexity and action for warped AdS black holes," *JHEP*, vol. 09, p. 013, 2018.

[120] D. Kastor, S. Ray, and J. Traschen, "Enthalpy and the Mechanics of AdS Black Holes," *Class. Quant. Grav.*, vol. 26, p. 195011, 2009.

[121] L. V. Iliesiu, M. Mezei, and G. Sárosi, "The volume of the black hole interior at late times," *JHEP*, vol. 07, p. 073, 2022.

[122] R. Auzzi, S. Baiguera, G. B. De Luca, A. Legramandi, G. Nardelli, and N. Zenoni, "Geometry of quantum complexity," *Phys. Rev. D*, vol. 103, no. 10, p. 106021, 2021.

[123] M. A. Nielsen, M. R. Dowling, M. Gu, and A. C. Doherty, "Optimal control, geometry, and quantum computing," *Physical Review A*, vol. 73, 2006.

[124] M. R. Dowling and M. A. Nielsen, "The geometry of quantum computation," *Quantum Information and Computation*, vol. 8, pp. 861–899, 2008.

[125] J. Milnor, "Curvatures of Left Invariant Metrics on Lie Groups," *Adv. Math.*, vol. 21, pp. 293–329, 1976.

[126] V. I. Arnold, "Mathematical Methods of Classical Mechanics," vol. 60 of *Graduate Texts in Mathematics*, Springer, New York, NY, 1978.

[127] P. Petersen, "Riemannian Geometry," vol. 171 of *Graduate Texts in Mathematics*, Springer, New York, NY, 2006.

[128] J. M. Lee, "Riemannian Manifolds," in *An Introduction to Curvature*, vol. 176 of *Graduate Texts in Mathematics*, Springer-Verlag, 1997.

[129] D. V. Anosov, "Geodesic flows on closed Riemannian manifolds of negative curvature," vol. 90 of *Proceedings of the Steklov Institute of Mathematics*, American Mathematical Society, Providence, R.I., 1969.

[130] K. Burns and M. Gerber, "Real analytic Bernoulli geodesic flows on S2," *Ergodic Theory and Dynamical Systems*, vol. 9, no. 1, p. 27–45, 1989.

[131] R. J. Caginalp and S. Leutheusser, "Complexity in One- and Two-Qubit Systems," 10 2020.

[132] M. A. Nielsen and I. L. Chuang, *Quantum Computation and Quantum Information*. Cambridge University Press, 2010.

[133] A. L. Besse, "Einstein Manifolds," Ergebnisse der Mathematik und ihrer Grenzgebiete, Springer, Berlin, Heidelberg, 1987.

[134] T. Sakai, "Cut loci of Berger's spheres," *Hokkaido Mathematical Journal*, vol. 10, pp. 143–155, 1981.

[135] E. Poisson, *A Relativist's Toolkit: The Mathematics of Black-Hole Mechanics*. Cambridge University Press, 2004.

[136] A. Raychaudhuri, "Relativistic cosmology. 1.," *Phys. Rev.*, vol. 98, pp. 1123–1126, 1955.

[137] S. M. Carroll, *Spacetime and Geometry: An Introduction to General Relativity*. Cambridge University Press, 2019.

[138] A. V. Podobryaev, "Diameter of the Berger Sphere," *Mathematical Notes*, vol. 103, pp. 846–851, 05 2018.

[139] M. Gu, A. Doherty, and M. A. Nielsen, "Quantum control via geometry: An explicit example," *Physical Review A*, vol. 78, 2008.

[140] A. R. Brown, "A Quantum Complexity Lowerbound from Differential Geometry," 12 2021.

[141] R. Bishop, "A relation between volume, mean curvature, and diameter," *Notices of the American Mathematical Society*, vol. 10, p. 364, 1963.

[142] A. R. Brown, "Polynomial Equivalence of Complexity Geometries," 5 2022.

[143] R. Auzzi, S. Baiguera, A. Legramandi, G. Nardelli, P. Roy, and N. Zenoni, "On subregion action complexity in AdS_3 and in the BTZ black hole," *JHEP*, vol. 01, p. 066, 2020.

[144] R. Auzzi, S. Baiguera, A. Mitra, G. Nardelli, and N. Zenoni, "Subsystem complexity in warped AdS," *JHEP*, vol. 09, p. 114, 2019.

[145] S.-M. Ruan, "Purification Complexity without Purifications," *JHEP*, vol. 01, p. 092, 2021.

[146] O. Ben-Ami and D. Carmi, "On Volumes of Subregions in Holography and Complexity," *JHEP*, vol. 11, p. 129, 2016.

[147] R. Abt, J. Erdmenger, H. Hinrichsen, C. M. Melby-Thompson, R. Meyer, C. Northe, and I. A. Reyes, "Topological Complexity in AdS_3/CFT_2," *Fortsch. Phys.*, vol. 66, no. 6, p. 1800034, 2018.

[148] R. Abt, J. Erdmenger, M. Gerbershagen, C. M. Melby-Thompson, and C. Northe, "Holographic Subregion Complexity from Kinematic Space," *JHEP*, vol. 01, p. 012, 2019.

[149] M. Alishahiha, K. Babaei Velni, and M. R. Mohammadi Mozaffar, "Black hole subregion action and complexity," *Phys. Rev. D*, vol. 99, no. 12, p. 126016, 2019.

[150] E. Cáceres, J. Couch, S. Eccles, and W. Fischler, "Holographic Purification Complexity," *Phys. Rev. D*, vol. 99, no. 8, p. 086016, 2019.

[151] P. Roy and T. Sarkar, "Note on subregion holographic complexity," *Phys. Rev. D*, vol. 96, no. 2, p. 026022, 2017.

[152] P. Roy and T. Sarkar, "Subregion holographic complexity and renormalization group flows," *Phys. Rev. D*, vol. 97, no. 8, p. 086018, 2018.

[153] E. Bakhshaei, A. Mollabashi, and A. Shirzad, "Holographic Subregion Complexity for Singular Surfaces," *Eur. Phys. J. C*, vol. 77, no. 10, p. 665, 2017.

[154] A. Bhattacharya, K. T. Grosvenor, and S. Roy, "Entanglement Entropy and Subregion Complexity in Thermal Perturbations around Pure-AdS Spacetime," *Phys. Rev. D*, vol. 100, no. 12, p. 126004, 2019.

[155] B. Chen, W.-M. Li, R.-Q. Yang, C.-Y. Zhang, and S.-J. Zhang, "Holographic subregion complexity under a thermal quench," *JHEP*, vol. 07, p. 034, 2018.

[156] R. Auzzi, G. Nardelli, F. I. Schaposnik Massolo, G. Tallarita, and N. Zenoni, "On volume subregion complexity in Vaidya spacetime," *JHEP*, vol. 11, p. 098, 2019.

[157] L. Lehner, R. C. Myers, E. Poisson, and R. D. Sorkin, "Gravitational action with null boundaries," *Phys. Rev. D*, vol. 94, no. 8, p. 084046, 2016.

[158] K. Parattu, S. Chakraborty, B. R. Majhi, and T. Padmanabhan, "A Boundary Term for the Gravitational Action with Null Boundaries," *Gen. Rel. Grav.*, vol. 48, no. 7, p. 94, 2016.

[159] J. W. York, Jr., "Role of conformal three geometry in the dynamics of gravitation," *Phys. Rev. Lett.*, vol. 28, pp. 1082–1085, 1972.

[160] G. W. Gibbons and S. W. Hawking, "Action Integrals and Partition Functions in Quantum Gravity," *Phys. Rev. D*, vol. 15, pp. 2752–2756, 1977.

[161] G. Hayward, "Gravitational action for space-times with nonsmooth boundaries," *Phys. Rev. D*, vol. 47, pp. 3275–3280, 1993.

[162] S. Chapman, H. Marrochio, and R. C. Myers, "Complexity of Formation in Holography," *JHEP*, vol. 01, p. 062, 2017.

[163] S. Chapman, D. Ge, and G. Policastro, "Holographic Complexity for Defects Distinguishes Action from Volume," *JHEP*, vol. 05, p. 049, 2019.

[164] B. Czech, J. L. Karczmarek, F. Nogueira, and M. Van Raamsdonk, "The Gravity Dual of a Density Matrix," *Class. Quant. Grav.*, vol. 29, p. 155009, 2012.

[165] V. E. Hubeny and M. Rangamani, "Causal Holographic Information," *JHEP*, vol. 06, p. 114, 2012.

[166] A. C. Wall, "Maximin Surfaces, and the Strong Subadditivity of the Covariant Holographic Entanglement Entropy," *Class. Quant. Grav.*, vol. 31, no. 22, p. 225007, 2014.

[167] H. Casini, M. Huerta, and R. C. Myers, "Towards a derivation of holographic entanglement entropy," *JHEP*, vol. 05, p. 036, 2011.

[168] A. Lewkowycz and J. Maldacena, "Generalized gravitational entropy," *JHEP*, vol. 08, p. 090, 2013.

[169] M. Ghodrati, "Complexity growth in massive gravity theories, the effects of chirality, and more," *Phys. Rev. D*, vol. 96, no. 10, p. 106020, 2017.

[170] H. Dimov, R. C. Rashkov, and T. Vetsov, "Thermodynamic information geometry and complexity growth of a warped AdS black hole and the warped AdS_3/CFT_2 correspondence," *Phys. Rev. D*, vol. 99, no. 12, p. 126007, 2019.

[171] K. A. Moussa, G. Clement, and C. Leygnac, "The Black holes of topologically massive gravity," *Class. Quant. Grav.*, vol. 20, pp. L277–L283, 2003.

[172] A. Bouchareb and G. Clement, "Black hole mass and angular momentum in topologically massive gravity," *Class. Quant. Grav.*, vol. 24, pp. 5581–5594, 2007.

[173] G. Clement, "Warped AdS(3) black holes in new massive gravity," *Class. Quant. Grav.*, vol. 26, p. 105015, 2009.

[174] E. Tonni, "Warped black holes in 3D general massive gravity," *JHEP*, vol. 08, p. 070, 2010.

[175] G. Compere, S. Detournay, and M. Romo, "Supersymmetric Godel and warped black holes in string theory," *Phys. Rev. D*, vol. 78, p. 104030, 2008.

[176] S. Detournay and M. Guica, "Stringy Schrödinger truncations," *JHEP*, vol. 08, p. 121, 2013.

[177] P. Karndumri and E. O. Colgáin, "3D Supergravity from wrapped D3-branes," *JHEP*, vol. 10, p. 094, 2013.

[178] M. Banados, G. Barnich, G. Compere, and A. Gomberoff, "Three dimensional origin of Godel spacetimes and black holes," *Phys. Rev. D*, vol. 73, p. 044006, 2006.

[179] G. Barnich and G. Compere, "Conserved charges and thermodynamics of the spinning Godel black hole," *Phys. Rev. Lett.*, vol. 95, p. 031302, 2005.

[180] M. Gürses, "Perfect Fluid Sources in 2+1 Dimensions," *Class. Quant. Grav.*, vol. 11, no. 10, p. 2585, 1994.

[181] F. Jugeau, G. Moutsopoulos, and P. Ritter, "From accelerating and Poincare coordinates to black holes in spacelike warped AdS_3, and back," *Class. Quant. Grav.*, vol. 28, p. 035001, 2011.

[182] A. Akhavan and F. Omidi, "On the Role of Counterterms in Holographic Complexity," *JHEP*, vol. 11, p. 054, 2019.

[183] P. C. W. Davies, "Thermodynamics of Black Holes," *Proc. Roy. Soc. Lond. A*, vol. 353, pp. 499–521, 1977.

[184] M. Moosa, "Divergences in the rate of complexification," *Phys. Rev. D*, vol. 97, no. 10, p. 106016, 2018.

[185] Y. Ling, Y. Liu, and C.-Y. Zhang, "Holographic Subregion Complexity in Einstein-Born-Infeld theory," *Eur. Phys. J. C*, vol. 79, no. 3, p. 194, 2019.

[186] Y.-T. Zhou, M. Ghodrati, X.-M. Kuang, and J.-P. Wu, "Evolutions of entanglement and complexity after a thermal quench in massive gravity theory," *Phys. Rev. D*, vol. 100, no. 6, p. 066003, 2019.

[187] Y. Ling, Y. Liu, C. Niu, Y. Xiao, and C.-Y. Zhang, "Holographic Subregion Complexity in General Vaidya Geometry," *JHEP*, vol. 11, p. 039, 2019.

[188] N. Zenoni, R. Auzzi, S. Caggioli, M. Martinelli, and G. Nardelli, "A falling magnetic monopole as a holographic local quench," *JHEP*, vol. 11, p. 048, 2021.

[189] N. Zenoni, "A falling magnetic monopole as a local quench," *PoS*, vol. EPS-HEP2021, p. 722, 2022.

[190] P. Calabrese and J. Cardy, "Entanglement and correlation functions following a local quench: a conformal field theory approach," *J. Stat. Mech.*, vol. 0710, no. 10, p. P10004, 2007.

[191] T. Shimaji, T. Takayanagi, and Z. Wei, "Holographic Quantum Circuits from Splitting/Joining Local Quenches," *JHEP*, vol. 03, p. 165, 2019.

[192] M. Nozaki, T. Numasawa, and T. Takayanagi, "Quantum Entanglement of Local Operators in Conformal Field Theories," *Phys. Rev. Lett.*, vol. 112, p. 111602, 2014.

[193] P. Caputa, M. Nozaki, and T. Takayanagi, "Entanglement of local operators in large-N conformal field theories," *PTEP*, vol. 2014, p. 093B06, 2014.

[194] M. Nozaki, "Notes on Quantum Entanglement of Local Operators," *JHEP*, vol. 10, p. 147, 2014.

[195] G. 't Hooft, "Magnetic Monopoles in Unified Gauge Theories," *Nucl. Phys. B*, vol. 79, pp. 276–284, 1974.

[196] A. Jahn and T. Takayanagi, "Holographic entanglement entropy of local quenches in AdS4/CFT3: a finite-element approach," *J. Phys. A*, vol. 51, no. 1, p. 015401, 2018.

[197] D. S. Ageev, "Sharp disentanglement in holographic charged local quench," 3 2020.

[198] A. Esposito, S. Garcia-Saenz, A. Nicolis, and R. Penco, "Conformal solids and holography," *JHEP*, vol. 12, p. 113, 2017.

[199] E. Witten, "Multitrace operators, boundary conditions, and AdS / CFT correspondence," 12 2001.

[200] M. Berkooz, A. Sever, and A. Shomer, "'Double trace' deformations, boundary conditions and space-time singularities," *JHEP*, vol. 05, p. 034, 2002.

[201] I. Papadimitriou, "Multi-Trace Deformations in AdS/CFT: Exploring the Vacuum Structure of the Deformed CFT," *JHEP*, vol. 05, p. 075, 2007.

[202] T. Faulkner, G. T. Horowitz, and M. M. Roberts, "Holographic quantum criticality from multi-trace deformations," *JHEP*, vol. 04, p. 051, 2011.

[203] M. M. Caldarelli, A. Christodoulou, I. Papadimitriou, and K. Skenderis, "Phases of planar AdS black holes with axionic charge," *JHEP*, vol. 04, p. 001, 2017.

[204] A. R. Lugo and F. A. Schaposnik, "Monopole and dyon solutions in AdS space," *Phys. Lett. B*, vol. 467, pp. 43–53, 1999.

[205] A. R. Lugo, E. F. Moreno, and F. A. Schaposnik, "Monopole solutions in AdS space," *Phys. Lett. B*, vol. 473, pp. 35–42, 2000.

[206] G. T. Horowitz and N. Itzhaki, "Black holes, shock waves, and causality in the AdS / CFT correspondence," *JHEP*, vol. 02, p. 010, 1999.

[207] V. Balasubramanian and P. Kraus, "A Stress tensor for Anti-de Sitter gravity," *Commun. Math. Phys.*, vol. 208, pp. 413–428, 1999.

[208] S. de Haro, S. N. Solodukhin, and K. Skenderis, "Holographic reconstruction of space-time and renormalization in the AdS / CFT correspondence," *Commun. Math. Phys.*, vol. 217, pp. 595–622, 2001.

[209] T. Faulkner, A. Lewkowycz, and J. Maldacena, "Quantum corrections to holographic entanglement entropy," *JHEP*, vol. 11, p. 074, 2013.

[210] C. A. Agón, S. F. Lokhande, and J. F. Pedraza, "Local quenches, bulk entanglement entropy and a unitary Page curve," *JHEP*, vol. 08, p. 152, 2020.

[211] T. Albash and C. V. Johnson, "Holographic Studies of Entanglement Entropy in Superconductors," *JHEP*, vol. 05, p. 079, 2012.

[212] H. Casini, H. Liu, and M. Mezei, "Spread of entanglement and causality," *JHEP*, vol. 07, p. 077, 2016.

[213] D. D. Blanco, H. Casini, L.-Y. Hung, and R. C. Myers, "Relative Entropy and Holography," *JHEP*, vol. 08, p. 060, 2013.

[214] J. Bhattacharya, M. Nozaki, T. Takayanagi, and T. Ugajin, "Thermodynamical Property of Entanglement Entropy for Excited States," *Phys. Rev. Lett.*, vol. 110, no. 9, p. 091602, 2013.

[215] A. O'Bannon, J. Probst, R. Rodgers, and C. F. Uhlemann, "First law of entanglement rates from holography," *Phys. Rev. D*, vol. 96, no. 6, p. 066028, 2017.

[216] I. Akal, "Weighting gates in circuit complexity and holography," *PTEP*, vol. 2021, no. 9, p. 093B02, 2021.

[217] S. Chapman, J. Eisert, L. Hackl, M. P. Heller, R. Jefferson, H. Marrochio, and R. C. Myers, "Complexity and entanglement for thermofield double states," *SciPost Phys.*, vol. 6, no. 3, p. 034, 2019.

[218] G. Di Giulio and E. Tonni, "Subsystem complexity after a global quantum quench," *JHEP*, vol. 05, p. 022, 2021.

[219] A. Mounim and W. Mück, "Reparameterization dependence is useful for holographic complexity," *JHEP*, vol. 07, p. 010, 2021.

[220] A. Mounim and W. Mück, "Reparametrization dependence and holographic complexity of black holes," *Phys. Rev. D*, vol. 105, no. 2, p. 026024, 2022.

[221] P. Bueno, V. S. Min, A. J. Speranza, and M. R. Visser, "Entanglement equilibrium for higher order gravity," *Phys. Rev. D*, vol. 95, no. 4, p. 046003, 2017.

[222] M. Alishahiha, A. Faraji Astaneh, A. Naseh, and M. H. Vahidinia, "On complexity for F(R) and critical gravity," *JHEP*, vol. 05, p. 009, 2017.

[223] W.-D. Guo, S.-W. Wei, Y.-Y. Li, and Y.-X. Liu, "Complexity growth rates for AdS black holes in massive gravity and $f(R)$ gravity," *Eur. Phys. J. C*, vol. 77, no. 12, p. 904, 2017.

[224] M. M. Qaemmaqami, "Complexity growth in minimal massive 3D gravity," *Phys. Rev. D*, vol. 97, no. 2, p. 026006, 2018.

[225] P. Caputa, J. Simón, A. Stikonas, and T. Takayanagi, "Quantum Entanglement of Localized Excited States at Finite Temperature," *JHEP*, vol. 01, p. 102, 2015.

[226] A. Bernamonti, F. Galli, J. Hernandez, R. C. Myers, S.-M. Ruan, and J. Simón, "First Law of Holographic Complexity," *Phys. Rev. Lett.*, vol. 123, no. 8, p. 081601, 2019.

[227] A. Bernamonti, F. Galli, J. Hernandez, R. C. Myers, S.-M. Ruan, and J. Simón, "Aspects of The First Law of Complexity," 2 2020.

[228] G. Di Giulio and E. Tonni, "Subsystem complexity after a local quantum quench," *JHEP*, vol. 08, p. 135, 2021.

[229] T. Ugajin, "Two dimensional quantum quenches and holography," 11 2013.

List of publications

- N. Zenoni, "A falling magnetic monopole as a local quench," *PoS*, vol. EPS-HEP2021, p. 722, 2022.
- N. Zenoni, R. Auzzi, S. Caggioli, M. Martinelli and G. Nardelli, "A falling magnetic monopole as a holographic local quench," *JHEP*, vol. 11, p. 048, 2021 [arXiv:2106.13757 [hep-th]].
- R. Auzzi, S. Baiguera, G. B. De Luca, A. Legramandi, G. Nardelli and N. Zenoni, "Geometry of quantum complexity," *Phys. Rev. D*, vol. 103, no.10, p. 106021, 2021 [arXiv:2011.07601 [hep-th]].
- R. Auzzi, S. Baiguera, A. Legramandi, G. Nardelli, P. Roy and N. Zenoni, "On subregion action complexity in AdS_3 and in the BTZ black hole," *JHEP*, vol. 01, p. 066, 2020 [arXiv:1910.00526 [hep-th]].
- R. Auzzi, G. Nardelli, F. I. Schaposnik Massolo, G. Tallarita and N. Zenoni, "On volume subregion complexity in Vaidya spacetime," *JHEP*, vol. 11, p. 098, 2019 [arXiv:1908.10832 [hep-th]].
- R. Auzzi, S. Baiguera, A. Mitra, G. Nardelli and N. Zenoni, "Subsystem complexity in warped AdS," *JHEP*, vol. 09, p. 114, 2019 [arXiv:1906.09345 [hep-th]].

Before the start of the PhD:

- R. Auzzi, S. Baiguera, M. Grassi, G. Nardelli and N. Zenoni, "Complexity and action for warped AdS black holes," *JHEP*, vol. 09, p. 013, 2018 [arXiv:1806.06216 [hep-th]].

FACOLTÀ DI SCIENZE MATEMATICHE, FISICHE E NATURALI
DIPARTIMENTO DI MATEMATICA E FISICA
THEORETICAL PHYSICS GROUP
Via della Garzetta 48
25133 Brescia
nicolo.zenoni@unicatt.it

FACULTY OF SCIENCE
DEPARTMENT OF PHYSICS AND ASTRONOMY
THEORETICAL PHYSICS GROUP
Celestijnenlaan 200D
B-3001 Leuven
nicolo.zenoni@kuleuven.be
https://www.kuleuven.be/wieiswie/en/person/00132386